



# Atomic-scale spin-sensing with a single molecule at the apex of a scanning tunneling microscope

Benjamin Verlhac

## ► To cite this version:

Benjamin Verlhac. Atomic-scale spin-sensing with a single molecule at the apex of a scanning tunneling microscope. Physics [physics]. Université de Strasbourg, 2019. English. ⟨NNT : 2019STRAE007⟩. ⟨tel-02303489⟩

**HAL Id: tel-02303489**

**<https://theses.hal.science/tel-02303489v1>**

Submitted on 2 Oct 2019

**HAL** is a multi-disciplinary open access archive for the deposit and dissemination of scientific research documents, whether they are published or not. The documents may come from teaching and research institutions in France or abroad, or from public or private research centers.

L'archive ouverte pluridisciplinaire **HAL**, est destinée au dépôt et à la diffusion de documents scientifiques de niveau recherche, publiés ou non, émanant des établissements d'enseignement et de recherche français ou étrangers, des laboratoires publics ou privés.



HAL Authorization



*ÉCOLE DOCTORALE Physique Chimie-Physique (ED 182)*

Institut de Physique et Chimie des Matériaux de Strasbourg

**THÈSE** présentée par :

**Benjamin Verlhac**

soutenue le : **03 mai 2019**

pour obtenir le grade de : **Docteur de l'université de Strasbourg**

Discipline/ Spécialité : Nano-Physique

**Atomic-scale spin-sensing with a single  
molecule at the apex of a scanning  
tunneling microscope**

**THÈSE dirigée par :**  
**M. LIMOT Laurent**

Chargé de Recherche, IPCMS-CNRS, Université de Strasbourg

**RAPPORTEURS :**  
**M. BRUNE Harald**  
**M. RODITCHEV Dimitri**

Professeur, EPFL-LNS, Lausanne  
Professeur, INSP-CNRS-UPMC, Paris

---

**AUTRES MEMBRES DU JURY :**

**Mme SICOT Muriel**  
**M. TERNES Markus**  
**M. BULOU Hervé**

Chargée de Recherche, IJL-CNRS-Université de Lorraine, Nancy  
Professeur, RWTH-Aachen University  
Chargé de Recherche, IPCMS-CNRS, Université de Strasbourg









# Acknowledgements

For giving me the opportunity to realize my thesis, I would first like to thank the direction of the IPCMS, the direction of the University of Strasbourg and the direction of the Ecole Doctorale.

I would like to thank also the members of the jury: Dimitri Roditchev, Harald Brune, Muriel Sicot, Markus Ternes and Hervé Bulou. I thank you for reviewing my work and granting me the title of "Docteur de la Physique".

I have grown up during these four years and it is mainly due to my PhD supervisor Laurent Limot. There are many kinds of supervisors and Laurent belongs to the best kind: the one that cares about his students. Not all PhD supervisors invest themselves as much as he did, and I'll be always thankful for that. All the discussions that we had, the scientific ones as well as the non-scientific ones (like the discussions about the MCU), made these years really enjoyable and created a relationship far beyond subordination.

Of course we were not alone in the team, so let's continue by thanking Nicolas "The Legend" Bachellier. I'd like to thank him for breaking so many things in the machine that I could use an almost brand new STM during my thesis. The tales of his misfortune will be known by countless generations of students in the STM team and beyond. Jokes apart, I appreciated the good scientist and the good friend. However, his enjoyment of races in the mud involving electroshock is still dreadful to me. Then I would like to thank is Maider Ormaza. Discussions were always interesting with her, in particular, concerning experimental results and their interpretations. Her stubbornness to believe on those, made me realize many iterations of measurements with a high standard of quality. The nice-looking results I show in this thesis are really due to her pushing me to do better, even though I tend to be a quality maniac. Last, I'd like to thank Léo "Jesus" Garnier which is a skillful PhD student and a promising legend worthy successor of Nicolas. We had many funny moments in and out the lab.

In the lab, we were not the only one doing STM, the other team was lead by Guillaume Schull which I thank for the many fruitful conversations and for the many excellent advices he

gave me. If we were a family with Laurent the father, Guillaume the uncle, I should next thank Fabrice Scheurer that would be the granpa. I've learnt a lot at his contact, including during the week at the synchrotron. He has always been of good help and of good advice. Let's go now to the cousins, Guillaume's PhD students. I'll start with Dr. M.C. Chong, one of the nicest guy I've ever met, a shame he couldn't attend my PhD defense. When I started he was already experienced and could give me useful advices about the chores in the lab. Then I'd like to thank Benjamin Doppagne, the guy with too many nicknames. We've shared the same office for 3 years and I must admit, we were not really efficient. I'd like to thank Luis Parra Lopez which is also a nice guy, so nice that he gave us a plastic poop in our office. We would not have these results without the help of Virginie Speisser who took care for so many things for us in the lab, so thank you. Seeing you terrorizing students was always delightful. I would like to thank Michelangelo Romeo too, for all his help and jokes. Together we coded the program of the pump-probe setup that unfortunately, I couldn't test before my defense. I will finish by thanking all the rest of the DSI including Hervé Bulou, Christine Goyhenex, Adele Carrado, Jacques Faerber, Olivier Bengone and Corinne Bouillet.

I would also like to thank the people of the technical support for their help and all other people from the IPCMS, students and researchers.

Finally I want to thank my family for their support. I will finish by the most important person, the one that supported this for 4 years, Agathe that shares my life for nearly 10 years and without whose support it would have been difficult to finish my thesis.





# Contents

<b>Résumé</b>	<b>III</b>
0.1 Introduction (Chapitre 1)	III
0.1.1 Mise en contexte du projet de thèse	III
0.1.2 Introduction générale	III
0.1.3 STM polarisé en spin	V
0.1.4 Effet Kondo	VI
0.1.5 Spectroscopie d'excitation de spin	VIII
0.2 Microscopie et spectroscopie à effet tunnel/ dispositif expérimental (Chapitre 2)	X
0.3 Caractérisation de l'adsorption et des propriétés magnétique du nickelocène (Chapitre 3)	XII
0.3.1 Détermination de l'adsorption du nickelocène	XII
0.3.2 Propriétés magnétiques du nickelocène	XIV
0.4 Fonctionnalisation de la pointe par un nickelocène et changement de spin (Chapitre 4)	XV
0.4.1 Adsorption et propriétés du nickelocène sur la pointe	XV
0.4.2 Changement de spin	XVII
0.5 Détection de spin au moyen d'une pointe fonctionnalisée par un nickelocène (Chapitre 5)	XVIII
0.5.1 Preuve de concept : Fe/Cu(100)	XIX
0.5.2 Application : Co(111)/Cu(111)	XXI
0.6 Conclusion	XXIII
<b>1 Single-spin detection with STM</b>	<b>1</b>
1.1 Spin-polarized STM	3



1.2	Detecting a Kondo atom with STM . . . . .	6
1.2.1	Overview . . . . .	6
1.2.2	Tunneling into a single Kondo impurity . . . . .	9
1.3	Spin excitation spectroscopy . . . . .	12
1.3.1	Working principle . . . . .	12
1.3.2	Magnetic anisotropy . . . . .	15
1.3.3	Spin-spin coupling . . . . .	17
1.3.4	Spin pumping . . . . .	19
1.3.5	Kondo scattering . . . . .	20
1.4	Conclusion . . . . .	22
<b>2</b>	<b>Scanning tunneling microscopy</b>	<b>23</b>
2.1	STM basics . . . . .	24
2.1.1	One dimensional tunnel barrier . . . . .	24
2.1.2	Bardeen's theory . . . . .	25
2.1.3	WKB theory . . . . .	28
2.2	Scanning tunneling spectroscopy . . . . .	29
2.2.1	Inelastic tunneling . . . . .	30
2.3	Experimental detection . . . . .	30
2.3.1	Lock-in signal . . . . .	30
2.3.2	Line shape broadening in STS . . . . .	33
2.3.3	Line shape broadening in IETS . . . . .	35
2.4	Experimental setup . . . . .	36
2.4.1	Principle of image acquisition . . . . .	36
2.4.2	The microscope used in this thesis . . . . .	37
<b>3</b>	<b>Nickelocene on a copper surface</b>	<b>41</b>
3.1	Adsorption of nickelocene on copper . . . . .	43
3.1.1	Sample preparation . . . . .	43
3.1.2	Isolated nickelocene . . . . .	45
3.1.3	Self-assembled layers . . . . .	47
3.2	Magnetism of adsorbed nickelocene . . . . .	52
3.2.1	Magnetism of free nickelocene . . . . .	52

3.2.2	Spin-polarized DFT calculations . . . . .	54
3.2.3	XMCD measurements . . . . .	55
3.3	Spin excitation and electron scattering . . . . .	57
3.3.1	Spin excitation spectroscopy of nickelocene . . . . .	57
3.3.2	Inelastic versus elastic conductance . . . . .	60
3.3.3	Electron scattering . . . . .	62
3.4	Conclusion . . . . .	64
<b>4</b>	<b>Nickelocene on the apex of a STM tip</b>	<b>67</b>
4.1	Nickelocene-terminated tip . . . . .	68
4.1.1	Adsorption of nickelocene on the tip apex . . . . .	68
4.1.2	Spin excitation spectroscopy on the tip apex . . . . .	69
4.2	Double spin excitation . . . . .	73
4.3	Controlled spin switching of a nickelocene tip . . . . .	76
4.3.1	Tunnel versus contact regime . . . . .	76
4.3.2	Discussion . . . . .	78
4.3.3	Evidence for spin switching: DFT calculations . . . . .	82
4.4	Conclusion . . . . .	86
<b>5</b>	<b>Spin-spin coupling with a nickelocene tip</b>	<b>87</b>
5.1	Magnetically probing a Fe adatom . . . . .	89
5.1.1	Spin excitation spectra above a Fe atom . . . . .	89
5.1.2	Exchange field between Fe and nickelocene . . . . .	91
5.1.3	Spin asymmetry above Fe . . . . .	95
5.1.4	Computed electronic structure and spin polarization . . . . .	97
5.2	Detecting the surface magnetism of Co islands . . . . .	99
5.2.1	Adsorption of nickelocene in the presence of Co islands . . . . .	99
5.2.2	Spin excitation spectra above a Co island . . . . .	100
5.2.3	Imaging the exchange interaction . . . . .	102
5.2.4	Spin polarization of the islands . . . . .	105
5.3	Conclusion . . . . .	106
	<b>Conclusion and perspectives</b>	<b>109</b>

---

<b>Appendix A</b>	<b>Appendix: X-ray adsorption spectroscopy</b>	<b>115</b>
A.1	Generalities . . . . .	115
A.2	Sumrules . . . . .	116
<b>Bibliography</b>		<b>119</b>
<b>List of figures</b>		<b>133</b>
<b>Curriculum Vitae</b>		<b>137</b>
<b>Publications and presentations</b>		<b>139</b>



# Résumé

## 0.1 Introduction (Chapitre 1)

### 0.1.1 Mise en contexte du projet de thèse

La thèse présentée ici est une thèse expérimentale dont le principal instrument utilisé est le microscope à effet tunnel (STM). De manière générale, cette thèse porte sur l'étude du magnétisme d'objets uniques et de leur interaction avec un environnement métallique. Ce travail fut effectué en ultra-vide et à basse température (2.4 K) pour des soucis de contamination et de stabilité des objets étudiés. Le travail expérimental réalisé au cours de la thèse faisait partie d'un projet ANR dont le support théorique fut réalisé par les équipes de M.L. Bocquet, Directrice de Recherche à ENS-CNRS-UPMC à Paris et N. Lorente, Professeur au CFM à San Sebastian en Espagne. Au cours de la thèse, j'ai aussi eu l'occasion d'effectuer des mesures de dichroïsme magnétique de rayons X au synchrotron SOLEIL, au sein de la ligne Deimos gérée par Phillipe Orhesser. Les résultats de ces mesures sont présentés dans le chapitre 3.

### 0.1.2 Introduction générale

Ma thèse se concentre donc sur la détection et la manipulation de spins au sein d'une jonction tunnel. Cela s'inscrit dans l'étude du magnétisme pour des objets élémentaires tels que les atomes et les molécules. Ce genre d'étude permet le développement de savoirs et de techniques ayant pour finalité l'utilisation de spins en tant que bit de données pour des systèmes de stockage de très haute densité. Cette finalité a motivé le développement nouvelles de techniques de détection sensibles au spin jouissant d'une très haute résolution spatiale. Nous pouvons citer comme exemple la microscopie à force de résonance magnétique (MRFM), nano-SQUIDs, ou la microscopie utilisant des centres NV (pour nitrogen vacancy) qui parviennent à obtenir une

résolution de l'ordre du nanomètre. Ma thèse porte ainsi sur l'application de cette thématique au microscope à effet tunnel (STM) et exploite les possibilités de fonctionnalisation de cet instrument afin d'obtenir une sensibilité liée au spin d'un objet à l'échelle atomique.

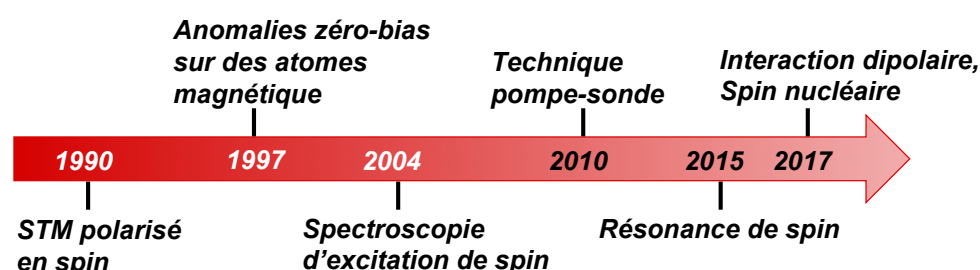


FIGURE 1 : **Détection du magnétisme de surface sous STM.** Flèche temporelle des avancées notables de la détection du magnétisme de surface sous STM.

En effet, le STM a fait ses preuves en terme de détection de spin ou de détection du magnétisme de surface. La flèche temporelle en figure 1 présente les avancées les plus notables dans la détection du magnétisme sous STM. Ces avancées concernent la détection de signatures dans la conductance différentielle propres aux propriétés de spin d'objets uniques (anomalies à bias zéro et spectroscopie d'excitations de spin pour des atomes uniques [1–3]). Mais elles concernent aussi le développement de techniques telles que le STM polarisé en spin (SP-STM). Ces dernières années, dans la continuité de ces avancées, d'autres techniques ont été développées comme les mesures temporelles au moyen de la technique du pompe-sonde tout électrique [4] mais surtout comme l'implantation de la résonance de spin au sein d'un STM [5]. Cette dernière technique a ouvert la voie à la détection du couplage hyperfin au sein d'un atome ou encore du couplage dipolaire entre deux atomes sur une surface [6–9].

Dans ce contexte de détection de spin sous STM, ma thèse a donc pour but de démontrer qu'en utilisant un objet présentant une excitation de spin au bout de la pointe d'un STM nous pouvons développer une technique de caractérisation d'objets magnétiques en surface. C'est une approche d'optimisation du STM afin de donner à sa pointe-sonde des propriétés liées à un spin unique. L'objet sur la pointe que nous avons étudié est la molécule de nickelocène ( $\text{NiCp}_2$ ) dont l'étude sur une surface  $\text{Cu}(100)$  est montrée en chapitre 3. L'étude de la pointe moléculaire est, quant à elle, traitée en chapitre 4 et l'utilisation de cette pointe moléculaire pour sonder un objet magnétique en surface est présentée dans le chapitre 5.

Le premier chapitre de ma thèse se concentre donc sur l'introduction à cette thématique de

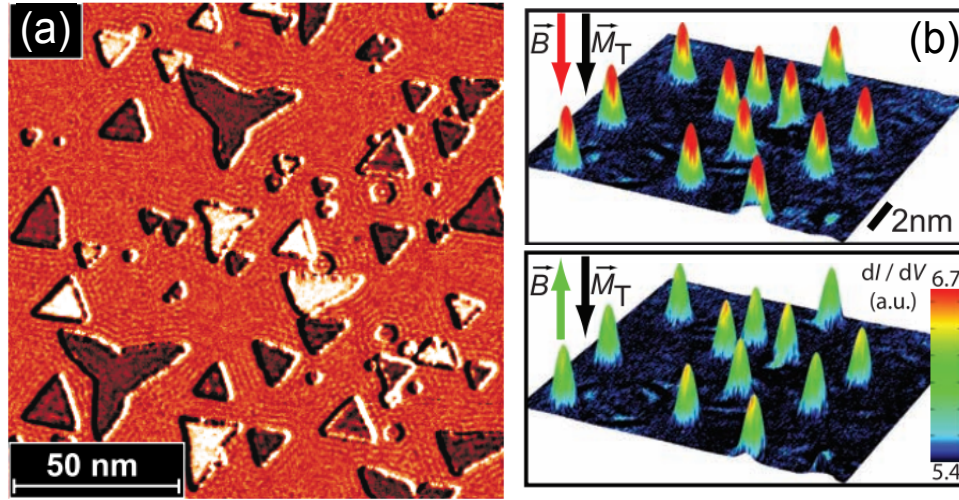


FIGURE 2 : **STM Polarisé en spin.** (a) Carte de conductance différentielle acquise avec un pointe STM magnétique. Elle montre des îlots de cobalt sur Cu(111). Ces îlots présentent un signal polarisé en spin qui distingue les îlots dont les aimantations sont alignées ou antialignées avec l'aimantation de la pointe. (Extrait de [10]). (b) Carte 3D d'atomes de Co adsorbés sur Pt(111). Le signal de cette carte est la conductance différentielle qui présente une différence suivant l'orientation du champ magnétique appliqué par rapport à l'aimantation de la pointe. Cette différence observée est ensuite utilisée pour réaliser une courbe de polarisation de ces atomes en fonction du champ appliqué. (Extrait de [11].)

détection du magnétisme en surface sous STM et détaille les notions d'intérêts que sont le STM polarisé en spin, l'excitation de spin et l'effet Kondo dont les prochaines sections donneront les grandes lignes.

### 0.1.3 STM polarisé en spin

L'utilisation d'une pointe magnétique pour sonder des objets magnétique en surface fut expérimentée au début des années 1990 par R.Wiesendanger [12]. Cette étude fut le point de départ du STM polarisé en spin (SP-STM) qui a grandement contribué à l'étude du magnétisme de surface. Le principe du SP-STM donc repose sur l'utilisation d'une pointe magnétique pour sonder des objets en surface eux-mêmes magnétiques. Le modèle de Wortmann [13] permet d'expliquer les observations réalisées en SP-STM. En effet ce modèle repose sur l'expression de la conductance différentielle incluant un terme dépendant des aimantations respectives de la pointe et de l'objet en surface comme suit :

$$dI/dV(V) = \rho_t \rho_s(eV) + M_t M_s(eV) \cos \theta, \quad (1)$$

Avec  $\rho_s$  et  $\rho_t$  les densités d'états respectives de la surface et de la pointe,  $M_s$  et  $M_t$  les aimantations respectives de la surface et de la pointe et  $\theta$  l'angle entre les deux. Sur la carte de conductance différentielle en figure 2(a) nous observons une différence de signal entre les différents îlots de Co sur Cu(111) [10]. Ces îlots présentent une aimantation hors du plan avec les deux sens d'aimantation possibles. Cette carte fut acquise au moyen d'une pointe magnétique avec une aimantation en partie dans l'axe normal à la surface. Le contraste observé est donc dû, si on se réfère au modèle de Wortmann à la différence de conductance entre la configurations des deux aimantations de manière alignée ou anti-alignée.

Le SP-STM a ainsi ouvert la voie au développement de techniques de détection du magnétisme de spins uniques. Un exemple notable est la réalisation de courbes d'aimantation d'atomes uniques (SAMC) permettant de caractériser directement le comportement de moments magnétiques d'atomes en surface [11]. En figure 2(b), nous avons deux cartes de conductance différentielle réalisées avec une pointe magnétique au dessus d'atome de Co sur Pt(111). Ces cartes ont été réalisées pour deux orientations du champ magnétique externe, à savoir alignée avec l'aimantation de la pointe ou anti-alignée avec celle-ci. Ces atomes possèdent un comportement paramagnétique sous l'effet du champ magnétique. Cela permet d'obtenir la différence de signal observée avec une conductance plus élevée dans le cas où le champ magnétique, et par conséquent les moments magnétiques des atomes, sont alignés à l'aimantation de la pointe. L'exploitation de ce contraste en faisant varier l'intensité du champ magnétique permet au final de réaliser une courbe de polarisation de ces atomes.

#### 0.1.4 Effet Kondo

Cette thèse fait apparaître en son sein deux marqueurs spectroscopiques liés à un changement de moment de spin d'une molécule. Le premier de ces marqueurs qui est présenté est l'effet Kondo. Historiquement, il fut observé dans la conduction de l'or possédant des impuretés de Fe [14]. Le comportement attendu aurait été que la résistance diminue jusqu'à une valeur qui serait uniquement due aux défauts de structure et aux impuretés. Hors, il a été observé qu'en diminuant la température, la résistance de ce matériau atteint un minimum pour augmenter ensuite en dessous d'une certaine température.

Afin d'expliquer cette anomalie, plusieurs modèles furent développés. Le premier, par P.W.



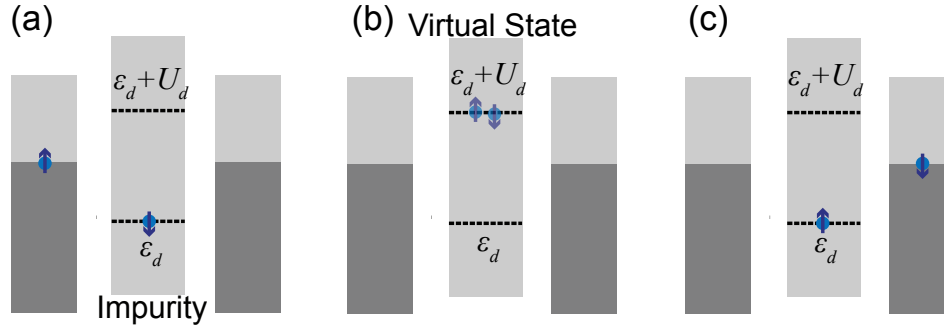


FIGURE 3 : **Principe de l'effet Kondo.** Schémas d'une jonction comprenant deux électrodes et une impureté. Cette impureté est couplée aux bandes électroniques des électrodes. Un électron passe de l'électrode de gauche (a) vers l'électrode de droite (c) en passant par un état virtuel dans l'impureté (b). Ce processus a pour conséquence de changer le moment de spin de l'impureté.  $\epsilon_d$  correspond à l'énergie de l'orbital  $d$  partiellement occupée (qui présente donc une polarisation en spin) et  $\epsilon_d + U_d$  l'énergie liée à l'occupation totale de l'orbital. L'état fondamental de l'impureté étant à  $\epsilon_d$ .

Anderson [15], exprimait cette anomalie par un mélange des orbitales  $d$  des impuretés et les bandes électroniques  $s$  du métal environnant. Quelques années plus tard, J. Kondo formula cette anomalie en terme de couplage d'échange entre l'impureté et les bandes du métal, provoquant de la diffusion de spin [16]. La figure 3 schématise la conduction d'un électron au travers d'une impureté en respectant le processus de diffusion de spin lié à l'effet Kondo. En effet, ce qu'on remarque dans ce schéma c'est que l'on assiste à une inversion du moment magnétique de l'électron et un changement du moment magnétique de l'électron de l'impureté (et donc du moment magnétique de l'impureté elle-même) par la réalisation de ce processus.

Les hamiltoniens d'Anderson et de Kondo sont traités dans le chapitre correspondant (§ 1.2). Le message principal de cette section est cette formulation de l'effet Kondo par un couplage d'échange  $\mathcal{J}$  entre l'impureté et les bandes électronique du métal. On peut associer une grandeur à ce couplage, la température Kondo  $T_K$ , qui sert de valeur critique entre les régimes de forte interaction ( $T < T_K$ ) et de faible interaction ( $T > T_K$ ) schématisé en figure 4. Enfin les modèles d'Anderson et de Kondo sont reliés par la transformation de Schrieffer et Wolff [17], qui permet d'exprimer  $\mathcal{J}$  en fonction de  $\epsilon_d$  et  $U_d$  paramètres liés à la configuration électronique de l'impureté.

La fin de la section sur l'effet Kondo montre des exemples de résonances Kondo étudiées

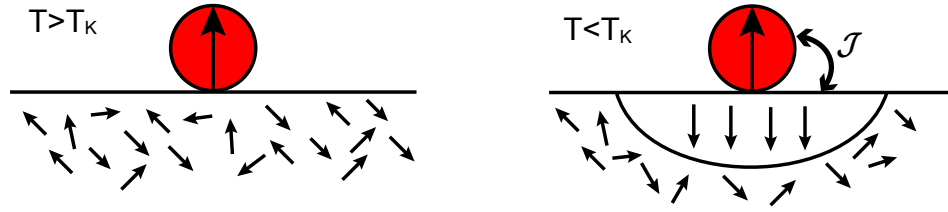


FIGURE 4 : **Couplage d'échange avec le bain électronique.** Représentation de la signification physique de  $T_K$ . Pour une température supérieure à  $T_K$ , l'impureté n'est pas affectée par l'écrantage dû aux électrons du métal. Pour une température inférieure à  $T_K$  l'écrantage par les électrons du métal devient non négligeable et définit l'état fondamental de l'impureté comme  $(|\uparrow, \downarrow\rangle + |\downarrow, \uparrow\rangle)/\sqrt{2}$ .

en STS [18–20]. Ces résonances peuvent prendre la forme d'un pic au niveau de Fermi qui peut être simulé au moyen de la fonction de Frota [21] dont la section §1.2 fournit quelques précisions que je ne détaillerai pas ici.

### 0.1.5 Spectroscopie d'excitation de spin

Le second et principal marqueur spectroscopique lié au spin rencontré au sein de cette thèse est l'excitation de spin. Ce genre d'excitation est observé au sein d'un STM au moyen de la spectroscopie inélastique (IETS) qui fait intervenir du tunneling inélastique. Cela veut dire que des canaux de conduction apparaissent à certaines énergies seuils et correspondent aux électrons cédant de l'énergie à un système en franchissant la barrière tunnel. Ce tunneling inélastique est brièvement détaillé en chapitre 2.

Les excitations de spin furent pour la première fois observées par A. Heinrich en 2004 pour des atomes de Mn adsorbés sur un oxyde  $\text{Al}_2\text{O}_3$  sur une surface  $\text{NiAl}(100)$  figure 5(a). En comparant avec l'application ou non d'un champ magnétique externe et en comparant les atomes adsorbés sur le métal [figure 5(b)] ou sur l'oxyde [figure 5(c)], on remarque différents comportements. Pour les atomes sur le métal l'application du champ ne change pas le spectre obtenu, tandis que pour les atomes sur l'oxyde l'application du champ fait apparaître un gap autour du niveau de Fermi. Mn sur l'oxyde correspond à un spin  $S=5/2$ , et l'application d'un champ magnétique permet une levée de dégénérescence de ses états de moment de spin par effet Zeeman comme montré en figure 5(d). Ainsi l'excitation de spin observée correspond au processus montré en figure 5(e) où un électron dans l'état  $\downarrow$  excite l'atome de l'état  $M = 5/2$

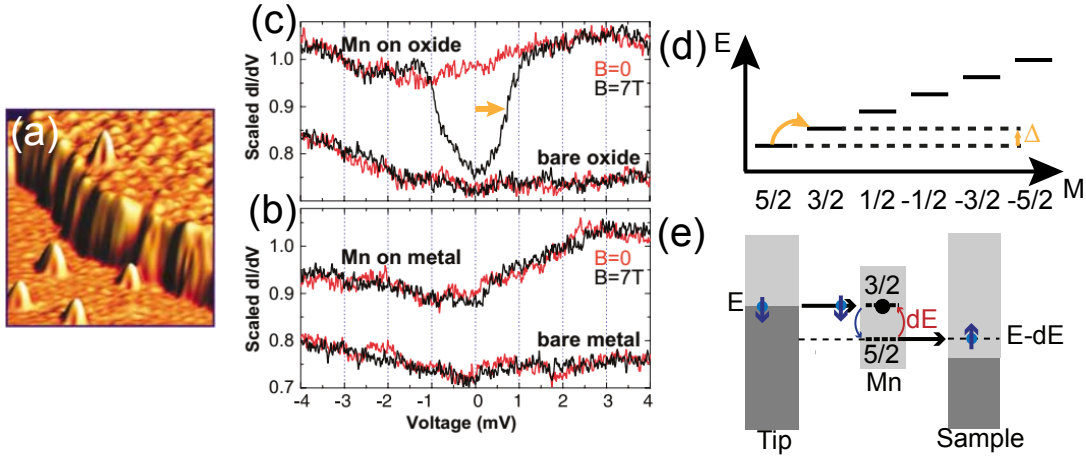


FIGURE 5 : **Spectroscopie d'excitation de spin.** (a) Image STM d'atomes de Mn adsorbés sur une surface NiAl(110) partiellement couverte d'oxyde  $\text{Al}_2\text{O}_3$ . (b) Spectres en  $dI/dV$  obtenus sur un atome de Mn sur NiAl(110). (c) Spectres en  $dI/dV$  obtenus sur un atome de Mn sur  $\text{Al}_2\text{O}_3$ . (d) Diagramme en énergie des états de moment de spin de l'atome de Mn sur  $\text{Al}_2\text{O}_3$  sous un champ magnétique appliqué. (e) Processus de tunneling inélastique correspondant à l'excitation de spin. [(a,b,c) extraits de [3]]

verse l'état  $M = 3/2$ . Ce processus respectant la conservation du moment de spin total l'électron tunnel passe de l'état  $\downarrow$  vers l'état  $\uparrow$ .

Bien que ce premier exemple concernait une excitation entre deux niveaux Zeeman, d'autres effets peuvent être observés par une excitation de spin. En effet, certains systèmes, en absence de champ magnétique, peuvent présenter des états de moment de spin non dégénérés. Ce phénomène, appelé Zero-Field-Splitting, a été observé sur tout une collection d'atomes adsorbés sur une surface semi-isolante [22–25]. La manifestation de cet effet se traduit par l'existence d'une anisotropie magnétique dont l'hamiltonien peut s'exprimer de la manière suivante :

$$\mathcal{H} = D\hat{S}_z^2 + E(\hat{S}_x^2 - \hat{S}_y^2) \quad (2)$$

Il faut noter que de manière générale, la convention veut que l'axes de quantification choisi pour le système étudié, le soit de manière à ce que le coefficient anisotropie  $D$  soit supérieur au coefficient d'anisotropie  $E$ . Cette anisotropie magnétique est très importante dans cette thèse puisque le système étudié possède une anisotropie  $D$  non nulle qui produit une excitation de spin en STS.

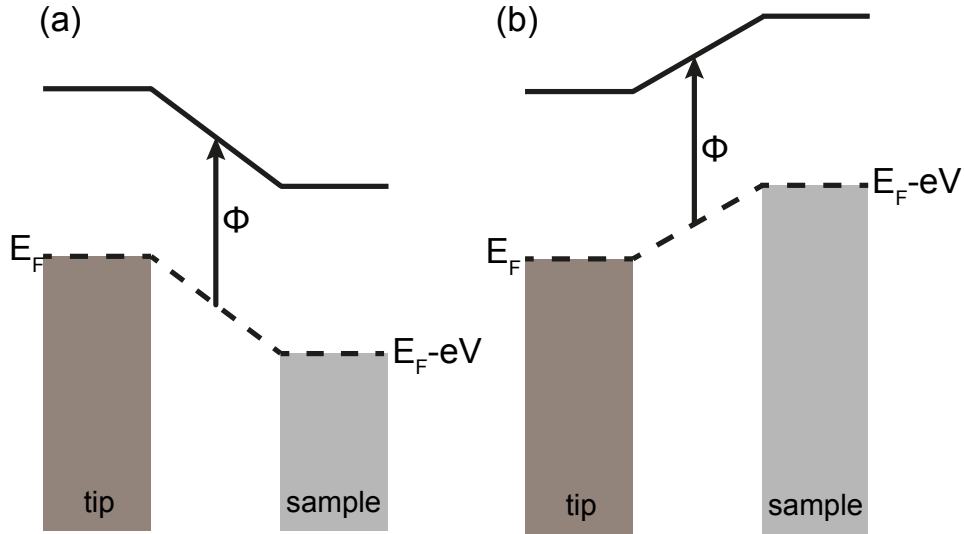


FIGURE 6 : **Principe du microscope à effet tunnel.** Schémas d'un électron tunnelant d'un état de la pointe vers un état de la surface. (a) tension positive. (b) tension négative.

## 0.2 Microscopie et spectroscopie à effet tunnel/ dispositif expérimental (Chapitre 2)

Le second chapitre de ma thèse se concentre sur les aspects fondamentaux et techniques de la microscopie et spectroscopie à effet tunnel ainsi que de la description du dispositif expérimental utilisé pendant la thèse. L'outil en lui-même est basé sur le principe de l'effet tunnel et fut développé par G. Binnig et H. Rohrer au laboratoire IBM de Zurich en 1982 [26]. Son premier fait d'arme fut la détermination de la structure de reconstruction d'une surface Si(111) [27]. Le principe du STM repose sur la détection du courant dit "tunnel" des électrons passant de la pointe à la surface ( $V > 0$ ) ou de la surface vers la pointe ( $V < 0$ ) comme décrit en figure 6. Il existe plusieurs modèles pour exprimer le courant tunnel suivant le type d'approche effectuée [28–32]. L'approche semi-classique de Wentzel-Kramers-Brillouin [29, 33, 34] permet une relativement simple (en comparaison aux autres) expression de ce courant de la manière suivante :

$$I(z, V) \propto \int_{-\infty}^{\infty} \mathcal{T}(z, E, V) [f(E - eV) - f(E)] \rho_t(E - eV) \rho_s(E) dE \quad (3)$$

Cette expression fait intervenir la transmission de la jonction  $\mathcal{T}$ , la fonction de Fermi-Dirac  $f$  et les densités d'états de la pointe  $\rho_t$  et de la surface  $\rho_s$ . La transmission, elle, peut s'exprimer

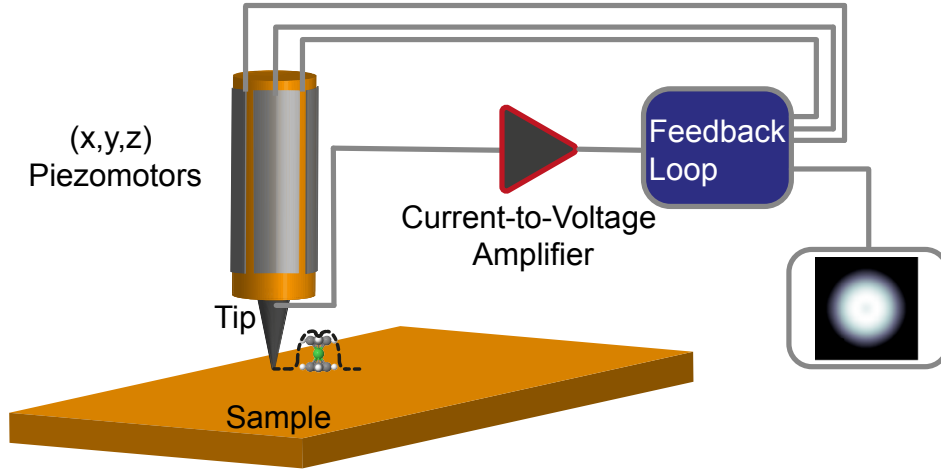


FIGURE 7 : **Boucle d'asservissement du mode courant constant d'un STM.**

en fonction des paramètres de la jonction comme suit :

$$\mathcal{T}(z, E, V) \propto \exp \left[ -kz \sqrt{\phi + \frac{eV}{2} - (E - E_{\parallel})} \right], \quad (4)$$

La transmission possède donc une dépendance suivant l'épaisseur de la barrière tunnel. Cette dépendance permet la réalisation de topographies de surfaces, montrant une résolution spatiale pouvant aller jusqu'à l'échelle atomique. Un mode de fonctionnement pour de telles topographies consiste donc à réguler la hauteur de la pointe du STM afin de maintenir la valeur du courant constante. La boucle d'asservissement de ce mode de fonctionnement est présentée en figure 7, où le contrôle du mouvement de la pointe est réalisé par des moteurs piezoélectriques, mouvement dont le déplacement vertical nécessaire pour maintenir  $I$  constant est enregistré lors du balayage latéral de la pointe, permettant l'obtention d'une topographie d'objets en surface comme la molécule de nickelocène montrée dans la figure.

Le deuxième aspect intéressant du STM est que le courant observe une dépendance par rapport aux densités d'états de la pointe et de la surface. Ainsi, au moyen d'un balayage de la tension appliquée  $V$ , il est possible de sonder les différentes structures dans la configuration électronique de la jonction. Plus particulièrement, la présence de ces structures se reflètent dans la conductance différentielle. Si l'on considère la densité d'états  $\rho_t$  de la pointe constante, l'expression de la conductance différentielle sous l'approche de WKB fait apparaître une dépendance

directe envers la densité d'états de la surface :

$$\frac{dI}{dV}(z, V) \propto \rho_s(V) \mathcal{T}(z, eV, V). \quad (5)$$

Cette dépendance permet l'étude des propriétés électroniques de systèmes en surface avec, par exemple, les molécules dont on peut déterminer les énergies de certaines orbitales moléculaires et en particulier le gap HOMO-LUMO. Cependant, et cela à été mentionné dans le chapitre introductif, il existe d'autres processus de tunneling pour les électrons. L'effet Kondo peut présenter une signature dans la conductance différentielle dans la forme d'une résonance au niveau de Fermi. L'excitation de spin, en revanche, se présente comme une marche liée à du tunneling inélastique. Ce tunneling inélastique est le marqueur spectroscopique d'électrons qui tunnelent en cédant de l'énergie à un système, permettant d'exciter celui. Comme vu précédemment, cela peut concerner une excitation de spin. Cependant le tunneling inélastique fut en premier observé pour une excitation d'états vibrationnels [35, 36].

La suite du chapitre est vouée à la détection synchrone que nous utilisons pour acquérir la conductance différentielle. C'est aussi l'occasion de mentionner la résolution en énergie que l'on a en spectroscopie en exprimant la largeur de structures, élastiques (telle qu'une résonance Kondo) et inélastiques, en fonction des effets thermiques et de la modulation utilisée pour la détection synchrone. Pour ce qui est de la largeur, pour le cas élastique les effets thermiques produisent un élargissement des structures  $\delta_T = 3.5k_B T$  tandis que la modulation induit  $\delta_M = 2.44V_M[\text{rms}]$ . Concernant la résolution en énergie pour les phénomènes inélastiques,  $\delta_T = 5.5k_B T$  et  $\delta_M = 2.44V_M[\text{rms}]$ . Le chapitre 2 se termine par une brève description du dispositif expérimental. Le STM à basse température que l'on utilise nous permet d'atteindre 2.4K et usuellement nous utilisons une modulation de 150  $\mu\text{V}$  [rms] conférant une résolution en énergie  $\delta_E = 800 \mu\text{eV}$  pour les structures élastiques et  $\delta_E = 1.1 \text{ meV}$ . pour les structures inélastiques.

## 0.3 Caractérisation de l'adsorption et des propriétés magnétique du nickelocène (Chapitre 3)

### 0.3.1 Détermination de l'adsorption du nickelocène

La molécule étudiée est le nickelocène (Nc) qui est de la famille des métallocènes, qui sont des molécules composées d'un atome de métal de transition couplés à deux ligands cyclopentadié-

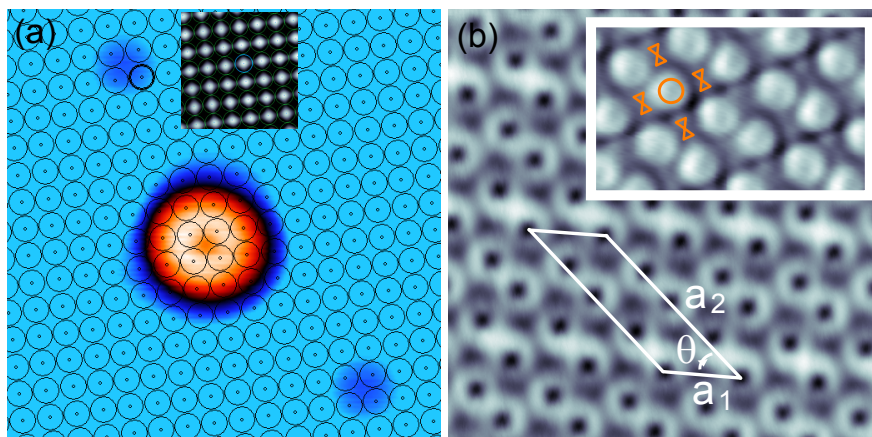


FIGURE 8 : (a) Image STM d'un Nc isolé et de deux adatoms de Fe ( $40 \times 40 \text{ \AA}^2$ , 20 mV, 50 pA). Encadré image en régime contact de la surface Cu(100) ( $16.5 \times 16.5 \text{ \AA}^2$ , 10 mV, 8 nA) (b) Image STM d'un réseau par de molécules montrant les différents paramètres de maille. ( $70 \times 70 \text{ \AA}^2$ , 20 mV, 20 pA) Encadré : Image STM du même réseau montrant des molécules verticales (cercle) et des molécules horizontales (sabliers). ( $28 \times 28 \text{ \AA}^2$ , 1 mV, 10 pA).

nyles (Cp). Ce Nc a la particularité d'avoir un spin 1 en phase gaz, ce qui est une particularité intéressante dans le contexte de l'étude du magnétisme d'objets en surface. Les travaux présentés dans cette section sont publiés dans ces deux articles [37, 38]. Le nickelocène lorsque déposé sur une surface de Cu(100) s'adsorbe en molécules isolées et en réseaux moléculaires (sous certaines conditions de dépôt pour ceux-ci mentionnées en § 3.1.1). L'adsorption en molécule isolée se fait avec la molécule sur le site "hollow" avec un seul ligand en contact avec la surface, donnant une forme annulaire sur la topographie STM en figure 8(a). Nous avons déterminé cette adsorption au moyen d'une image en quasi-contact donnant l'orientation du réseau de la surface [encadré figure 8(a)] suivant la méthode utilisée dans cet article [39] qui permet d'obtenir la résolution atomique de la surface. Puis nous avons utilisé l'adsorption connue d'un atome de Fe (qui est en site "hollow") afin de déterminer la position de la molécule de Nc montrée en figure 8(a). Les simulations de l'adsorption au moyen de la DFT ont confirmé ces résultats.

L'adsorption de Nc peut aussi se faire sous forme de deux types de réseaux. Ces réseaux sont dénommés "réseau par paires de molécules" et "réseau compact". En figure 8(b) nous avons une image du réseau par paires de molécules. Nous avons déterminé les paramètres de maille de ces réseaux et démontré qu'ils sont composés de molécules verticales (cercle sur l'encadré en figure

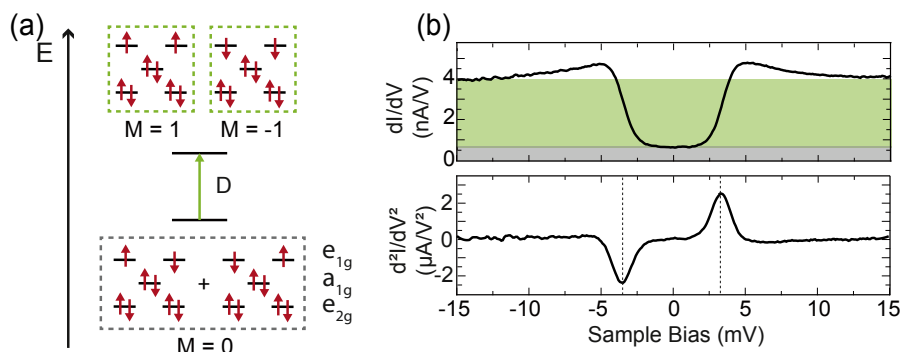


FIGURE 9 : (a) Diagramme en énergie des états de moment de spin du nickelocène. (b) STS faisant apparaître  $dI/dV$  et  $d^2I/dV^2$  réalisée sur un Nc. ( $I = 50$  pA;  $V = -15$  mV).

8(b)) mais aussi de molécules horizontales (sabliers sur cette même figure). Ces molécules horizontales correspondent à la configuration où les deux ligands "touchent" la surface. Ces résultats d'adsorption sont à comparer à ceux obtenus pour le ferrocène qui présentaient des réseaux similaires sur le plan structurel [40].

### 0.3.2 Propriétés magnétiques du nickelocène

La seconde partie de la caractérisation du Nc sur Cu(100) concerne l'étude de ses propriétés magnétiques. Pour cela nous avons étudié Nc en STS. Nous avons aussi effectué des mesures de dichroïsme magnétique de rayons X (XAS/XMCD) au synchrotron Soleil sur la ligne Deimos, afin de vérifier le caractère magnétique de cette molécule lorsqu'elle est adsorbée sur Cu(100). Le but de cette étude était de confirmer le caractère magnétique du Nc lorsqu'adsorbé en surface. L'étude en XAS/XMCD réalisée (voir section § 3.2.3) a montré un signal fortement dichroïque et anisotrope sur les seuils  $L_{2,3}$  liés au Ni. Une étude en température du signal XMCD a démontré que Nc sur la surface possède un spin 1 une anisotropie  $D = 3.2$  meV. Cette anisotropie magnétique donne l'état de moment de spin  $M = 0$  comme fondamental, et l'état de moment de spin  $M = \pm 1$  comme état excité comme montré en figure 9(a). De plus, nos collaborateurs ont effectué des calculs basés sur la DFT. Une analyse de charge de Bader montre un faible transfert de charge de la molécule vers la surface (0.1e). D'après la DFT, le moment magnétique du Nc est conservé par l'adsorption et possède une valeur de  $1.96\mu_B$  qui induit donc une valeur de spin  $S=1$ . La STS réalisée sur un Nc en surface [figure 9(a)] montre un signature inélastique avec une tension de seuil à 3.2 mV. En considérant les résultats du



XAS/XMCD et de la DFT nous pouvons conclure la signature inélastique observée en STS correspond à l'excitation de l'anisotropie précédemment définie.

Chaque indice donné par la STS, le XAS/XMCD et la DFT pointe donc sur la conservation du spin 1 de Nc sur Cu(100) mais aussi de son anisotropie qui possède une signature marquée dans la STS. Une certaine importance est donnée à l'analyse de la signature du nickelocène dans la STS. En effet, cette dernière présente un rapport entre les conductances élastiques et inélastiques intense en comparaison aux systèmes observés usuellement [3, 22–25]. Nous avons fait le lien entre cette intensité peu usuelle et une certaine proximité de la symétrie particule/trou de la configuration électronique du nickelocène (*id est*  $\epsilon_d/U_d = -0.5$  avec  $\epsilon_d$  la position en énergie de l'orbitale moléculaire occupée et  $\epsilon_d + U_d$  celle de l'orbitale moléculaire inoccupée). De plus, la STS du nickelocène porte des marqueurs sur ses marches de conductance, ce qui s'apparente à des épaulements. Ces marqueurs sont liés à des processus de diffusion électronique très similaires à ceux rencontrés pour une résonance Kondo. En utilisant le programme de simulation de spectres de M. Ternes [41], nous avons pu extraire les paramètres liés au couplage d'échange du nickelocène aux électrons du métal et exploitant les relations en ces paramètres et la configuration électronique du nickelocène au moyen de la transformation de Schrieffer-Wolff [17], nous avons quantifié cette proximité à la symétrie particule/trou et trouvé  $\epsilon_d/U_d = -0.4$ . Cette signature et son évolution par l'action de divers couplages est le coeur de mon projet de thèse comme cela va être présenté dans les sections suivantes.

## 0.4 Fonctionnalisation de la pointe par un nickelocène et changement de spin (Chapitre 4)

### 0.4.1 Adsorption et propriétés du nickelocène sur la pointe

Une autre particularité de la molécule de nickelocène c'est que l'on peut la transférer de la surface vers la pointe. Le chapitre 4 se focalise donc sur la caractérisation du nickelocène lorsqu'il est adsorbé sur la pointe du STM. Pour avoir le nickelocène sur la pointe, un simple contact sur une molécule est nécessaire. Ayant fonctionnalisé notre pointe avec un Nc, nous pouvons obtenir des informations sur l'adsorption de la molécule sur la pointe en effectuant des images d'atomes isolés sur la surface. Une telle image est montrée en figure 10(a), celle-ci comporte deux adatoms de Fe sur Cu(100). Ils présentent une forme annulaire justifiant la

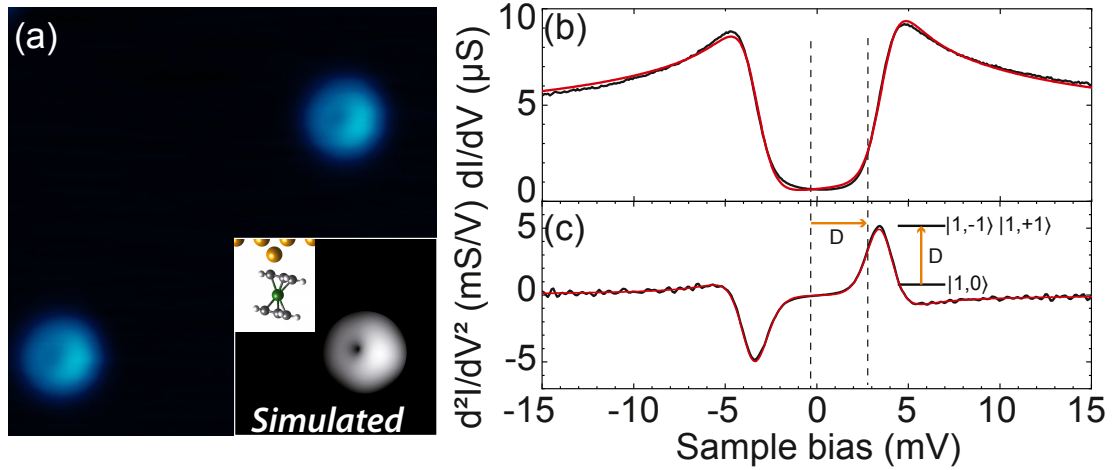


FIGURE 10 : (a) Image STM d'un adatoms de Fe sur Cu(100) réalisé avec la pointe de Nc ( $2 \times 2 \text{ nm}^2$ ,  $-15 \text{ mV}$ ,  $30 \text{ pA}$ ). Encadré : simulation par DFT de la pointe moléculaire avec la simulation de l'apex de la pointe. (b) Spectre en  $dI/dV$  de la pointe moléculaire au dessus de la surface ed Cu(100) ( $I = 1 \text{ nA}$ ,  $V = -20 \text{ mV}$ ). (c) Spectre en  $d^2I/dV^2$  correspondant.

présence du Nc sur la pointe. Afin d'expliquer cette forme apparente, nous pouvons dire ici que tout se passe comme si nous imagions le Nc sur la pointe avec un adatome de la surface. En plus de cette forme annulaire, nous remarquons que cet anneau semble posséder une certaine orientation, suggérant l'existence d'un angle entre l'axe de la molécule et l'axe vertical. Nos collaborateurs ont la possibilité de simuler cette pointe par DFT en positionnant la molécule sur un adatome de cuivre comme sur la figure 10(a). Cette simulation montre l'existence d'un angle entre l'axe de la molécule et l'axe vertical qui induit un anneau orienté sur la simulation de l'apex montré sur cette même figure 10(a). Au cours de ce chapitre, nous avons ensuite démontré que les propriétés magnétiques du nickelocène sur la pointe, ne diffèrent que peu par rapport à la molécule sur la surface. Le Nc sur la pointe est donc un spin 1 avec une anisotropie magnétique  $D = 3.5 \text{ meV}$  qui est marquée par une excitation de spin dans la STS réalisée avec la pointe moléculaire au dessus de la surface de Cu(100). En analysant cette excitation de spin nous remarquons aussi que le rapport entre la conductance inélastique et la conductance élastique est important. Il est supérieur à celui obtenu pour le molécule en surface et au moyen du programme [41], précédemment utilisé, nous concluons que le nickelocène sur la pointe est encore plus proche de la symétrie particule/trou (ici  $\epsilon_d/U_d = -0.49$ ).

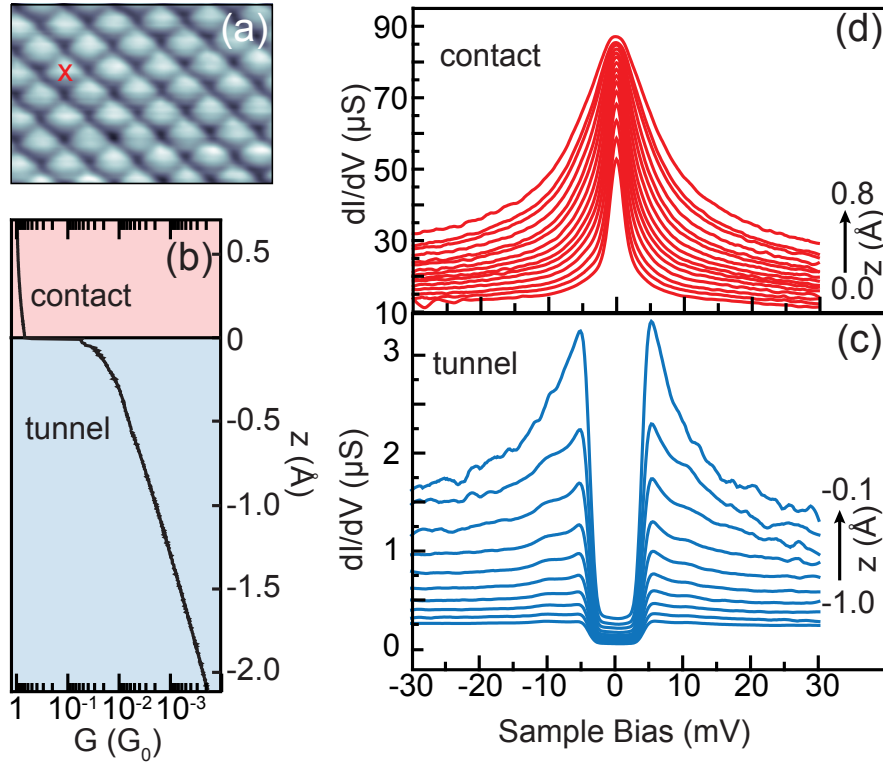


FIGURE 11 : (a) Image STM réalisé avec la pointe moléculaire en contact avec la surface Cu(100) ( $2 \times 1.4 \text{ nm}^2$ , 30 mV, 300 nA) (b)  $G/G_0(z)$  réalisé en top (croix rouge (a)) d'un atome avec le régime tunnel (en bleu) et le régime contact (en rouge) démarqués par un saut de conductance positionné en zéro définissant le point de contact. (c) Spectre en  $dI/dV$  en régime tunnel. (d) Spectre en  $dI/dV$  en régime de contact (rouge).

#### 0.4.2 Changement de spin

La seconde partie de ce chapitre se consacre à une étude réalisée avec cette pointe fonctionnalisée, et de sa signature spectroscopique, lorsqu'on décroît la distance pointe-surface. Cette étude est publiée ici [42]. Cette pointe permet de résoudre aisément la structure atomique de la surface au moyen d'une image en contact [figure 11(a)]. Ainsi nous pouvons choisir le site de la surface sur lequel nous voulons travailler, à savoir pour la suite en "top" d'un atome de la surface (croix rouge en figure 11(a)). En réalisant une courbe de conductance en fonction de la distance de la pointe à la surface [Figure 11(b)] nous pouvons définir les régimes de conductance tunnel et en contact. Si nous comparons les spectres acquis en régime tunnel [Fig. 11(c)] et en régime contact [Fig. 11(d)] nous remarquons une différence dans le type de structure spectrale obser-

vée. Le régime tunnel présente des signatures qui correspondent à l'excitation de spin du Nc, qui, après une analyse profonde des spectres comme fait précédemment avec le programme [41], montrent une croissance de l'hybridation du Nc avec les électrons de la surface. Cependant, les signatures observées en régime contact correspondent à une résonance Kondo. La transition entre les deux est si abrupte que cela suggère un changement de conformation de la molécule au sein de la jonction. Nous démontrons que cette résonance correspond à un Kondo d'un spin  $1/2$  par une analyse complète de cette résonance au moyen de la fonction de Frota [21]. Nous avons donc un changement de spin pour Nc sur la pointe entre les deux régimes de conduction. Les calculs basés sur la DFT permettent de simuler la jonction pour différentes distances entre la pointe et la surface. Les calculs de transport correspondant démontrent un changement du moment magnétique du Nc entre le régime tunnel et le régime contact. Ces mêmes calculs montrent qu'entre les deux régimes, il y a une forte augmentation de l'hybridation de l'orbital moléculaire du Nc avec le bain électronique ainsi qu'une forte réduction du terme de répulsion coulombienne  $U_d$ , expliquant la réduction du moment magnétique.

## 0.5 Détection de spin au moyen d'une pointe fonctionnalisée par un nickelocène (Chapitre 5)

Le dernier chapitre de ma thèse correspond à une étude plus approfondie du potentiel de la pointe fonctionnalisée par un nickelocène [43]. Ce chapitre commence dans un premier temps par la présentation du concept d'utilisation du nickelocène comme sonde de magnétisme, au moyen d'une étude de la signature du Nc sur la pointe lorsque celui-ci est approché d'un atome de Fe sur Cu(100). La seconde partie du chapitre est consacrée à l'application de ce concept à l'étude d'une surface ferromagnétique à travers l'exemple des îlots de Co sur Cu(111). Il existe déjà des études en SP-STM de ces îlots [10, 44, 45] montrant une structure électronique polarisée en spin portée par les orbitales  $d$  et la bande  $sp$  des îlots [46]. Plus récemment, une étude de ces îlots fût aussi réalisée au moyen d'une pointe supraconductrice [47]. Cette surface ferromagnétique est donc un système de choix afin de tester la pointe de Nc.

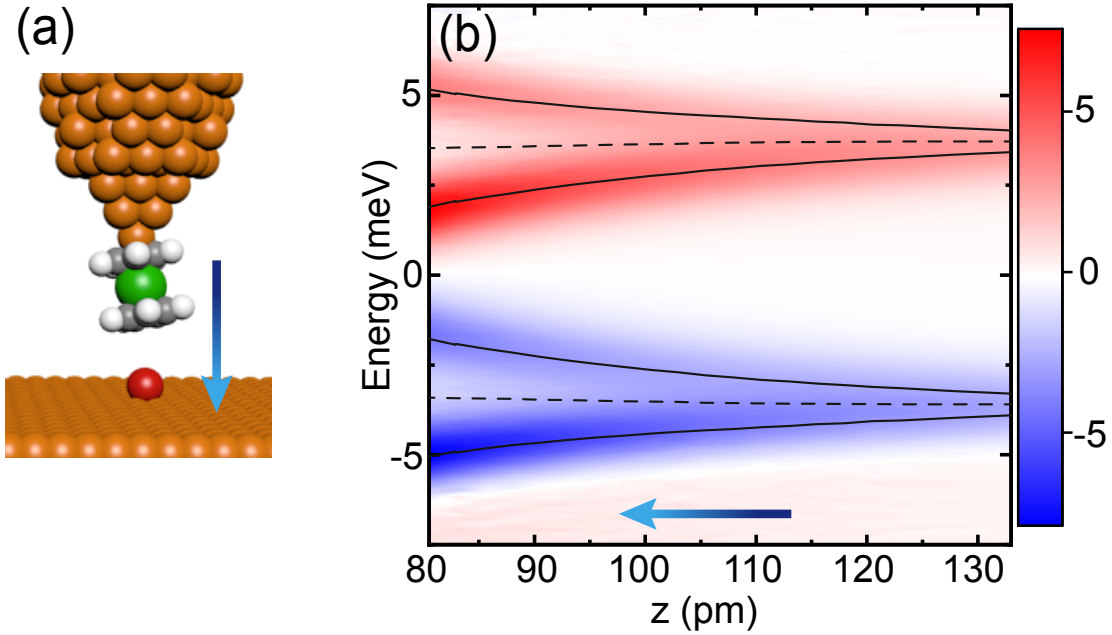


FIGURE 12 : (a) Représentation de la jonction avec la pointe STM fonctionnalisée par un Nc et un adatome de Fe adsorbé sur la surface. (b)  $d^2I/dV^2$  réalisé avec la pointe moléculaire au dessus d'un adatome de Fe pour une distance  $z$  entre Nc et Fe de 133 pm et 80 pm.

### 0.5.1 Preuve de concept : Fe/Cu(100)

Pour démontrer ce concept, nous avons donc réalisé une étude de la signature du nickelocène qui est sur la pointe. Nous approchons cette pointe près d'un adatome de Fe sur une surface Cu(100), qui est magnétique. La géométrie de la jonction est présentée en figure 12(a). En figure 12(b) est présenté une carte en  $d^2I/dV^2$  suivant l'évolution de celle-ci pour une distance Nc-Fe de 133 pm à 80 pm. Sur cette figure est observé la séparation graduelle du pic en  $d^2I/dV^2$  quand la distance Nc-Fe est diminuée. Nous remarquons aussi que cette séparation d'effectue de manière symétrique par rapport à la valeur de  $D$ . En figure 13(a), le spectre réalisé à 80 pm montre que deux informations peuvent être extraites. La séparation en énergie des pics et l'asymétrie de leur intensité. Afin d'interpréter la séparation des pics, nous avons utilisé un hamiltonien prenant en compte l'anisotropie du Nc et un terme Zeeman incluant un champ magnétique dit d'échange appliqué au Nc.

$$\hat{H} = D\hat{S}_z^2 - g\mu_B B\hat{S}_z. \quad (6)$$

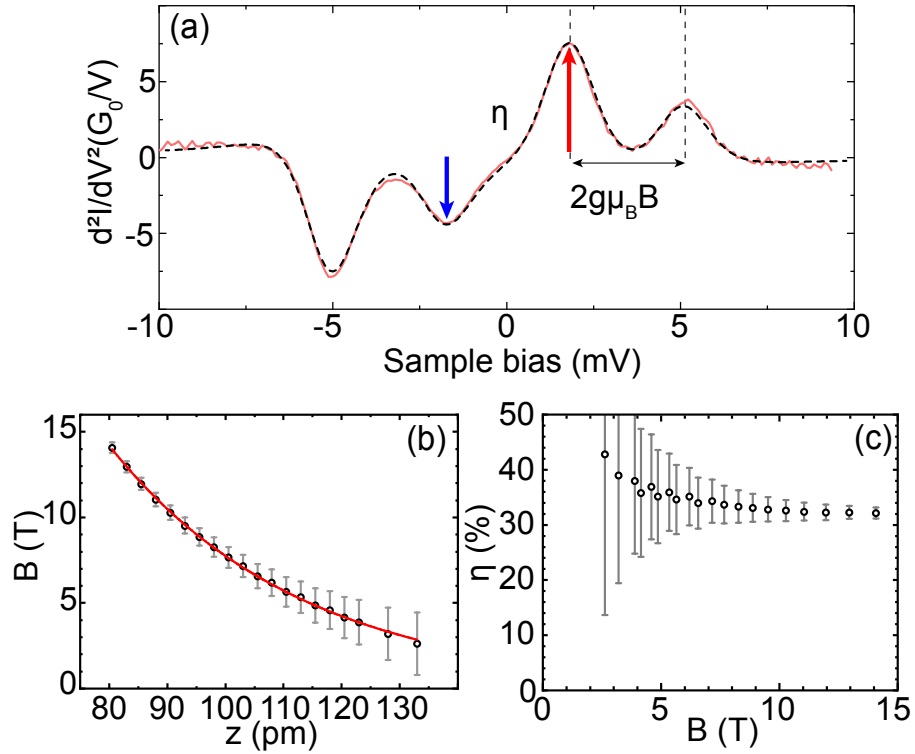


FIGURE 13 : (a) Spectre en  $d^2I/dV^2$  réalisé à 80 pm présentant la définition de du champ d'échange  $B$  et de l'asymétrie  $\eta$ . (b) Champ d'échange  $B$  modélisant le couplage en fonction de  $z$ . (c) Asymétrie  $\eta$  extraite des spectres en fonction du champ d'échange.

Cet hamiltonien nous sert d'outil pour quantifier l'effet de la présence du Fe sur les états propres du Nc. L'hamiltonien réel est plus complexe et moins pratique en terme de pédagogie. Le raisonnement montrant l'équivalence quantitative entre ces deux hamiltoniens est fait dans la section § 5.1.2. En effet, l'utilisation d'un hamiltonien de cette simplicité nous permet d'obtenir une information comparable entre cette expérience avec l'adatom de Fe et celle qui est présentée dans la suite avec les îlots de Co sur Cu(111). Au moyen du programme de M. Ternes [41] nous avons donc extrait la valeur du champ d'échange  $B$  en fonction de la distance Nc-Fe. Son évolution est présentée en figure 13(b). La variation de celui-ci est exponentielle (simulation par une fonction exponentielle en rouge) comme on peut s'attendre d'un couplage de type échange entre deux objets magnétiques. Notons toutefois que ce couplage d'échange présente les mêmes symétries qu'un couplage d'Ising. La deuxième information que l'on peut tirer des spectres est l'asymétrie présente sur l'intensité des pics, asymétrie qui est noté  $\eta$ , et présente une valeur

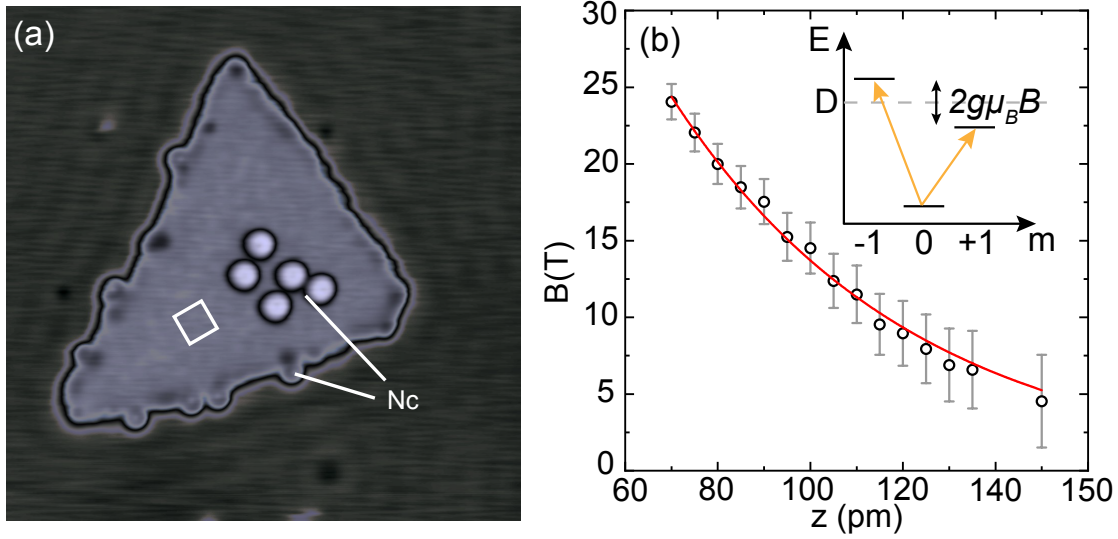


FIGURE 14 : (a) Image STM d'un îlot de Co avec des Nc sur Cu(111) ( $25 \times 25 \text{ nm}^2$ ,  $-20 \text{ mv}$ ,  $20 \text{ pA}$ ) (b) Champ d'échange  $B$  en fonction de  $z$  pour la pointe de Nc au dessus d'un îlot de Co. Encadré : diagramme en énergie pour les états de moment de spin de Nc.

d'environ 30% pour les champs d'échange les plus élevés [figure 13(d)]. Cette asymétrie est déterminée de la façon suivante :  $\eta = (h_+ - h_-)/(h_+ + h_-)$  avec  $h_+$  et  $h_-$  les intensités en valeur absolue des pics respectivement à  $V > 0$  et  $V < 0$ . Cette asymétrie est une notion connue et a déjà été observée [48]. Cependant, bien que dans cet article [48] elle a été associée à une polarisation de densité d'états, dans notre cas précis cela ne correspond pas. C'est en partie dû au fait que cette asymétrie fait intervenir les termes de transmission entre la molécule et l'adatome qui dépendent des orbitales sources et puits. Nous devons donc exprimer cette asymétrie comme étant lié à la polarisation de la transmission. Les simulations au moyen de la DFT de nos collaborateurs permettent d'associer cette asymétrie la polarisation de la transmission entre l'orbitale moléculaire et les orbitales  $4s$  et  $4p$  du Fe (à défaut des orbitales  $3d$  du Fe qui possèdent le plus de densité d'états au niveau de Fermi).

### 0.5.2 Application : Co(111)/Cu(111)

La seconde partie de chapitre se consacre donc l'application du concept de la pointe de Nc, sonde de magnétisme, à l'étude des îlots de Co sur Cu(111). En figure 14(a), une image STM montre un îlot de Co avec des Nc qui peuvent s'adsorber sur et contre l'îlot. Lorsque nous

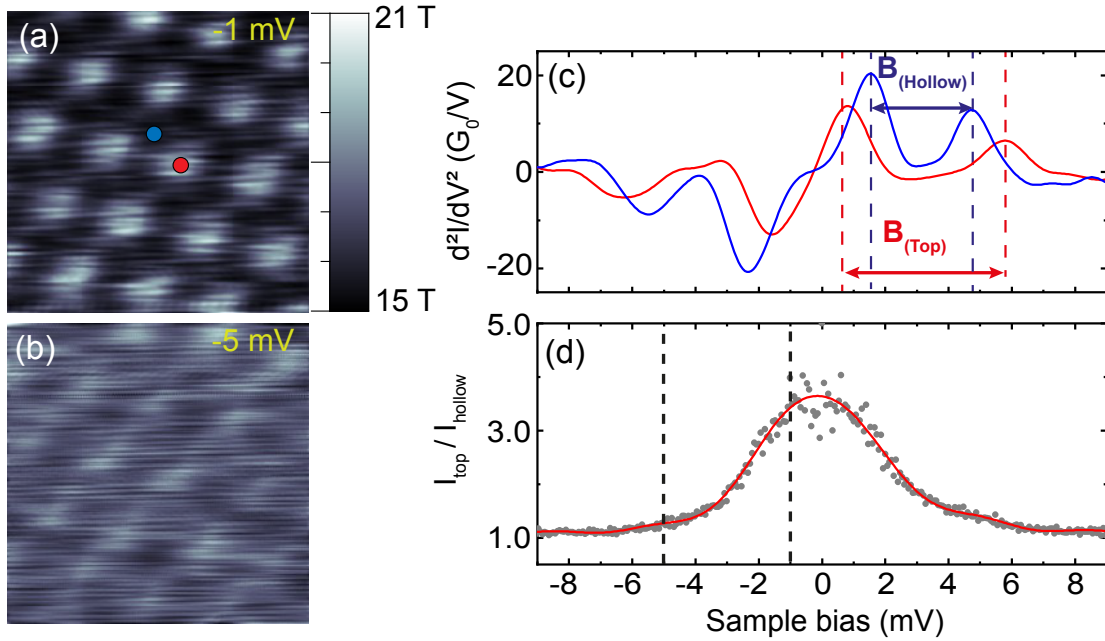


FIGURE 15 : (a) Image STM à hauteur constante montrant la résolution atomique de l'îlot. ( $z = 80$  pm,  $V = -1$  mV,  $1 \times 1$  nm<sup>2</sup>) (b) Même image mais réalisée à  $V = -5$  mV (c)  $d^2I/dV^2$  réalisé avec la pointe moléculaire au dessus du site "top" (bleu) et au dessus du site "hollow" (rouge) de l'îlot de Co ( $z = 80$  pm) (d) Rapport entre le courant mesuré en position "top" et le courant mesuré en position "hollow" pour  $z = 80$  pm.

approchons la pointe moléculaire près de l'îlot nous observons aussi un levée de dégénérescence de l'état excité du Nc comme pour les mesures avec Fe. L'évolution du champ d'échange est présenté en figure 15(b). Cette fois, l'asymétrie  $\eta \approx 5\%$ , mais cette valeur n'indique en rien l'absence de polarisation des îlots et une application numérique réalisée dans le chapitre 5 permet d'avoir une estimation de la polarisation de transmission, cohérente avec celle mesurée par une pointe supraconductrice [47]. La valeur ajoutée de cette étude c'est qu'en exploitant le couplage d'échange et son aspect local, nous sommes en mesure de réaliser une topographie du champ d'échange. En effet, nous observons une résolution atomique en imagerie du courant [Fig. 15(a)] au dessus de l'îlot, pour des paramètres d'imagerie (à savoir 80 pm et  $-1$  mV) qui ne donne pas de résolution atomique au dessus de la surface de Cu(111). Si on compare cette image à celle réalisée dans les mêmes conditions mais pour  $-5$  mV [Fig. 15(b)] nous remarquons que le contraste est fortement atténué. Pour se convaincre de la nature de ce contraste, nous



commençons par regarder la rapport entre le courant mesuré en "top" et le courant mesure en "hollow" [Fig. 15(c)]. Le contraste observé se traduit donc ici par ce rapport étant assez supérieur à 1 autour du niveau de Fermi. Si maintenant, nous comparons les spectres en  $d^2I/dV^2$  pour les positions "top" (bleu) et "hollow" (rouge) pour une distance de 80 pm (Fig. 15(d)), nous remarquons que  $B$  est plus intense en top (21 T) qu'en hollow (15 T). Cette différence se traduit par une plus grande proportion de courant inélastique à  $-1$  mV en "top" qu'en "hollow" expliquant le comportement de la figure 15(c). Ce résultat ouvre donc la voie à la cartographie du champ d'échange pour les surfaces magnétiques sous STM.

## 0.6 Conclusion

Cette thèse a donc porté sur l'étude de la molécule de nickelocène pour une utilisation de sonde locale de magnétisme. Cela s'inscrit dans la continuité des avancées de la détection de spin au moyen d'un STM. Nous avons donc d'abord caractérisé cette molécule lorsqu'elle est adsorbée sur une surface Cu(100). Le résultat marquant est la conservation du spin 1 de cette molécule mais surtout l'observation d'une excitation de spin due à son anisotropie magnétique. Cela a été démontré à l'aide de mesures XAS/XMCD et au moyens de calculs basés sur la DFT. Cette excitation de spin est aussi observée lorsque l'on transfère la molécule sur la pointe du STM, indiquant la conservation du spin 1 et de l'anisotropie de la molécule dans cette configuration.

L'étude suivante est celle consistant à étudier le comportement des propriétés de spin lorsque qu'une jonction moléculaire est réalisée en approchant au contact la pointe moléculaire. Ce que nous observons entre les régimes de conduction tunnel et en contact c'est un changement d'un spin 1 vers un spin 1/2 marqué par un changement de marqueur spectroscopique, d'une excitation de spin vers une résonance Kondo. Ce changement de spin est dû à une hybridation de l'orbitale moléculaire du nickelocène avec les électrodes, ce qui est confirmé par des calculs réalisés au moyen de la DFT.

Enfin, la dernière partie est consacrée à l'utilisation du nickelocène sur la pointe et de ses propriétés magnétiques pour sonder le magnétisme d'objets en surface. Avec les expériences de la pointe moléculaire au dessus d'un adatome de Fe sur Cu(100) nous montrons que nous pouvons exploiter l'effet de la présence du Fe sur la signature du nickelocène pour extraire le couplage d'échange entre Nc et Fe, modélisé par un champ d'échange, et la polarisation de la transmission en Nc et Fe. Ensuite, les expériences réalisées avec cette pointe moléculaire au

dessus des îlots de Co sur Cu(111) ont permis d'appliquer le concept introduit plus tôt. Ces mesures ont permis entre-autre de mettre en évidence la possibilité de cartographier le couplage d'échange et la polarisation de transmission entre la pointe moléculaire et les îlots.

Au cours de cette thèse, nous avons principalement étudié un métallocène de spin 1. Cependant, nous avons aussi travaillé avec le cobaltocène qui est un spin 1/2. Cette molécule possède donc des caractéristiques assez similaires au nickelocène, mais au lieu de présenter une excitation de spin, cette molécule présente une résonance Kondo dans son spectre. Nos résultats préliminaires sur cette molécule montrent qu'il est possible de l'utiliser comme sonde locale de magnétisme. De plus, de part son spin 1/2, cette molécule serait plus appropriée pour une application de la résonance de spin (ESR) au moyen d'une pointe moléculaire.

## CHAPTER 1

# Single-spin detection with STM

The necessity for an atomic-scale magnetometry is primarily motivated by the field of ultra-dense storage technology, which depends on our ability to address single spins within complex magnetic structures. This requirement has accelerated the pace towards the development of new spin-sensitive techniques with increased spatial resolution. Several of these, *e.g.* magnetic resonance force microscopy, scanning nano-SQUIDs, or nitrogen vacancy centers in diamond, can achieve nanometer resolution. Scanning tunneling microscopy (STM) is one of the rare scanning probe techniques allowing for spin detection and magnetic imaging with atomic-scale resolution. Improving the spin-sensitivity of STM is for this reason central to upstream research in this domain.

The first experiments showing the detectability of magnetic objects in with STM were first achieved thirty years ago by measuring the tunneling magnetoresistance with spin-polarized STM (SP-STM) [12, 49]. A decade later, the spin detection of a single object with STM was achieved by observing zero-bias anomalies in the differential conductance of magnetic atoms (Fig. 1.1) [2, 50–52]. A breakthrough in STM spin detection was achieved in 2004 with the development by Heinrich *et al.* of spin excitation spectroscopy [3]. This technique uses inelastic electron tunneling spectroscopy to determine the magnetic states of a single object with knowledge of the nearby environment [22] and can manipulate the occupation of these states through an electrically-driven spin excitation [48]. This electrical control can be exploited within a pump-probe setup to collect information on spin relaxation times [53].

Magnetic objects couple to their local environment via a broad range of interactions, like the exchange, superexchange, or Ruderman-Kittel-Kasuya-Yosida interaction. In the presence

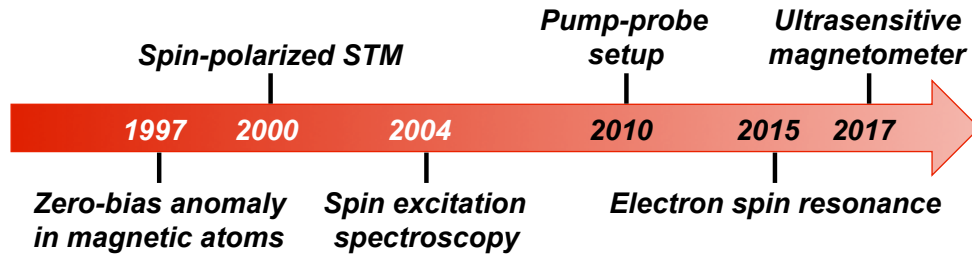


Figure 1.1: **Spin-detection with STM.** Evolution of STM spin detection during the past twenty years.

of these interactions, their magnetic states shift in energy. The above-mentioned spectroscopic techniques can then be used to monitor these changes, hence to map the magnetic environment of the target object under investigation. In other words, once the isolated target object is magnetically characterized, it can be employed as a sensor to detect these interactions. However, these techniques are solely based on the measurement of the differential conductance. In a low-temperature STM, the smearing of the Fermi-Dirac distribution limits then their energy resolution to about 1 meV. With this resolution, it is only possible to detect a Zeeman splitting of (effective) magnetic fields of a few teslas or higher, which are typically associated to two objects magnetically exchange coupled [20].

The development of electron spin resonance STM (ESR-STM) in 2015 represents an important step forward in this domain [5]. The spectroscopic measurement is similar to a technique known as electron paramagnetic resonance. By applying a radio-frequency voltage between the microscope tip and the target object in the presence of a small magnetic field ( $< 1$  T), a change in the conductance is detected whenever the voltage frequency matches a Larmor frequency of the object. The energy resolution of ESR-STM depends solely on the radio-frequency generator and for this reason exceeds by several orders of magnitude the one of conventional STM techniques. This technique provides new opportunities to study weak magnetic interactions at the atomic level, such as dipolar [6, 7] or even hyperfine [8, 9] interactions.

The ultra-sensitiveness to a single spin and its electrical control are tools that make STM appealing for research in quantum computing. Quantum bits that are encoded by spins are in fact very attractive as they benefit from the steady progress in nano-fabrication and allow for an electrical readout of their magnetic states. This was nicely demonstrated by Thiele *et al.* who succeeded in the electrical manipulation of a nuclear spin of a well-known single-molecule

magnet placed in a three-terminal transistor [54]. Soon after these experiments, it was proposed to transpose such an experiment to the junction of a cryogenic STM [55], where an increased control over the electrical contacts of the molecule can be exerted. In the long run, STM may therefore serve for testing concepts in atomic-scale quantum computing.

The scope of this chapter is to present some of the above mentioned spin-sensitive scanning probe techniques. We will restrain the presentation to the techniques and topics that are directly linked to the thesis. We start by presenting SP-STM (§ 1.1) and show how a spin-dependent contrast may be obtained in the images when probing magnetic nanostructures and single atoms. We then turn to the Kondo effect of a single magnetic atom (§ 1.2). We give a brief introduction to Kondo physics and show how this effect may be detected in the tunneling spectrum acquired with an STM. Next, we present spin excitation spectroscopy (§ 1.3). We will recall the working principle of this technique, show, on the basis of some examples, how it can be used to determine very accurately the magnetic properties of single adsorbates, and highlight some similarities with the Kondo effect. We end the chapter with some conclusive remarks (§ 1.4).

## 1.1 Spin-polarized STM

The idea to use a magnetic tip to probe magnetic surfaces became reality in the early 1990 [12] and confirmed in 2000 [13, 49], making it possible to produce a magnetic tunnel junction in the STM. Spin-polarized STM is nowadays often used for the characterization of surface magnetism with atomic-scale resolution. As an example of SP-STM, we present in Fig. 1.2 spin-polarized images of Co nanoscale islands grown on Cu(111) —we will be using these islands in Chapter 5. The images correspond to the spatial variation of the differential conductance ( $dI/dV$ ) at a given sample bias, also known as  $dI/dV$  maps [10, 44]. Pietzsch *et al.* used for the measurements a tungsten tip coated with chromium and acquired the images under different external magnetic fields. The chromium-coated tip ensures that the tip magnetization is perpendicular to the surface normal. At zero magnetic field, roughly half of the islands appear bright and the other half appear dark. This contrast reflects a change in the  $dI/dV$  among the islands. To explain this contrast in the differential conductance, several models can be invoked. We consider here the one proposed by Wortmann *et al.* [13], which expresses the spin-polarized

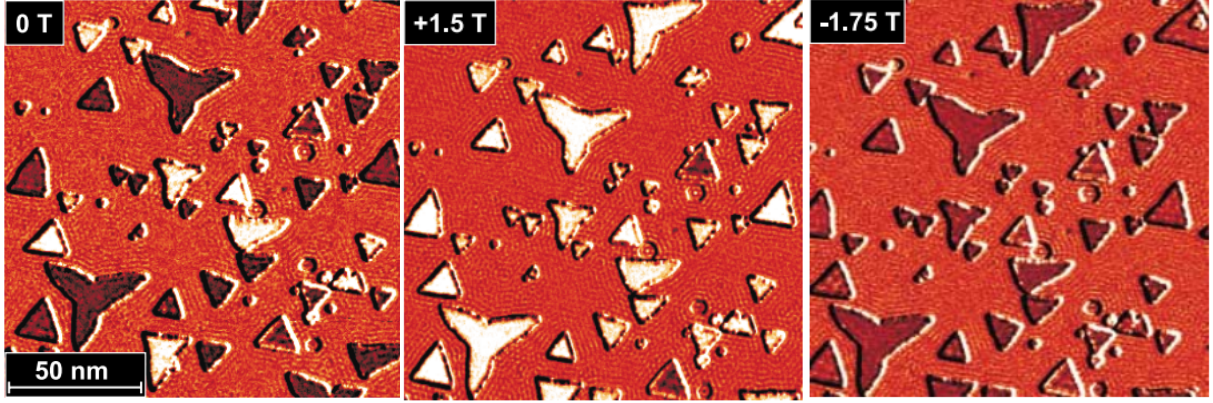


Figure 1.2: **Spin-polarized STM of cobalt islands.** Spin-polarized maps of the differential conductance acquired above Co islands on Cu(111). The images were recorded at a sample bias  $V = -0.18$  V in variable perpendicular magnetic fields. Adapted from [10].

$dI/dV$  as a function of tip and sample density of states (DOS):

$$dI/dV(V) = \rho_t \rho_s(eV) + M_t M_s(eV) \cos \theta, \quad (1.1)$$

where  $\rho_t$  and  $\rho_s$  are the DOS of the tip and sample, respectively.  $M_t$  is the magnetization DOS of the foremost tip atom,  $M_s$  the magnetization DOS of the sample at the location where the electrons tunnel, and  $\theta$  is the angle between the two magnetizations. The contrast can be explained by recalling that the cobalt islands possess a magnetization that is aligned along the surface normal at low temperatures [56]. Statistically, half of the islands have a magnetization pointing in a parallel direction to the tip magnetization, while the other half have a magnetization pointing in a antiparallel direction. The angle between the tip and island magnetizations is then, respectively, either  $\theta = 0^\circ$  or  $\theta = 180^\circ$ , and, in view of Eq. (1.1), a contrast is observed when imaging the differential conductance. As shown in Fig. 1.2, a field of +1.5 T is required to align the magnetization of most of the islands with the tip magnetization, while a magnetic field of at least  $-1.5$  T is required to reverse the direction of their magnetization. Note that higher values of the external magnetic field are needed to change the orientation of the tip magnetization.

Spin-polarized STM is also a powerful tool for characterizing the magnetic properties of single atoms [57,58] and molecules [59–61] on a surface. In particular, it is possible to record with SP-STM the magnetization curve of a single atom (SAMC) [11,62], the foremost tip atom acting then as a detector for the magnetization of the adsorbed atom (adatom). As an example,

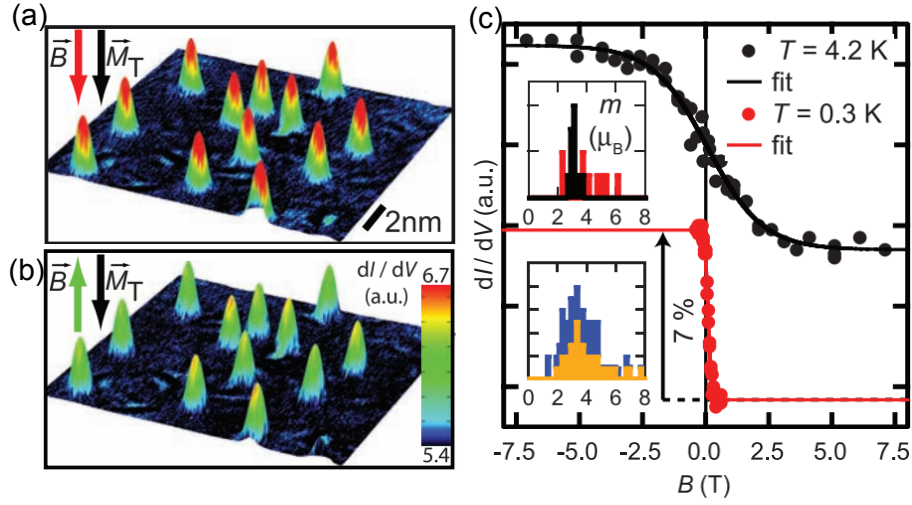


Figure 1.3: **Single-atom magnetization curve.** Pseudo-3D images of Co atoms adsorbed on Pt(111), colorized with the spin-polarized  $dI/dV$  map acquired with: (a)  $B = -0.5$  T parallel to the tip magnetization, and, (b)  $B = +0.5$  T antiparallel to the tip magnetization ( $T = 0.3$  K). (c) Magnetization curves from the same atom taken at different temperatures (dots). The solid lines are fits to the data. The insets show the resulting histograms of the fitted magnetic moments (in  $\mu_B$ ) at 4.2 K (black) and at 0.3 K (red). Adapted from [11].

we consider the experiments by Meier *et al.* [11] on single Co atoms on a Pt(111) surface. On this surface, cobalt atoms have large effective magnetic moments, close to  $3 \mu_B$  (with a large orbital contribution) and a strong out-of-plane anisotropy that forces at low temperature the atom magnetization along the surface normal [63]. The  $dI/dV$  maps recorded in an external magnetic field either parallel or antiparallel to the tip magnetization show a contrast as visible in Figs. 1.3(a) and 1.3(b), respectively. This contrast arises because the atom magnetization is blocked in a up or down direction depending on the orientation chosen for the field. A SAMC consists in gradually sweeping the field and concomitantly recording the  $dI/dV$  over a single Co atom [Fig. 1.3(c)]. This curve depends on temperature, saturating at a field of 0.3 T when the temperature is 0.3 K, and at 5 T when the temperature is 4.2 K. A quasi-classical model is appropriate to describe the measured SAMC [63]. The model-based fits show a good agreement with the data [solid lines in Fig. 1.3(c)], if we assume an effective magnetic moment close to  $3.7 \mu_B$  for a cobalt atom [Inset of Fig. 1.3(c)].

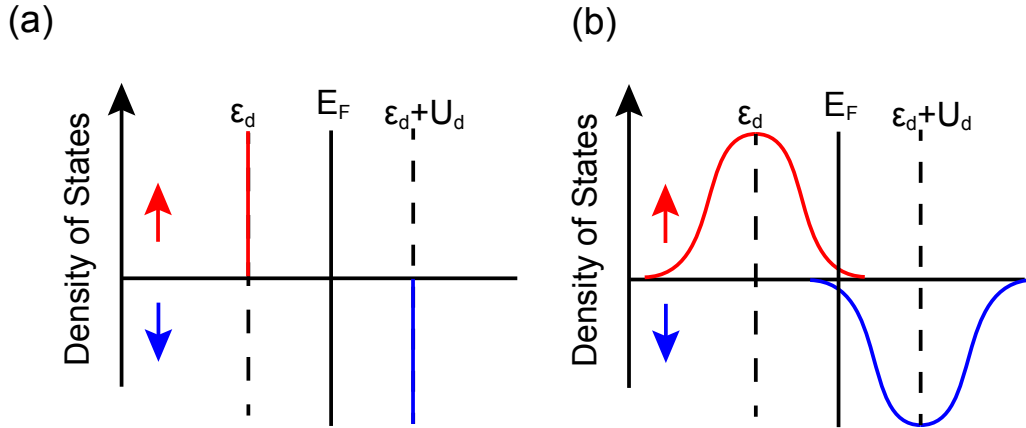


Figure 1.4: **Anderson model.** Density of states of a metal with a localized  $d$  impurity without (left) and with (right)  $s - d$  mixing.

## 1.2 Detecting a Kondo atom with STM

The Kondo effect of a single impurity is a fascinating phenomenon of condensed matter physics, which is known since the beginning of the 20th century. At the time, it was well established that atomic vibrations are frozen in a metal when the temperature is reduced, the resistivity decreasing with temperature and finally stabilizing to a residual resistance due to structural defects and impurities. Surprisingly, the resistivity of a gold metal with iron impurities was instead found to increase with decreasing temperature [14]. J. Kondo theoretically explained this observation in terms of spin-flip scattering events involving the spin of the magnetic impurity and the spins of the conduction electrons of the host metal [16]. The model proposed a logarithmic increase of the resistivity below a critical temperature in a second order perturbation theory. Nowadays this effect is the so-called Kondo effect. The logarithmic increase of the resistivity is associated to the screening of the magnetic impurity by the spins of the conduction electrons in the host metal and is therefore a many-body phenomenon involving electron-electron correlations.

### 1.2.1 Overview

In an effort to elucidate this anomaly, P.W. Anderson developed a model involving a half-filled  $d$ -orbital hybridized with a  $s$ -band [15]. The magnetic moment of the impurity is described by



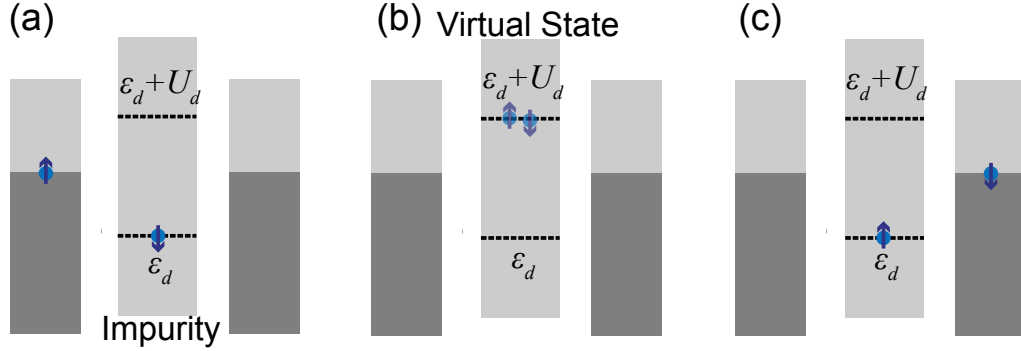


Figure 1.5: **Elastic spin-flip scattering.** Electron tunneling between the conduction band and the impurity before the tunneling process (left), during the “virtual” state where the two electrons combine with opposite spin (middle), and after the tunneling process (right).

the  $d$ -orbital with energy  $\epsilon_d$  and is occupied by only one electron [Fig. 1.4(a)]. An electron with opposite spin that would like to occupy the same level sees the repulsive Coulomb interaction  $U_d$  of the electron already occupying the level. Therefore only the  $\epsilon_d + U_d$  level is available for this additional electron,  $U_d$  accounting for the repulsion between electrons of opposite spin when occupying the  $d$  orbital. As long as this level is above the Fermi energy, the impurity has a net magnetic moment. But this can change since the  $d$ -orbital is hybridized to the electron  $s$ -band leading to a coupled system described by the Hamiltonian:

$$\mathcal{H} = \sum_{\kappa, \sigma} \epsilon_{\kappa} \hat{c}_{\kappa\sigma}^{\dagger} \hat{c}_{\kappa\sigma} + \epsilon_d \sum_{\sigma} \hat{d}_{\sigma}^{\dagger} \hat{d}_{\sigma} + U_d \hat{n}_{d\uparrow} \hat{n}_{d\downarrow} + \mathcal{H}_{\kappa d}, \quad (1.2)$$

where  $\epsilon_{\kappa}$  is the unperturbed energy of the  $s$  electrons in the metal, while the operators  $\hat{c}_{\kappa\sigma}^{\dagger}$  ( $\hat{c}_{\kappa\sigma}$ ) and  $\hat{d}_{\sigma}^{\dagger}$  ( $\hat{d}_{\sigma}$ ) create (destroy) an electron in state  $|\kappa, \sigma\rangle$  and  $|d, \sigma\rangle$ , respectively.  $\hat{n}_{d\sigma}$  is the occupation number operator of the state  $|d, \sigma\rangle$  defined by  $\hat{n}_{d\sigma} = \hat{d}_{\sigma}^{\dagger} \hat{d}_{\sigma}$ . The last term of the Hamiltonian

$$\mathcal{H}_{\kappa d} = \sum_{\kappa\sigma} (V_{\kappa\sigma} \hat{d}_{\sigma}^{\dagger} \hat{c}_{\kappa\sigma} + V_{\kappa\sigma}^* \hat{c}_{\kappa\sigma}^{\dagger} \hat{d}_{\sigma}), \quad (1.3)$$

describes the elastic scattering of conduction electrons onto the impurity [64]. The  $s-d$  mixing term  $V_{\kappa d}$  shortens the lifetime of the  $d$ -state causing it to broaden in energy. The half width at half maximum of the  $d$  state is expressed by  $\Delta = \sqrt{\pi} |V_{\kappa d}|$ . For a strong coupling, the width of the  $d$  state is large enough to cross the Fermi level, leading to a reduction of the magnetic

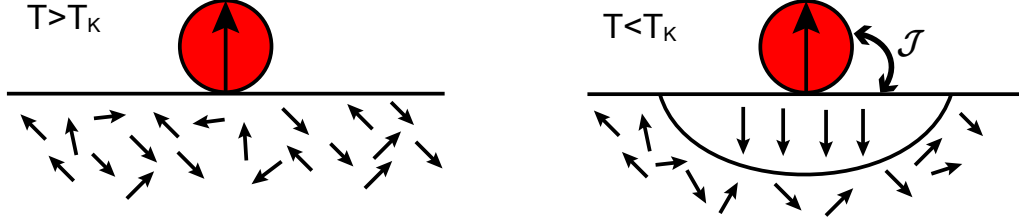


Figure 1.6: **Kondo ground state.** Electron scattering by a magnetic impurity without screening above  $T_K$  (left), and with screening below  $T_K$  (right). The Kondo state consists in a linear combination of  $|\uparrow\uparrow, \downarrow\rangle$  and  $|\downarrow\downarrow, \uparrow\rangle$ .

moment of the impurity (Fig. 1.4). The scattering of the conduction electrons occurs through the tunneling of the impurity electron into the conduction band and the concomitant tunneling of one electron of the conduction band into the impurity (Fig. 1.5). Due to the Pauli principle the two electrons have opposite spins, so that after the scattering event, the impurity spin and the conduction electrons spin have flipped. This tunneling process is energetically cost-less, *i.e.* elastic.

In 1964, J. Kondo proposed to use perturbation theory to describe the scattering of electrons by magnetic impurities [16]. This model is only valid below a critical temperature called Kondo temperature (noted  $T_K$ ) and predicts that the resistivity diverges when the temperature goes to zero. The Kondo effect describes an elastic spin exchange between the magnetic impurity and the spin of the conduction electrons (Fig. 1.5). The Hamiltonian proposed by Kondo is similar to Anderson's, except that the  $s - d$  term is replaced by an exchange term

$$\mathcal{H}_{ex} = \mathcal{J} \hat{S} \cdot \hat{s} = -\frac{\mathcal{J}}{2N} \sum_{\kappa, \kappa'} [(\hat{c}_{\kappa'\uparrow}^\dagger \hat{c}_{\kappa\uparrow} - \hat{c}_{\kappa'\downarrow}^\dagger \hat{c}_{\kappa\downarrow}) \hat{S}_z + \hat{c}_{\kappa'\uparrow}^\dagger \hat{c}_{\kappa\downarrow} \hat{S}_- + \hat{c}_{\kappa'\downarrow}^\dagger \hat{c}_{\kappa\uparrow} \hat{S}_+], \quad (1.4)$$

where  $\mathcal{J}$  is the amplitude of the  $s - d$  exchange interaction between the impurity spin and the spin of the conduction electrons. In this expression, the total spin momentum has to be conserved. When the  $\hat{S}_+$  operator rises the spin of the impurity from down to up, the operators  $\hat{c}_{\kappa'\downarrow}^\dagger \hat{c}_{\kappa\uparrow}$  change the conduction electrons spin from up to down. The exchange term  $\mathcal{H}_{ex}$  therefore describes a spin-flipping process between the local moment carried by the impurity and the spins of the  $N$  electrons. The Kondo Hamiltonian leads to a new magnetic ground state below  $T_K$  with

$$k_B T_K = W \sqrt{2\rho |\mathcal{J}|} \exp(1/2\rho \mathcal{J}), \quad (1.5)$$

where  $W \simeq E_F$  ( $E_F$ : Fermi energy) is the bandwidth of the conduction electrons and  $\rho$  is their density of states of the host metal. The ground state comprises a correlated “cloud” of electronic spins of the host metal that screen the magnetic moment of the impurity (Fig. 1.6). This many-body ground state is doubly degenerate as it can be expressed as a linear combination  $(|\uparrow, \downarrow\rangle + |\downarrow, \uparrow\rangle)/\sqrt{2}$ , where the large arrows stand for the conduction electrons and the small arrows for the impurity.

The Kondo and Anderson models are equivalent as demonstrated in 1966 by Schrieffer and Wolff [17]. In the limit of a small  $s - d$  mixing ( $\Delta \ll \epsilon_d$ ), a canonical transformation enables to re-express the  $\mathcal{H}_{\kappa d}$  term of the Anderson model as the  $\mathcal{H}_{ex}$  term of the Kondo model. A relation between  $\mathcal{J}$  and the Anderson parameters can then be established as:

$$\mathcal{J} = -\frac{2}{\pi} \Delta^2 \frac{U_d}{|\epsilon_d| |\epsilon_d + U_d|}, \quad (1.6)$$

where it can be seen that  $\mathcal{J}$  is antiferromagnetic ( $\mathcal{J} < 0$ ).

### 1.2.2 Tunneling into a single Kondo impurity

In 1998, the first experimental observation of the Kondo effect in a single object was reported in a quantum dot bridging two metallic leads [65, 66]. The Kondo effect is detected through a zero-bias anomaly in the differential conductance that is associated to the formation of a sharp peak in the density of states near  $E_F$ , known as Abrikosov-Suhl resonance or, simply, the Kondo resonance. In the same year, the Kondo resonance was observed for the first time in a single magnetic atom adsorbed on a non magnetic surface by STM [2, 51]. The amplitude of the resonance was shown to be maximum when positioning the tip above the center of the single atom and was progressively lost when moving away laterally, confirming that the effect is localized at the atom site. Figures 1.7(a) and 1.7(b) present a nice example of a Kondo effect as detected in STM [18]. The Kondo effect is carried in this case by an organic radical ( $\text{C}_{28}\text{H}_{25}\text{O}_2\text{N}_4$ ) weakly coupled to a Au(111) surface, behaving as a spin  $S = 1/2$  system. The Kondo resonance is seen to broaden and decrease in amplitude when the temperature is increased from 1.5 K to 15.7 K [Fig. 1.7(a)]. This is expected as above the Kondo temperature, which is estimated to be  $T_K = 5.4$  K for this system, thermal fluctuations destroy the coherence of the ground state (see Fig. 1.6), eventually wiping the resonance out when  $T > 5T_K$  [67]. When a magnetic field  $B$  is applied, the Kondo ground state undergoes a Zeeman splitting and

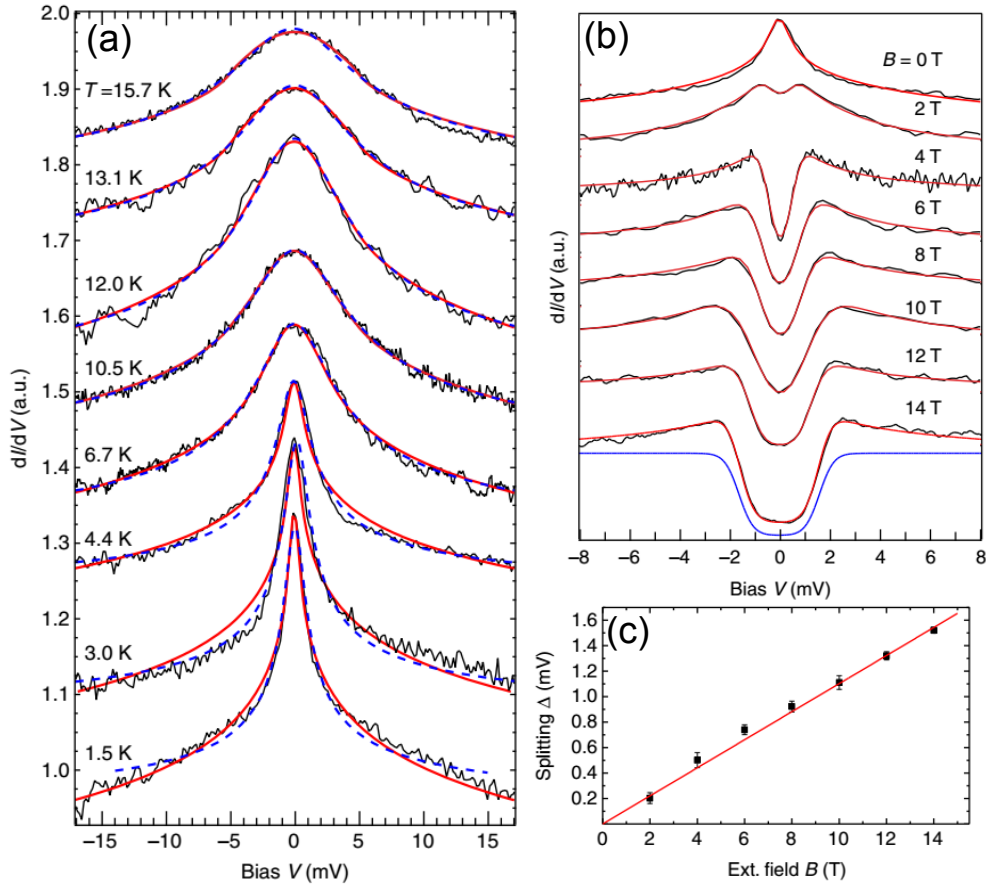


Figure 1.7: **Detecting the Kondo resonance with STM.** (a)  $dI/dV$  spectra acquired on an organic radical ( $C_{28}H_{25}O_2N_4$ ) at various temperatures. Frota fits to the curves are plotted as blue dashed lines. (b)  $dI/dV$  spectra taken at successively increased magnetic fields on the organic radical ( $T = 1.8$  K). (c) Splitting of the Kondo resonance versus applied magnetic field. All spectra are normalized and offset for visual clarity. Adapted from [18].

the Kondo resonance splits apart [Figs. 1.7(b) and 1.7(c)]. Interestingly, the local magnetic environment of the atom can act as an effective magnetic field and Zeeman split the line shape of the Kondo resonance. Through a line shape analysis, it is then possible to sense a rich variety of magnetic phenomena at the nanoscale, which include magnetic interactions of the Kondo atom to surrounding atoms [68–73], magnetic anisotropy [23, 74–77], ferromagnetism [20, 78] and spin-polarized tunneling electrons [79].

The Kondo line shape at  $B = 0$  can be accurately simulated with a Frota function [blue

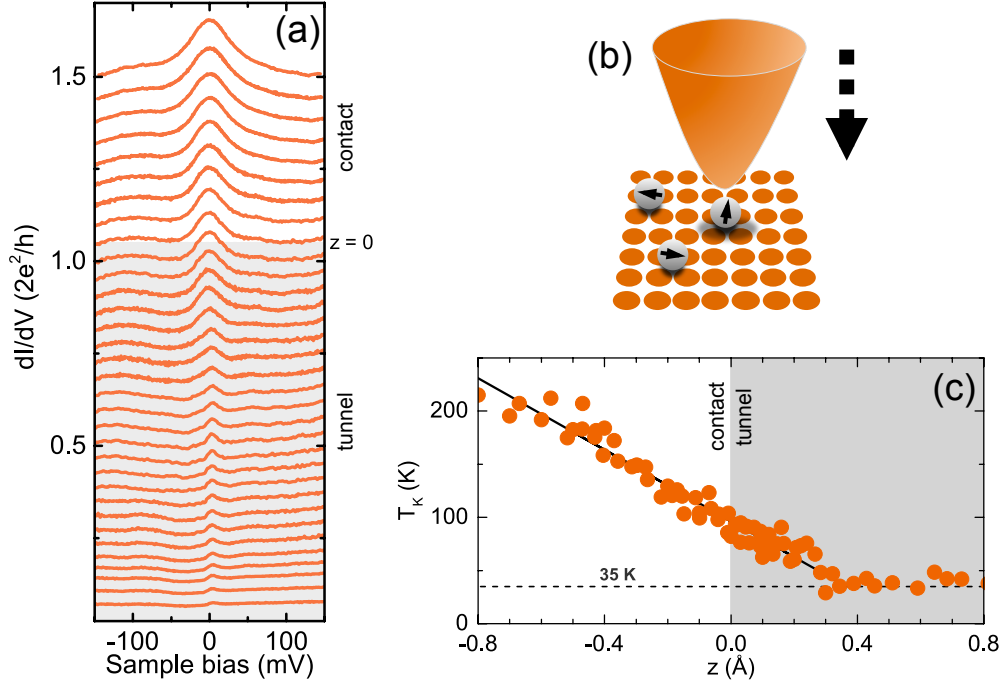


Figure 1.8: **Kondo effect from tunnel to contact.** (a) Sketch showing a copper-coated tip moving into contact with a Co atom on Cu(100). (b)  $dI/dV$  spectrum acquired above a cobalt atom at various tip-atom distances ( $T = 4.4$  K).  $z = 0$  marks the transition from the tunnel (grey background) to the contact (white background) regimes. The tip-atom distance was calibrated through conductance-versus- $z$  traces (not shown). (c) Kondo temperatures extracted from the  $dI/dV$  spectra using a Frota fit [Eq. (1.7)]. Adapted from [80,81].

dashed lines in Fig. 1.7(a)] [21], which is defined as:

$$\sigma(eV) = h \Re \left( \sqrt{\frac{i}{i+x}} \right) + \sigma_0, \quad (1.7)$$

where  $x = (eV - \epsilon_K)/(1.455k_B T_K)$  [82], and  $\epsilon_K$ ,  $h$  and  $\sigma_0$  are constants. Equation (1.7) can be used to extract  $T_K$  from the Kondo resonance (see also § 4.3.2). The values of the Kondo temperature for adsorbed atoms are generally lower compared to when they are embedded in bulk due to their reduced coordinance. For example, for cobalt  $T_K$  is approximately 30 K on a copper surface while in bulk copper  $T_K$  is around 500 K. From Eq. (1.5), we then can estimate the exchange coupling to be of order  $|\mathcal{J}| \sim 1$  eV. To a minor degree, the surface structure

can also modify  $T_K$  by changing the equilibrium position of the adsorbed atom. The Kondo temperature is in fact exponentially sensitive to changes of the coupling  $\Delta$  between the atom and the metal host [Eqs. (1.5) and (1.6)] [83]. The tip can even be used to artificially modify this equilibrium position and therefore controllably tune the Kondo temperature [80, 81]. To illustrate this, we present the evolution of the Kondo effect when a STM tip is moved into contact with a cobalt atom on Cu(100) [Fig. 1.8(a)]. As visible in Fig. 1.8(b), the line shape of the Kondo resonance is unchanged up to a tip-atom distance of  $z = 0.3 \text{ \AA}$ —the distance  $z = 0$  corresponding to a tip-atom contact. Below  $z = 0.3 \text{ \AA}$ ,  $T_K$  increases nearly linearly as the tip is further moved towards the atom, reaching a maximum value of 220 K (beyond  $z = -0.8$  the junction is unstable). In Chapter 4, we will show that the behavior evidenced here for a single atom in contact with the tip is also valid for a single Kondo molecule (§ 4.3.1).

## 1.3 Spin excitation spectroscopy

Soon after the development of STM, surface-science physicists envisioned to use inelastic electrons in the tunneling junction of the STM to probe the excitations of an atom, of a molecule or of an atomic structure [84, 85]. Above a threshold voltage, inelastic electrons can transfer energy to these excitations during the tunneling process. This additional tunneling channel results in an upward step in the differential conductance that occurs at a threshold voltage corresponding to the energy of the excitation. The experimental proof came in 1998 when Stipe *et al.* measured the vibrational excitation of a single acetylene molecule adsorbed on a Cu(100) surface [35, 36, 86]. These vibrational signatures give a chemical sensitivity to the STM, which is usually absent in standard operating modes of the microscope. At the end of the 90s, low-temperature STM appeared paving the way towards the detection of lower-energy excitations. The detection of excitations among Zeeman levels in the  $dI/dV$  spectrum is known as spin excitation spectroscopy.

### 1.3.1 Working principle

In 2004, Heinrich *et al.* [3] showed that spin excitations in a single-magnetic atom could be detected with an STM operated in an external magnetic field. This seminal experiment by Heinrich *et al.* was carried out at 0.6 K on Mn atoms deposited on  $\text{Al}_2\text{O}_3$  islands [Fig. 1.9(a)]. The aluminum oxide greatly facilitates the experimental identification of the spin excitations.

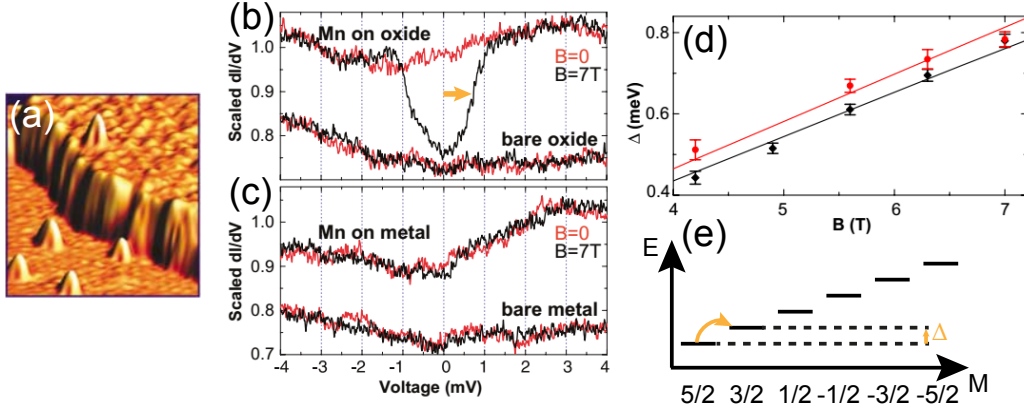


Figure 1.9: **Spin excitation spectrum of a Mn atom on Al<sub>2</sub>O<sub>3</sub>.** (a) NiAl(110) surface partially covered with Al<sub>2</sub>O<sub>3</sub> with adsorbed Mn atoms. (b)  $dI/dV$  spectra obtained on the Mn atom and on the bare oxide with and without the magnetic field. (c)  $dI/dV$  spectra recorded on a Mn atom adsorbed on NiAl(110). (d) Step separation as a function of applied magnetic field. (e) Spin-state diagram and spin excitation of Mn on Al<sub>2</sub>O<sub>3</sub>/NiAl(110) in the presence of a magnetic field along  $z$ . Adapted from [3].

It preserves the spin of the Mn atom by minimizing the  $s - d$  mixing between Mn and the host metal. It also ensures a partial decoupling of Mn from the metal, thus extending the electronic lifetimes for the spin states of the Mn atom. Several salient aspects can be noted in the data: i) When a magnetic field is applied, steps appear in the  $dI/dV$  spectrum above a single Mn atom that are located at threshold biases of  $\pm 0.7$  mV [Fig. 1.9(b)]; ii) The steps correspond to a 25% increase with respect to the elastic conductance —the elastic conductance corresponds to the  $dI/dV$  signal below the threshold biases; iii) The steps disappear when the field is absent [Fig. 1.9(b)] and when Mn is placed on NiAl(110) [Fig. 1.9(c)]; iv) The threshold biases shift linearly with the magnetic field [Fig. 1.9(d)].

These findings can be rationalized by assuming the existence of a Zeeman effect for the total momentum  $\hat{\mathbf{J}}$  of the Mn atom

$$\mathcal{H} = -g\mu_B \hat{\mathbf{J}} \cdot \hat{\mathbf{B}}, \quad (1.8)$$

where  $g$  is the gyromagnetic factor,  $\mu_B$  the Bohr magneton and  $\mathbf{B}$  the applied magnetic field. In the case of the Mn atom in the gas phase, the orbital momentum is zero ( $3d^5$ ) and the total momentum  $J$  refers to the spin only, where  $S = 5/2$ . Supposing this is also the case

once the Mn atom is adsorbed on  $\text{Al}_2\text{O}_3$ , when a magnetic field is applied, it is possible to lift the degeneracy of the  $S = 5/2$  state, having then  $M = +5/2$  as the ground state and the  $M = +3/2$  as the first excited state —  $M$  is the projected spin momentum. Within this viewpoint, the threshold biases of  $\pm 0.7$  mV correspond to a  $M = +5/2 \rightarrow M = +3/2$  excitation of the Mn atom [Fig. 1.9(e)]. This excitation changes the projected spin momentum by  $\delta M = +1$ , forcing the tunneling electron to flip its spin from a  $|\uparrow\rangle$  to  $|\downarrow\rangle$  in order to conserve the total angular momentum. We will see further on that spin excitations with  $\delta M = -1$  are also possible. In this latter case the tunneling electron must flip its spin from a  $|\downarrow\rangle$  to  $|\uparrow\rangle$  to conserve the total angular momentum. These spin flips limit the detection of spin excitations to transitions with  $\delta M = \pm 1$ .

During the very short collisional time between the atom and the tunneling electron, the electron spin couples with the adsorbate spin either through a direct dipolar interaction or through an exchange interaction. The two form a transient collisional intermediate state, where the interaction with the environment can be neglected [87, 88]. This process is remarkably efficient compared to vibrational excitations. The inelastic contribution to the  $dI/dV$  in the case of a spin excitation can be comparable [see Fig. 1.10(b)] or, as we show in Chapter 3, even exceed the elastic conductance, while in the case of a vibrational excitation it is usually a few per cent of the elastic signal. This difference can be traced back to the strengths of the interactions at play. While the spin-spin coupling is of order 1 eV (§ 1.2.2), the electron-vibration coupling is of order 10 meV [89].

Figures 1.9(b) and 1.9(c) demonstrate that the presence of the insulating layer is essential for observing the spin excitation in the  $dI/dV$  spectrum. This is a consequence of the finite lifetime of the excited states. Nowadays, spin excitation spectroscopy is mostly carried out on atoms adsorbed on an insulating  $\text{Cu}_2\text{N}$  layer and, more recently, on a MgO layer [5, 6]. In these systems, the lifetimes are typically in the range of a few 10 ns [53, 90] to 1 ms [91] for  $3d$  atoms, reaching 1 hour (at 2.5 K) for a  $4f$  atom of Ho deposited on MgO [92]. When the magnetic atoms are directly adsorbed on a metal substrate the lifetime is greatly reduced. This leads to an increased broadening of spectral features and the excitations are poorly resolved in energy so that spin excitation spectroscopy is in general harder to carry out on a metal surface [93–95]. For example, Khajetoorians *et al.* have estimated a lifetime of 200 fs for the magnetic excitations of individual Fe atoms on Cu(111) [62] with step heights representing only 5% of the elastic conductance. Interestingly, the magnetic moment of Fe on Cu(111) is determined to be  $3.4 \mu_B$  from a SAMC measurement (§ 1.1), which is lower compared to the  $4.0 \mu_B$  found for Fe on the



insulating layer of Cu<sub>2</sub>N [24]. The decreased value of the Fe magnetic moment is attributed to the strong hybridization of the Fe atom with the metallic substrate. The lifetime limiting process can then be traced back to substrate electrons colliding onto the magnetic adsorbate and causing a de-excitation of the system. The only example known of spin lifetimes of the order of minutes for atoms on a metal is Ho on Pt(111), but this study remains controversial [96,97].

### 1.3.2 Magnetic anisotropy

The spin-orbit coupling favors a preferential spin orientation in some structures. This phenomenon, also known as magnetic anisotropy, has been the focus of research for decades as the bistability it introduces in nanoscale systems is potentially appealing for storing binary information. Recent activity in this domain has consisted in testing whether it is possible to downscale these systems from several nanometers to a single object. Spin excitation spectroscopy is particularly appealing as it offers the possibility to characterize the magnetic anisotropy of single atoms.

Magnetic anisotropy introduces a small energy difference between two spin orientations called magnetic anisotropy energy. This weak energy difference, typically of the order of a few meV, renders these spin states accessible to spin excitation spectroscopy, even in the absence of a magnetic field. Magnetic anisotropy in single objects can be induced by molecular ligands in the case of organometallic compounds [98] (see also Chapter 3) and by structural properties of the substrate as in the case of metal atoms on thin films —MgO or Cu<sub>2</sub>N [22–25]. The spin Hamiltonian describing the magnetic properties of a single object can be written as:

$$\mathcal{H} = D\hat{S}_z^2 + E(\hat{S}_x^2 - \hat{S}_y^2) - g\mu_B \hat{\mathbf{S}} \cdot \hat{\mathbf{B}}, \quad (1.9)$$

where the  $z$  axis, *i.e.* the quantization axis, is chosen along the surface normal.  $D$  expresses the axial anisotropy, which is the tendency of the spin to be aligned along the  $z$  axis. A negative value of  $D$  will favor a spin parallel to the  $z$  axis, whereas a positive value will keep the spin in the  $xy$  plane. The parameter  $E$ , called transverse anisotropy, accounts for a privileged direction of the spin in the  $xy$  plane. The last term is a Zeeman term.

To experimentally illustrate how magnetic anisotropy can be evidenced in spin excitation spectroscopy, we briefly recall the work of Hirjibehedin *et al.* on iron atoms [24]. In this study,

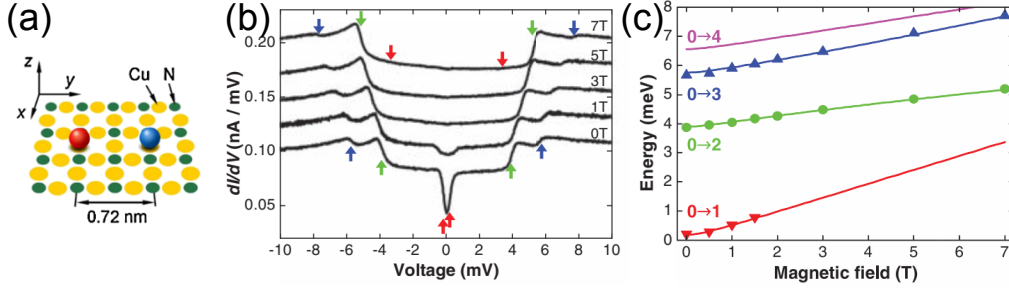


Figure 1.10: **Spin excitation spectrum revealing magnetic anisotropy.** (a) Sketch showing an iron atom on a Cu<sub>2</sub>N surface (Fe: blue, Co: red, Cu: yellow, N: green). Iron adsorbs on top of a Cu atom with two N atoms as its horizontal nearest neighbors. (b)  $dI/dV$  spectra acquired above a Fe atom with a magnetic field ranging from 0 to 7 T. The changes in energy and intensity of these excitations as a function of  $B$  confirm the magnetic origin of these excitations. (c) Energies for the first (red triangles), second (green circles), and third (blue triangles) steps observed in the spectra acquired by varying the magnetic field  $B$ . The transitions correspond  $\epsilon_0 \rightarrow \epsilon_1$  (noted  $0 \rightarrow 1$ ),  $\epsilon_0 \rightarrow \epsilon_2$  (noted  $0 \rightarrow 2$ ),  $\epsilon_0 \rightarrow \epsilon_3$  (noted  $0 \rightarrow 3$ ). The energies  $\epsilon_0, \epsilon_1, \epsilon_2, \epsilon_3$  are given in Eq. (1.10). The magnetic field is applied along the axis running between two nearest-neighbor N atoms. Adapted from [24] and [69].

individual Fe atoms are separated from a Cu(100) crystal by a monolayer of copper nitride Cu<sub>2</sub>N [Fig. 1.10(a)]. The spin excitation spectra recorded above isolated Fe atoms exhibit three transitions [colored arrows in Fig. 1.10(b)] that are attributed to spin excitations from the ground state to the accessible eigenenergies of Eq. (1.9). Supposing that the spin of Fe is that of a free iron atom, *i.e.*  $S = 2$ , the eigenenergies  $\epsilon_n$  in zero magnetic field ( $B = 0$ ) are

$$\begin{aligned}
 \epsilon_0 &= 2D(1 + \sqrt{1 + 3E^2/D^2}), \\
 \epsilon_1 &= 4D, \\
 \epsilon_2 &= (D - 3E), \\
 \epsilon_3 &= (D + 3E), \\
 \epsilon_4 &= 2D(1 + \sqrt{1 - 3E^2/D^2}).
 \end{aligned} \tag{1.10}$$

The axial term splits the degeneracy of the spin states on the basis of the  $|S = 2, M\rangle$  states, whereas the transverse term mixes states of different  $M$ . Hirjibehedin *et al.* identified three transitions ( $\epsilon_0 \rightarrow \epsilon_1$ ,  $\epsilon_0 \rightarrow \epsilon_2$  and  $\epsilon_0 \rightarrow \epsilon_3$ ) by monitoring the shift of the inelastic steps in

different strengths and orientations of the external magnetic field. For example, in Figs. 1.10(b) and 1.10(c) the field is oriented along the axis running between two nearest-neighbor N atoms ( $B_x \neq 0$ ). It is possible then to extract from these spectra  $D = -1.55$  meV and  $E = 0.31$  meV. This constitutes the first measurement of a magnetic anisotropy at the single-atom level.

The eigenvectors  $\psi_n$  of Eq. (1.9) are expressed as a linear combination of  $|S = 2, M\rangle$  states. By analogy with neutron scattering, if one defines  $\psi_i$  and  $\psi_f$  as respectively the initial and final eigenvectors, the relative step heights for the above transitions were found to be well described by the expression:

$$I_{i \rightarrow f} = \frac{1}{2} |\langle \psi_f | \hat{S}_+ | \psi_i \rangle|^2 + \frac{1}{2} |\langle \psi_f | \hat{S}_- | \psi_i \rangle|^2 + |\langle \psi_f | \hat{S}_z | \psi_i \rangle|^2. \quad (1.11)$$

In the zero-field experiment, this yields  $I_{0 \rightarrow 1} = 3.88$ ,  $I_{0 \rightarrow 2} = 1.62$ ,  $I_{0 \rightarrow 3} = 0.49$  and  $I_{0 \rightarrow 4} = 0.03$ , which corresponds to a relative weight of 65%, 27%, 8% and 0%, respectively, in good agreement with experiments. However, this approach makes wrong predictions for the elastic conductance. Indeed, the elastic contribution would yield  $I_{0 \rightarrow 0} = 0.95$  and thus is greatly underestimated when compared to the measurements [Fig. 1.10(b)]. Following the study of Hirjibehedin *et al.*, several theoretical models based on one-electron approaches were developed [99, 100], but none are able to model the ratio between the inelastic and elastic conductances. In Chapter 3, we will present a prototypical spin system possessing magnetic anisotropy, where we were able to provide a qualitative explanation for this ratio using a theory developed by N. Lorente [38].

### 1.3.3 Spin-spin coupling

Spin excitation spectroscopy can be used to collect magnetic information from a variety of spin systems, *e.g.* phthalocyanine molecules on an oxide [98] and in molecular multi-layers [101], or magnetic impurities on semiconductors [102]. The interactions between spins in individual atomic-scale magnetic structures were investigated as well by controllably assembling linear chains with the STM tip, one magnetic atom at a time on  $\text{Cu}_2\text{N}$  [22] [Fig. 1.11(a)]. Remarkably, the spin excitation spectra acquired on linear chains of 1 to 10 manganese atoms ( $S = 5/2$ ) reveal excitations associated to coupled atomic spins [Fig. 1.11(b)]. Manganese atoms on  $\text{Cu}_2\text{N}$  have negligible magnetic anisotropy —  $D = 0.2$  meV [24], and the spin Hamiltonian can

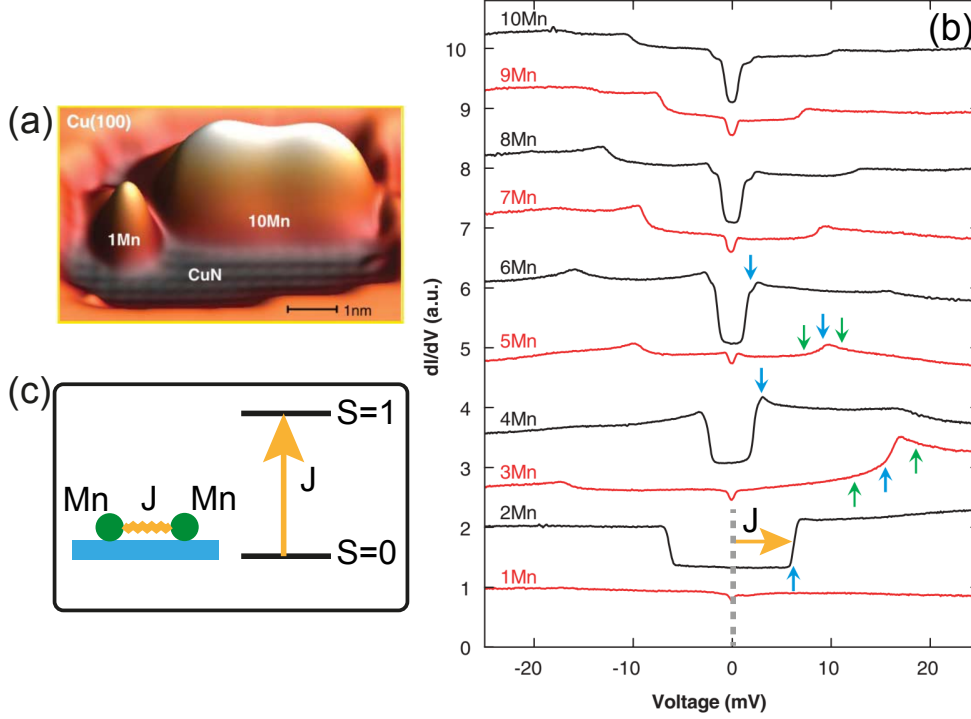


Figure 1.11: **Spin excitation spectrum of coupled spins.** (a) Pseudo-3D image of a tip-assisted engineered Mn chain of 10 atoms on Cu<sub>2</sub>N. (b)  $dI/dV$  spectra of the Mn chains taken with the tip positioned above the center of the chains ( $T = 0.6K$ ,  $B = 0$  T). The spectra are vertically offset by one unit for clarity. (c) Spin-state diagram and spin excitation of a Mn<sub>2</sub> chain, *i.e.* a Mn dimer, on Cu<sub>2</sub>N. Adapted from [22].

be expressed then as:

$$\mathcal{H} = J \sum_{i=1}^{N-1} \hat{\mathbf{S}}_i \cdot \hat{\mathbf{S}}_{i+1} + 1, \quad (1.12)$$

where  $\hat{\mathbf{S}}_i$  is the spin operator for the  $i$ -th site along the chain and  $J$  is the coupling strength. This model includes only identical nearest-neighbor exchange interactions between the spins. For a dimer, the ground state of the antiferromagnetic ( $J < 0$ ) Heisenberg chain is a singlet  $|S = 0\rangle$  and the first excited state is a triplet  $|S = 1\rangle$  with energy separation  $J$  [Fig. 1.11(c)]. The energy spacing between the ground state and the first excited state provides a direct measure of the coupling strength  $J$ . From the spectrum acquired on the dimer [Fig. 1.11(b)], one determines  $J = -6.2$  meV. In this case, the excitation does not necessarily require the tunnel electron to flip its spin. We may in fact have  $|S = 0, M = 0\rangle \rightarrow |S = 1, M = 0\rangle$  where

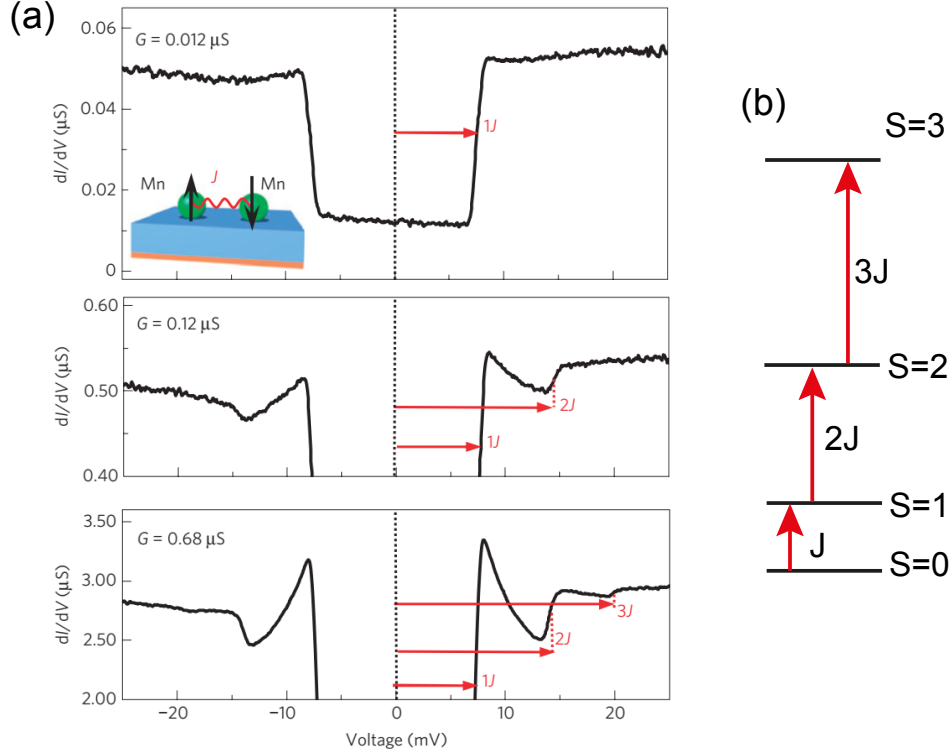


Figure 1.12: **Spin excitation spectrum revealing spin pumping.** (a) The panel shows the evolution of the  $dI/dV$  spectrum acquired above one Mn atom of the dimer when the junction conductance is increased, *i.e.* when the tip-atom distance is decreased. (b) Spin-state diagram of the Mn dimer. The arrows indicate the spin excitations when spin pumping is active. Inset: Sketch showing a Mn dimer on  $\text{Cu}_2\text{N}$ . Adapted from [48].

no spin-flip occurs as  $\delta M = 0$ , and  $|S = 0, M = 0\rangle \rightarrow |S = 1, M = \pm 1\rangle$  where a spin flip occurs as  $\delta M = \pm 1$ .

### 1.3.4 Spin pumping

Other studies have shown that spin states can be excited at a higher rate than the spontaneous relaxation of the atom towards its magnetic ground state. At low currents, a tunneling electron encounters the spin in its ground state because spontaneous relaxation is more frequent than excitation by tunneling electrons. At sufficiently high currents there is a significant probability for a tunneling electron to encounter the spin already in an excited state and excitations into even higher states are possible. To illustrate how spin pumping can be evidenced in spin

excitation spectroscopy we present the measurements by Loth *et al.* on the Mn dimer on Cu<sub>2</sub>N of § 1.3.3 [Inset of Fig. 1.12(a)] [48]. Figure 1.12(a) shows how spin pumping imprints a signature onto the spin excitation spectrum of the Mn dimer —the spectra are acquired above one of the Mn atoms. At low current [top spectrum of Figure 1.12(a)], the presence of steps in the spectrum at  $\pm 7.4$  mV corresponds to the Mn dimer being excited into its triplet state,  $|S = 0\rangle \rightarrow |S = 1\rangle$ . The onset yields an antiferromagnetic coupling  $J = -7.4$  meV, which is slightly larger than the one determined in [22]. Remarkably, more steps appear in the spectrum at energies  $2J$  and  $3J$  when the tunnel current is increased [middle and bottom panel of Figure 1.12(a)]. As no excitations with energy  $2J$  exists out of the ground state, the presence of the observed steps proves the existence of successive excitations into higher states as sketched in Fig. 1.12(b). Similar current-induced pumping to higher excitation states has been observed for small Fe clusters containing only a few atoms on Cu(111) [103], or for Fe-OEP-Cl (Fe-octaethylporphyrin-chloride) molecules adsorbed on Pb(111) [90]. Note that as long as the tip is not spin-polarized, the current induced pumping into higher states cannot lead to an inversion of the state occupancy. This behavior changes drastically when a spin-polarized tip is used [104, 105] and the spin-pumping experiment is then close to the phenomenon at work in lasers [48].

### 1.3.5 Kondo scattering

As presented in § 1.2, the Kondo effect is detected in STM through a zero-bias anomaly in the  $dI/dV$  spectrum acquired above a magnetic impurity. This singular behavior is also present in a spin excitation spectrum where a Kondo-like effect is predicted to cause a logarithmic decay of the differential conductance above the inelastic steps [77, 106, 107]. Such a decay is visible in the  $dI/dV$  spectra of the Mn dimer in Fig. 1.12(a) and is increasingly more pronounced as the tip approaches closer to the dimer. To model this effect it is necessary to include in the spin Hamiltonian of the atom, or of the molecule, magnetic anisotropy as well as a coupling to the environment. As we will show in Chapter 4, this can be done by parameterizing the environment through the product of the Kondo exchange interaction with the density of states of the substrate electrons at the Fermi energy,  $\rho\mathcal{J}$  [Eq. (1.6)].

Many-body effects can also shift the inelastic thresholds. A renormalization of the spin excitations can take place due to the exchange coupling  $\rho\mathcal{J}$  of the spin with the conduction electrons [74], even in the complete absence of the Kondo effect in the ground state [108]. This

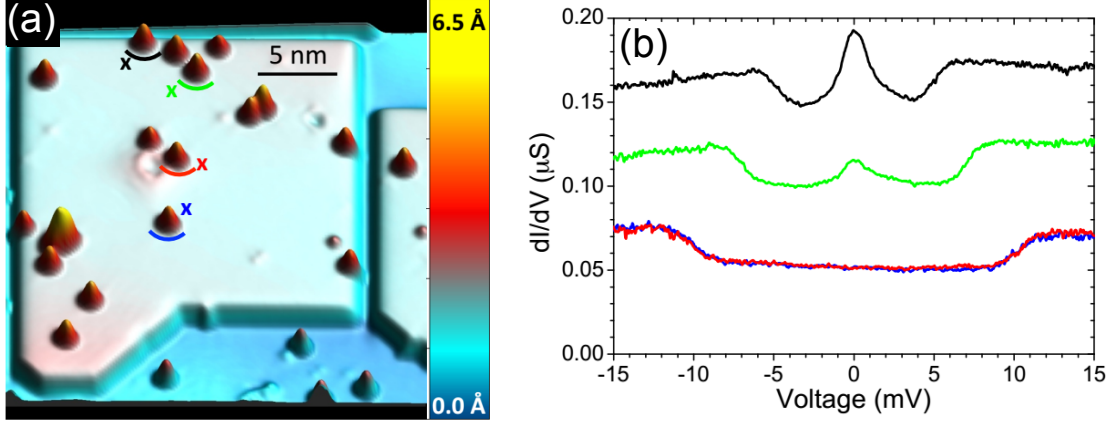


Figure 1.13: **Spin excitation spectrum revealing Kondo scattering.** (a) Image of Co atoms adsorbed on a large  $\text{Cu}_2\text{N}$  island ( $18.6 \times 20.5 \text{ nm}^2$ ). The crosses indicate the location where the spectra of panel (b) were acquired. (b)  $dI/dV$  spectra acquired on top of the four atoms labeled in (a). The spectra are offset vertically for clarity. Adapted from [74].

is observed experimentally as a reduction of the axial magnetic anisotropy [74, 77]. Oberg *et al.*, for example, observed that the spin excitation spectrum of a Co atom on a large  $\text{Cu}_2\text{N}/\text{Cu}(100)$  island changes dramatically depending on its lateral distance to the edge of the island [Fig 1.13(a)]. As cobalt approaches the edge, the relative height of the Kondo resonance increases and the inelastic steps shift to lower energy [Fig 1.13(b)]. This behavior can be explained using both Kondo and Anderson models through second-order perturbation theory. A renormalized energy  $\Delta$  for the spin excitation can then be expressed as

$$\Delta = \Delta_0 \left[ 1 - \frac{3}{16} (\mathcal{J}\rho)^2 \ln \left( \frac{2W}{\pi k_B T} \right) \right], \quad (1.13)$$

where  $\Delta_0$  is the bare excitation energy,  $W$  the bandwidth of the conduction electron and  $T$  the temperature. The equation links the Kondo peak to the spin excitation spectrum as  $\rho\mathcal{J}$  also determines the Kondo temperature of cobalt [Eq. (1.5)]. Qualitatively, the above relation accounts for the experimental observation: as  $\rho\mathcal{J}$  decreases, the Kondo temperature decreases, and at the same time the spin excitation energy goes up.

## 1.4 Conclusion

In this chapter we have presented how STM can detect spin signatures at the atomic level. We have restrained the presentation to the techniques and topics in direct relation to the thesis. We have shown that SP-STM exploits spin-polarized electrons to gather information on the spin orientation of a magnetic sample. With SP-STM, it is even possible to acquire a single-atom magnetization curve with an external magnetic field and determine the magnetic moment of the atom. We have then briefly introduced the Kondo effect, and showed how it can be detected and characterized by tunneling spectroscopy. Finally, we have extensively presented spin excitation spectroscopy. This technique, which is at the heart of this thesis, exploits inelastic electrons to trigger spin excitations in single atoms or molecules. The spectroscopic fingerprints produced by these inelastic events allows gathering magnetic information on the spin system. We aim in this thesis at using spin excitation spectroscopy to characterize the magnetic properties of surfaces at the atomic-scale. We will show that this is possible with the help of a simple molecule, nickelocene. By attaching this molecule to the tip apex of the STM, we will show that spin excitation spectroscopy can be performed freely above the surface. Our study presents the first attempt to visualize surface magnetism at the atomic-scale using inelastic electrons.



## CHAPTER 2

# Scanning tunneling microscopy

Scanning tunneling microscopy (STM) is a technique that has proven to be of great efficiency to study surface science. It has been developed by G. Binnig and H. Rohrer in 1982 in the IBM labs [26]. The first great achievement of this technique was to determine the reconstruction pattern in real space of the Si(111) surface [27], fixing once and for all the way this surface reconstructs. Since its early steps, several spin-off techniques using STM have been developed. The objective of this chapter is to briefly introduce the theoretical background of STM (§ 2.1). We will first present the one dimensional tunnel barrier in order to introduce the concept of tunneling transmission. Then we will use Bardeen's theory in order to introduce the tunneling matrix elements  $M_{\mu\nu}$  that carry all the information about the tunneling processes in a junction. This tunneling matrix is fundamental to relate experiment to calculation and is, at the same time, a limiting factor as it is difficult to estimate its value. To bypass this limitation, we will present the WKB theory, which replaces the tunneling matrix by a transmission term to simplify the interpretation of the experiments. Using this WKB theory we will show why tunneling spectroscopy, also known as scanning tunneling spectroscopy (STS), can locally measure the vacuum density of states (DOS) of a surface (§ 2.2). As it is an important aspect of this thesis, we will introduce the inelastic tunneling and its fingerprint in tunneling spectroscopy—a more detailed presentation focused on spin-related inelastic tunneling will be presented in § 1.3. We then determine the energy resolution in tunneling spectroscopy (§ 2.3) and conclude the chapter by a brief description of the experimental setup used (§ 2.4).

## 2.1 STM basics

### 2.1.1 One dimensional tunnel barrier

To introduce the tunneling effect and the notion of transmission we consider a one dimensional potential barrier of width  $d$  and height  $U_0$ . According to Fig. 2.1, the total potential  $U$  is defined by:

$$U = \begin{cases} 0, & \text{if } z < 0, \\ U_0, & \text{if } 0 < z < d, \\ 0, & \text{if } z > d. \end{cases}$$

An electron encountering this barrier must obey the Schrödinger equation:

$$-\frac{\hbar^2}{2m_e} \frac{\partial^2 \Psi(z)}{\partial z^2} + U(z)\Psi(z) = E\Psi(z),$$

which gives the following eigenfunctions:

$$\Psi = \begin{cases} \Psi_{(1)}(z) = \exp(ikz) + r \exp(-ikz), \\ \Psi_{(2)}(z) = A \exp(-\kappa z) + B \exp(\kappa z), \\ \Psi_{(3)}(z) = t \exp(ikz), \end{cases} \quad (2.1)$$

with  $k = \sqrt{2m_e E}/\hbar$  and  $\kappa = \sqrt{2m_e(U_0 - E)}/\hbar$ . The reflectivity and transmissibility of the junction are labeled  $r$  and  $t$ , respectively. As  $\Psi(z)$  and  $d\Psi(z)/dz$  must be continuous functions at  $z = 0$  and  $z = d$ , the amplitudes  $A$  and  $B$  in Eq. (2.1) can be expressed in terms of  $k$ ,  $\kappa$ ,  $r$  and  $t$  as:

$$A = \frac{1}{2} \left[ 1 + r + \frac{ik}{\kappa}(1 - r) \right] = \frac{t}{2} \left[ 1 + \frac{ik}{\kappa} \exp(ikd - \kappa d) \right],$$

$$B = \frac{1}{2} \left[ 1 + r - \frac{ik}{\kappa}(1 - r) \right] = \frac{t}{2} \left[ 1 + \frac{ik}{\kappa} \exp(ikd + \kappa d) \right].$$

From these expressions we can deduce  $r$  and  $t$ , and introduce the transmission probability, which is defined by  $\mathcal{T} = |t|^2$ . With a wide enough tunnel barrier ( $\kappa d \gg 1$ ), we have:

$$\mathcal{T} = 16 \frac{\kappa^2 k^2}{(k^2 + \kappa^2)^2} \exp(-2\kappa d).$$

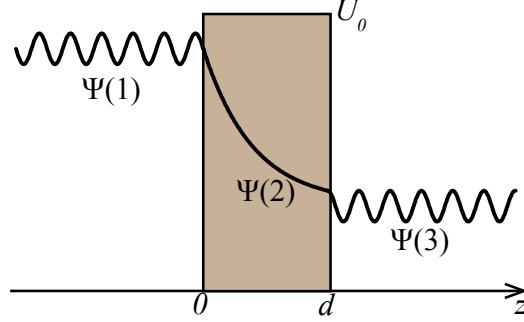


Figure 2.1: **Electron tunneling across a one-dimensional barrier.** Sketch of the one-dimensional potential barrier of width  $d$  and height  $U_0$ .  $\Psi_{(1)}$ ,  $\Psi_{(2)}$  and  $\Psi_{(3)}$  are electron wave packets.

This result shows that even in this simple case of the one dimensional barrier, the transmission shows an exponential dependance to the tunnel barrier thickness.

### 2.1.2 Bardeen's theory

In this section, we will review the theory developed by Bardeen [28, 101]. To describe the tunneling of an electron from the sample to the tip Bardeen expresses the Schrödinger equation for an electron of the tip:

$$\left(-\frac{\hbar^2}{2m_e}\Delta + U_t\right)\chi_\nu = E_\nu\chi_\nu, \quad (2.2)$$

and of the sample:

$$\left(-\frac{\hbar^2}{2m_e}\Delta + U_s\right)\psi_\mu = E_\mu\psi_\mu, \quad (2.3)$$

with  $U_t$  (respectively  $U_s$ ) the potential related to the tip (respectively to the sample),  $\chi_\nu$  (respectively  $\psi_\mu$ ) the wave function of an electron of the tip (respectively sample) with an energy  $E_\nu$  (respectively  $E_\mu$ ). Merging Eqs. (2.2) and (2.3) yields the time-dependent Schrödinger equation describing the electron tunneling from the sample to the tip:

$$i\hbar\frac{\partial\Psi}{\partial t} = \left(-\frac{\hbar^2}{2m_e}\Delta + U_s + U_t\right)\Psi, \quad (2.4)$$

A solution to Eq. (2.4) is the wave function  $\Psi$ :

$$\Psi = \psi_\mu e^{-E_\mu t/\hbar} + \sum_{\nu=1}^{\infty} c_\nu(t) \chi_\nu e^{-iE_\nu t/\hbar}. \quad (2.5)$$

The coefficient  $c_\nu(t)$  is related to the probability to transfer an electron from a state of the sample described by  $\psi_\mu$  to a state of the tip described by  $\chi_\nu$ . Since at first we consider the electron in the sample, we have  $c_\nu(t=0) = 0$ . One of the approximations of Bardeen is to consider  $\psi_\mu$  and  $\chi_\nu$  as nearly orthogonal, implying that  $|c_\nu|^2$  can be considered as an infinitesimal quantity. By injecting Eq. (2.5) in Eq. (2.4) we can express the time-dependent evolution of the coefficient  $c_\nu(t)$  as:

$$i\hbar \sum_{\nu=1}^{\infty} \frac{dc_\nu(t)}{dt} \chi_\nu e^{-iE_\nu t/\hbar} = U_s \psi_\mu e^{-iE_\mu t/\hbar} + U_t \sum_{\lambda=1}^{\infty} c_\lambda(t) \chi_\lambda e^{-iE_\lambda t/\hbar}. \quad (2.6)$$

By restraining to first order, we have:

$$i\hbar \frac{dc_\nu(t)}{dt} = \int_{\Omega_T} \psi_\mu U_s \chi_\nu^* d^3\mathbf{r} e^{-i(E_\mu - E_\nu)t/\hbar},$$

$\Omega_T$  is the integration subspace (in 3 dimensions) linked to the tip. We can solve this equation, leading to the expression of the coefficient  $c_\nu(t)$ :

$$c_\nu(t) = M_{\mu\nu} \frac{e^{-i(E_\mu - E_\nu)t/\hbar} - 1}{E_\mu - E_\nu}.$$

The so-called tunneling matrix  $M_{\mu\nu}$  is defined by:

$$M_{\mu\nu} = \int_{\Omega_T} \psi_\mu U_s \chi_\nu^* d^3\vec{r},$$

We can also express the tunneling matrix as a surface integral on  $\Sigma$ , the surface domain corresponding to the separation between the tip and the sample. It leads to the following expression:

$$M_{\mu\nu} = \int_{\Sigma} (d\vec{S} \chi_\nu^* \vec{\nabla} \psi_\mu - \psi_\mu \vec{\nabla} \chi_\nu^*). \quad (2.7)$$

Using this tunneling matrix we can now express the tunneling current corresponding here to a

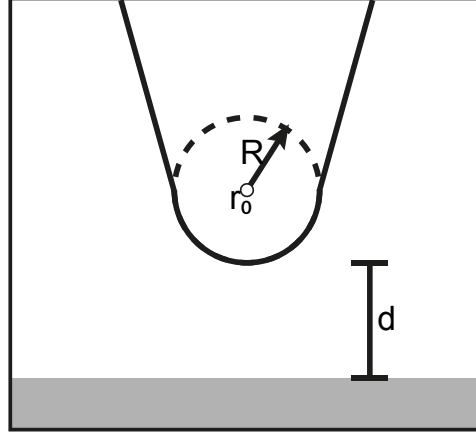


Figure 2.2: **Representation of the spherical tip considered by Tersoff and Hamann.** The spherical tip has a radius  $R$  and is positioned at  $\vec{r}_0$ . The tip distance to the surface is noted  $d$ . Adapted from [33].

flow of electrons from the sample to the tip. This yields:

$$I = \frac{2e^2}{\hbar} V \sum_{\mu\nu} |M_{\mu\nu}|^2 \delta(E_\nu - E_F) \delta(E_\mu - E_F). \quad (2.8)$$

The current can also be expressed by replacing the sum on all the tip and sample states by using the DOS of the tip ( $\rho_t$ ) and of the sample ( $\rho_s$ ), respectively. This yields the simplified expression:

$$I = \frac{2e^2}{\hbar} |M|^2 \rho_t(E_F) \rho_s(E_F) V. \quad (2.9)$$

$M$  and in general all the elements  $M_{\mu\nu}$  hold all the information concerning the tunneling junction as they are linked to the hamiltonian, and are in general not easy to determine. For example, to determine the tunneling matrix elements in the presence of Kondo scattering (§ 1.2), it is necessary to use the Kondo Hamiltonian and account for tunneling electrons as well as for electrons tunneling into the Kondo impurity from the host metal. Given the difficulty encountered in expressing  $M_{\mu\nu}$ , several models have simplified Bardeen's approach.

In a simplified version of Bardeen's model, Tersoff and Hamann [29, 33] demonstrated that the STM can possess a spatial resolution high enough to image a surface corrugation. Using Eqs. (2.8) and (2.7) for a tip with  $s$  orbitals only (Fig. 2.2), they obtained the following

expression for the tunnel current:

$$I = \frac{32\pi^3 e^2 \phi^2 V \rho_t(E_F) \rho_s(\vec{r}_0, E - E_F) R^2}{\hbar \kappa^4} \exp(-\kappa R), \quad (2.10)$$

where  $\phi$  is the average work function of tip and sample,  $\vec{r}_0$  is the position of the center of the tip,  $R$  is the radius of the tip and  $\kappa = \hbar(2m\phi)^{-1/2}$ . Tersoff and Hamann applied their approach to the reconstructed Au(110) surface that was studied experimentally by Binnig *et al.* [27]. They simulated  $\rho_s(\vec{r}_0, E)$  for a tip radius of  $R = 9 \text{ \AA}$  and they found a good agreement between the experimental resolution and their calculations. Although this approach gives a good idea of the spatial resolution that can be attained with a STM, it can be further improved by considering  $p$  or  $d$  orbitals [30–32].

### 2.1.3 WKB theory

We have seen that the expression of the current using Bardeen's theory is not handy for describing a tunnel junction due to the complexity of the tunneling matrix  $M_{\mu\nu}$ . In the following, we will express the current and its derivatives using the Wentzel-Kramers-Brillouin theory (WKB). This theory is a semi-classical approach [29, 33, 34] applied to a tunneling junction as shown in Figs. 2.3(a) and 2.3(b). The tunneling current for a bias  $V$  and a tip-surface distance  $z$  is expressed as :

$$I(z, V) \propto \int_{-\infty}^{\infty} \mathcal{T}(z, E, V) [f(E - eV) - f(E)] \rho_t(E - eV) \rho_s(E) dE \quad (2.11)$$

where  $f$  is the Fermi-Dirac distribution. The transmission coefficient  $\mathcal{T}$  depends on the shape of the tunneling barrier. A good approximation for the tunneling barrier is a trapezoidal shape [109–111] (Fig. 2.3), leading to the following expression:

$$\mathcal{T}(z, E, V) \propto \exp \left[ -kz \sqrt{\phi + \frac{eV}{2} - (E - E_{\parallel})} \right], \quad (2.12)$$

with  $k = 1.025 \text{ \AA}^{-1} \text{ eV}^{-1/2}$ . The energy  $E_{\parallel}$  is the component of the kinetic energy that is parallel to the junction interface and does not play an important role in the tunneling process as electrons mainly tunnel with a momentum perpendicular to the surface. Typically,  $\phi \simeq 4 \text{ eV}$  for metals, so  $\mathcal{T}$  imposes a change by a factor 10 in current per each angström.

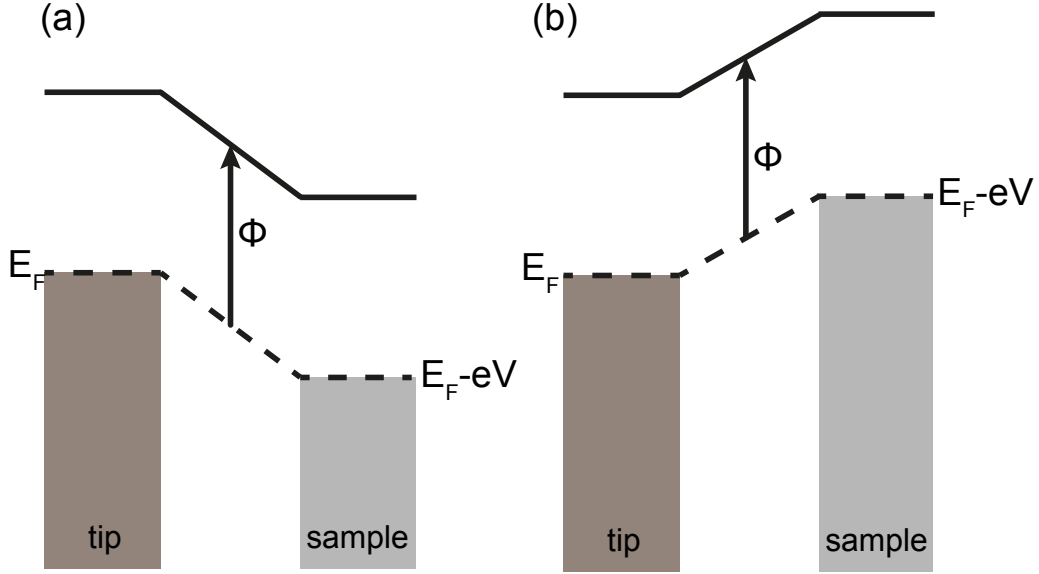


Figure 2.3: **Tunneling barrier for positive and negative sample biases.** Sketch of the tunneling barrier used in the WKB theory. (a) Positive bias, (b) negative bias.

## 2.2 Scanning tunneling spectroscopy

The WKB theory shows that the tunneling current depends on the DOS of one electrode with respect to the other [Figs. 2.3(a) and 2.3(b)], implicitly meaning that the DOS of the sample may be probed by measuring the tunneling current at different biases. This operation is called scanning tunneling spectroscopy (STS) and has to be carried out at a fixed tip-sample distance  $z$ . Equation (2.12) shows that the tip and the sample DOS equally contribute to the tunneling current as  $\rho_s$  and  $\rho_t$  can be interchanged. If the tip DOS is taken to be constant and the Fermi-Dirac distribution is approximated by a step function, a simplified expression of the current can be obtained as:

$$\frac{dI}{dV}(z, V) \propto \mathcal{T}(z, E = eV, V) \rho_s(V) + \int_0^V \rho_s(E) \frac{d\mathcal{T}(z, E, V)}{dV} dE, \quad (2.13)$$

where the Fermi level is used as the reference energy ( $E_F = 0$ ). Using the expression of the transmission coefficient [Eq. (2.12)] yields:

$$\frac{dI}{dV}(z, V) \propto \rho_s(V) \mathcal{T}(z, eV, V) - \frac{\phi}{4z} I(z, V). \quad (2.14)$$

For usual tip-sample distances, the differential conductance spectrum gives information on the sample DOS. At small distances, *i.e.* high tunnel currents, the contribution from the second term increases and can sometimes become stronger than the first term producing a negative differential conductance [112]. However, this situation is rare and Eq. (2.14) usually simplifies to

$$\frac{dI}{dV}(z, V) \propto \rho_s(V) \mathcal{T}(z, V, V). \quad (2.15)$$

This equation shows that the differential conductance carries information about the sample DOS and is therefore a powerful tool for investigating the electronic properties of surfaces around the Fermi energy with atomic-scale resolution.

### 2.2.1 Inelastic tunneling

As shown in § 1.3, it is possible to use tunneling spectroscopy to detect electrically-driven excitations in a single object (atom or molecule). This tunneling spectroscopy, which uses inelastic tunnel electrons, is called inelastic electron tunneling spectroscopy (IETS). The inelastic tunneling occurs when the electrons can transfer part of their energy to excite the single object during the tunneling process. Formally, inelastic tunneling occurs when  $e|V| \geq \delta$  with  $\delta$  being the transition energy between the ground state and the excited state of the object. It opens a new conductance leading to a change in slope in the current-versus-bias curve at a threshold bias  $\pm\delta$  [Fig. 2.4(a)], or to a step at  $\pm\delta$  in the differential conductance [Fig. 2.4(b)], or to a dip at  $eV = -\delta$  and a peak at  $eV = +\delta$  in the  $d^2I/dV^2$  [Fig. 2.4(c)]. Inelastic processes in the tunneling junction are associated to an excitation between two Zeeman levels [3] (§ 1.3), a vibration [35] or a rotation [113] of the object under investigation. They can also be related to a plasmon excitation in the tip-sample cavity [114].

## 2.3 Experimental detection

### 2.3.1 Lock-in signal

To detect properly the derivatives of the tunneling current, it is faster to use the lock-in based detection instead of numerically differentiating the current. Indeed, the latter presents an intrinsic source of noise degrading the quality of the signal. The lock-in detection allows the analogical acquisition of the derivatives and given good setting parameters, allows a better



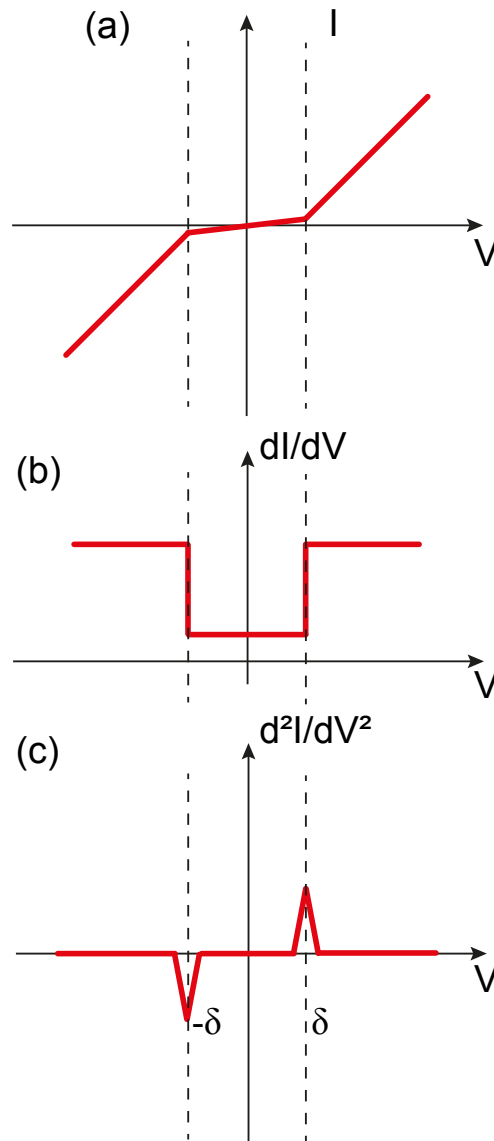


Figure 2.4: **Inelastic tunneling in transport measurements.** The panels sketch how inelastic tunneling can be detected in transport measurements. The detection is possible through: (a) a change in the slope at of the current-versus-bias curve occurring at  $eV = \pm\delta$ , (b) the occurrence of steps at  $eV = \pm\delta$  in the  $dI/dV$ , (c) the occurrence of dip (peak)  $eV = -\delta$  ( $eV = +\delta$ ) in the  $d^2I/dV^2$ .

signal to noise ratio for the same acquisition time than the numerical differentiation. The main idea of the lock-in phase sensitive detector (simply called lock-in hereafter) is to add a sinusoidal modulation wave to the input signal of the STM (the sample bias) and then deduce the derivative of the output signal (the differential conductance) from the harmonics of the modulation wave. The modulation frequency is selected in a frequency range where the noise of the tunnel current is minimal.

Formally, we can write the tunneling current as

$$I = I[V + V_m \cos(\omega t + \theta)], \quad (2.16)$$

and using a small enough amplitude  $V_m$  for the modulation ( $V_m \ll |V|$ ), one can Taylor-expand Eq. (2.16) as

$$I[V + V_m \cos(\omega t + \theta)] = I(V) + a_1 \frac{dI(V)}{dV} V_m \cos(\omega t + \theta) + a_2 \frac{d^2 I(V)}{dV^2} V_m \cos(2\omega t + \theta) + \dots \quad (2.17)$$

To detect the harmonic at  $\omega t$ , Eq. (2.17) is multiplied by the phase-shifted modulation signal  $V' \cos(\omega t + \phi)$  where  $V'$  is the constant amplitude of the modulating signal. The expression of the signal detected by the lock-in corresponds to the first order term of the Taylor expansion:

$$\left[ \frac{dI(V)}{dV} \right]_{\text{lock-in}} = V' \cos(\omega t + \phi) \times \left[ a_1 \frac{dI(V)}{dV} V_m \cos(\omega t + \theta) \right], \quad (2.18)$$

which can be re-expressed as

$$\left[ \frac{dI(V)}{dV} \right]_{\text{lock-in}} = a_1 \frac{V'}{2} \frac{dI(V)}{dV} V_m [\cos(\theta - \phi) + \cos(2\omega t + \theta + \phi)]. \quad (2.19)$$

By using a low-pass filter, the phase sensitive detector (PSD) can extract only the first term which includes the differential conductance. The setting of the bandwidth and the rolloff are important to optimize the signal to noise ratio as it needs to extract the most signal without taking too much of the noise components. Note that experimentally this phase shift is induced by all the circuit and changes with the gain used in the current amplifier, and depends also on the frequency  $\omega$  used. Setting the phase  $\phi$  on the lock-in to match the phase shift of the signal allows for a better signal-to-noise ratio.

In our case, the spectra of interest are located in a bias range  $|V| < 10$  mV as the spin excitation

observed in this thesis are in the range of a few mV. In order to satisfy the conditions of the Taylor expansion, we used a modulation amplitude of a few hundreds  $\mu\text{V}$  —the amplitude is taken as root mean square (rms). The choice of the modulation amplitude is important as it influence both the signal-to-noise ratio and the broadening of the line shape of the tunneling spectrum as we show here below. A balance has to be found for the modulation amplitude as a strong modulation will induce a less noisy detected signal but will induce a broadening of the line shape.

### 2.3.2 Line shape broadening in STS

In this section we will treat the broadening of the line shape in the  $dI/dV$  spectrum produced by temperature and by the lock-in detection technique. To ease the treatment, we will use the WKB formalism (§ 2.1.3).

#### Temperature

The finite width of the Fermi-Dirac distribution causes the  $dI/dV(V)$  spectra to broaden with increasing temperature. Recalling Eq. (2.12) and considering  $\mathcal{T}$  and  $\rho_t$  constant, we have

$$\frac{dI(V)}{dV} \propto \int_{-\infty}^{\infty} \rho_s \frac{df(E - eV)}{dV} dE, \quad (2.20)$$

that can be rewritten as a convolution product

$$\frac{dI(V)}{dV} \propto \rho_s * \chi_T(E - eV), \quad (2.21)$$

where

$$\chi_T(E - eV) = \frac{df}{dV}(E - eV) = \left( \frac{\chi_T(0)}{\cosh[(E - eV)/(2k_B T)]} \right)^2, \quad (2.22)$$

and  $\chi_T(0) = e/(k_B T)$ . This broadening function is plotted in Fig. 2.5 (a) and has a Full Width Half Maximum (FWHM) of  $\delta_T = 3.5 k_B T$ . In other words, the higher the temperature, the stronger the smearing of the spectrum. At our working temperature of 2.4 K we have then  $\delta_T = 700 \mu\text{eV}$ .

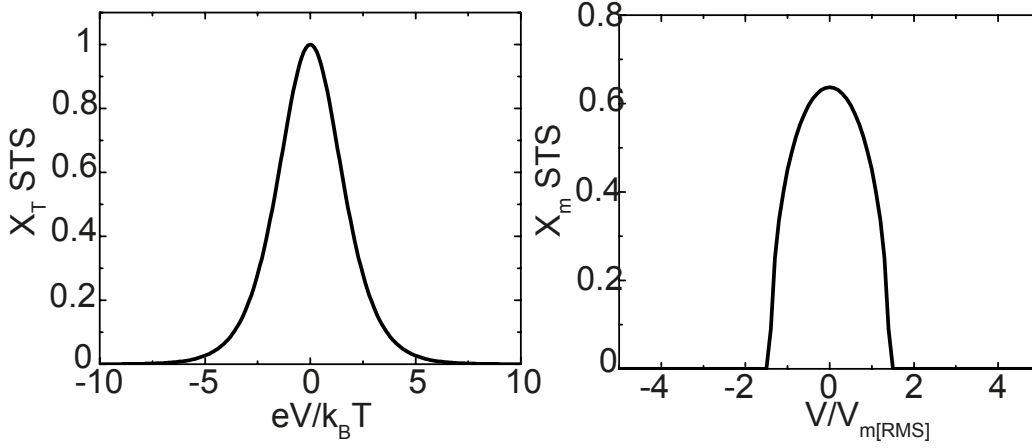


Figure 2.5: **Smearing functions in STS.** (a) Thermal smearing function. (b) Lock-in smearing function.

### Lock-in detection

Another source of broadening is the noise present in the signals entering to and exiting from the STM. As said earlier, a major source of broadening is the lock-in itself since it introduces a periodic modulation in the bias applied to the junction. This may be rationalized by considering the first harmonic obtained through the lock-in by

$$I_{\omega 1} = \frac{1}{\tau} \int_{-\tau/2}^{\tau/2} I[V + V_M \cos(\omega t)] \cos(\omega t) dt \quad (2.23)$$

where  $\tau$  is the measurement interval time. With some mathematical treatments described in [115], the conductance spectrum measured with the lock-in appears as a convolution product:

$$\left[ \frac{dI(V)}{dV} \right]_{\text{lock-in}} = \int_{-\infty}^{\infty} \frac{dI}{dV}(V - V') \chi_M(V') dV', \quad (2.24)$$

where

$$\chi_M(V') = \frac{2\sqrt{V_M^2 - V'^2}}{\pi V_M^2}, \quad (2.25)$$

is the broadening function of the lock-in signal [Fig. 2.5(b)]. The modulation has then a FWHM of  $\delta_M = 2.44 V_M[\text{rms}]$ .

If we take into account both temperature and lock-in smearing, the line shape broadening has

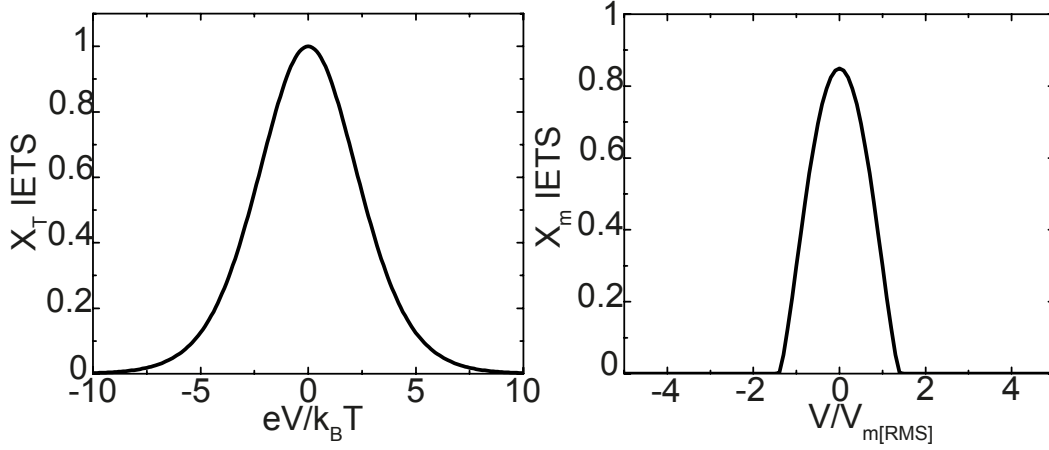


Figure 2.6: **Smearing functions in IETS.** (a) Thermal smearing function. (b) Lock-in smearing function.

the general expression:

$$\left[ \frac{dI(V)}{dV} \right]_{\text{measured}} \propto \rho_s * \chi_T * \chi_M. \quad (2.26)$$

The FWHM of the smearing function  $\chi_T * \chi_M$  depends on both  $\delta_T$  and  $\delta_M$ , and the energy resolution achieved in the tunneling spectra can be approximated as

$$\delta_{eV} \simeq \sqrt{(\delta_T)^2 + (\delta_M)^2}. \quad (2.27)$$

In our setup, *i.e.*  $T = 2.4$  K and a modulation of  $150 \mu\text{V}$ , we have an energy resolution in STS of  $\delta_{eV} = 800 \mu\text{eV}$ . Note that this energy resolution applies to elastic features in the STS such as Kondo resonances. It means that the Kondo temperature (see section 1.2) will be polluted by a broadening of  $800 \mu\text{eV}$ .

### 2.3.3 Line shape broadening in IETS

The line shape of an inelastic tunneling spectrum is also affected by broadening due to both thermal effects and lock-in detection. The smearing of it can also be deduced in a similar manner as above. This was extensively shown by Klein *et al.* [115] and we limit here our presentation to some salient aspects. We consider the expression of the inelastic tunneling current ( $I_i$ ) of

Lambe and Jaklevic [116],

$$I_i = C e(V - V_0) \frac{\exp[e(V - V_0)/k_B T]}{\exp[e(V - V_0)/k_B T] + 1}. \quad (2.28)$$

The constant  $C$  depends on the tunneling parameters and only affects the apparent height of the inelastic step in the differential conductance spectra.  $V_0$  refers to the energy threshold for the inelastic process. Differentiating twice Eq. (2.28), we obtain the expression of the thermal smearing function for the inelastic tunneling spectrum [Fig. 2.6(a)]. This function presents a FWHM of  $\delta_T = 5.4k_B T$ . The lock-in detection smearing function is presented in Fig. 2.6(b), and yields a FWHM of  $\delta_M = 1.73 V_M$  [rms]. Since our measurements are performed at 2.4 K with a modulation of 150  $\mu V$  rms, our energy resolution in IETS is dominated by the thermal broadening and corresponds to 1.1 meV. This value corresponds then to the lower limit of the width of the inelastic step which is different to the energy resolution in STS mentioned earlier. Here it means that we cannot differentiate two steps being below 1.1 meV apart.

## 2.4 Experimental setup

### 2.4.1 Principle of image acquisition

As we showed in § 2.1.3, the WKB theory provides a simplified model showing that the tunnel current has an exponential dependency on the distance between the tip and the sample. This exponential dependency is the key point for the STM imaging process. A common mode for the topography of a surface is to adapt the height of the tip according to the value of the current. This so-called constant-current mode necessitates a feedback loop in the experimental setup [Fig. 2.7]. As the tip is scanned above the sample, the feedback loop modifies the tip-sample distance so to keep the current constant. The changes in distance are recorded and a topographic image may then be obtained by associating each pixel of the image to a tip vertical displacement. Alternatively, the feedback loop can be opened so that changes in the tunnel current are instead recorded. This so-called constant-height image can only be performed on small areas, typically  $1 \times 1 \text{ nm}^2$ , with prior knowledge of the topography. Note that during the STS and IETS measurements, the feedback loop is deactivated.

The tip position is controlled using piezoelectric ceramics. A first group of piezoelectric ceramics is responsible for the so-called coarse-motion and can move the tip either by steps of

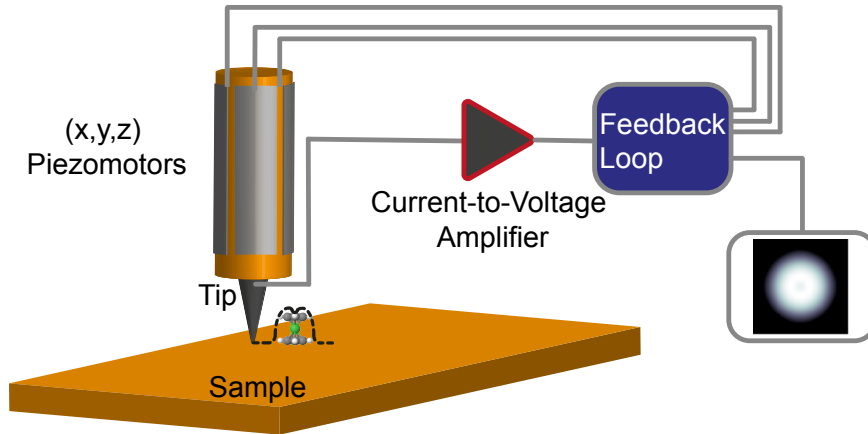


Figure 2.7: **Image acquisition in STM.** The figure shows the basic elements needed for acquiring an image with the STM. Among these we have: a piezoelectric tube, a feedback loop and a current-to-voltage preamplifier.

around 100 nm when a voltage pulse is applied (usually between 150 V and 400 V) of continuously when a periodic signal of similar voltage amplitude is applied. These piezo-elements are therefore used to bring the tip within tunneling distance from the surface. Once in the tunnel regime, a piezoelectric tube (Fig. 2.7) enables to scan a small area of the sample surface, the area having a maximum extension of  $2 \times 2 \mu\text{m}^2$ . The calibration of the motion of the piezoelectric tube can be achieved using a well-known sample crystal. In our case, we used the step height of Cu(100) to calibrate the  $Z$ -motion of the piezoelectric tube. We calibrated the  $X$  and  $Y$  motion via the atomic resolution obtained when scanning with the tip in contact with the surface [117].

## 2.4.2 The microscope used in this thesis

The STM of our team is a modified low-temperature microscope from Omicron operating in ultrahigh vacuum (UHV). The microscope comprises an STM chamber and a preparation chamber that are separated by a gate valve. The UHV is ensured via different pumping stages: i) The primary stage consists in a scroll pump working from atmosphere pressure down to  $10^{-2}$  mbar, ii) The secondary stage comprises a turbo-molecular pump to further lower the pressure and an ion pump —each chamber has its own turbo-molecular pump and ion pump. The base pressure is  $10^{-10}$  mbar in the preparation chamber and  $10^{-11}$  mbar in the STM chamber. Despite these low pressures, our samples and tips can get contaminated with time. According

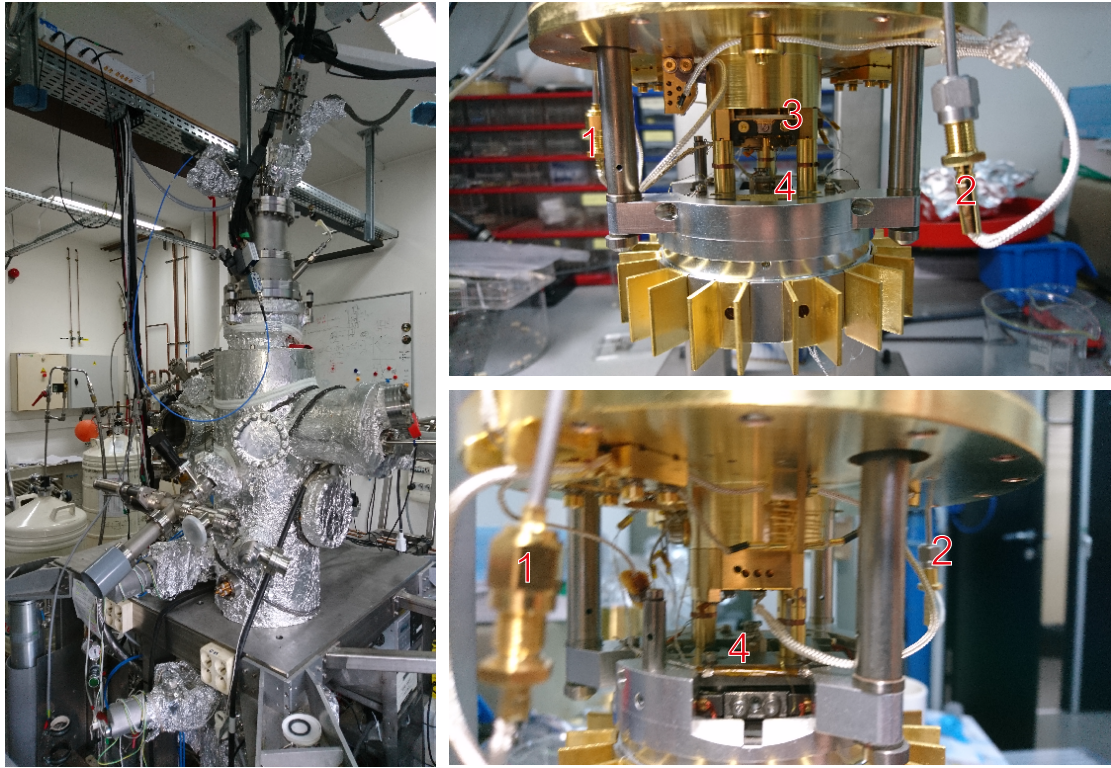


Figure 2.8: **The STM used in this thesis.** (a) Picture of the STM vacuum chamber. Panels (b) and (c) present pictures of the STM. The numbering corresponds to: 1 : SMA connector for the cable carrying the sample bias, 2 : SMA connector for the cable carrying the current, 3 : sample, 4 : tip.

to the Hertz-Knudsen formula [118], at  $10^{-11}$  mbar the amount of impurities increases with a rate of 1 monolayer per  $10^5$  seconds, meaning that we can ideally keep the sample clean for a few weeks. To minimize the impurities, we routinely sublimate titanium into the chambers.

A picture of the STM chamber is presented in Fig. 2.8(a). During my thesis we made a few modifications. We replaced the stainless steel cables of the bias voltage and of the current by coaxial cables with a bandwidth of 1 GHz. The coaxial cables are intended for performing time-resolved STM measurements in the near future. Each semi-rigid coaxial cable runs from the flench to the bottom of the STM. There, an SMA connector ensures a relay with a flexible copper coaxial cable [noted 1 for the bias and 2 for the current in Figs. 2.8(b) and 2.8(c)]. The preparation chamber is connected to a load-lock where we transfer samples and tips from ambient pressure to UHV. The preparation chamber is equipped with an ion gun and a heating



stage for tip and sample cleaning, with two e-beams for growing magnetic layers, and with a home-made molecular evaporator. We use single-metallic crystals as samples, in particular Cu(100) and Cu(111). They are cleaned in the preparation chamber by repeated cycles of argon sputtering (base pressure of  $10^{-6}$  mbar and voltage of 3 kV) and annealing around 500° C. The STM tips are made of a tungsten wire with a purity of 99% that is chemically etched using a NaOH solution. As shown in [32], the curvature radius of the tip obtained with such an etching method is lower than 1  $\mu\text{m}$ . The tips are also cleaned *in vacuo* via argon sputtering.

The measurements shown in this thesis were acquired at a temperature of 2.4 K. To reach this temperature we start with a filled helium cryostat at 4.4 K. We then pump the cryostat by slowly increasing the pumping power until the sample reaches 3 K. We then pump at full power to reach 2.4 K in about an hour. The standing time is at least 12 hours at 2.4 K, while at 4.4 K the standing time is 35 hours for a helium dewar of 3.5 liters.



## CHAPTER 3

# Nickelocene on a copper surface

Nickelocene belongs to the family of metallocenes, which are characterized by their simple structure comprising a metallic atom (noted  $M$ ) coupled to two cyclopentadienyl ligands ( $C_5H_5$ , noted Cp hereafter). In their most common version, metallocenes are composed by one of the six elements in the middle of the  $3d$  row (V, Cr, Mn, Fe, Co, Ni). Figure 3.1 presents three examples of metallocenes,  $FeCp_2$  (ferrocene),  $CoCp_2$  (cobaltocene) and  $NiCp_2$  (nickelocene). The previous thesis in our group by N. Bachellier treated the adsorption of  $FeCp_2$  [40] and its doping by a magnetic atom [119]. This thesis is devoted to characterizing and exploiting the magnetic properties of a nickelocene molecule placed in a metallic environment.

To date there is a lack of knowledge concerning its interaction with a metal. For instance, nickelocene (Nc hereafter), is well representative of magnetic metallocenes [120]. The  $d^8$  configuration of nickel results in an electronic structure of  $(e_2)^4(a_1)^2(e_1)^2$  for nickelocene [Fig. 3.1], which provides the molecule with a spin  $S = 1$  as demonstrated by several studies conducted in the gas phase [121] or on powder samples [120–125]. As a rule of thumb, half of the spin  $S = 1$  is carried by the Ni atom, while the two Cp rings carry the other half.

Due to its open valence shell, nickelocene is chemically reactive. Upon adsorption onto a metal, such a reactivity causes a charge transfer towards the surface [126, 127], which could potentially quench the magnetic moment of the molecule, or even affect the chemical integrity of the molecule [128, 129]. The adsorption of nickelocene on a metal has motivated some studies [128–132], none being carried out at the single-molecule level. Contradictory results have been obtained by macroscopic averaging techniques regarding the assembly of nickelocene molecules on metal surfaces, in particular on Ag(100). In one study, nickelocene was reported

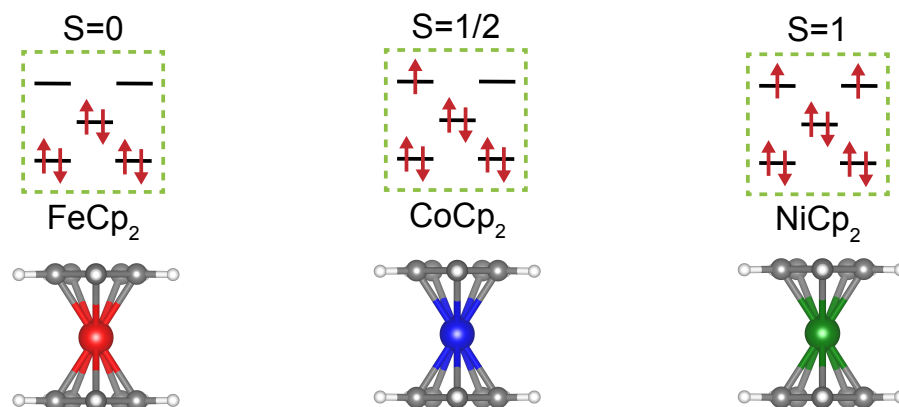


Figure 3.1: **Structure and configuration of metallocenes.** The panels show the structure of ferrocene, cobaltocene, and nickelocene. The atoms are: C (grey), H (white), Fe (red), Co (blue), Ni (green). The electronic configuration of the molecules is presented above their chemical structure.

to bond with the molecular axis tilted with respect to the surface normal [128]. In another study [131], two bonding configurations were reported, one with the molecular axis along the surface normal and another appearing at higher coverages where the axis is tilted. The adsorption of nickelocene on a metal has remained elusive up to now, as well as its electronic and magnetic properties when the molecule is in contact with a metallic electrode.

The purpose of this chapter is to show that the structural, electronic and magnetic properties of nickelocene are preserved on a copper surface. We first describe the adsorption of nickelocene on copper (§ 3.1) by restraining the presentation to Cu(100) as the results we obtained on Cu(111) are similar. We then focus on the magnetic properties (§ 3.2), in particular their characterization by XMCD and DFT calculations. The DFT calculations were carried out within a collaboration with the groups of M.-L. Bocquet (ENS Paris) and N. Lorente (CFM, Donostia-San Sebastián). We then characterize the magnetic properties of a single nickelocene through spin excitation spectroscopy (§ 3.3). We will analyze the spin excitation spectrum in the light of analytical models developed by N. Lorente [38] and M. Ternes [41]. We end the chapter with some conclusive remarks (§ 3.4). The results presented in this chapter were published in Phys. Rev. B **93**, 195403 (2016) [37] and Nano Lett. **17**, 1877 (2017) [38].

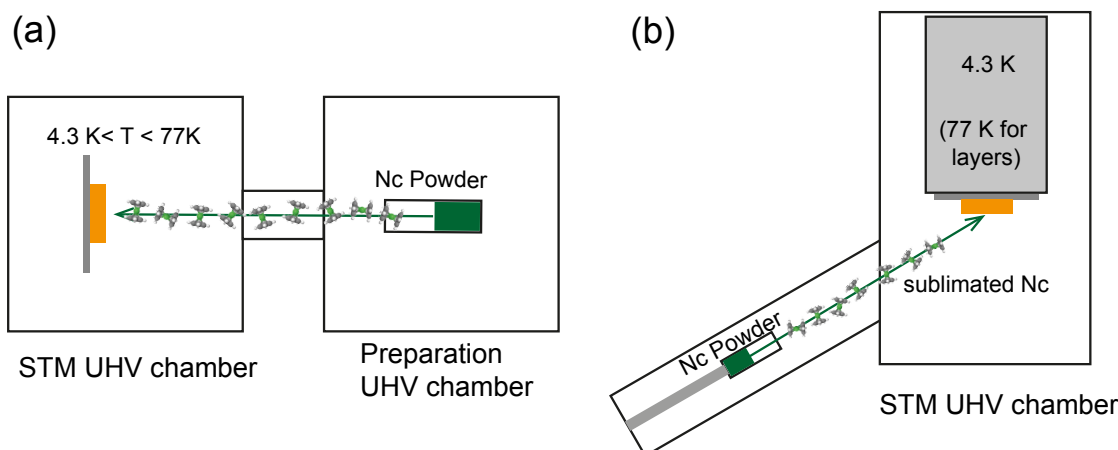


Figure 3.2: **Deposition setup.** (a) Sketch of the usual configuration that we use for depositing nickelocene. The sample is exposed to the molecular flux outside of the STM. (b) Sketch of the setup for depositing nickelocene on a surface inside the STM. The exposure of a surface at 4.4 K to a molecular flux results in isolated Nc molecules, while at 77 K self-assembled layers are observed.

## 3.1 Adsorption of nickelocene on copper

### 3.1.1 Sample preparation

The Nc molecules are sublimated from a crucible placed in UHV onto a Cu(100) surface, previously cleaned by several sputter/anneal cycles. The nickelocene powder was acquired from Sigma-Aldrich. The melting point of the powder, which is  $172^\circ \text{C}$  in ambient pressure, lowers to room temperature for pressures  $< 10^{-7} \text{ mbar}$  [133] resulting in a stable and reproducible molecular flux in UHV. The flux can be controlled by covering the crucible with a lid that disposes of a hole with a diameter of 1 mm. As we present below, depending on the exposure time of the surface to the flux, isolated molecules or large self-assembled of Nc may be obtained.

To preserve the Nc chemical integrity, the molecule must be deposited on a cold metal surface, typically  $< 200 \text{ K}$ . In our setup, we have two possible procedures for depositing nickelocene. The first and more frequently used is the one presented in Fig. 3.2(a): i) We take the sample out of the chamber and keep it on the wobble stick up to four minutes. From previous work on ferrocene [40], we estimate that the sample temperature remains below 150 K. An approximate control of the temperature is possible by adjusting this waiting time. ii) We

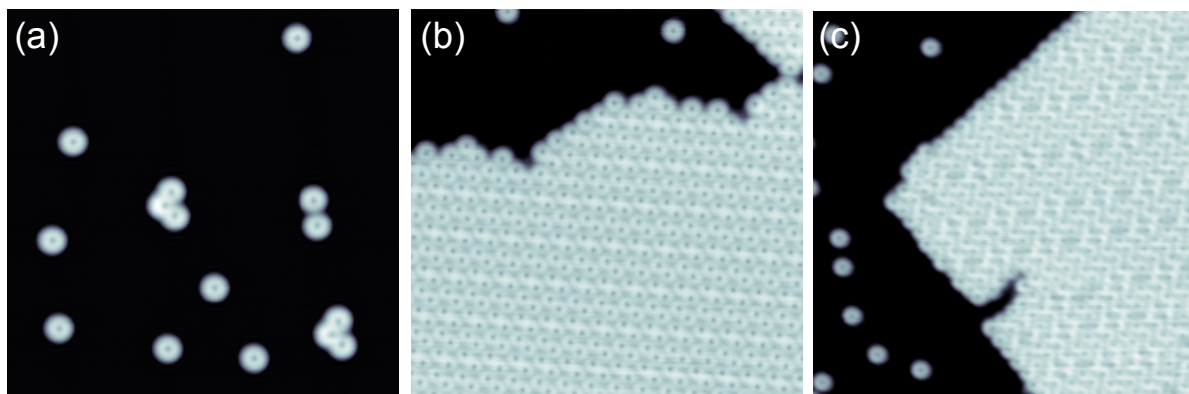


Figure 3.3: **Adsorption geometries of nickelocene.** (a) Single Nc molecules on Cu(100) ( $I = 20$  pA,  $V = 10$  mV,  $14.5 \times 14.5$  nm<sup>2</sup>). Panels (b) and (c) present a Nc layer on Cu(100) in the so-called paired ( $I = 20$  pA,  $V = 20$  mV,  $19 \times 19$  nm<sup>2</sup>) and compact ( $I = 20$  pA,  $V = 20$  mV,  $23 \times 23$  nm<sup>2</sup>) configurations, respectively.

expose the sample to the molecular flux for times ranging from a few seconds to a couple of minutes with a distance between the sample and the crucible of roughly 25 cm. The exposure time, as well as the angle of the sample relative to the flux, allows for approximate control of the quantity of molecule deposited. We usually have a flux of  $0.025$  monolayer  $\text{min}^{-1}$  for the sample normal collinear to the flux. The other setup, consists in sublimating nickelocene onto a sample placed in the STM [Fig. 3.2(b)]. In this configuration, the crucible is placed on a transfer rod, the molecular flux being then adjusted by varying the crucible-sample distance. The molecules are deposited through an opening of the cryostat shield on a surface held either at 4.4 K or 77 K. Although the second procedure is more controlled than the first one, it comes at the expense of exposing the STM to the molecular flux. In the long run, this can be source of contamination and cause problems with the piezo motion. During this thesis, we have therefore privileged the first procedure [Fig. 3.2(a)]. The second procedure was used for measurements at the synchrotron (§ 3.2.3).

The deposition of nickelocene onto the Cu(100) surface gives rise to large surface areas covered by isolated molecules [Fig. 3.3(a)], but also results in well-ordered molecular assemblies [Figs. 3.3(b) and 3.3(c)]. In the next sections, we will analyze first the adsorption of the isolated molecule (§ 3.1.2) and then the self-assembled layers (§ 3.1.3).

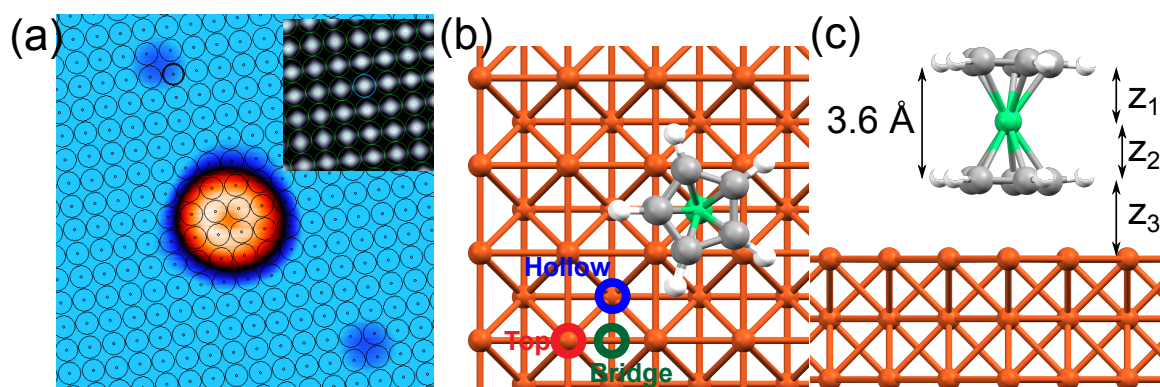


Figure 3.4: **Single-molecule adsorption.** (a) The image shows a single Nc and two Fe adatoms ( $I = 50$  pA,  $V = 20$  mV,  $40 \times 40 \text{ Å}^2$ ). Inset: Atomically-resolved image of Cu(100) using a tip-assisted manipulation ( $I = 80$  nA,  $V = 10$  mV,  $16.5 \times 16.5 \text{ Å}^2$ ). (b) Top view of the DFT-simulated adsorption. Top, hollow and bridge positions are indicated by red, blue and green circles, respectively. (c) Side view of the simulated adsorption.  $z_1$  ( $z_2$ ) corresponds to the distance between Ni and the top (bottom) Cp.  $z_3$  is the distance between the bottom Cp ring and the surface

### 3.1.2 Isolated nickelocene

A typical image of isolated Nc molecules on Cu(100) is presented in Fig. 3.3(a). The molecule is imaged as a ring, suggesting that one Cp ring is exposed to vacuum while the other one is bonded to the surface. The principal molecular axis, which goes from one Cp center to the other, is normal relative to the surface, in other words the molecule adsorbs “vertically” relative to the surface. Nickelocene has an apparent height of  $(3.5 \pm 0.1) \text{ Å}$  relative to Cu(100) (see line profile in Fig. 3.5), but can lower to  $(2.9 \pm 0.1) \text{ Å}$  with different tunneling parameters. The detail of this variation will be presented further in this chapter as it is related to the fingerprint of the magnetic properties of the molecule in the spin excitation spectra (§ 3.3).

In order to determine the adsorption site of nickelocene, it is necessary to image the surface atoms of the (100) lattice. This is a task that is not straightforward under usual tunneling conditions due to the weak electronic corrugation of the (100) surface. To circumvent this problem, we co-deposited Fe atoms in order to mark the position of the hollow sites of Cu(100). The evaporation was carried out through an opening in the liquid-helium shield of the cryostat by heating a degassed Fe wire ( $> 99.99\%$  purity) wound around a W wire. The manipulation of a single iron atom with the STM tip then allows for routinely imaging the atoms of the

	PBE	optPBE	DFT-D2
hollow	−0.30	−0.93	−1.33
bridge	−0.27	−0.90	−1.23
top	−0.22	−0.84	−1.17

Table 3.1: **Computed adsorption energies.** Adsorption energy (eV) for the three Cu(100) sites calculated with the PBE, Opt-PBE and DFT-D2 functionals. The adsorption energy is defined as  $E_{\text{ads}} = (E_{\text{full system}} - n \times E_{\text{molecule}} - E_{\text{surface}})/n$  where  $n$  is the number of nickelocene molecules per unit cell.

	Nc/Cu(100)	Fc/Cu(100)	Nc (gas phase)
$z_1$	1.77	1.64	1.79
$z_2$	1.78	1.62	1.81
$z_3$	2.35	3.15	

Table 3.2: **Computed adsorption distances.** Computed distances  $z_1$ ,  $z_2$  and  $z_3$  (Å) [see Fig. 3.4(b)] for Nc and ferrocene (Fc) on Cu(100), and for Nc in the gas phase.

copper surface [39]. Typical tunneling parameters are 5 mV for the sample bias and 10 nA or higher for the tunneling current. An image is then acquired by scanning a surface area next to the molecule with an Fe atom (adatom) trapped under the tip [inset of Fig. 3.4(a)]. A grid representing the Cu(100) surface is then extracted from this “manipulated-atom image” and subsequently positioned on Fig. 3.4(a) so that the Fe adatoms in the image are located in a hollow position. It can then be concluded that the Cp ring bond to Cu(100) is centered onto a hollow position of the surface.

To further elucidate how nickelocene adsorbs on Cu(100), we performed DFT calculations within the Perdew-Burke-Ernzerhof (PBE), DFT-D2 and optPBE density functionals approaches [134]. We consider only the eclipsed geometry of nickelocene ( $D_{5h}$  symmetry) as, for the free molecule, it is 23 meV lower in energy compared to the staggered geometry ( $D_{5d}$  symmetry), *i.e.* two Cp rings rotated by  $36^\circ$  with respect to each other. We compared the adsorption energy of a nickelocene relaxed in three high-symmetric sites by centering the Cp ring in a top, bridge and hollow site of Cu(100) [Fig. 3.4(b)]. Our calculations indicate that when nickelocene has its principal axis parallel to the surface, its energy is higher by roughly 400 meV compared to the vertical configuration. This is in agreement with the experimental observations on isolated molecules. For the vertical adsorption, we find that the hollow position is always lower in energy whatever the functional used (Tab. 3.1). The adsorption energy linked to this configuration is



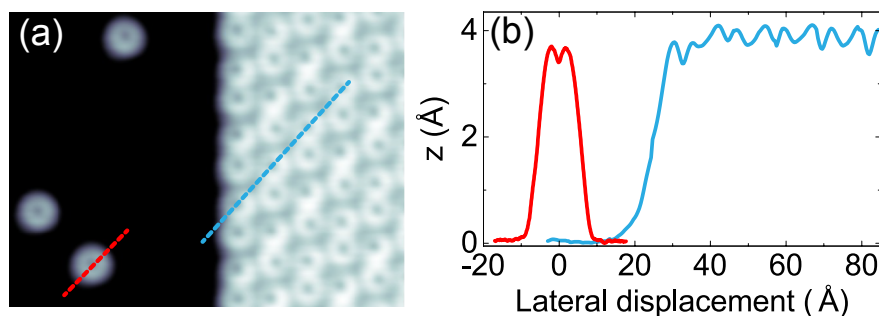


Figure 3.5: **Apparent height of single molecules and molecular layers.** (a) The image shows the edge of a paired layer and isolated Nc molecules ( $I = 50$  pA,  $V = 20$  mV,  $75 \times 90$  Å<sup>2</sup>). (b) Line profiles acquired along the dashed lines indicated in panel (a). The isolated Nc is in red, the Nc in the layer is in blue.

−0.93 eV within the OptPBE functional and −1.33 eV with DFT-D2 functional. The Bader charge analysis [135, 136] shows a minor 0.1e charge transfer from the molecule to the surface. These values correspond to a moderate chemisorption.

With the adsorption geometry simulated, it is of interest to compare the computed bonding distance for Nc and for the ferrocene molecule on Cu(100). This distance is presented as  $z_3$  in Fig. 3.4(b) and Tab. 3.2. Ferrocene has a closed-shell valence configuration of  $(e_2)^4 (a_1)^2$ . This valence configuration reduces the ability to interact with the surface, then favoring a ferrocene adsorption governed by Van der Waals interactions [40]. Consistent with this viewpoint, we find a higher  $z_3$  for ferrocene compared to Nc, which is instead weakly chemisorbed. The structure of Nc is preserved upon the adsorption on Cu(100), but we note that the intramolecular bonding distances [ $z_1$  and  $z_2$  in Fig. 3.4(b)] decrease by 2% with respect to the gas phase.

### 3.1.3 Self-assembled layers

Other adsorption geometries can be found in self-assembled Nc layers. As shown in Figs. 3.3(b) and 3.3(c), Nc self-assembles following two distinct arrangements that are equally represented on the surface. These can be distinguished by the fact that one presents a pairing of two molecules [see Fig. 3.6(a)], while the second one shows a seemingly compact structure with a zigzag pattern [see Fig. 3.8(a)]. We will designate the first assembly as “paired”, and the second by “compact”. These two self-assembled layers have similar geometries to those observed for the ferrocene molecule [40]. The apparent height of the molecules in both layer geometries

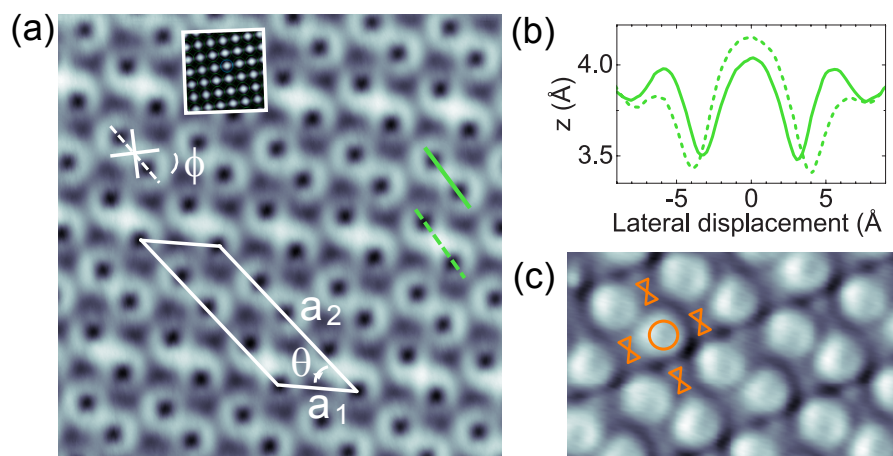


Figure 3.6: **Paired layer.** (a) Paired layer ( $I = 20$  pA,  $V = 20$  mV,  $70 \times 70 \text{ Å}^2$ ) with lattice vectors  $\vec{a}_1$ ,  $\vec{a}_2$  making an angle  $\theta$ . The orientation of the layer relative to the [011] and [01-1] directions of Cu(100) is indicated by the angle  $\phi$ . The inset shows an atomically-resolved image of Cu(100). (b) Line profiles of two pairs indicated by the solid and dashed green lines in panel (a). (c) Low-bias image ( $I = 10$  pA,  $V = 1$  mV,  $28 \times 46 \text{ Å}^2$ ) revealing the presence of horizontal molecules flanking vertical molecules. Horizontal Nc are depicted as hourglasses, vertical Nc as circles.

is  $(4.0 \pm 0.2) \text{ Å}$ , which is  $0.5 \text{ Å}$  higher than the isolated Nc, as it is shown for the paired layer in Figs. 3.5(a) and 3.5(b). As we will see later, these differences result from the presence in the layer of Nc molecules with the molecular axis parallel to the surface, which we define as “horizontal” nickelocenes. Similar molecular assemblies are observed on Cu(111) (see lattice parameters in Tab 3.3) and are therefore independent of the surface symmetry, hinting towards a weak coupling of the layer to the copper surface.

**Paired layer.** Figure 3.6(a) presents a close-up view of the paired layer. There are two types of dimer-like pairs: one with Nc-Nc spacing of  $(7.9 \pm 0.3) \text{ Å}$  [solid line in Fig. 3.6(a)] and one with a spacing of  $(6.5 \pm 0.3) \text{ Å}$  [dashed line in Fig. 3.6(a)]. The spacing among the two dimer-like pairs is  $(9.0 \pm 0.3) \text{ Å}$ . The corresponding line profiles are presented in Fig. 3.6(b), where it is seen that the corrugation is at most  $0.6 \text{ Å}$ . Some differences are evident among the two types of pairs. In the pairs with smallest Nc-Nc spacing, the ring-like protrusion of the Cp rings has nearly the same corrugation. The molecules are vertical and, therefore, in a configuration similar to that of isolated molecules. On the contrary, for the larger Nc-Nc spacing, the corrugation

<b>Paired</b>	<b><math>a_1</math> (Å)</b>	<b><math>a_2</math> (Å)</b>	<b><math>\theta</math> (°)</b>
Nc/Cu(100)	$12.6 \pm 0.3$	$32.3 \pm 0.8$	$41 \pm 3$
Nc/Cu(111)	$12.9 \pm 0.4$	$31.9 \pm 0.4$	$42 \pm 3$

<b>Compact</b>	<b><math>a_1</math> (Å)</b>	<b><math>a_2</math> (Å)</b>	<b><math>\theta</math> (°)</b>
Nc/Cu(100)	$8.8 \pm 0.4$	$15.1 \pm 0.5$	$90 \pm 2$
Nc/Cu(111)	$8.5 \pm 0.4$	$15.7 \pm 0.4$	$90 \pm 3$
Fc/Cu(111)	$8.9 \pm 0.3$	$15.5 \pm 0.3$	$90 \pm 3$

Table 3.3: **Lattice parameters of the nickelocene layers.** Unit cell parameters ( $a_1$ ,  $a_2$ ,  $\theta$ ) for the paired and compact layers on Cu(100) and on Cu(111). We have included the lattice parameters for the compact layer of ferrocene (Fc) on Cu(111) [40].

increases by  $0.15 \text{ Å}$  in the center of the pair and, concomitantly, decreases by the same amount at the edges of the pair, indicating that the two molecules are tilted with opposite angles. As the two type of pairs are arranged in alternating rows, the unit cell is a parallelogram with lattice parameters  $a_1$ ,  $a_2$  and angle  $\theta$  (Tab. 3.3) as shown by the solid white line in Fig. 3.6(a). Four possible orientations relative to the copper surface are evidenced for both configurations with angles  $\phi = (53 \pm 3)^\circ$ ,  $-\phi$ ,  $(90^\circ + \phi)$  and  $(90^\circ - \phi)$  [see  $\phi$  in Fig. 3.6(a)].

As anticipated above, the nickelocene layer also bears “horizontal” molecules that have their molecular axis parallel to the surface. Contrary to the ferrocene layer [40], these molecules are not visible in usual tunneling conditions. As we show in § 3.3.3, this is a consequence of the strong contribution from inelastic tunneling electrons, which increases the apparent height of vertical nickelocene molecules. To completely capture the molecular arrangement, it is then essential to cancel this contribution by acquiring images at biases  $< |2| \text{ mV}$ . This is shown in Fig. 3.6(c) where the circular-like molecules correspond to vertical Nc, while the rod-like molecules correspond to horizontal molecules. The lattice of this layer includes then four vertical and four horizontal molecules per unit cell and the packing density is  $0.030 \text{ molecules/Å}^2$ , which is remarkably close to the packing density of  $0.029 \text{ molecules/Å}^2$  of ferrocene on Cu(111) [40]. Given the similarity with ferrocene, we attribute this molecular arrangement to a intermolecular van der Waals interaction that favors a T-shaped stacking geometry. To complete the study, we performed DFT-D2 calculations as shown in Fig. 3.7(a) where we present the top view of the optimized paired layer. The simulation of a STM image in Fig. 3.7(b) nicely reproduce the molecular pattern seen experimentally. From the simulated structure, we find that the two type of Nc-Nc pairs have tilt angles of roughly  $3^\circ$  [red-circled pair in Fig. 3.7(c)] and of  $8^\circ$

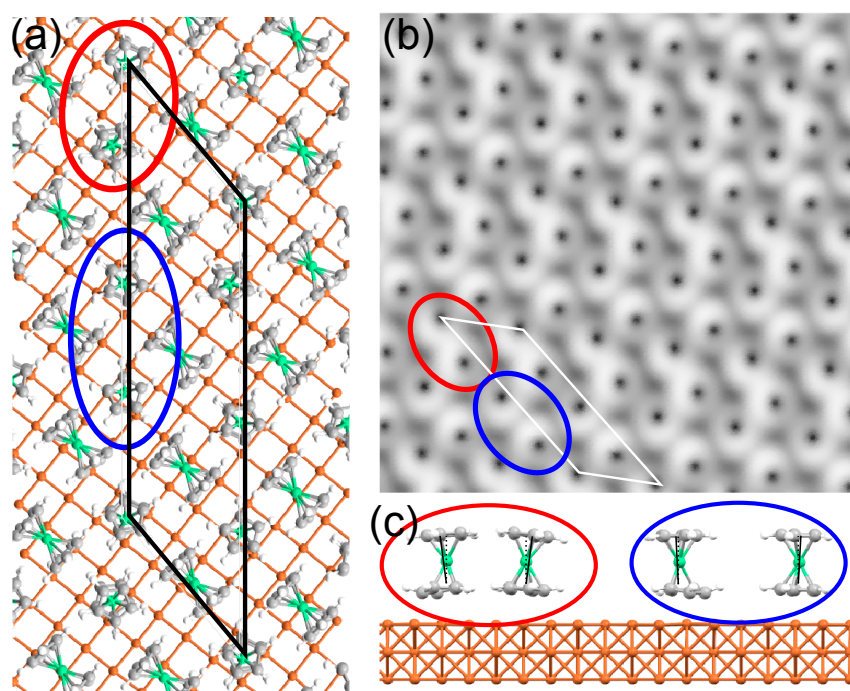


Figure 3.7: **Computed paired layer.** (a) Top view of the DFT-computed layer. Only one layer of copper is presented. (b) Simulated STM image of the paired layer. (c) Side view of the paired layer showing the tilt of vertical molecules. Horizontal molecules are hidden for clarity. The two types of Nc-Nc pairs are highlighted in blue and red, respectively.

[blue-circled pair in Fig. 3.7(c)] respectively.

**Compact layer.** The second nickelocene assembly encountered is the compact layer, which is presented in Fig. 3.8(a). It has a rectangular unit cell with a maximum corrugation of  $0.5 \text{ \AA}$  [solid line in Fig. 3.8(b)]. The unit cell is close to the one of the ferrocene compact layer on Cu(111) (Tab. 3.3) [40]. The layer includes two vertical and two horizontal molecules per unit cell as revealed by low-bias images [Fig. 3.8(c)], resulting in a packing density of  $0.030 \text{ molecules/\AA}^2$  as for the paired layer. The compact assembly of nickelocene, unlike the ferrocene one, presents defects that are imaged as dim spots in the layer. One defect is highlighted by a dashed circle in Fig. 3.8(a). Given the  $0.2 \text{ \AA}$  corrugation of a defect [dashed line in Fig. 3.8(b)], we can exclude that it corresponds to a missing horizontal molecule, as artificially-created vacancies with the STM tip results at least in corrugations higher than  $1.5 \text{ \AA}$ . The exact nature of these defects is still unclear and will need further work to be determined. As for the paired layer, we have performed extensive DFT+D2 calculations and simulated the corresponding STM images (not

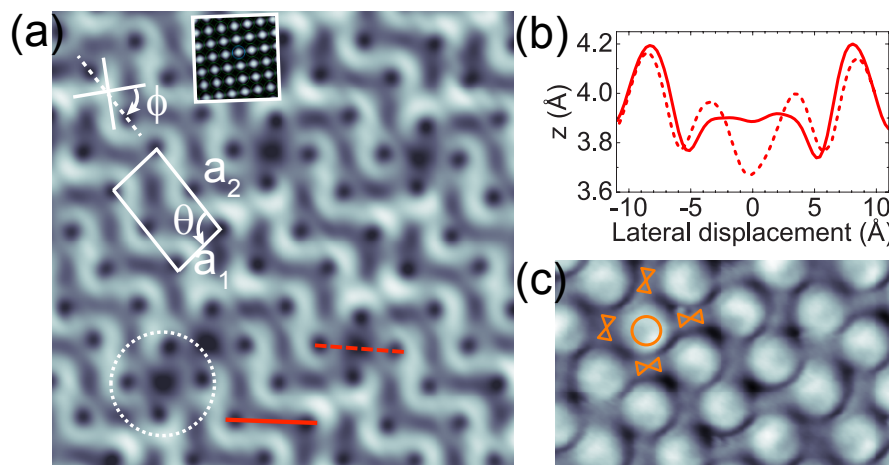


Figure 3.8: **Compact layer.** (a) Compact layer ( $I = 20$  pA,  $V = 20$  mV,  $70 \times 70 \text{ \AA}^2$ ) with lattice vectors  $\vec{a}_1$ ,  $\vec{a}_2$  and  $\theta$ . The orientation of the layer relative to the [011] and [01-1] directions of Cu(100) is indicated by the angle  $\phi$ . The inset shows an atomically-resolved image of Cu(100). Dashed circle: defect (b) Line profiles along the solid and dashed red lines in panel (a). (c) Low-bias image of the compact layer ( $I = 10$  pA,  $V = 1$  mV,  $28 \times 46 \text{ \AA}^2$ ) revealing the presence of horizontal molecules flanking vertical molecules. Horizontal Nc is depicted as hourglasses, vertical Nc as a circle.

shown). While the carbon-surface distance for Nc is shorter than for ferrocene, the compact structure is strictly analogous to the one we previously proposed for ferrocene on Cu(111) [40], confirming the similarities between the molecular layers of the two metallocenes.

We conclude this section by focusing on the adsorption energy of the paired and compact layers. The adsorption energy is  $-1.52$  eV for both layers, pointing to a weak chemisorption as previously found for the isolated molecules. Without the horizontal molecules, however, only 15% of the adsorption energy comes from the nearest neighbors, increasing instead to 50% when the horizontal molecules are present. This shows that the surface-molecule interaction is weakened in the layer compared to an isolated nickelocene, but compensated by the interaction with the adjacent nickelocene molecules. Moreover, the presence of horizontal molecules is necessary to closely reproduce the structural features extracted from the experimental images. We have already mentioned that horizontal molecules introduce a geometrical constraint causing the vertical molecules to tilt in the paired layer [see Fig. 3.7(c)]. They also push up the vertical Nc stabilizing them at a position  $0.1 \text{ \AA}$  higher than the isolated Nc position [Fig. 3.5].

## 3.2 Magnetism of adsorbed nickelocene

### 3.2.1 Magnetism of free nickelocene

The miniaturization of magnetic devices calls for the development of low-dimensional spintronic materials. Metallocenes are extremely appealing for testing new spintronic concepts at the nanoscale. For example, chains of metallocene molecules —eventually encapsulated into carbon nanotubes [137,138], are predicted to be half-metals and could serve as efficient filters for spin-polarized charge carriers [139–143]. We will show in this thesis that even individual nickelocene molecules are also appealing for this area of research. Before focusing on how the presence of a metal affects the magnetism of nickelocene, we will first introduce the magnetic properties of gas-phase or free nickelocene.

As mentioned previously, nickelocene is a spin  $S = 1$  system in the gas phase. Susceptibility measurements on a Nc powder show that the molecule also possesses an uniaxial magnetic anisotropy (noted  $D$  hereafter) with  $D = 3.2$  meV [121]. Slightly higher values are found with susceptibility measurements on a Nc crystal ( $D = 3.6$  meV) [123], or with neutron scattering measurements on Nc cristallites ( $D = 4$  meV) [122]. The existence of an uniaxial magnetic anisotropy implies that the spin Hamiltonian of the molecule reads

$$\hat{H} = D\hat{S}_z^2. \quad (3.1)$$

The molecule has a magnetic ground state  $|S = 1, M = 0\rangle$  [Fig. 3.9(a)], with  $M$  as the magnetic quantum number projected onto the axis perpendicular to the carbon cycles. It also possesses two degenerate excited states  $|S = 1, M = \pm 1\rangle$ . The electronic configuration of the magnetic ground state is presented in Fig. 3.9(b). The crystal field with a  $D_{5h}$  symmetry energetically favors the triplet  $S = 1$  state compared to the  $S = 0$  singlet state, while the zero-field splitting, which translates in this into a positive magneto-cristalline anisotropy  $D$ , leads to  $|S = 1, M = 0\rangle$  as the magnetic ground state. In the following, we will prove that upon adsorption on a Cu(100) surface, nickelocene preserves these magnetic properties. We will exclusively focus on an isolated molecule. As we will show, at our working temperature (2.5 K) the magnetism of nickelocene within the layers is that of isolated nickelocene on the surface.

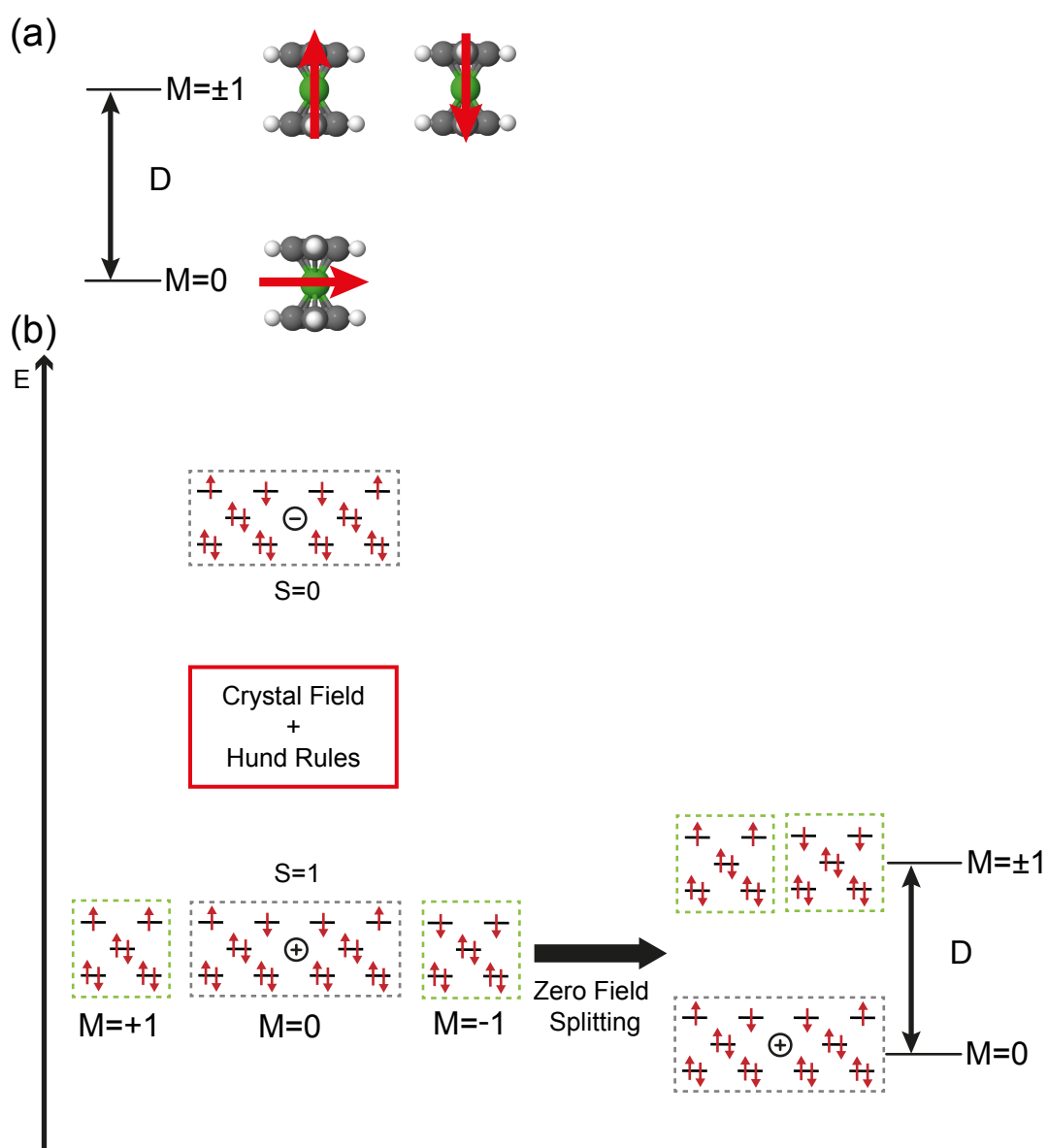


Figure 3.9: **Magnetic configuration of free nickelocene.** (a) Sketch of the magnetic moment of nickelocene accounting for uniaxial magnetic anisotropy. (b) Energy diagram of nickelocene.

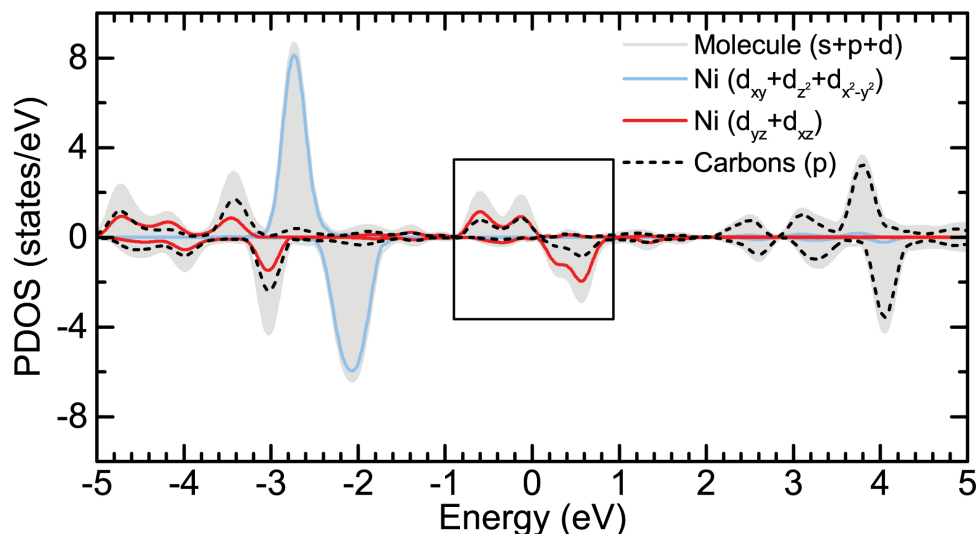


Figure 3.10: **DFT-computed spin-polarized PDOS of single nickelocene on Cu(100).** Spin-polarized PDOS of nickelocene onto different molecular and atomic orbitals (up arrow: majority spins; down arrow: minority spins). The light-grey area corresponds to the entire molecule projected on the  $s$ ,  $p$  and  $d$  orbitals. The Ni  $d$  orbital is grouped as  $d_{xz} + d_{yz}$  (solid red line) and as  $d_{xy} + d_{z^2} + d_{x^2-y^2}$  (solid blue line). The dashed black line corresponds to the contribution of all carbons  $p$  orbitals. The box between  $-1$  and  $1$  eV shows the spin-polarized LUMO.

### 3.2.2 Spin-polarized DFT calculations

In § 3.1.2 we carefully characterized the adsorption of isolated nickelocene on Cu(100). We use here the previously computed adsorption (hollow adsorption site, vertical geometry and eclipsed configuration) to focus on the electronic structure of nickelocene and determine its effective spin on the surface. The DFT-computed projected density of states (PDOS) is presented in Fig. 3.10. We have plotted the  $p$ -orbital PDOS of the carbon atoms (black dashed line) and the  $d$ -orbital PDOS of Ni. For the latter, we plot the sum of the  $d_{xy}$ ,  $d_{z^2}$  and  $d_{x^2-y^2}$  orbitals PDOS (blue line), and the sum of the  $d_{xz}$  and  $d_{yz}$  orbitals PDOS (red line). The sum of all  $s$ ,  $p$  and  $d$  orbitals PDOS is represented by the light-grey area. The lowest unoccupied molecular orbital of Nc [LUMO, see box in Fig. 3.10] can be qualitatively represented by the mixing of the  $p$ -orbitals of C with the  $d_{xz}$  and  $d_{yz}$  orbitals of Ni. It is spin polarized, giving a magnetic character to the molecule. The rest of the  $3d$  orbitals are filled, hence non-magnetic. The total magnetic moment of Nc amounts to  $1.96 \mu_B$ , which almost corresponds to an effective spin of



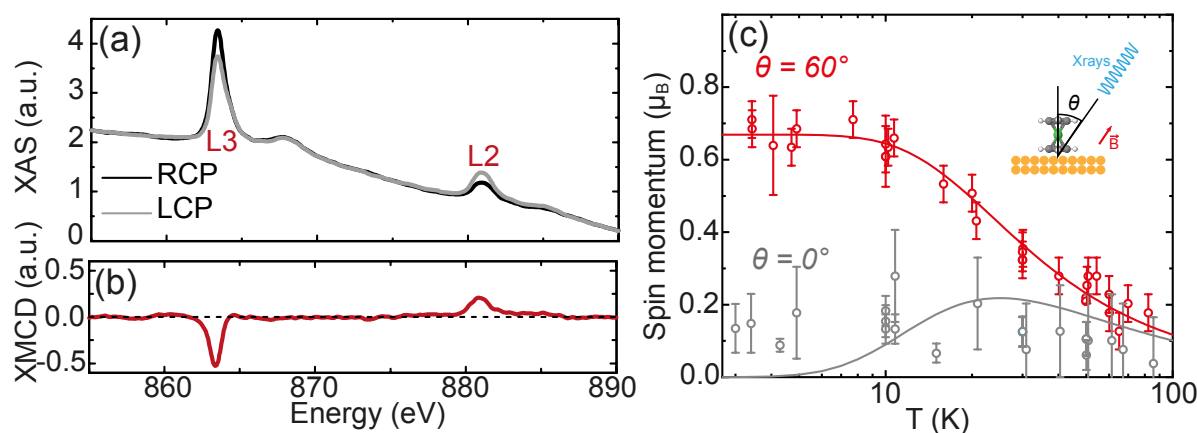


Figure 3.11: **XMCD measurements of nickelocene on Cu(100).** (a) XAS for the L<sub>2,3</sub> edges of Ni ( $B = 6.5$  T,  $T = 4.3$  K, black: right-circular polarization, gray: left-circular polarization). (b) XMCD signature related to the XAS. (c) Evolution of the projection of the spin momentum as a function of temperature for  $\theta = 0^\circ$  and  $\theta = 60^\circ$ . Inset: Schematic view of the XMCD geometry.

$S = 1$ . The Ni atom contributes with  $1.18 \mu_B$  to the magnetic moment, the rest being shared by the two Cp rings. Remarkably, the DFT calculations predict that the magnetism of Nc on Cu(100) is pretty much the same as in the gas phase. To experimentally validate such a finding, we carried out XMCD measurements on a collection of molecules (§ 3.2.3) and spin excitation spectroscopy on a single molecule (§ 3.3).

### 3.2.3 XMCD measurements

The XMCD measurements were performed at the synchrotron Soleil [144]. Care was taken to deposit onto the surface only isolated molecules (§ 3.1.1). To do so, we limited the exposure time to the molecular flux and deposited nickelocene on a 4.5 K-cooled Cu(100) surface in order to restrain the formation of self-assembled layers. The XMCD measurements were carried out at the L<sub>2,3</sub> edges of Ni in a magnetic field of 6.5 T. These measurements allow to characterize the magnetism of a specific atomic species, here the Ni atom of nickelocene and in particular its 3d orbitals.

Figure 3.11(a) presents the X-ray adsorption spectra (XAS) on the L<sub>2,3</sub> edges of Ni for the left-circular and right-circular polarized X-ray beam-light. The difference between these spectra, the so-called XMCD spectrum, presents a non-vanishing signal, in other words a dichroic

signal as shown in Fig. 3.11(b). This indicates that nickelocene is magnetic on Cu(100). To quantify this magnetic signature, we applied the so-called sum rules [145, 146] (see appendix A). The number of  $d$ -holes necessary to the sum rules application is taken as  $N_d = 1.8$ . This represents an average value between the DFT-computed  $d$ -holes number ( $N_d = 1.6$ ) known to underestimate this value and the  $d$ -holes number of a  $\text{Ni}^{2+}$  ion ( $N_d = 2.0$ ). We estimate the experimental spin moment for Ni near 0 K to be  $0.8 \mu_B$ , which agrees fairly well with the DFT value of  $1.18 \mu_B$  determined above in § 3.2.2.

To evidence the presence of magnetic anisotropy, we investigated the temperature and angular dependence of the spin momentum calculated via the sum rules. The results are presented in Fig. 3.11(c). Two angles were investigated,  $\theta = 0^\circ$  and  $60^\circ$ , where  $\theta$  is the angle between the field and the surface normal [inset of Fig. 3.11(c)]. At low temperature, the signal shows an angular dependence revealing the existence of an easy plane perpendicular to the molecular axis. For the sake of comparison, we model the temperature dependence of the magnetization of a spin 1 system in the presence of magnetic anisotropy [dashed lines in Fig. 3.11(c)]. At lowest order, the system can be described by the following spin Hamiltonian

$$\hat{H} = D\hat{S}_z^2 - g\mu_B \mathbf{B} \cdot \hat{\mathbf{S}}. \quad (3.2)$$

Compared to Eq. (3.1), we introduce a second term corresponding to the Zeeman energy, where  $\mathbf{B}$  is the applied external magnetic field and  $g = 2$  the gyromagnetic factor. To account for the XMCD geometry [inset of Fig. 3.11(c)], we project the Hamiltonian on the  $x$  and  $z$  directions

$$\hat{H} = D\hat{S}_z^2 - g\mu_B (B\hat{S}_z \cos \theta + B\hat{S}_x \sin \theta). \quad (3.3)$$

Since XMCD measures the projection of the magnetization on the photon beam axis, which is parallel to the applied magnetic field, we express the magnetization as

$$\langle \hat{S} \rangle = \langle \hat{S}_z \rangle \cos \theta + \langle \hat{S}_x \rangle \sin \theta, \quad (3.4)$$

where  $\langle \hat{S}_x \rangle$  and  $\langle \hat{S}_z \rangle$  are the thermal averages of the two spin operators at a temperature  $T$  in an applied field  $\mathbf{B}$ . Their thermal average is given by

$$\langle \hat{S}_i \rangle = \frac{1}{Z} \sum_j \langle j | \hat{S}_i | j \rangle \exp\left(-\frac{\epsilon_j}{k_B T}\right), \quad (3.5)$$

where  $\epsilon_j$  corresponds to an eigenvalue of the Hamiltonian of Eq. (3.3) associated to the eigenvector  $|j\rangle$ , while  $Z$  is the partition function defined as

$$Z = \sum_j \exp\left(-\frac{\epsilon_j}{k_B T}\right).$$

To obtain  $\epsilon_j$  and  $|j\rangle$  at an arbitrary angle  $\theta$ , we numerically diagonalized the Hamiltonian. To mimic the XMCD setup we fix the magnetic field to 6.5 T and consider two angular orientations,  $\theta = 0^\circ$  and  $\theta = 60^\circ$ . Adjusting the simulation curve of the spin magnetic momentum to the data can be done through the adjustment of  $D$ . When  $S = 1/2$ , the magnetization shows no angular dependence since the magnetic anisotropy does not play any role then. When  $S = 1$  instead,  $\langle \hat{S} \rangle$  shows a clear angular dependence [dashed lines in Fig. 3.11(c)], which reflects the existence of an easy magnetization direction. The experimental data is found to be properly fitted using  $D = 3.2$  meV for the magnetic anisotropy, the simulation nicely capturing the low-temperature the spin magnetic momentum data performed for the grazing orientation of the magnetic field. Based on these results, we can assert first that  $D$  is positive, implying that  $|S = 1, M = 0\rangle$  corresponds to the ground state of nickelocene and the  $|S = 1, M = \pm 1\rangle$  to the excited states and that this magnetic anisotropy presents a comparable value to the one presented in § 3.2.1.

## 3.3 Spin excitation and electron scattering

### 3.3.1 Spin excitation spectroscopy of nickelocene

To complete the magnetic characterization of nickelocene on copper we acquired spin excitation spectra above Nc molecules on Cu(100). A typical spectrum for an isolated Nc is presented in Fig. 3.12(a). In the  $dI/dV$  curve we observe a step at  $(3.2 \pm 0.1)$  mV, which corresponds to an inelastic threshold. The step translated into a dip (peak) at negative (positive) bias in the  $d^2I/dV^2$  curve. Vibrational excitation energies were measured for Nc on Ag(100) by macroscopic averaging techniques [132] and give values ranging from 40 meV to 400 meV. The excitation observed here may therefore safely be assigned to a spin excitation. Based on the information gathered previously (§ 3.2), the spin Hamiltonian of nickelocene is that of Eq. (3.1). We assign then the threshold observed to an excitation occurring between the ground state  $|S = 1, M = 0\rangle$  and the excited states  $|S = 1, M = \pm 1\rangle$  [Fig. 3.12(b)], the threshold energy

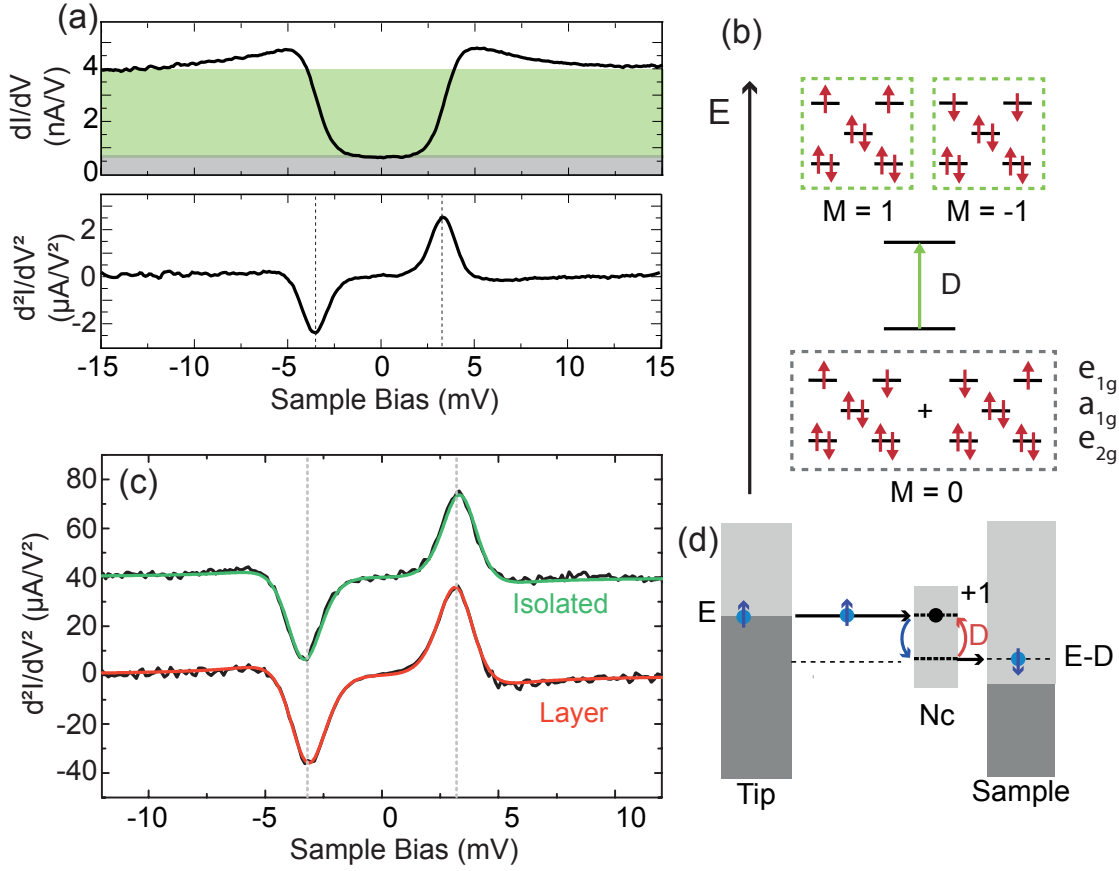


Figure 3.12: **Spin excitation spectroscopy of nickelocene on Cu(100).** (a) Spin excitation spectrum of isolated Nc (top:  $dI/dV$ , bottom:  $d^2I/dV^2$ ). The grey (green) area highlights the elastic (inelastic) contribution to the the  $dI/dV$ . Feedback loop opened at  $I = 50$  pA,  $V = -15$  mV. (b) Energy diagram showing the excitation process for nickelocene. (c) Spin excitation spectrum of isolated Nc and of Nc in the layer. The latter is displaced upward vertically for clarity. Feedback loop opened at  $I = 50$  pA,  $V = -15$  mV. (d) Sketch showing a spin excitation. Note the spin-flip of the tunnel electron.

corresponding to the axial magnetic anisotropy we have then  $D = (3.2 \pm 0.1)$  meV. The value of  $D$  agrees with the one determined by the XMCD measurements (§ 3.2.3). As shown in Fig. 3.12(c), the spin excitation spectra for vertical molecules within the layer is similar to the isolated molecule one. This suggests that the magnetic coupling among nickelocene molecules in the layer, if present, is below the detectability of our setup, *i.e.* below 0.5 meV.

As illustrated in Fig. 3.12(d), the excitation of Nc from the ground to its first excited

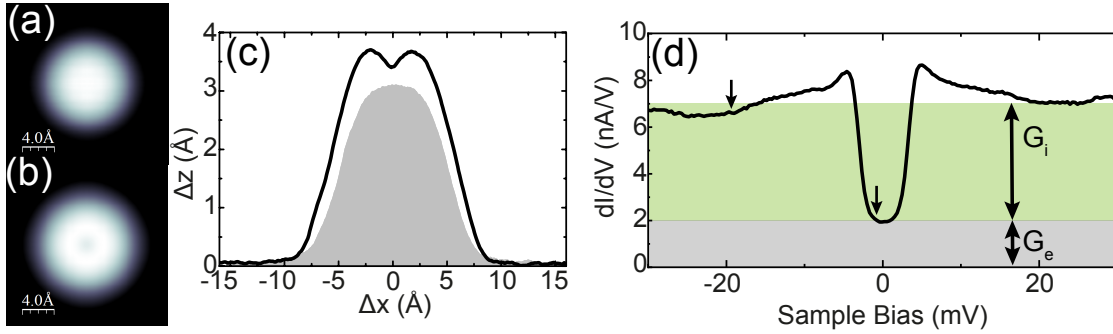


Figure 3.13: **Inelastic conductance versus apparent height of nickelocene on Cu(100).** Nickelocene on Cu(100) (a) without inelastic conduction channel ( $I = 20$  pA,  $V = -2$  mV,  $1 \times 1$  nm<sup>2</sup>), (b) with an active inelastic channel ( $I = 20$  pA,  $V = -20$  mV,  $1 \times 1$  nm<sup>2</sup>). (c) Corresponding line profiles showing the difference in apparent height. (d)  $dI/dV$  spectrum showing the elastic and the inelastic conductance channels.

state  $|S = 1, M = +1\rangle$ , requires a change in spin angular momentum of  $\delta M = +1$ . Since the total angular momentum has to be conserved it can only be induced by electrons that compensate for this moment by flipping their spin direction during the tunneling process from  $|\uparrow\rangle$  to  $|\downarrow\rangle$ . Similarly, the excitation of Nc from the ground state to its second excited state  $|S = 1, M = -1\rangle$  requires electrons starting in a  $|\downarrow\rangle$  state and ending in a  $|\uparrow\rangle$  state. Hence, inelastic electrons flip their spin direction during the tunneling process.

A remarkable aspect of the spectrum is the amplitude of the inelastic conductance [ $G_i$ , green area in Fig. 3.12(a)] compared to the elastic conductance [ $G_e$ , grey area in Fig. 3.12(a)]. We found a factor  $4 \pm 1$  ratio between the two conductances depending on the tips used, which differs notably from other known systems. For example, Fe/Cu<sub>2</sub>N [24] and Co/Cu<sub>2</sub>N [23] give a ratio of 0.3, while Mn/Cu<sub>2</sub>N [4] gives a ratio of 1. The ratio found here has a strong impact on the STM images, depending if the inelastic conduction channel is open ( $|eV| > D$ ) or closed ( $|eV| < D$ ) as shown in Figs. 3.13(a) and 3.13(b). When the inelastic conductance channel is closed, the upper Cp ring of nickelocene is not imaged and the apparent height of the molecule drops from  $(3.5 \pm 0.1)$  Å to  $(2.9 \pm 0.1)$  Å [Fig. 3.13(c)]. The trace of this topographical difference can be seen in Fig. 3.13(d), where the inelastic conductance channel is about 3 times the elastic one. As showed in § 3.1.3, by closing the inelastic channel we were able to image the horizontal molecules in the self-assembled layers.

### 3.3.2 Inelastic versus elastic conductance

In this section, we will present the analytical model developed by N. Lorente to explain the origin of the unusually high value observed experimentally for  $G_i/G_e$  [38]. Deriving this ratio directly from a spin Hamiltonian, e.g. Eq. (3.14), is not trivial and requires to develop an approach other than existing ones [41, 99]. The model is based on the strong coupling theory [87, 147], which uses a Anderson-like hamiltonian, the notion of spin symmetries and a  $T$ -matrix formalism.

To start, we need to express the tunneling current  $I$  in terms of the scattering matrix  $\hat{T}$ . To do so, the spin excitation is described via a three-step inelastic collision model for the tunneling electron as follows: an electron is injected into an empty state of the molecule, creating a virtual state of a negatively charged molecular ion. Then, this ion decays by donating one electron to the substrate. We consider that the magnetic anisotropy is “inactive” during the tunneling process as the tunneling lifetime is short compared to the lifetime of Nc spin excitation—this is the so-called sudden approximation. We instead consider the magnetic anisotropy active at the beginning and at the end of the tunneling process. This assumptions constitute the so-called impulsive approximation formulated by Persson [99]. We can then express the current as [147]

$$I = C \sum_{i,f} \left| \langle \phi_i | \hat{T} | \phi_f \rangle \right|^2 \delta(E_i - E_f) \quad (3.6)$$

where  $C$  is a constant.  $|\phi_i\rangle$  and  $|\phi_f\rangle$  correspond to the wave functions describing the initial and final states of the molecule and of the tunneling electron. The initial and final states have energies  $E_i$  and  $E_f$ , respectively. Considering the spin  $S = 1$  and uniaxial magnetic anisotropy of Nc, we have  $|\phi_i\rangle = |s = 1/2, m = \pm 1/2; S = 1, M = 0\rangle$  and  $|\phi_f\rangle = |s = 1/2, m = \mp 1/2; S = 1, M = \pm 1\rangle$ , where  $s$  and  $m$  are the spin and spin angular momentum of the tunneling electron, respectively.

The trick consists in introducing the total spin of the system  $\vec{S}_T = \vec{s} + \vec{S}$ ;  $S_T$  can have two values:  $1 + 1/2 = 3/2$  and  $1 - 1/2 = 1/2$ . Using again the sudden approximation, we can split the contribution to the  $T$ -matrix in collision channels of total spin  $T^{S_T}$ . From Eq. (3.6) and following [87, 147], we can express the elastic conductivity  $G_e$  and the inelastic conductivity  $G_i$  as

$$G_e \propto \frac{2}{9} \left| 2T^{3/2} + T^{1/2} \right|^2, \quad (3.7)$$

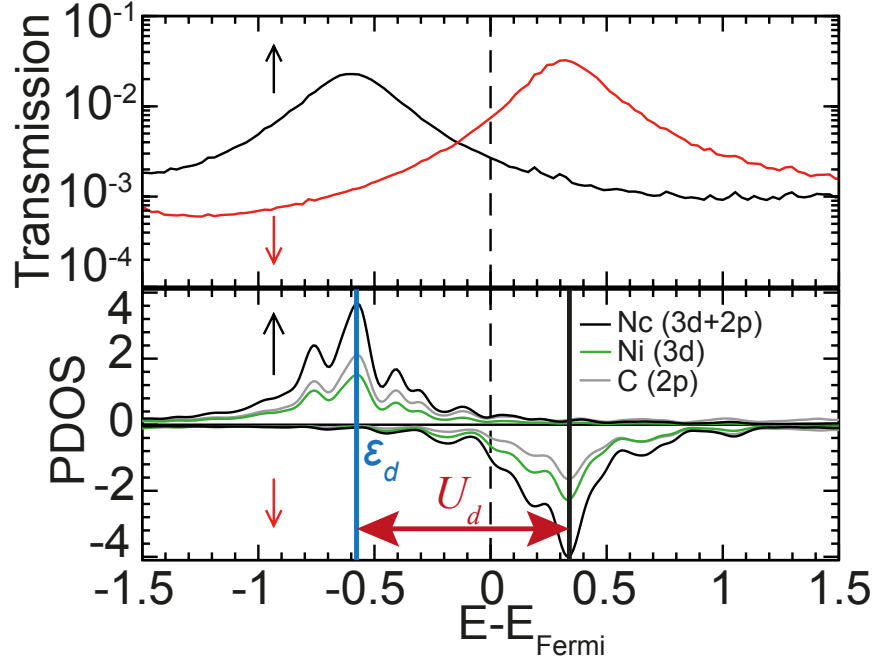


Figure 3.14: **NEGF-DFT calculations.** (a) Spin-polarized elastic transmission as a function of energy. The junction is composed by two semi-infinite Cu(100) surfaces with a nickelocene adsorbed on one of the surfaces. The majority ( $\uparrow$ ) spin transmission is shown in black and the minority ( $\downarrow$ ) spin transmission in red. (b) PDOS of selected molecular orbitals of Nc (see also Fig. 3.10). The Anderson parameters  $\epsilon_d$  and  $U_d$  are indicated.

and

$$G_i \propto \frac{4}{9} |T^{3/2} - T^{1/2}|^2, \quad (3.8)$$

which leads to the ratio

$$\frac{G_i}{G_e} = \frac{2 |T^{3/2} - T^{1/2}|^2}{|2T^{3/2} + T^{1/2}|^2}. \quad (3.9)$$

Here, the difficulty resides in estimating the values of  $T^{3/2}$  and  $T^{1/2}$ . Recalling Persson's approach [99]—and assuming the spherical approximation underlying the sudden approximation,  $T^{1/2}$  and  $T^{3/2}$  can be written in terms of a new set of transmission coefficients  $T_0$  and  $T_1$ . These, in turn, can be estimated through DFT-based transmission calculations. Indeed, we have

$$T^{3/2} = T_0 + 0.5T_1, \quad (3.10)$$

$$T^{1/2} = T_0 - T_1. \quad (3.11)$$

Moreover, using a Schrieffer-Wolff transformation [17], we can link  $T_0$  to  $T_1$

$$T_1 = -2T_0 \frac{U_d}{U_d + 2\epsilon_d} \quad (3.12)$$

where  $\epsilon_d$  the energy of the highest occupied molecular orbital (HOMO) in our case and  $U_d$  is the Hubbard term in the Anderson hamiltonian. The position of the LUMO is defined by  $\epsilon_d + U_d$ . Finally, introducing Eqs. (3.10), (3.11) and (3.12) into the expression of  $G_i/G_e$  [Eq. (3.9)], we obtain

$$\frac{G_i}{G_e} = \frac{2U_d^2}{(U_d + 2\epsilon_d)^2}. \quad (3.13)$$

As anticipated above, we can then estimate the ratio by using the values  $U_d$  and  $\epsilon_d$  obtained from DFT calculations. More specifically a non-equilibrium Green function calculation based on DFT (NEGF-DFT) was carried out. Figure 3.14 shows the transmission and the density of states, calculated for Nc between two Cu(100) electrodes. From Fig. 3.14, we estimate  $\epsilon_d = -0.6$  eV and  $U_d = 0.9$  eV, and obtain a ratio  $G_i/G_e = 18$ , well above the experimental ratio. However, DFT calculations tend to overestimate the position of the unoccupied orbital hence to overestimate the value of  $U_d$ . Reducing  $U_d$  to 0.8 eV gives in fact a better agreement as the ratio is then 8.

The ratio  $G_i/G_e$  shows a huge sensibility towards the position of the occupied and unoccupied orbitals, and the estimation of it from the DFT calculations should be handled with care and treated only qualitatively. Finally, we would like to stress that based on Eq. (3.13), the ratio  $G_i/G_e$  presents a singularity when  $U_d = -2\epsilon_d$ , *i.e.* when the spin system approaches particle-hole symmetry. The strong  $G_i/G_e$  ratio found for Nc means that this system is close to particle-hole symmetry.

### 3.3.3 Electron scattering

To complete the line shape analysis of the spin excitation spectrum, we use the dynamical scattering model of M. Ternes [41, 148]. The model can simulate the spectral line shape and thereby provides some information about the electron scattering occurring between the Nc and the electronic bath of copper (see § 1.3.5). Several studies have in fact pointed out the



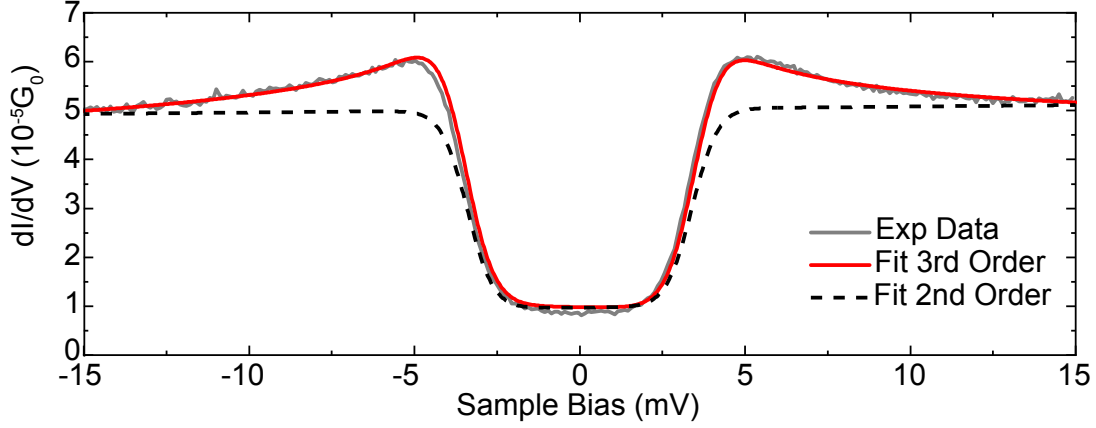


Figure 3.15: **Simulated spin excitation spectrum of nickelocene on Cu(100).**  $dI/dV$  spectrum of Nc/Cu(100) [same as Fig. 3.12(b)]. Feedback loop opened at  $I = 50$  pA,  $V = -15$  mV. Solid red line: Simulated spectrum using a dynamical scattering model with the parameters of Tab. 3.4. Dashed green line: Simulated spectrum using  $\mathcal{J} = \mathcal{U} = 0$ .

importance to account for electron scattering, including Kondo-like phenomena [106, 107], to properly reproduce the line shape. Accordingly, the spin Hamiltonian of Eq. (3.1) is re-expressed to include two new terms

$$\hat{H} = D\hat{S}_z^2 + \mathcal{J}\hat{\sigma}\cdot\hat{\mathbf{S}} + \mathcal{U}\hat{I}, \quad (3.14)$$

where  $\mathcal{J}$  represents the antiferromagnetic exchange scattering between the electronic spins of copper and the localized spin of Nc (also known as Kondo scattering parameter),  $\mathcal{U}$  the scattering potential and  $\hat{I}$  the identity operator. These two new terms originate from the single-impurity Anderson model [149], which is well adapted for Nc because of its half-filled spin-polarized LUMO near the Fermi level (Figs. 3.10 and 3.14). Figure 3.15 presents a spin excitation spectrum for Nc/Cu(100), along with a line shape simulation based on Eq. (3.14). The scattering parameters used for the simulation are given in Tab. 3.4. The simulation was computed with a program kindly provided by M. Ternes. Figure 3.15 also includes a simulation where we have purposely suppressed the electron scattering (dashed line), *i.e.*  $\mathcal{J} = \mathcal{U} = 0$ . In this case, the simulation fails to capture the cusps at the excitation threshold.

To interpret these values, it is of interest to express  $\mathcal{J}$  and  $\mathcal{U}$  in terms of the Anderson

$D$ (meV)	$T_{\text{eff}}$ (K)	$\mathcal{J}$ (eV)	$\mathcal{U}$ (eV)
3.5	3.2	-0.15	0.03

Table 3.4: **Parameters for simulating the spin excitation spectrum of nickelocene on Cu(100).** Parameters of the dynamical scattering model that were used for the simulation of Fig. 3.15.  $T_{\text{eff}}$  is the effective temperature of the spin system at thermal equilibrium.

parameters of § 3.3.2. Using again the Schrieffer-Wolff transformation [17], we have

$$\mathcal{J} = \frac{2}{\pi} \Delta^2 \frac{U_d}{\epsilon_d(\epsilon_d + U_d)}, \quad (3.15)$$

and

$$\mathcal{U} = \frac{2}{\pi} \Delta^2 \frac{2\epsilon_d + U_d}{\epsilon_d(\epsilon_d + U_d)}, \quad (3.16)$$

where  $\Delta$  is the width of the molecular states. Using the ratio  $\mathcal{J}/\mathcal{U}$  and the above expressions, we can then estimate the ratio between  $\epsilon_d$  and  $U_d$  to be  $\epsilon_d/U_d = -0.4$ . This value is close to the particle-hole symmetry ( $\epsilon_d/U_d = -0.5$ ), the HOMO being slightly closer to the Fermi level than the LUMO. It is consistent with the analysis of § 3.3.2.

## 3.4 Conclusion

In this chapter we presented a combined experimental and theoretical study aimed at characterizing the magnetism of an adsorbed Nc molecule on Cu(100). Nickelocene is either isolated or forms well-ordered layers governed by van der Waals interactions. In both cases, Nc is found to be weakly chemisorbed to the surface. This weak coupling to the surface allows preserving the spin  $S = 1$  and uniaxial magnetic anisotropy of free nickelocene. Clear signatures of the magnetism were experimentally unveiled through macroscopic averaging measurements (XMCD) and single-molecule measurements, *i.e.* spin excitation spectroscopy. In particular, we evidenced the weak coupling of nickelocene to the copper surface through the presence of electron scattering in the spin excitation spectrum. We also demonstrated through a careful analysis of the spin excitation spectrum that nickelocene is a spin system close to particle-hole symmetry. In the next chapter, we will further explore how the environment of Nc affects its magnetism by transferring the molecule to the STM tip or by placing it in contact with both

tip and surface to create a molecular junction.



## CHAPTER 4

# Nickelocene on the apex of a STM tip

We saw in the previous chapter that the spin excitations in a single nickelocene are preserved in the presence of a metal, possibly owing this behavior to the cyclic  $\pi^*$  orbital of the Cp rings sandwiching the Ni atom. This behavior is remarkable, differentiating nickelocene from other conventional spin systems, which have their spin excitations quenched by the presence of a metal [24, 63, 92, 150]. In this chapter, we attach a single nickelocene to the tip apex of the STM and show that spin excitations are also preserved in this environment (§ 4.1). This non-conventional setup offers the possibility to explore new effects involving spin excitations, as the interaction between the nickelocene tip (Nc-tip hereafter) and the sample may be tuned with picometer resolution. We will specifically address the magnetic interaction between the Nc-tip and the sample in Chapter 5. Here we will focus on some other original properties. In particular, we will show how that one can generate double spin excitations (§ 4.2) and how the spin of the Nc-tip can be switched in a controlled fashion (§ 4.3). DFT calculations were carried out within a collaboration with the group of N. Lorente (CFM, Donostia-San Sebastián). The results were published in *Nano Lett.* **17**, 1877 (2017) [38] and *Nat. Commun.* **8**, 1974 (2017) [42].

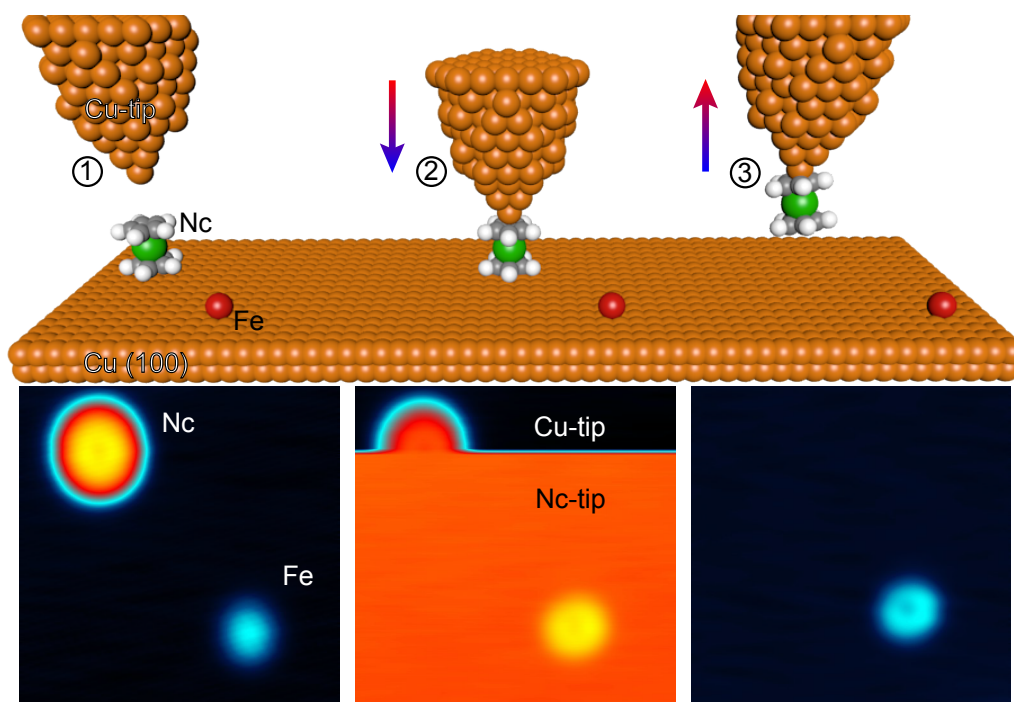


Figure 4.1: **Attaching nickelocene to the tip apex.** The panels noted from (1) to (3) present sketches and images describing the attachment procedure: (1) The panel depicts a metallic tip scanning a Cu(100) surface on which is adsorbed a Nc molecule and an atom. The corresponding image was acquired at  $G = 1$  nS ( $I = 30$  pA,  $V = -50$  mV). (2) The molecule is transferred to the tip. The top part of the image is acquired with a metallic tip at  $G = 1$  nS. Once the tip is above the molecule, the line scan is frozen. As soon as the conductance increased, for example to  $G = 200$  nS ( $I = 200$  pA,  $V = -1$  mV), the molecule transfers to the tip. The transfer is detected by monitoring changes in the lateral trajectory of the tip. The line scan is then unfrozen and the conductance lowered back to  $G = 1$  nS to complete the image (with a Nc-tip). (3) When imaging again the area, we see that the molecule is no longer present on the surface and that the atom presents a molecular pattern. All the images have a size of  $5 \times 5$  nm<sup>2</sup>.

## 4.1 Nickelocene-terminated tip

### 4.1.1 Adsorption of nickelocene on the tip apex

Attaching a nickelocene to the tip apex is a straightforward procedure. We usually start by covering our W tip with surface material through soft indentations into the pristine surface. It is essential to ensure a mono-atomically sharp metallic apex. A single nickelocene can then

be attached to the tip by vertically moving the tip into contact with the molecule through a current-versus-tip displacement measurement [151]. Similarly, one may scan the tip across the molecule close to the contact regime. This procedure, which provides a better control than a vertical displacement of the tip toward the molecule, is depicted in Fig. 4.1 for a nickelocene molecule on Cu(100). As shown, we first start by imaging the molecule with a typical tunnel conductance of  $G = 1$  nS (panel noted 1). When scanning across the molecule, we then increase the conductance to  $G = 200$  nS by approaching the tip to the surface, the bias polarity being negative (panel noted 2). Upon decreasing afterwards the conductance back to 1 nS, the molecule is no longer on the surface (panel noted 3). The presence of nickelocene on the tip apex is detected though the molecular pattern visible when imaging surface objects, in particular single adsorbed atoms (adatoms) as shown in panel (3). Adatoms have a featureless structure when imaged with a metal tip (panel 1), but exhibit a molecular pattern when imaged with a molecule on the tip. These images, also known as counter images, were, for example, used for determining the orientation of a  $C_{60}$  molecule on a metallic tip apex [152, 153].

Some typical counter-images for a Nc-tip are shown in Figs. 4.2(a) and 4.2(b) where a ring-shaped pattern is evidenced when imaging adatoms. The pattern reveals that the tip is terminated by a Cp ring of a tilted Nc molecule. The tilt angle  $\theta$ , which exhibits some tip dependency, is estimated by recording the line profile of one atom [Fig. 4.2(c)]. The tilt angle  $\theta$ , between the Cp plane and the plane of the surface, is estimated via the height difference between the left and right protrusion of the line profile yields typically  $\theta = 10^\circ$ . To confirm this assignment we mimicked the molecular tip through DFT calculations by considering a Nc molecule adsorbed on a Cu atom on Cu(100) [Inset of Fig. 4.2(a)]. The molecule is undeformed, the molecular axis is tilted by  $13^\circ$  with respect to the surface normal and linked through two C atoms to the Cu atom. The corresponding simulated image in Fig. 4.2(d) is in good agreement with the experimental counter-images. The Nc tip is robust to mechanical perturbations as tip-surface point contacts may be routinely carried out without damaging the tip (see § 4.3). It is also “safe” to scan above nickelocene molecules, either isolated [Fig. 4.2(b)] or self-assembled [Fig. 4.2(d)].

### 4.1.2 Spin excitation spectroscopy on the tip apex

The magnetic properties of a nickelocene on a tip are very similar to those of nickelocene on a metal surface. The two spin systems have in fact similar spin excitation spectra. Figures 4.3(a)

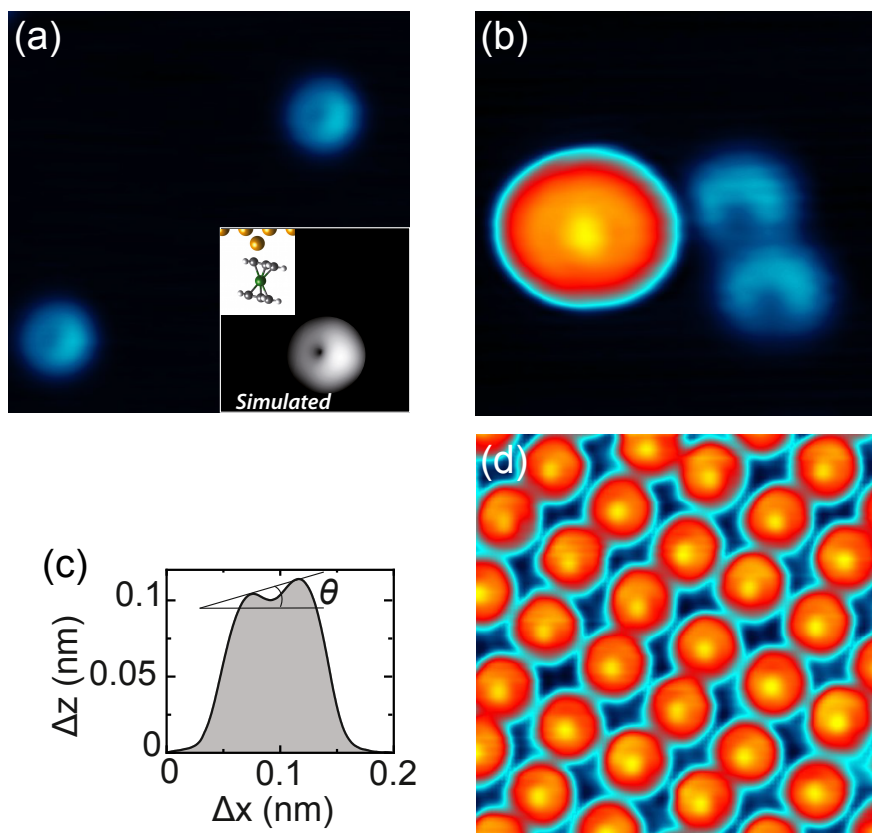


Figure 4.2: **Imaging with a nickelocene tip.** The images in panels (a) and (b) were acquired with two different Nc-tips. Panel (a) shows two iron adatoms ( $I = 30$  pA,  $V = -15$  mV,  $5 \times 5$  nm<sup>2</sup>), and panel (b) shows a nickelocene molecule and two iron adatoms ( $I = 30$  pA,  $V = -15$  mV,  $4.9 \times 4.9$  nm<sup>2</sup>). Inset panel (a): Calculated relaxed configuration of a Nc molecule on top of a Cu adatom on Cu(100), together with the simulated STM image. Atom colors: Cu (yellow), C (grey), H (white) and Ni (green). (c) Line profile of one adatom in panel (a) and definition of the tilt angle  $\theta$ . (d) Image of a compact network of Nc recorded with a Nc-tip ( $I = 30$  pA,  $V = -15$  mV,  $4.9 \times 4.9$  nm<sup>2</sup>). Nickelocene molecules imaged with a Nc-tip exhibit a complex pattern as visible in panels (b) and (d). This pattern reflects a convolution between the bottom Cp ring of the Nc-tip and the top Cp ring of the nickelocene molecule on the surface. The protrusion in the center may be associated to a configuration where the Cp rings of the tip and of the surface are facing one another.

and 4.3(b) present the  $dI/dV$  and  $d^2I/dV^2$ , respectively, acquired with a Nc-tip positioned above a bare Cu(100) surface. The solid red lines are the line-shape simulations obtained using the dynamical scattering model described in § 3.3.3 [41]. The line shape is well reproduced



assuming that nickelocene has a spin  $S = 1$  and a uniaxial magnetic anisotropy of  $D = (3.7 \pm 0.3)$  mV —the error bar on  $D$  reflects its dependency related to different tips. We safely conclude that the inelastic threshold observed corresponds to an excitation occurring between the ground state  $|S = 1, M = 0\rangle$  and the excited states  $|S = 1, M = \pm 1\rangle$ .

From the line-shape simulation (§ 3.3.3), we find a Kondo scattering parameter of  $\mathcal{J} = -0.69$  eV and a scattering potential of  $\mathcal{U} = 0.02$  eV. The ratio  $\mathcal{J}/\mathcal{U}$  allows estimating the ratio  $\epsilon_d/U_d = -0.51$ , which indicates that the Nc-tip is even closer to particle-hole symmetry than nickelocene on Cu(100) (where  $\epsilon_d/U_d = -0.4$ ). Consistent with this viewpoint (§ 3.3.2), we find that the ratio between the inelastic conductance ( $G_i$ ) and the elastic conductance ( $G_e$ ) doubles compared to nickelocene on copper, reaching  $G_i/G_e = (9 \pm 2)$  [see Fig. 3.12(a) for the definition of  $G_i$  and  $G_e$ ]. The molecular spin is well preserved from scattering events with itinerant electrons of the tip.

The magnetic anisotropy of a Nc-tip is up to 15% larger compared to a nickelocene on copper (§ 3.3.3). To elucidate why  $D$  increases, we performed DFT calculations to compare Nc in three situations: gas phase [Fig. 4.3(c)], adsorbed on Cu(100) [Fig. 4.3(d)] and attached to a metal tip [Fig. 4.3(e)]. The later is simulated by adsorbing Nc on a Cu adatom on Cu(100) —to simplify calculations the molecule is forced to be centered with respect to the Cu adatom underneath. The spin density is similar in the three cases showing that the molecule has a spin equal to 1, in agreement with the line shape analysis described above. Moreover, while a charge transfer of 0.1e occurs from Nc to Cu(100) (§ 3.1.2), a reversed charge transfer of 0.14e is observed from the tip to Nc. This leads to a larger molecular height of 3.62 Å for the Nc on the tip compared to the height of 3.54 Å for Nc on the surface. The elongation of nickelocene along its principal molecular axis translates into a different magnetic anisotropy energy (MAE). We computed the MAE within the framework of DFT using a spin-orbit coupling (SOC). It is defined as

$$MAE = E_{||}^{SOC} - E_{\perp}^{SOC}, \quad (4.1)$$

where  $E_{||}^{SOC}$  is the energy obtained with the magnetic moment in the plane parallel to the surface and  $E_{\perp}^{SOC}$  the energy obtained with the magnetic moment perpendicular to the surface. The MAE is smallest when the molecule is on the surface ( $-1.27$  meV) and recovers the gas phase value ( $-1.54$  meV) when adsorbed on the Cu atom ( $-1.49$  meV). The negative values of the MAE corresponds to an easy plane of magnetization according to the definition of Eq. (4.1), in other words to a positive value of  $D$  in agreement with the experimental

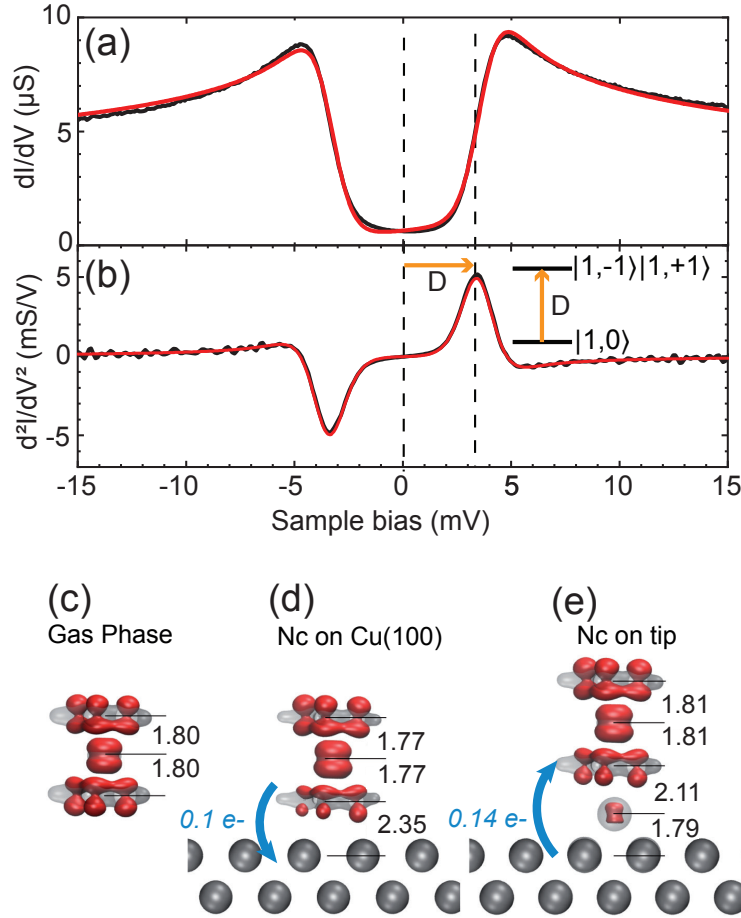


Figure 4.3: **Spectroscopic fingerprint of a nickelocene tip.** (a)  $dI/dV$  and (b)  $d^2I/dV^2$  spectra of a Nc-tip above Cu(100). Feedback loop opened at  $I = 1$  nA,  $V = -20$  mV. (c)-(e) Calculated spin density (majority spin in red, negligible minority spin) and total electron density (grey transparent) of gas phase Nc with MAE =  $-1.54$  meV (c), adsorbed Nc on Cu(100) with MAE =  $-1.27$  meV (d) and adsorbed Cu-Nc on Cu(100) with MAE =  $-1.49$  meV (e). The isosurface of the spin (total electron) density is 0.02 (1.3) electron per  $\text{\AA}^3$ . The inter-atomic distances are given in  $\text{\AA}$ . Note that in the three cases the spin is  $S = 1$ , the orbital moment having a negligible value of  $0.1 \mu_B$ .

findings. The 17% difference in the MAE for the different geometries is also consistent with the experimental changes found for  $D$ . This shows that the molecular adsorption impacts the magnetic anisotropy as remarked in other systems [154]. We stress that the absolute values of

the MAE should correspond, in principle, to  $|D|$  given the spin  $S = 1$  of nickelocene. The discrepancy observed is due to time constraints imposed on the DFT calculations, which result in a scaling error.

## 4.2 Double spin excitation

The Nc-tip allows to freely position a nickelocene molecule above surface-supported objects. The first object we investigated consisted in a isolated nickelocene molecule on Cu(100). As we showed in Fig. 4.2(b), the Nc-tip can be scanned above a nickelocene. This shows that the molecular junction of the form tip/Nc/Nc/surface is stable [Fig. 4.4(a)]. The spin excitation spectra acquired with a Nc-tip above Cu(100) and above a nickelocene on Cu(100) are presented in Figs. 4.4(b) and 4.4(c), respectively. The spectra were acquired with the same Nc-tip. Above Cu(100) [Fig. 4.4(b)], we observe the usual line shape with an excitation threshold of  $|3.7 \pm 0.2|$  mV and a ratio between inelastic and elastic channels of  $G_i/G_e = 8$ . Above nickelocene [Fig. 4.4(c)], we observe instead two conductance steps, which translate into two peaks (dips) in the  $d^2I/dV^2$  spectrum in Fig. 4.4(d). The first threshold bias corresponds to  $|3.4 \pm 0.2|$  mV, and the second corresponds to  $|6.9 \pm 0.4|$  mV. To explain the observed thresholds, we described the spin system with the following spin Hamiltonian

$$\hat{H} = D_1 \hat{S}_{1,z}^2 + D_2 \hat{S}_{2,z}^2, \quad (4.2)$$

where the numbers 1 and 2 refer to a nickelocene on the surface and on the tip, respectively. The magnetic anisotropy of the two molecules is slightly different with  $D_1 < D_2$  (§ 4.1.2). We have assumed that the two nickelocene molecules are magnetically uncoupled. Figure 4.4(e) presents the state diagram of Eq. (4.2), along with the spin states of the system  $|S = 1, M_1; S = 1, M_2\rangle$ , which, for simplicity, we express by  $|M_1; M_2\rangle$ .

Since during the tunneling process, the total angular momentum must be conserved, only three spin excitations may occur in the system [indicated by arrows in Fig. 4.4(e)]. The first spin excitation corresponds to an energy  $|eV| = D_1 = 3.2$  meV where a tunnel electron excites the nickelocene on the surface from  $|M_1 = 0; M_2 = 0\rangle$  to  $|M_1 = \pm 1; M_2 = 0\rangle$ . The second excitation corresponds to a energy  $|eV| = D_2 = 3.7$  meV where a tunnel electron excites the Nc-tip from  $|M_1 = 0; M_2 = 0\rangle$  to  $|M_1 = 0; M_2 = \pm 1\rangle$ . In principle, two excitation thresholds should be observed at  $\pm D_1$  and  $\pm D_2$  in Fig. 4.4(c), but their detection is beyond our energy

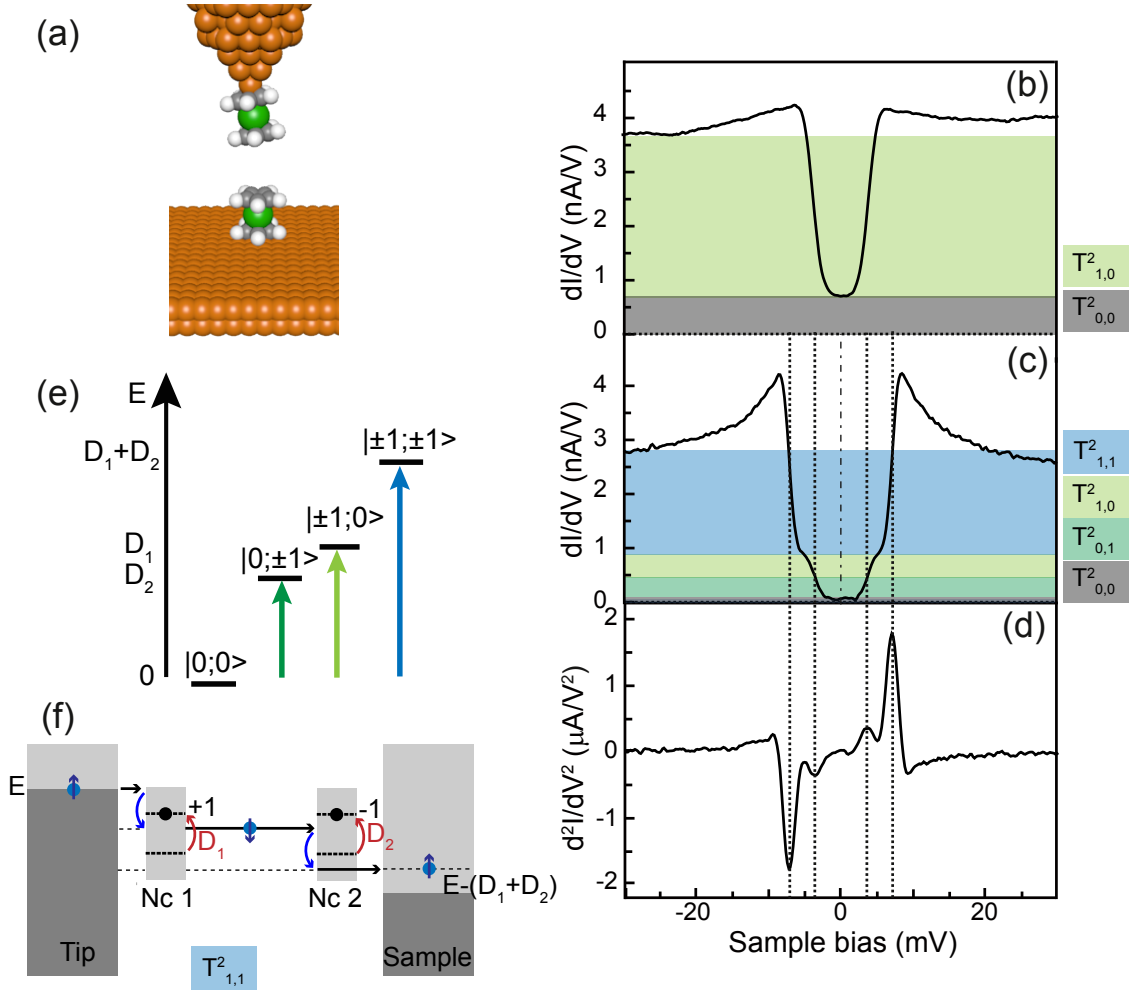


Figure 4.4: **Double spin excitation.** (a) Sketch of a Nc-tip positioned above a Nc/Cu(100). (b)  $dI/dV$  spectrum of a Nc-tip above Cu(100). The gray filled area corresponds to the elastic conductance channel and the light green corresponds to the inelastic conductance channel. (c)  $dI/dV$  spectrum of Nc-tip above an on-surface Nc. The gray area corresponds to the elastic conductance channel while the light green, green and blue correspond respectively to the inelastic channels of the Nc-tip excitation, on-surface Nc excitation and both Nc excitations. (d)  $d^2I/dV^2$  spectrum of Nc-tip over an on-surface Nc. The spectra were acquired at ( $I = 100$  pA,  $V = -40$  mV). (e) State diagram of Eq. (4.2), along with the spin states of the system. The arrows indicate the three possible spin excitations. The transmission probabilities are also indicated (see text for definition). (f) Sketch showing a double spin excitation.

resolution. A single threshold is instead observed at an average position of  $\pm(D_1 + D_2)/2 \approx \pm 3.4$  meV. The third excitation corresponds to an energy  $|eV| = D_1 + D_2 = 6.9$  meV where a tunnel electron inelastically excites both molecules. The tunnel electron produces a double spin excitation as sketched in Fig. 4.4(f). As we mentioned in § 3.3.1, the inelastic tunnel electron flips its spin direction after exciting the molecule [see Fig. 3.12(d)]. Here, as the tunnel electron excites the two nickelocene molecules, it must flip its spin direction twice (§ 3.3.1). The spin angular momentum of the two nickelocene molecules needs to compensate for this double spin flip so that the final state is  $|M_1 = \pm 1; M_2 = \mp 1\rangle$ .

We complete this section by focusing on the most prominent effect associated to the double spin excitation, which is the drastic enhancement of the inelastic conductance  $G_i$ . A typical enhancement of a factor 50 is observed with respect to the elastic conductance  $G_e$  [green versus grey area in Fig. 4.4(c)]. To explain this, let us suppose that the conductance is proportional to the probability of taking one electron from one electrode (tip) into the other electrode (surface), in other words that the conductance is proportional to the  $T$ -matrix modulus squared. Since the  $T$ -matrix has now spin degrees of freedom in the tip and on the sample, we denote the new matrix elements as  $T_{n,m}$  where  $n$  is the number of excitations of the tip and  $m$  the number of excitations of the sample, with  $m, n \in \{0, 1\}$ . Then, the conductance will be proportional to  $\sum_{n,m} |T_{n,m}|^2$ , with a sum on the excitations since the channels are supposed independent. In this case,  $T_{0,0}$  corresponds to the elastic transmission of an electron from the tip to the surface or *vice versa*.  $T_{1,0}$  and  $T_{0,1}$  correspond to the case in which there is only one spin excitation in the molecule on the tip or on the surface, respectively. Finally,  $T_{1,1}$  is related to the probability of a double spin excitation. With these notations, the ratio  $G_i/G_e$  after a double spin excitation is expressed as

$$G_i/G_e = (|T_{0,0}|^2 + |T_{1,0}|^2 + |T_{0,1}|^2 + |T_{1,1}|^2)/|T_{0,0}|^2. \quad (4.3)$$

In order to quantify this ratio, we consider the inelastic conductance for the Nc-tip in Fig. 4.4(b), which yields

$$(|T_{1,0}|^2 + |T_{0,0}|^2)/|T_{0,0}|^2 \approx 9, \quad (4.4)$$

leading to  $|T_{1,0}|^2/|T_{0,0}|^2 \approx 8$ . From Fig. 3.12(b), we extract the inelastic conductance for Nc on the surface

$$(|T_{0,1}|^2 + |T_{0,0}|^2)/|T_{0,0}|^2 \approx 5, \quad (4.5)$$

leading to  $|T_{0,1}|^2/|T_{0,0}|^2 \approx 4$ . Finally, since the excitations of the molecule on the tip and on

the sample are independent, the transmission probability of a double spin excitation can be expressed by

$$|T_{1,1}|^2/|T_{0,0}|^2 = (|T_{1,0}|^2/|T_{0,0}|^2)(|T_{0,1}|^2/|T_{0,0}|^2) \approx 8 \cdot 4 = 32. \quad (4.6)$$

Using the above estimates in Eq. (4.3), we have  $G_i/G_e = 1 + 8 + 4 + 32 = 45$  which is close to the experimental value.

### 4.3 Controlled spin switching of a nickelocene tip

The active control of a molecular spin is of interest to the area of molecular spintronics. Spin manipulation is usually possible through molecule/surface interactions [60, 155–157], external parameters such as the mechanical [158] or the chemical modification of the molecule [77, 159–163], the application of electric fields [164–166], light or temperature [167, 168]. In recent STM experiments [74, 77, 169, 170], different surface topologies were used to tune the interaction between the spin and the underlying metal, and spin control was possible through hydrogen doping of transition metal atoms. The spin of single molecules was also changed through an atomic-scale contact between a metallic tip and a molecule [154, 171]. In this section, we demonstrate that we can switch the spin of a nickelocene from  $S = 1$  to  $S = 1/2$  by simply moving the Nc-tip into contact with a copper surface, the process being fully reversible. The spin switching is monitored through abrupt changes occurring in the differential conductance around the Fermi energy, which we attribute to the different nature of the spin-flip scattering events occurring in the two transport regimes.

#### 4.3.1 Tunnel versus contact regime

The molecular junction is engineered by bringing the Nc-tip into contact with Cu(100). We found in fact that in order to contact nickelocene between both electrodes, surface and tip, it is more stable to first transfer the molecule from the metallic surface to the tip. The contact is always performed atop a copper surface atom thanks to the use of atomically-resolved contact images [Fig. 4.5(a)]. These images were acquired by scanning the molecular tip while in contact with the surface [117, 172]. This is an indication of the robustness of a Nc-tip to external mechanical strain. Figure 4.5(b) shows the conductance ( $G/G_0$ ,  $G_0 = 2e^2/h$ ) recorded by

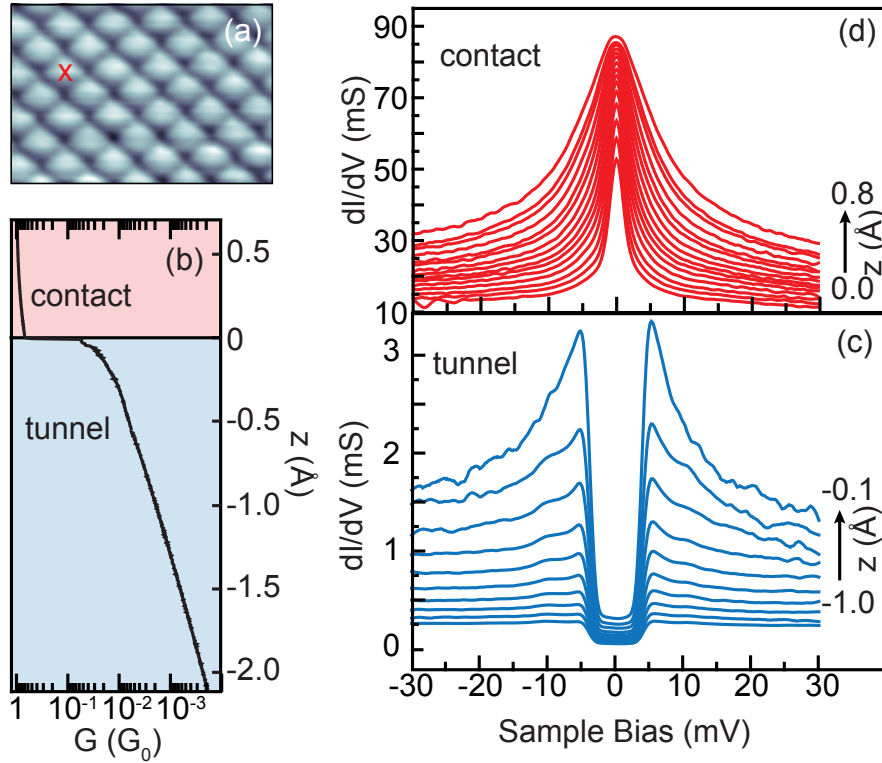


Figure 4.5: **Tunnel versus contact regime.** (a) Contact image of the Cu(100) surface using a Nc-tip ( $2 \times 1.4 \text{ nm}^2$ ; 300 pA, 30 mV). (b) Conductance-versus-distance trace recorded at a sample bias of  $-2 \text{ mV}$ . The red cross in panel (a) corresponds to the location where the conductance-versus-distance trace was recorded. Panels (c) and (d) present the  $dI/dV$  spectra acquired in the tunneling and the contact regime, respectively.

decreasing the tip-surface distance ( $z$ ) at a fixed bias of  $-2 \text{ mV}$ . The tip is here moved from its initial tunneling position  $z = -2.1 \text{ \AA}$  ( $G = 2 \times 10^{-4}$ ) up to  $z = 0$  ( $G = 0.04$ ) where an abrupt increase of  $G$  by more than a factor 10 ( $G = 0.7$ ) reveals the transition between the tunneling and the contact regime (indicated by a dashed line). As we show below, the sudden change in  $G$  is exclusively driven by a spin switch of nickelocene. Notice that the value of the contact jump presents some tip dependency and may also vary due to a  $0.2 \text{ \AA}$  error in the contact location.

The existence of a conductance jump hints to a change in the transport properties of nickelocene between the tunneling and contact regimes. To elucidate this change, we measured the  $dI/dV$  spectra by varying  $z$ . In the tunneling regime [Fig. 4.5(c)], the  $dI/dV$  spectra bear

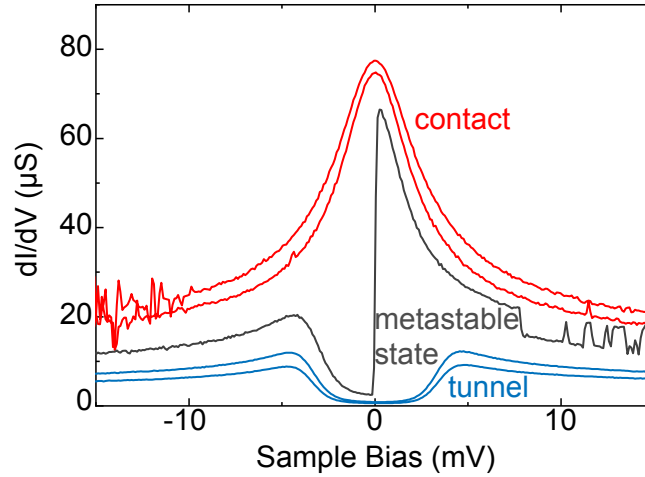


Figure 4.6: **Telegraphic spectra.**  $dI/dV$  spectra when the Nc-tip is in the tunneling regime (blue) and in the contact regime (red). The spectrum in black was acquired near  $z = 0$  and shows an abrupt change at zero-bias between the two spectroscopic signatures (Kondo peak versus inelastic spin excitation).

the typical signature of the spin excitation spectrum that was presented in § 4.1.2. The most striking result is found once the molecular contact to the surface is established ( $z > 0$ ). A sharp peak appears in the  $dI/dV$  at zero bias [Fig. 4.5(d)], while the inelastic excitation thresholds are lost. The transition between the two spectroscopic signature takes place within a  $0.2 \text{ \AA}$   $z$ -range. Within this range, the junction fluctuates between the two regimes and the  $dI/dV$  changes from one spectroscopic signature to the other causing a telegraphic noise [Fig. 4.6].

### 4.3.2 Discussion

**Tunnel regime.** As anticipated above, the  $dI/dV$  spectra in the tunnel regime corresponds to typical spin excitation spectra of nickelocene. The inelastic thresholds remain constant with  $z$ , indicating that the magnetic anisotropy  $D$  is constant with the distance. An enhancement of the differential conductance at voltages corresponding to the excitation threshold is however observed, which is increasingly pronounced as the contact point is approached ( $z > -0.5 \text{ \AA}$ ). This enhancement can be attributed to electron scattering (§ 3.3), or to a modification of the spin state populations due to spin pumping [41,53,104,105]. In the latter case, the lifetime of the excited state of nickelocene becomes comparable to the time between two inelastic collisions with



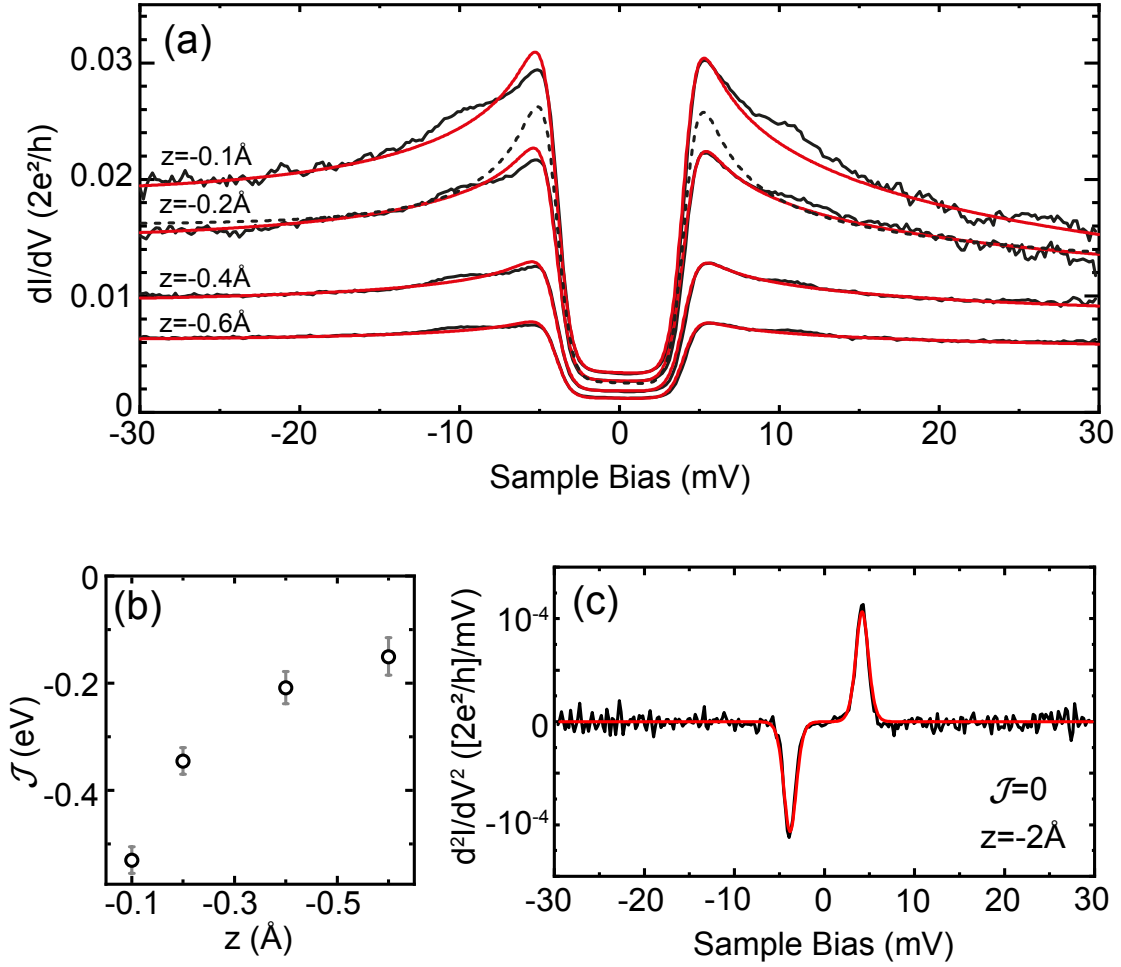


Figure 4.7: **Simulated spin excitation spectra versus tip-sample distance.** (a)  $dI/dV$  spectra at various  $z$  (indicated on the figure), along with their simulation based on a dynamical scattering model where we take into account only electron scattering [41] (solid red lines). The dashed line is a simulation also accounting for the finite lifetime of nickelocene, *i.e.* spin pumping. (b) Kondo scattering parameters  $\mathcal{J}$  extracted from the simulations in panel (a). (c)  $d^2I/dV^2$  spectrum for the tip at 2  $\text{\AA}$  from the contact point with a fit with  $\mathcal{J} = 0$ .

the incoming tunnel electrons, which may be expected in view of the increasingly large currents when approaching contact. To discern between the two contributions, we carried out a line shape analysis using the fitting program presented in § 3.3.3. A first set of simulations consisted in using only electron scattering to simulate the spectra. The agreement with the experimental spectra is already very satisfying as shown in Fig. 4.7(a). The Kondo scattering parameter  $\mathcal{J}$

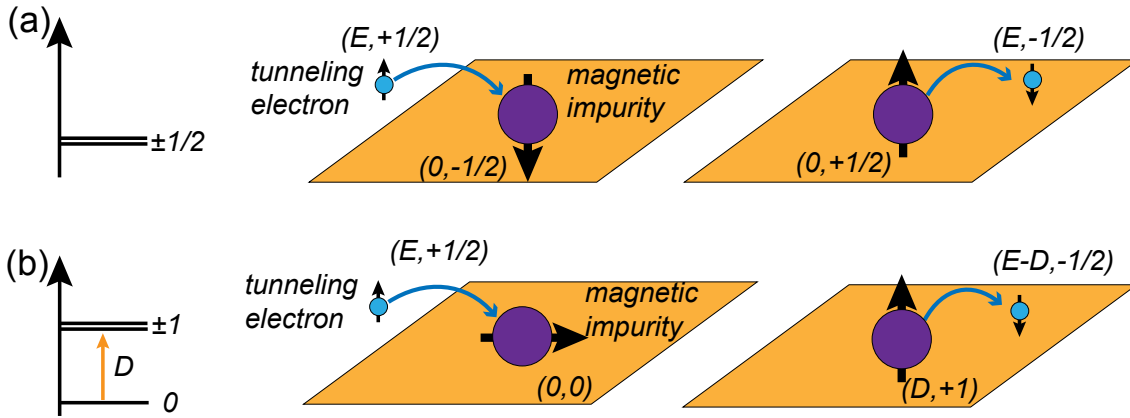


Figure 4.8: **Spin-flip scattering by an impurity.** Schematic view of a spin-flip scattering event for the (a) Kondo effect of a  $S = 1/2$  impurity, and, for (b) a spin excitation at a  $S = 1$  impurity with magnetic anisotropy  $D > 0$ .

increases when then tip-sample distance decreases [Fig. 4.7(b)] whereas the scattering potential  $\mathcal{U}$  remains constant at  $0.02 \pm 0.01$  eV. A second set of spectra was simulated by accounting for both electron scattering and spin pumping [41]. A typical simulation is presented as a dashed line in Fig. 4.7(a), where it can be seen that the cusps become more sharp compared to the experimental spectra. The enhancement of the cusps is then assigned to an increased hybridization of nickelocene with the surface as tip-sample distance is reduced. For  $z < -1$  Å we can consider that the Nc-tip is decoupled from the surface. The spin excitation spectrum of nickelocene is then practically cusp-less and the line-shape is mostly affected by the broadening due to the temperature of the junction. The width of the threshold step is  $\Delta E = 1.7$  meV as shown in Fig. 4.7(c), which then may be used as  $\tau \geq \hbar/(2\Delta E) = 200$  fs for a low estimate of the excitation lifetime of the spin excitation.

**Contact regime.** We assign the sharp zero-bias peak in the  $dI/dV$  spectra to a Kondo resonance. It is important to recall that the Kondo effect arises due to elastic spin-flip processes involving a localized spin carried by an impurity, here nickelocene, and the electronic spins of the host metal. This scattering leads to a many-body spin singlet below a characteristic temperature, the Kondo temperature ( $T_K$ ) [173]. The Kondo effect requires that the impurity ground state must be degenerate, with a difference of spin momentum between the two spin states of  $\delta M \pm 1$ . In the most simple situation, a Kondo effect can occur for an impurity with spin  $S = 1/2$  [Fig. 4.8(a)]. Higher spins show generally a more complex picture as they may

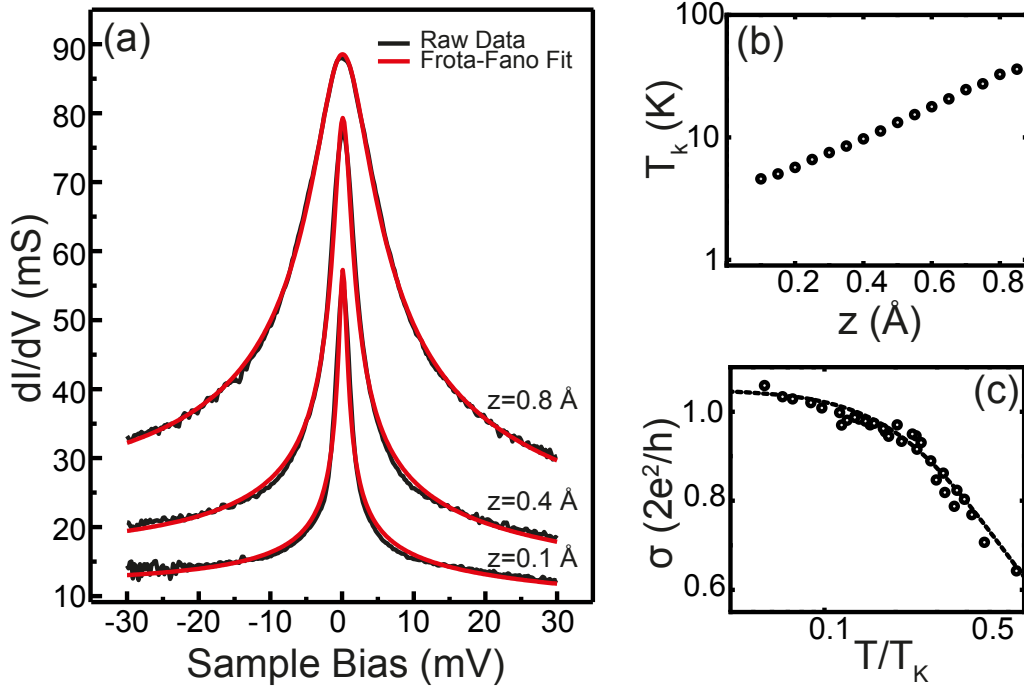


Figure 4.9: **Spin-1/2 Kondo effect.** (a)  $dI/dV$  spectra for different tip excursions beyond the contact point with corresponding Frota fit (dashed lines). (b) Evolution of the Kondo temperature versus the tip excursion  $z$ . (c) Universal curve of the Kondo peak amplitude vs the  $T/T_K$  ratio. The solid line is the calculated universal curve for a spin 1/2.

present magnetic anisotropy and the Kondo effect [23], the outcome of their interplay depending on the object's spin [41, 106, 107, 174] and on the relative weight of  $k_B T_K$  versus  $D$  [175, 176]. Interestingly, however, systems with an integer spin and possessing uniaxial magnetic anisotropy ( $D > 0$ ) cannot host a Kondo effect at the Fermi level as the ground state is not degenerate in spin momentum and therefore requires energy to flip the spin of a conduction electron of the host metal. This is shown in Fig. 4.8(b) for the particular case of a  $S = 1$  impurity with uniaxial magnetic anisotropy  $D > 0$ , which corresponds to nickelocene. The detection of a Kondo peak at contact hints therefore to a sudden change in the value of the spin for nickelocene. A careful analysis of the Kondo line shape actually points to nickelocene becoming a spin 1/2-system. First, the experimental peak is perfectly fitted by a Frota function [Fig. 4.9(a)], which is close to the exact line shape expected for a spin-1/2 Kondo system [21, 82]. From the fit, we find that the peak is centered at  $\epsilon_K = (0.0 \pm 0.1)$  meV for different used tips and up to the

highest tip excursion explored (0.8 Å). The line width, which is directly linked to the Kondo temperature  $T_K$  (§ 1.2), increases nearly exponentially with  $z$  [Fig. 4.9(c)]. This increased value of  $T_K$  reflects changes in the hybridization of nickelocene with Cu(100) as observed in metallic junctions comprising a single Kondo impurity [80, 81, 177]. Second, to further confirm the spin-1/2 nature of the Kondo effect, we recall that the resonance amplitude (noted  $\sigma$ ) should be a universal function of the normalized temperature  $T/T_K$ . For a quantitative analysis we therefore fit the curve in Fig. 4.9(c) to this universal function  $\sigma = [1 + (T/T_K)^2(2^{1/s} - 1)]^{-s}$  (in units of  $2e^2/h$ ) [178] and extract  $s = (0.29 \pm 0.02)$ , in remarkable agreement with the spin-1/2 Kondo effect of semiconductor quantum dots [179]. The amplitude of the resonance is close to the unitary limit and indicates a complete Kondo screening.

Our findings therefore strongly support the existence of a spin-1/2 Kondo effect in the contact regime. In other words, nickelocene changes (reversibly) its spin from 1 to 1/2 upon contact with the surface. Interestingly, several studies have pointed out that such a spin switching should set in via a progressive reduction of the magnetic anisotropy energy and a concomitant increase of the Kondo scattering (§ 1.3.5) [74, 77]. The abrupt transition we observe, instead, supports the idea that this reduction occurs suddenly following a rearrangement of the junction geometry upon contact formation. Hereafter, we confirm these conclusion through DFT calculations.

### 4.3.3 Evidence for spin switching: DFT calculations

The DFT calculations were performed by modeling the molecular tip by a Nc atop a Cu atom adsorbed on a Cu(100) plane [Fig. 4.10(a)]. The molecular tip was placed at different distances from a Cu(100) surface and the junction was fully relaxed for each distances. Figures 4.10(c)-(e) show the resulting molecular junctions for the three most representative configurations. In Fig. 4.10(c), the distance between the two Cu atomic planes (noted  $d$ ) is 12.17 Å which corresponds to the tunneling regime. Figures 4.10(d) shows the molecular junction at  $d = 11.14$  Å which corresponds to the transition between the tunneling and contact regimes. The transition point has been assigned to the point at which a change in structural parameters is observed, which also coincides with a slope change of the transmission probability [see Fig. 4.10(f)]. The molecule is distorted at the transition, but still bonded to the Cu adatom through two C atoms. Finally, Fig. 4.10(e) corresponds to  $d = 9.66$  Å and is representative of the molecular junction in the contact regime. The molecule exhibits Cp rings that are almost parallel to both metallic

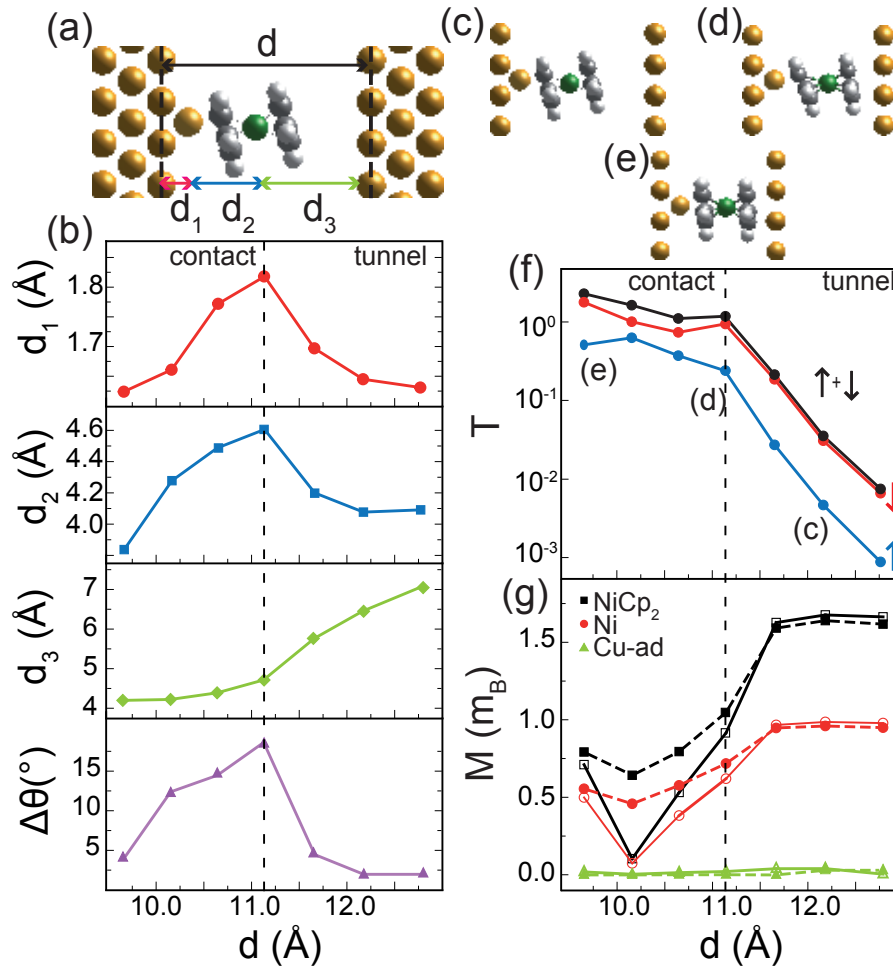


Figure 4.10: **DFT-computed single-nickelocene junction.** (a) Structure of the calculated molecular junction, including the main relevant distance parameters. (b) The panels show how the structural parameters  $d_1$ ,  $d_2$ ,  $d_3$ ,  $\Delta\Theta$  change as a function of  $d$ . The structure of the molecular junction is given for: (c) the tunneling regime ( $d=12.17$  Å), (d) the transition between the tunneling and the contact regimes ( $d=11.14$  Å), and (e) the contact regime ( $d=9.66$  Å). (f) Total transmission (black line) and the transmission per spin channel (red and blue lines) at the Fermi level for the explored configurations. (g) Magnetization of: Nc (black), Ni (red), Cu atom (green) as a function of  $d$ . Full symbols correspond to SIESTA (Mulliken) results and open symbols to VASP (Bader) results.

planes and the Cu atom is coordinated to five C atoms. Figure 4.10(b) quantifies the structural changes with  $d$ . As shown, at the transition point the distances between the Cu and Ni atom with respect to the tip electrode, noted  $d_1$  and  $d_1 + d_2$  respectively, is maximum, as well as the

tilt difference between the Cp rings, noted  $\Delta\Theta$ . The distance between the Ni atom and the surface-electrode (noted  $d_3$ ) instead decreases continuously with  $d$ . Experimentally, we have observed that in the tunneling regime, despite the slightly different initial orientations that the molecule might have on the tip, similar results are obtained in the  $dI/dV$  spectra for different molecular tips when going to contact. This indicates that the Nc molecule tends to adopt always the same configuration, with parallel Cp rings, when contacted between the tip and the surface.

Figure 4.10(g) presents how the total magnetization of the Nc molecule changes with  $d$ . In the tunneling regime, the calculated magnetic moment for Nc is  $1.7 \mu_B$ , the Ni atom carrying  $1 \mu_B$ . At the transition, these values decrease to  $1 \mu_B$  and  $0.7 \mu_B$ , respectively, and upon contact, stabilize around  $0.75 \mu_B$  and  $0.5 \mu_B$ . The Cu atom remains non-magnetic during the contact process. The initial magnetic moment of the molecule is halved when contacted between the two electrodes, meaning that the molecular spin changes from  $S = 1$  to  $S = 1/2$ . The calculations are in agreement with the spectroscopic fingerprints highlighted experimentally. This reduction in the magnetic moment is neither driven by the molecule-substrate charge transfer nor by the deformation suffered by the molecule. The molecular charge remains in fact comparable for the tunneling ( $-0.12e^-$  relative to free Nc) and the contact ( $+0.07e^-$  relative to free Nc) regimes. To discard the contribution of the charge transfer in the change of the magnetic moment, we calculated this magnetic moment for geometries of the nickelocene presented in Figs. 4.10(c)-(e) but removing the copper electrodes. No relevant difference was observed.

To explain the reduced magnetic moment, we present in Fig.4.11(a) the spin-resolved elastic transmission for the tunnel (thick line) and contact (thin line) regimes. The density of states projected (PDOS) onto the C(2p) and Ni(3d) atomic orbitals are shown in Fig.4.11(b). The transmission indicates that the transport is mainly due to the hybridization of surface electronic states with the frontier molecular orbitals, *i.e.* the  $d_{xz}$ - and  $d_{yz}$ - molecular orbitals (§ 3.2.2). The clear correspondence between spin up and spin down peaks in the transmission function (spin-up  $T_\uparrow$ , spin-down  $T_\downarrow$ ) and the PDOS makes it possible to assign both peaks to the spin-polarized degenerate frontier orbitals. The spin polarization of the molecular junction, which is defined as  $P = (T_\uparrow - T_\downarrow)/(T_\uparrow + T_\downarrow)$ , varies from  $-74\%$  in the tunneling regime to  $-55\%$  in the contact regime. The weaker spin polarization in the contact regime results from a shift of the spin up and spin down peaks towards the Fermi level, and from the concomitant reduction of their energy separation, *i.e.* their exchange splitting energy  $U_d$ . A more pronounced broadening ( $\Delta$ ) of the electronic structure is also observed in the PDOS. A careful analysis shows that

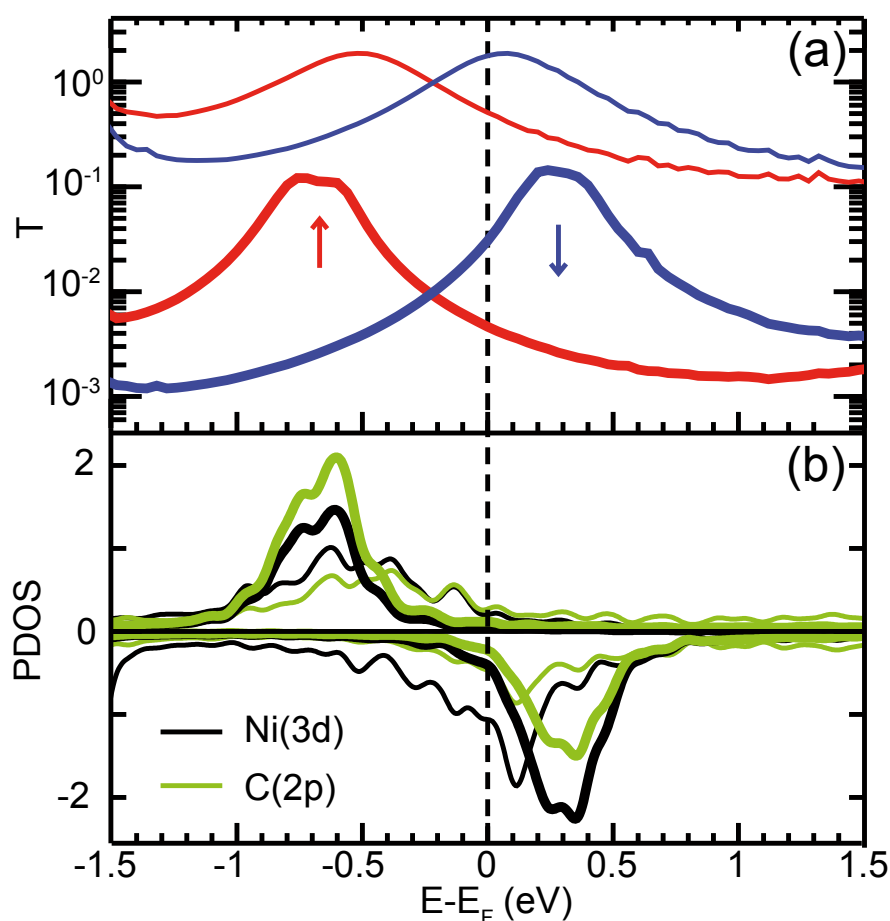


Figure 4.11: **Electronic structure in tunnel and contact regimes.** (a) Spin-resolved elastic transmission as a function of electron energy with respect to the Fermi energy for the Nc-tip above Cu(100). The thick line corresponds to the tunneling configuration [Fig. 4.10(c)] and the thin line to the contact configuration [Fig. 4.10(e)]. (b) Density of states projected (PDOS) onto the C(2p) and Ni(3d) atomic orbitals for the tunneling (thick line) and for the contact (thin line) regimes.

both the increase of  $\Delta$  and the reduction of  $U_d$  contribute to reduce the magnetic moment of the molecule in the contact regime. Recalling § 3.3.3, this means also that a stronger Kondo scattering  $\mathcal{J}$  is then favored [Eq. (3.15)].

## 4.4 Conclusion

In this chapter, we have seen that the magnetic properties of nickelocene, *i.e.* its spin  $S = 1$  and uniaxial magnetic anisotropy, are preserved upon adsorption on the STM tip. The portability of these properties offers to produce a spin excitation, hence to perform spin excitation spectroscopy, above a desired location of the surface. We have shown that when the Nc-tip is positioned above a nickelocene on the surface, we can trigger a double spin excitation, which increases dramatically the weight of the inelastic channel compared to the elastic one in a ratio close to 50. This double spin excitation does not involve any magnetic coupling among the two nickelocene molecules. We also studied the evolution of these properties when the Nc-tip is approached towards a metal surface. Through a line shape analysis of our conductance data, we evidenced a growth of the hybridization of nickelocene with the surface and a sudden switch in its spin when the contact point is reached. We have demonstrated that this spin switch is due to the conformation adopted by nickelocene upon contact with the surface, which tends to increase the spin down frontier molecular orbitals thereby halving the magnetic moment of the molecule. In the next chapter, we will study the magnetic coupling of a Nc-tip to various surface objects.



## CHAPTER 5

# Spin-spin coupling with a nickelocene tip

We have shown in Chapter 4 that when nickelocene is adsorbed on the tip, it is possible to perform spin excitation spectroscopy. In this chapter, we will show that when the Nc-tip magnetically couples to its local environment, the spin states of nickelocene undergo a perturbation. The spin excitation spectrum of nickelocene can be used to monitor these changes, hence to map on-surface magnetism. We will focus on model magnetic systems, *i.e.* a single adatom and a ferromagnetic surface. We start by investigating a single Fe atom on Cu(100) (§ 5.1), and show how magnetic information related to the atom may be extracted from the spin excitation spectrum of nickelocene. We then extend work to cobalt nanoislands grown on Cu(111) (§ 5.2). We will see that the Nc-tip is able to magnetically resolve the cobalt atoms of the nanoisland through a purely magnetic contrast linked to the exchange coupling between each single atom and the Nc-tip. We will also see that we can associate a spin asymmetry to each atom depending on their location in the island. We end the chapter by a brief summary (§ 5.3). The DFT calculations presented in this chapter were carried out within a collaboration with the group of M.-L. Bocquet (ENS Paris) and N. Lorente (CFM, Donostia-San Sebastián), while the dynamical scattering analysis was done with the help of M. Ternes (RWTH Aachen University and Peter Grünberg Institut, Jülich). The results are still under review at the moment when this thesis is written [43].

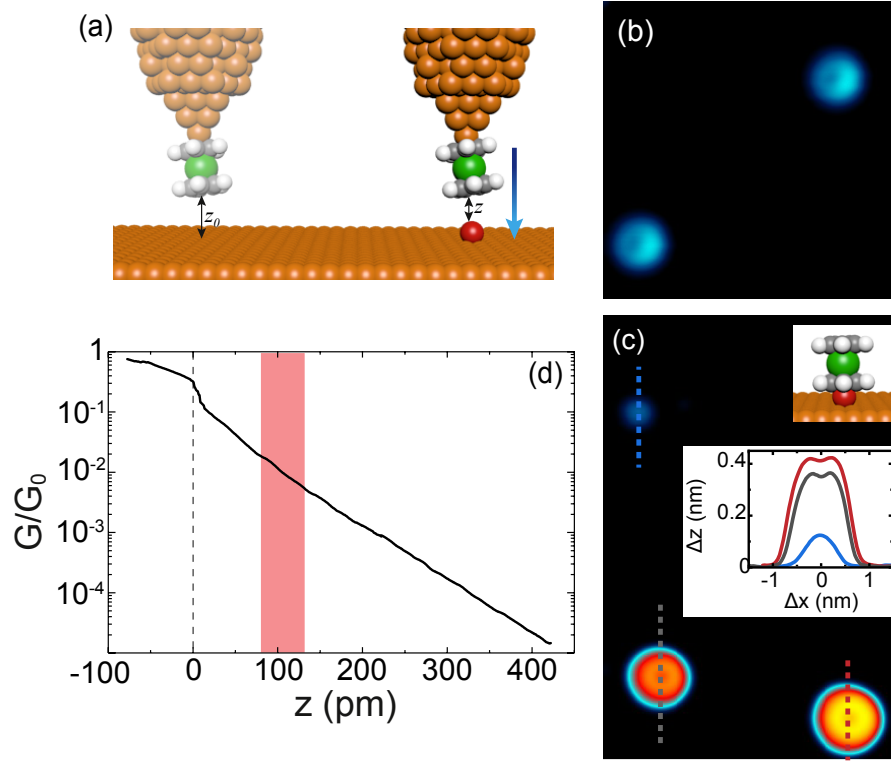


Figure 5.1: **Tip-adatom distance.** (a) Sketch showing the Nc-tip above the bare Cu(100) surface and the Fe adatom ( $z_0$ : tip-surface distance,  $z$ : tip-adatom distance). (b) Counter image acquired above Fe atoms on Cu(100) ( $V = -15$  mV,  $I = 30$  pA, size:  $5 \times 5$  nm<sup>2</sup>). (c) Image showing a Fe atom, a nickelocene and a Fe-nickelocene on Cu(100) that was acquired with a metallic tip ( $V = -15$  mV,  $I = 30$  pA, size:  $6 \times 9$  nm<sup>2</sup>). The corresponding line profiles are shown in the lower inset (Fe: blue, Nc: dark grey, Fe-Nc: red). In the upper inset, the geometry of the Fe-nickelocene complex is represented. (d)  $G$ -versus- $z$  curve. Feedback loop opened  $I = 1$  nA,  $V = -15$  mV. The sharp jump of § 4.3.1 is lost as we use a higher bias for recording the curve ( $-15$  mV instead of  $-2$  mV). The pink-colored rectangle indicates the  $z$ -range where we acquired the spin excitation spectra.

## 5.1 Magnetically probing a Fe adatom

### 5.1.1 Spin excitation spectra above a Fe atom

This section presents the results obtained with the Nc-tip positioned above an Fe adatom on Cu(100). The experiment consisted in carefully monitoring how the spin excitation spectrum of the Nc-tip varies when the tip-adatom distance is decreased. Figure 5.1(a) sketches the geometry of the tunnel junction, while Fig. 5.1(b) presents a typical counter image acquired above the Fe adatoms (§ 4.1.1). To start, we need to experimentally determine the tip-adatom distance. Unfortunately, this cannot be done by directly contacting a Fe adatom with the Nc-tip. Nickelocene in fact jumps into contact with the atom, irreversibly damaging the Nc-tip. Based on the image and line profiles acquired after such a jump [Fig. 5.1(c)], the Nc molecule sits on top of the Fe atom, identifying the new complex as a Fe-nickelocene molecule [See upper inset Fig. 5.1(c)]. A similar complex was also observed for another metallocene in earlier work [119]. To circumvent this problem, we first determine the distance between the tip and the bare Cu(100) surface through a  $G$ -versus- $z$  curve [Fig. 5.1(d)] as in § 4.3.1. We note the tip-surface distance by  $z_0$  as sketched in Fig. 5.1(a). The tip-atom distance  $z$  [Fig. 5.1(a)] is then determined by: i) moving the tip laterally above the adatom while keeping a constant height relative to the surface, ii) subtracting the apparent height  $h = 110$  pm of the Fe adatom so that finally  $z = z_0 - h$ . The  $dI/dV$  spectra presented hereafter were acquired between 140 pm and 80 pm [pink box in Fig. 5.1(d)]. This  $z$ -range was quite typical for the tips used. Below 80 pm, nickelocene jumps into contact with the Fe atom as stated above.

Figure 5.2(a) presents a set of  $dI/dV$  spectra acquired at various tip-adatom distances ranging from 133 pm to 80 pm. A sketch of the junction is presented in the inset of Fig. 5.2(a). As shown, the steps, which are positioned at a bias of  $eV = \pm D$ , progressively split apart as the tip-adatom distance is reduced. Figure 5.2(b) shows the  $d^2I/dV^2$  spectra, where in this case the peak (dip) at positive (negative) bias splits apart. Interestingly, the spectra without a splitting do not exhibit a signature proper to Fe, these spectra being identical to the ones recorded above the bare surface. The Fe adatom may therefore be regarded as “spectroscopically dark”. The peak and dip positions are presented as a function of the tip-adatom distance in Fig. 5.2(c), where it can be seen that the magnetic anisotropy  $D = 3.5$  meV, which corresponds to the average position of the spin-split peaks and dips, varies at most by 0.2 meV with distance. So far we tested several Nc-tips with tilt angles ranging from  $5^\circ$  to  $15^\circ$ , and all showed similar behavior

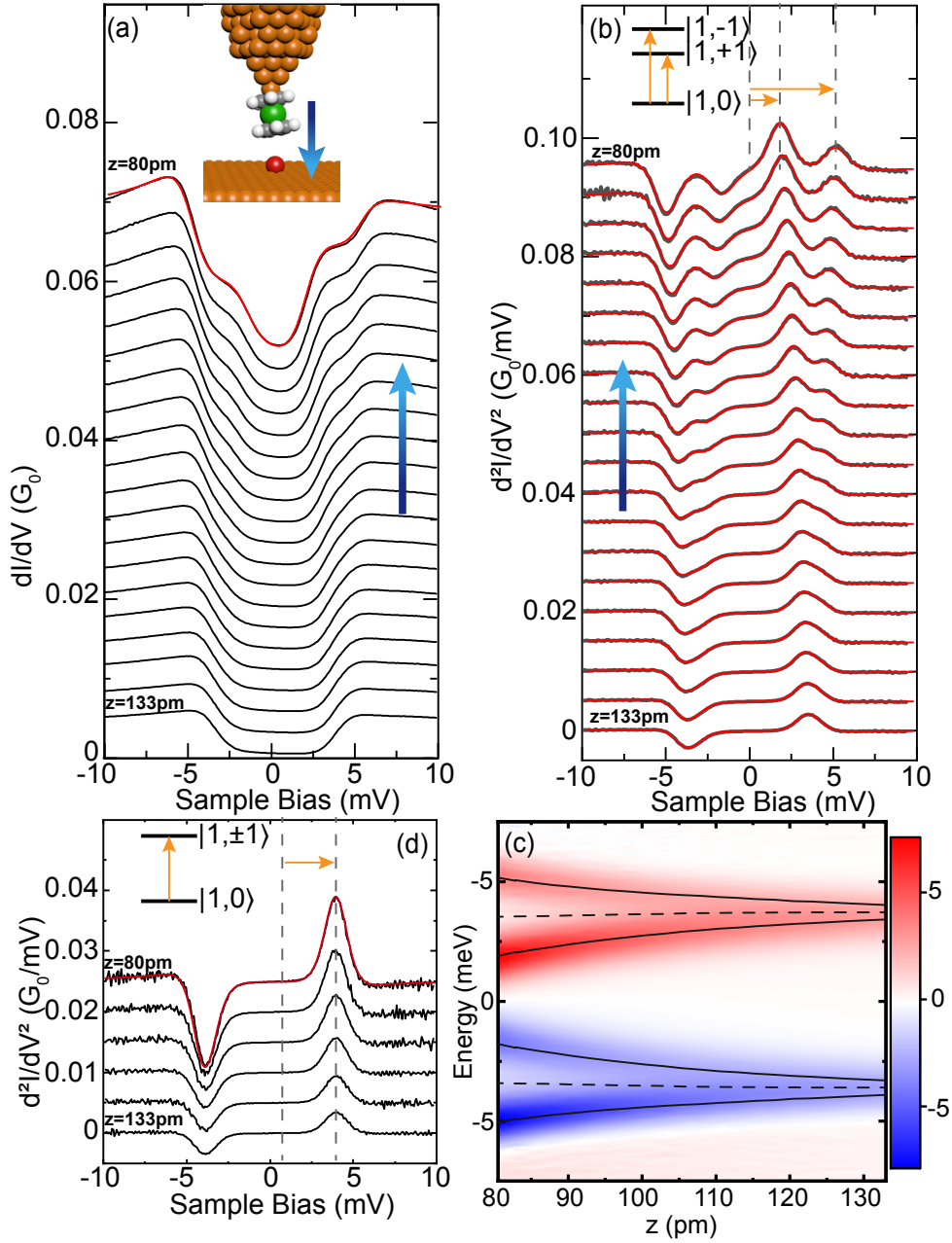


Figure 5.2: **Spin excitation spectra above the Fe adatom.** (a)  $dI/dV$  and (b)  $d^2I/dV^2$  spectra acquired with the Nc-tip above a Fe adatom, between  $z = 133$  pm and  $z = 80$  pm. The spectra are vertically shifted for clarity. Inset of panel (a): Sketch of the junction. (c) Energy positions of the peaks and dips as a function of the tip-surface distance. The color scale flanking the panel corresponds to the  $d^2I/dV^2$  amplitudes and is given in units of  $G_0/V$  ( $G_0 = 2e^2/h$ : quantum of conductance). (d)  $d^2I/dV^2$  spectra acquired with the Nc-tip above the bare surface between  $z = 133$  pm and  $z = 80$  pm. The solid red lines in panels (a), (b), and (d) are simulations carried out with a dynamical scattering model (§ 3.3.3). In panel (a) and (b), the simulations also include a magnetic field (see § 5.1.2).

—the distances for a given splitting changing only by  $\pm 10$  pm. Apart from the splitting, we also observe a striking bias asymmetry of the peaks and dips. While the amplitudes of the positive peak and negative dip are identical for the Nc-tip probed above the bare surface, here we find that at positive bias the energetically lower excitation has a higher peak amplitude than the energetically higher excitation, while at negative bias the dips show the opposite behavior compared to the peaks. A single peak (dip) is instead observed in the same  $z$ -range when the Nc-tip is positioned above the bare non-magnetic surface [Fig. 5.2(d)], pointing to the magnetic origin for the splitting.

### 5.1.2 Exchange field between Fe and nickelocene

The splitting and asymmetry of the line shape observed above Fe have a magnetic origin. To model our observations, we use the following spin Hamiltonian:

$$\hat{H} = D_{\text{Nc}} \hat{S}_{z,\text{Nc}}^2 + D_{\text{Fe}} \hat{S}_{z,\text{Fe}}^2 + \hat{\mathbf{S}}_{\text{Nc}} \cdot \mathbf{J} \cdot \hat{\mathbf{S}}_{\text{Fe}}, \quad (5.1)$$

where  $D_{\text{Nc}}$  is the magnetic anisotropy of Nc,  $D_{\text{Fe}}$  the magnetic anisotropy of Fe and  $\mathbf{J}$  the exchange coupling tensor between Nc and Fe. We define the  $z$ -axis along the molecular axis and neglect the tilt angle of Nc on the tip apex. Based on our DFT calculations, Fe on Cu(100) has a magnetic moment of  $3.4\mu_{\text{B}}$ , thus giving Fe an effective spin  $S \approx 3/2$ . An uniaxial magnetic anisotropy  $D_{\text{Fe}}$  can be expected for Fe given the  $C_{4v}$  symmetry of its adsorption site. This is validated by our observations, as the absence of magnetic anisotropy for Fe would result in a degenerated ground state for the spin system and additional spin excitations would be possible [Fig. 5.3(a)]. We would then observe a splitting into four peaks/dips when approaching the Fe-atom with the Nc-tip. This in turn means that the absolute value of the magnetic anisotropy  $D_{\text{Fe}}$  must be larger than  $k_{\text{B}}T$  (0.2 meV at our working temperature of 2.4 K) so that always only one degenerated doublet is significantly occupied, *i.e.*  $|D_{\text{Fe}}| > 0.2$  meV. A weak magnetic anisotropy of  $\approx 0.5$  meV was found for Fe on Cu(111) [62].

In Fig. 5.3(b), we present simulations based on a dynamical scattering model [41] using three different types of couplings: a isotropic Heisenberg coupling (noted  $J$ ), an Ising coupling along  $z$  (noted  $J_z$ ), and an Ising coupling along  $x$  (noted  $J_x$ ). The simulations show that the Heisenberg interaction can be ruled out, as it would produce an asymmetric splitting. In other words, the peaks (dips) would split-apart and shift in energy at the same time. The Ising

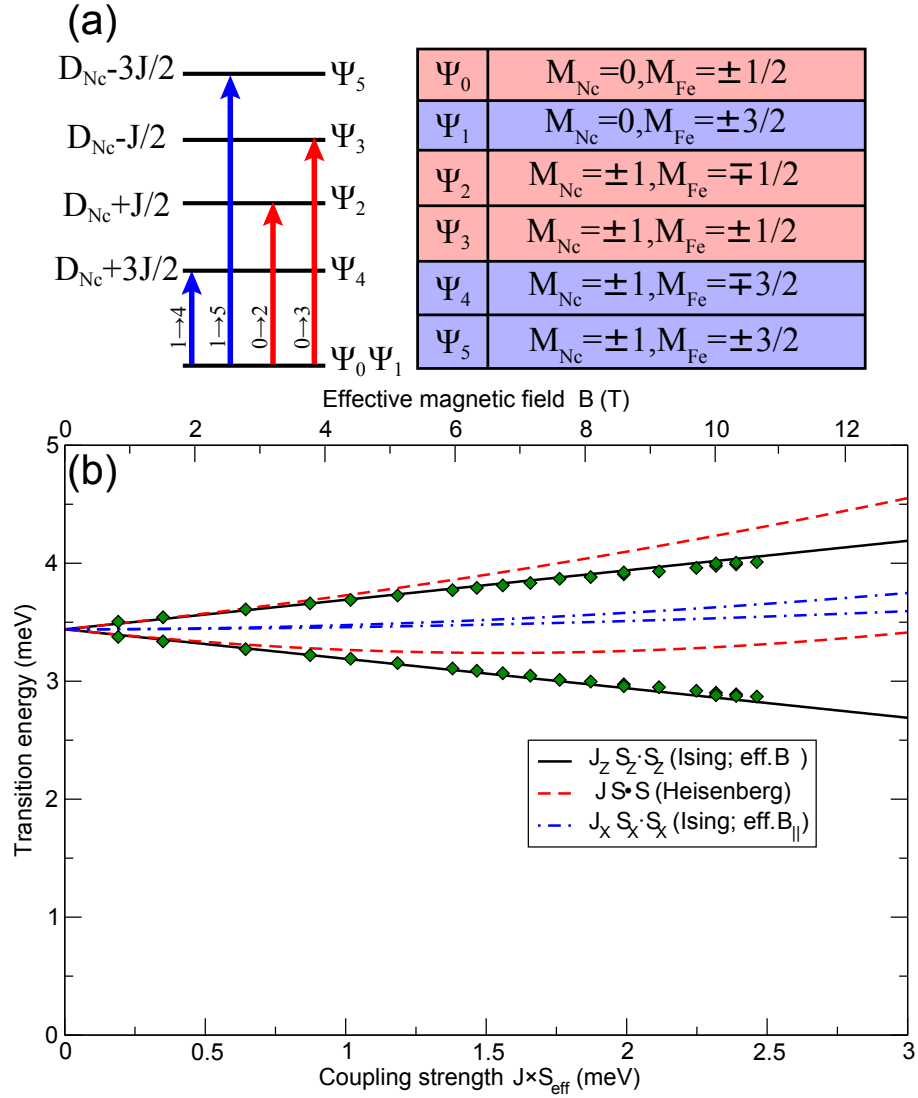


Figure 5.3: **Magnetic coupling.** (a) Spin-state diagram for a nickelocene exchange coupled to the Fe atom when  $D_{\text{Fe}} = 0$ . The eigenfunctions of the system,  $|\psi_i\rangle$  ( $i = 0, 1, 2, 3, 4, 5$ ), are a linear combination of  $|S_{\text{Nc}}, M_{\text{Nc}}; S_{\text{Fe}}, M_{\text{Fe}}\rangle$ . We take  $S_{\text{Nc}} = 1$  and  $S_{\text{Fe}} = 3/2$ . (b) Simulated peak (dip) splitting for an Ising- and Heisenberg-like coupling between the spins of nickelocene and of the Fe atom. Solid line: Ising model along the  $z$ -axis. Dashed red line: Heisenberg model. Dashed blue line: Ising model along the  $x$ -axis. The experimental data is represented as green dots.

interaction along  $z$  gives instead a splitting that is symmetric relative to  $D_{\text{Nc}}$ , in agreement with experimental observations [Fig. 5.2(c)]. The Ising interaction along  $x$  gives a negligibly small splitting that is, moreover, asymmetric. This demonstrates that the exchange interaction is governed by an Ising interaction along  $z$ .

In the following, we therefore simplify the spin Hamiltonian and reformulate the interaction term as  $J_z \hat{S}_{z,\text{Fe}} \hat{S}_{z,\text{Nc}} = g\mu_B B \hat{S}_{z,\text{Nc}}$ . The exchange interaction is replaced by an exchange field  $B$  exerted by Fe on Nc along  $z$

$$\hat{H} = D \hat{S}_z^2 - g\mu_B B \hat{S}_z. \quad (5.2)$$

The magnetic anisotropy and the spin operator for Nc are now simply noted  $D$  and  $\hat{S}_z$ , respectively. The exchange field is defined as  $B = J\langle S_{\text{Fe}} \rangle / g\mu_B$  within mean-field theory, where  $J$  is the Fe-Nc exchange coupling and  $\langle S_{\text{Fe}} \rangle \approx 3/2$  is the effective spin of Fe on the copper surface. We assume that the gyromagnetic factor is  $g = 2$ . Within this framework, the exchange field lifts the degeneracy between the two excited states  $|S = 1, M = +1\rangle$  and  $|S = 1, M = -1\rangle$  of nickelocene and causes the line shape to split apart. The resulting spin-state diagram is presented in Fig. 5.4(a). The average position of the two states yields  $D$  in good agreement with the experimental dashed line in Fig. 5.2(c). As noted above, this average value changes at most by 0.2 meV with distance, which may indicate that the molecular axis and the spin momentum of Fe are not perfectly collinear. This variation could also be explained by invoking changes in  $D$  due to the ligand field (see § 4.1.2).

The line shape is simulated using the dynamical scattering model [41], and includes a magnetic field  $B$  along  $z$  to account for the exchange field, as well as a spin asymmetry  $\eta$  (see § 5.1.3). We neglect the electron scattering (§ 3.3.3) as the Kondo scattering parameter  $\mathcal{J}$  obtained in § 4.3.2 becomes significant only below 50 pm. The simulation is plotted as a dashed line in Fig. 5.4(b). The simulation is very satisfactory, providing quantitative values for  $B$  and  $\eta$ . The field is plotted as a function of  $z$  in Fig. 5.4(c), along with an exponential fit (solid red line). The exponential dependency on  $z$  confirms that the Fe-Nc coupling is governed by an exchange interaction in this  $z$ -range. Using our DFT-computed effective spin for Fe, we estimate the experimental exchange coupling to be  $|J| \approx 0.9$  meV at  $z = 80$  pm.

It has been shown that the sign of the exchange interaction between a magnetic atom and a magnetic tip apex is determined by the competition of direct and indirect interactions and may vary with the tip-atom distance [180]. To gain insight into the exchange coupling between

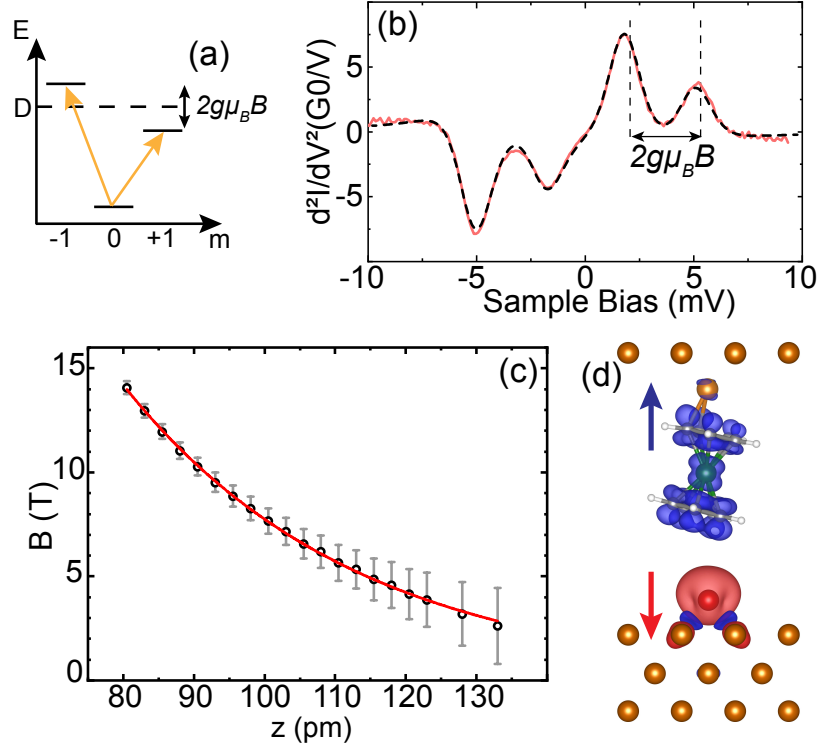


Figure 5.4: **Exchange field.** (a) Spin-state diagram for a nickelocene exchange coupled to the Fe atom. (b)  $d^2I/dV^2$  spectrum recorded at 80 pm. The dashed line is the simulated line shape using the dynamical scattering model that includes a magnetic field along  $z$  [41]. We define  $2g\mu_B B$  as the energy difference between the two peaks (dips). (c) Exchange field extracted from the fit versus the tip-adatom distance. The solid red line is an exponential fit. (d) DFT-calculated configuration of the tunnel junction for a distance of 100 pm with isosurface of the spin density (antiferromagnetic coupling).

the Nc-tip and Fe atom, we computed with DFT the fully relaxed junction geometry at various Nc-Fe distances using VASP (GGA-PBE and DFT-D2 functionals). We then estimated the exchange energy defined as  $E_{\text{ex}} = E_P - E_{AP}$  at these distances;  $E_P$  ( $E_{AP}$ ) is the total energy of the junction with the spin directions of Nc and Fe in a parallel (antiparallel) alignment. We find that the exchange interaction always favors an antiparallel alignment of the two spins [Fig. 5.4(d)], the junction geometry remaining constant up to 50 pm. The energy difference between antiparallel and parallel alignments is 13 meV at 120 pm, while no difference could be evidenced above 300 pm. The antiferromagnetic coupling is short ranged and attributed to the direct hybridization of the Fe  $d$ -orbitals with the frontier molecular orbitals of nickelocene.



### 5.1.3 Spin asymmetry above Fe

The bias asymmetry in the peaks and dips is a consequence of the selection rules governing the spin excitations of nickelocene [4, 104, 105]. Nickelocene acts as a spin filter differentiating spin up and spin down electrons that tunnel inelastically. This phenomenon is qualitatively similar to conventional spin-polarized STM [11] and, more generally, to spin valves [181] or to Kondo systems coupled to magnetic electrodes [20, 78, 79, 182].

This spin filtering mechanism is sketched in Figs. 5.5(a) and 5.5(b). Following the above DFT calculations, we consider an antiferromagnetic coupling between Nc and Fe ( $J < 0$ ). As illustrated in Fig. 5.5(a), the excitation of Nc from the ground state  $|S = 1, M = 0\rangle$  to its first excited state  $|S = 1, M = +1\rangle$ , requires a change in spin angular momentum of  $\delta M = +1$ . Since the total angular momentum has to be conserved it can only be induced by electrons that compensate for this moment by flipping their spin direction during the tunneling process from  $|\uparrow\rangle$  to  $|\downarrow\rangle$ . At negative bias, the tunneling process may be viewed as a  $|\uparrow\rangle$  electron hopping from the substrate (noted s) into the molecular orbital, while a  $|\downarrow\rangle$  electron is emitted from the molecular orbital towards the tip (noted t). Using second-order perturbation theory, we assign a transmission amplitude  $\mathcal{T}_{s,\uparrow}$  to the first process and  $\mathcal{T}_{t,\downarrow}$  to the second process [Fig. 5.5(c)], so that the transmission from sample to tip ( $s \rightarrow t$ ) is proportional  $\mathcal{T}_{s,\uparrow}\mathcal{T}_{t,\downarrow}$ . At positive bias, the tunneling direction reverts and the transmission from tip to sample ( $t \rightarrow s$ ) is proportional to  $\mathcal{T}_{t,\uparrow}\mathcal{T}_{s,\downarrow}$ . The relative height of the dip at low negative voltage ( $h_-$ ) compared to the peak at low positive voltage ( $h_+$ ) yields a quantitative measure of the spin asymmetry  $\eta = (h_+ - h_-)/(h_+ + h_-)$ , with  $h_- \propto \mathcal{T}_{s,\uparrow}\mathcal{T}_{t,\downarrow}$  and  $h_+ \propto \mathcal{T}_{t,\uparrow}\mathcal{T}_{s,\downarrow}$ . The excitation of Nc from the ground state to its second excited state  $|S = 1, M = -1\rangle$  requires instead electrons starting in a  $|\downarrow\rangle$  state and ending in a  $|\uparrow\rangle$  state [Fig. 5.5(c)], resulting in a spin asymmetry of  $-\eta$ . Due to the mixing of these spin-dependent transmission amplitudes, the spin asymmetry observed differs from the usual spin polarization measured with elastic electrons.

For the data presented in Figs. 5.2(b) and 5.2(c), we find a spin asymmetry of  $\eta = 32\%$  when  $B > 5$  T [Fig. 5.5(d)]. Below 5 T, the precision of the fit is not satisfactory enough to provide a meaningful value. The data collected on an ensemble of different Nc-tips on different Fe atoms yields a lower average value of  $\eta = 23\%$ .

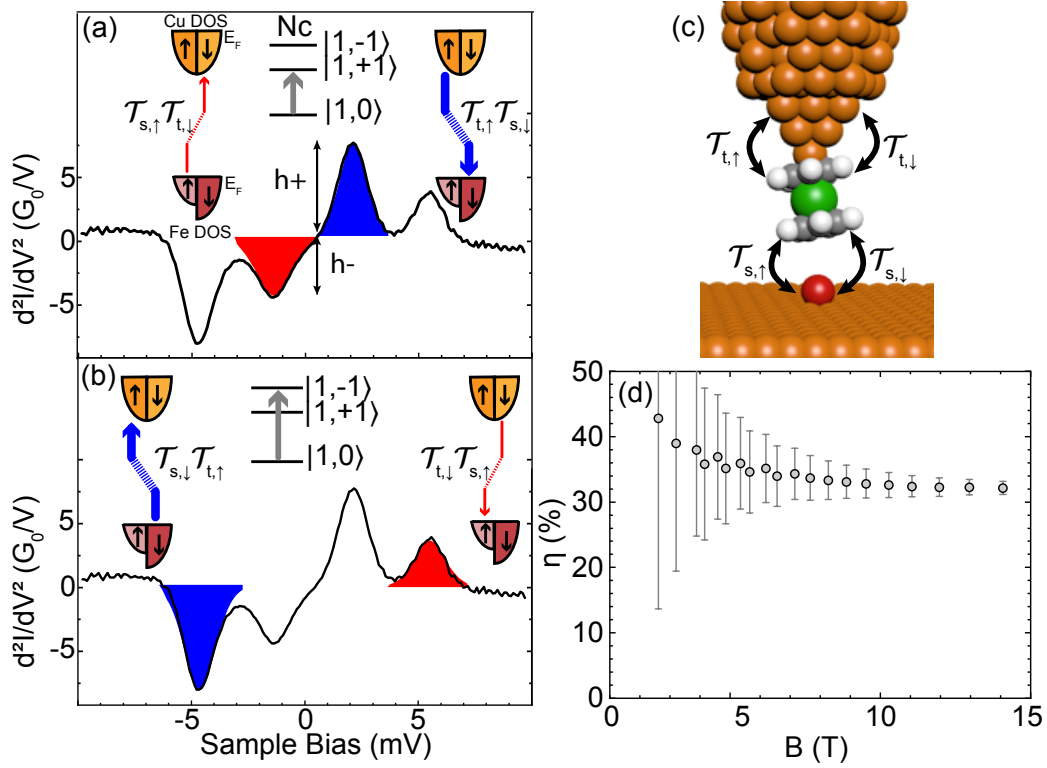


Figure 5.5: **Spin asymmetry.** Panels (a) and (b) sketch the spin filtering mechanism leading to the asymmetry in the  $d^2I/dV^2$  spectra acquired above Fe. (a) At negative bias, inelastic electrons tunnel from the spin-up states of the Fe atom to the spin-down states of the copper tip with transmission proportional to  $\tau_{t,\downarrow}\tau_{s,\uparrow}$ , leading to a dip in the  $d^2I/dV^2$  spectrum. At positive bias, instead, the junction polarity is reversed and inelastic electrons tunnel from the spin-up states of the copper tip to the spin-down states of the Fe atom with transmission proportional to  $\tau_{t,\uparrow}\tau_{s,\downarrow}$ , leading to a peak in the  $d^2I/dV^2$  spectrum. During the tunneling process, the electrons excite Nc from its ground to its first excited state. The weaker amplitude for the dip compared to the peak reflects the difference in the transmission ( $\tau_{t,\uparrow}\tau_{s,\downarrow} \neq \tau_{t,\downarrow}\tau_{s,\uparrow}$ ). DOS: density of states. (b) Same mechanism as (a) but for inelastic tunnel electrons exciting Nc from its ground state to its second excited state. (c) Sketch of the junction with the definition of the transmission terms related to the electron transfer from the Cu-tip DOS to the molecule (see text). (d) Spin-asymmetry  $\eta$  extracted from the spectra of Fig. 5.2(b).

### 5.1.4 Computed electronic structure and spin polarization

To improve our understanding of  $\eta$ , we computed the spin-dependent properties for the electron transport across a tunnel junction comprising a Nc-tip positioned above a single Fe atom on Cu(100). For the transport calculations we used TRANSIESTA, with a double- $\zeta$  plus polarization (DZP) basis set for Nc and a single- $\zeta$  basis set for the copper electrodes. The calculations are performed for a molecule-Fe distance of 350 pm as measured from the Fe atomic-plane to the closest molecular C-plane, which corresponds approximately to a distance of 100 pm from the contact regime, *i.e.* the experimental distance. We consider an AF coupling between Fe and Nc, and choose the spin-down direction to be parallel to the magnetic moment of the Fe atom. Figures 5.6(a) and 5.6(b) present, respectively, the elastic electron transmission and the density of states projected on the atomic orbitals (PDOS) of nickelocene. As may be concluded from the PDOS, the transmission at the Fermi level is dominated by the spin-down transmission originating from the molecular orbital of Nc, *i.e.* the  $d_{xz}$  and  $d_{yz}$  orbitals of Ni and the  $2p$  orbitals of C. The spin-down transmission of the Fe atom is instead carried by the  $4s$  and  $4p$  orbitals based on its PDOS [Figs. 5.6(c)-(e)]. From Fig. 5.6(a), we can estimate the transmission probabilities for the two spin channels (spin-up  $T_{\uparrow}$ , spin-down  $T_{\downarrow}$ ) at the Fermi level. We may then define a spin polarization on the basis of the elastic transmission as

$$P = \frac{T_{\uparrow} - T_{\downarrow}}{T_{\uparrow} + T_{\downarrow}} = -84\%. \quad (5.3)$$

The difficulty now resides in linking the computed spin polarization to the observed spin asymmetry  $\eta$ . To start, we express Eq. (5.3) as

$$P = \frac{\mathcal{T}_{t,\uparrow}\mathcal{T}_{s,\uparrow} - \mathcal{T}_{t,\downarrow}\mathcal{T}_{s,\downarrow}}{\mathcal{T}_{t,\uparrow}\mathcal{T}_{s,\uparrow} + \mathcal{T}_{t,\downarrow}\mathcal{T}_{s,\downarrow}}, \quad (5.4)$$

by remarking that  $T_{\uparrow} = \mathcal{T}_{t,\uparrow}\mathcal{T}_{s,\uparrow}$  and  $T_{\downarrow} = \mathcal{T}_{t,\downarrow}\mathcal{T}_{s,\downarrow}$ . Next, we consider a molecular junction comprising two copper electrodes in contact with a nickelocene. In this geometry, an electron hops from one electrode to the molecular orbital, while one electron is emitted from the molecular orbital to the other electrode with equal probability ( $\mathcal{T}_t = \mathcal{T}_s$ ). For this molecular junction, Eq. (5.4) simplifies to

$$P_0 = \frac{\mathcal{T}_{t,\uparrow}^2 - \mathcal{T}_{t,\downarrow}^2}{\mathcal{T}_{t,\uparrow}^2 + \mathcal{T}_{t,\downarrow}^2}. \quad (5.5)$$

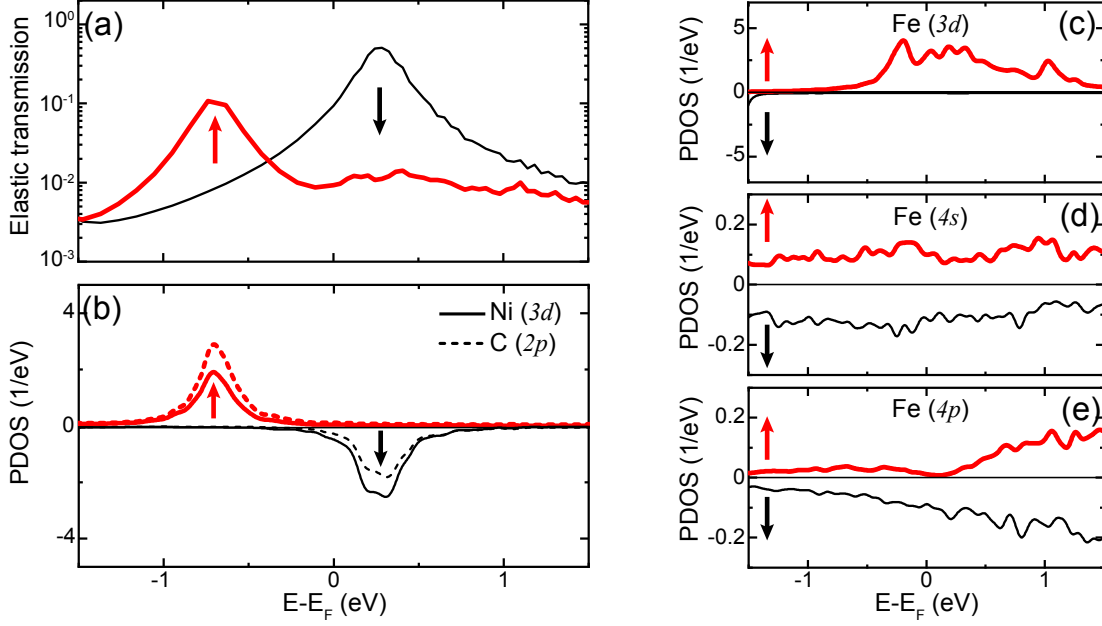


Figure 5.6: **Computed electronic structure for the Fe-Nc junction.** (a) Spin-resolved electron transmission as a function of electron energy with respect to the Fermi energy (majority spin, red; minority spin, black). (b) PDOS on the  $d$ -manifold of Ni (solid line) and on the  $p$ -orbitals of the C atoms (dashed line) of the Nc molecule. The results are shown for majority ( $\uparrow$ ) and minority ( $\downarrow$ ) spins. The transmission curves for each spin coincide with the contributions from the PDOS of Ni and C, showing the molecular character of the transmission close to the Fermi energy. Panels (c), (d) and (e) present the PDOS onto the  $3d$ ,  $4s$  and  $4p$  atomic orbitals of Fe, respectively.

Recalling that  $P_0 = -55\%$  (§ 4.3.3) [42], we then find that  $\mathcal{T}_{t,\uparrow}/\mathcal{T}_{t,\downarrow} = 0.54$ . Finally, if we consider the expression of the spin asymmetry

$$\eta = \frac{\mathcal{T}_{t,\uparrow}\mathcal{T}_{s,\downarrow} - \mathcal{T}_{s,\uparrow}\mathcal{T}_{t,\downarrow}}{\mathcal{T}_{t,\uparrow}\mathcal{T}_{s,\downarrow} + \mathcal{T}_{s,\uparrow}\mathcal{T}_{t,\downarrow}}, \quad (5.6)$$

we have then  $\mathcal{T}_{s,\uparrow}/\mathcal{T}_{s,\downarrow} = 0.34$  for the Fe atom using the experimentally determined value of  $\eta = 23\%$ . Using Eq. (5.4) and the ratios determined for  $\mathcal{T}_{t,\uparrow}/\mathcal{T}_{t,\downarrow}$  and  $\mathcal{T}_{s,\uparrow}/\mathcal{T}_{s,\downarrow}$ , we estimate the spin polarization of the elastic transmission to be  $-69\%$ , which is consistent with the value calculated directly by DFT [Eq. (5.3)]. We therefore have a situation in which the tip and sample transmissions compensate yielding a moderate value for  $\eta$ .

## 5.2 Detecting the surface magnetism of Co islands

### 5.2.1 Adsorption of nickelocene in the presence of Co islands

In this section, we extend the proof-of-concept for the Nc-tip to a magnetic surface by investigating nanoscale cobalt islands grown on Cu(111). The epitaxial growth of cobalt on Cu(111) and the resulting electronic and magnetic properties have been the subject of numerous studies since the early nineties. To grow the islands on Cu(111), we sublimated about 1 monolayer of Co with an *e*-beam evaporator at 0.75 monolayer/min onto the copper surface held at room temperature, transferring the sample immediately after into the STM at 4.4 K. The islands are triangular-like [Fig. 5.7] and grow as bi-layer high structures. They are known to possess a perpendicular magnetic anisotropy [10, 44], leading to an out-of-plane magnetization at liquid-helium temperature. Due to the island growth mode, surfaces of opposite magnetization can be accessed simultaneously with the STM tip, which is of particular interest for spin-polarized STM experiments [Figs. 5.7(a) and 5.7(b)] [44, 59]. The island electronic structure, which determines the spin polarization of the island, is complex. It is carried by majority *sp* and minority *d* states [46], showing dependance on the stacking fault of the island [10], as well as on the island size [45]. The electronic structure varies also spatially within the island. The *d* states, which are mainly carried by the single Co atoms [see Fig. 5.11(a)], are found to be spatially constant, but change at the island edges and corners [44, 45]. The *sp* states, which instead have a dispersive nature, exhibit a standing wave pattern due to their confinement within the island [46]. The spin polarization at the Fermi level therefore varies spatially within the island [Fig. 5.7(c)] [44, 183].

At the cobalt coverages we used, the typical size of the islands is in the nanometer range, making them suitable hosts for magnetic and nonmagnetic adsorbates [57, 59, 184]. After dosing a small amount of nickelocene onto the surface (§ 3.1.1), the molecules are found to preferentially adsorb on cobalt, either on top of the nanoislands or on the bottom edge of the island [Fig. 5.8(a)]. Similar adsorption geometries have been seen for other molecules [59].

Nc-tips were routinely prepared by transferring a molecule from the edge of the island to the Cu-tip apex [Fig. 5.8(b)]. Given the low molecular coverage, large pristine areas of cobalt can be found on the sample. Figure 5.8(c) presents a typical constant-height image acquired when scanning with a Nc-tip above a small area located in the center of a cobalt island [indicated by a white square in Fig. 5.8(a)] at a bias of  $V = -1$  mV, *i.e.* at a bias very close to  $E_F$ . This

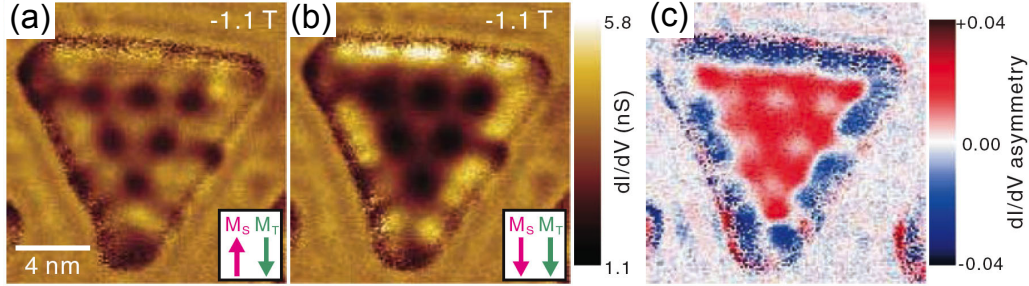


Figure 5.7: **Electronic structure of a cobalt island.** Panels (a) and (b) present spin-polarized images of the spatial dependence of the  $dI/dV$  (+30 mV) recorded in a magnetic field of 1.1 T using a Cr-Co-W tip. In panel (a), the field is antiparallel to the magnetization of the island, in panel (b) it is parallel. The insets represent the antiparallel (AP) and parallel (P) configurations. The feedback loop was opened at 0.5 V and 1.0 nA. (c) Spatial dependence of the spin polarization obtained from the images in (a) and (b) as  $(dI/dV_a - dI/dV_b) / (dI/dV_a + dI/dV_b)$ . Figure adapted from [183].

image reveals a surface structure strictly identical to that obtained by a dragging a copper atom on the island with a metallic STM tip [Fig. 5.8(d)] [39]. In both images, we find a triangular lattice with parameters  $a_1 = (2.55 \pm 0.05) \text{ \AA}$ ,  $a_2 = (2.55 \pm 0.05) \text{ \AA}$  and  $\phi = 60^\circ$ . As we show hereafter, the contrast obtained with the Nc-tip has magnetic origin.

### 5.2.2 Spin excitation spectra above a Co island

Similar to the Fe adatom, we investigated how the spin excitation spectrum of a Nc-tip changes upon reducing the tip-sample distance to the cobalt island. The Nc-tip was positioned above a Co atom of the surface, which could be routinely visualized via an atomically-resolved image of the surface [Fig. 5.8(c)]. The absolute tip-sample distance was determined by performing  $G$ -versus- $z$  curves above copper as in § 5.1.1 or, alternatively, above the cobalt surface, the two curves being nearly identical. The  $z$ -dependence of the spin excitation spectra acquired above a Co atom in the cobalt island is presented in Fig. 5.9(a). At a tip-island distance of  $z = 150 \text{ pm}$ , the spin excitation spectrum is similar to the spectra of Fig. 5.2(a). As for the Fe adatom, we conclude that the island is spectroscopically dark in the bias-range used. Interestingly, upon vertically approaching the Co atom, the peak and dip in the  $d^2I/dV^2$  spectrum progressively split apart. The spectra show weak spin asymmetry ( $\eta < 5\%$ ) (see § 5.2.4).

Taking the spin Hamiltonian of Eq. 5.2, we explain the evolution of the line shape by the

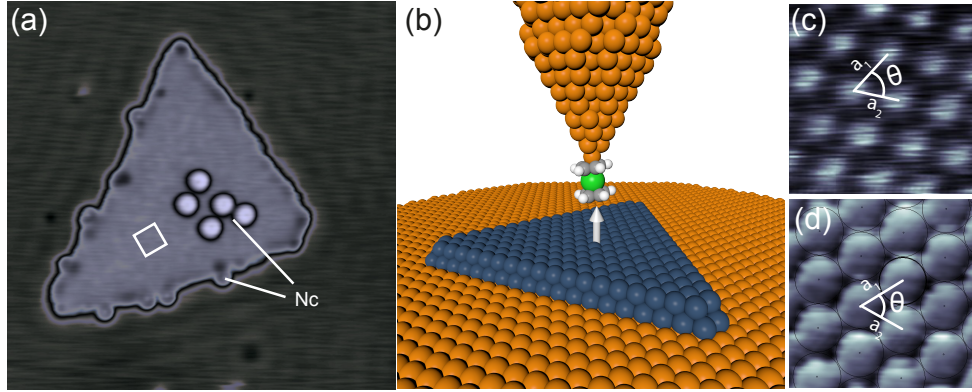


Figure 5.8: **Nickelocene adsorption on cobalt.** (a) Cobalt island on Cu(111) decorated with Nc molecules ( $V = -50$  mV,  $I = 20$  pA, size:  $25 \times 25$  nm<sup>2</sup>). The white lines highlight the presence of nickelocene. The white square corresponds to the area investigated in panel (c). (b) Sketch of the junction with Nc on the tip above the cobalt nanoisland. The white arrow represents an out-of-plane magnetization. (c) Constant-height image at  $z = 80$  pm with  $V = -1$  mV (size:  $1 \times 1$  nm<sup>2</sup>). (d) Image of the island acquired by dragging a copper atom with a metallic tip ( $I = 0.5$  nA,  $V = 100$ , mV, size:  $1 \times 1$  nm<sup>2</sup>). The lattice parameters of the island are shown in panels (c) and (d).

existence of an exchange field produced by the Co atom progressively lifting the degeneracy of the  $|S = 1, M = -1\rangle$  and  $|S = 1, M = +1\rangle$  states of nickelocene [Fig. 5.9(b)]. Using a gyromagnetic ratio of  $g = 2$ , we find that the exchange field varies exponentially, reaching values as high as 25 T at the shortest distances explored [ $z = 70$  pm, Fig. 5.9(c)]. This corresponds to an exchange coupling of  $|J| \approx 3.2$  meV taking our DFT-computed value of  $\langle S_{\text{Co}} \rangle \approx 0.9$  for the effective spin of a cobalt atom.

The line shape is simulated using a dynamical scattering model [41], and includes a magnetic field along  $z$  to mimic the exchange field as well as a spin polarization  $\eta$  to account for the spin asymmetry. We neglect the electron scattering (§ 3.3.3), but remark that unlike the simulations for Fe—or for the bare surface (§ 4.3.2), spin pumping (§ 1.3.4) needs to be taken into account to match the experimental curve. As an example, we present in Fig. 5.9(a) simulations for the spectrum acquired at 70 pm with (solid line) and without (dashed line) spin pumping. This highlights that the lifetime of the excited states is probably longer above the cobalt surface. Lifetime measurements using a pump-probe setup [53] could eventually provide a quantitative estimate.

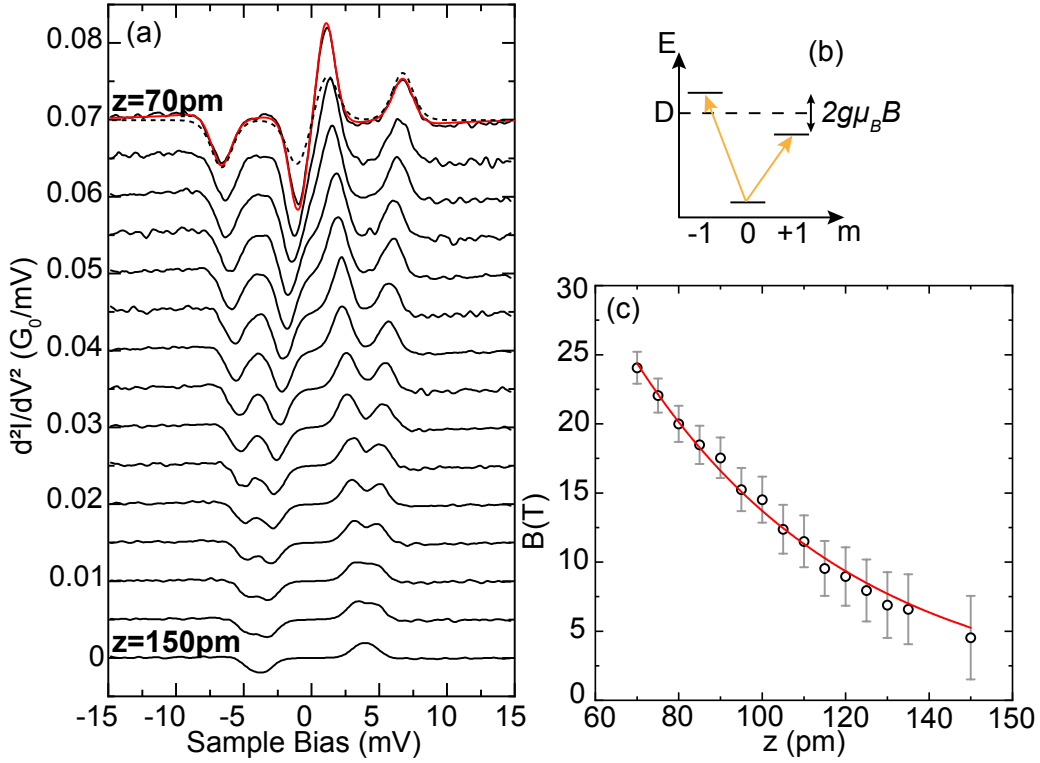


Figure 5.9: **Spin excitation spectra above a cobalt surface.** (a)  $d^2I/dV^2$  spectra acquired with the tip positioned above a Co atom of the island [see red dot in Fig. 5.10(a)]. The tip was moved from  $z = 145$  pm to  $z = 70$  pm. For clarity, the spectra are shifted vertically by  $5 \times 10^{-3} G_0/mV$ . The lines are the simulated line shapes using the dynamical scattering model [41] (dashed: without spin pumping; solid: with spin pumping). (b) Energy diagram of the spin system. (c) Exchange field  $B$  extracted from the spectra of panel (a) using Eq. (5.2). The solid red line is an exponential fit.

### 5.2.3 Imaging the exchange interaction

Figures 5.10(a) and 5.10(b) present images of the cobalt surface acquired with the Nc-tip —Fig. 5.10(a) is the same image as Fig. 5.8(c). The first image, which was acquired by freezing the tip-surface distance at  $z = 80$  pm and using a sample bias of  $-1$  mV, shows the cobalt atoms of the island as recognized in § 5.2.1. The contrast is almost lost in the second image acquired at same tip-surface distance but at a higher bias of  $-5$  mV. To understand the observed atomic resolution, we recorded the spin excitation spectra [Figs. 5.10(c) and 5.10(d)] with the Nc-tip



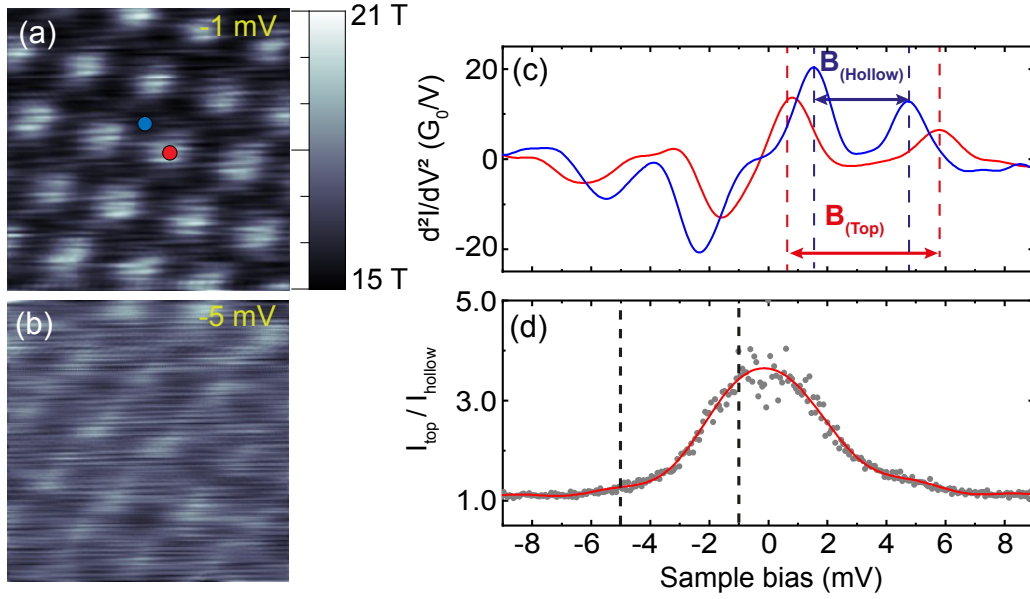


Figure 5.10: **Atomically resolving the exchange field.** (a) Constant-height image acquired in the center of the island of Fig. 5.8 (indicated by white square) at  $z = 80$  pm with  $V = -1$  mV (size:  $1 \times 1$  nm<sup>2</sup>). The image corrugation is calibrated using the spectra of panel (d). (b) Constant-height image of the same area as in (a) also acquired at  $z = 80$  pm, but with lower tunnel bias ( $-5$  mV). (c)  $d^2I/dV^2$  spectra acquired at  $z = 80$  pm. The solid red line corresponds to a spectrum acquired above a top site [red dot in panel (a)], the solid blue line to a spectrum acquired above a hollow site [blue dot in panel (a)]. (d) Ratio between the tunnel current with the Nc-tip above the top position ( $I_{top}$ ) and the tunnel current with the Nc-tip in the hollow position ( $I_{hollow}$ ) as a function of bias. Raw data: grey dots, Low-pass filter: red curve.

positioned on top of a Co atom [red dot in Fig. 5.10(a)] and above a hollow site of the surface [blue dot in Fig. 5.10(a)]. As shown, the peaks (dips) in Fig. 5.10(d) split apart more strongly when the tip is positioned in the top position compared to the hollow position, revealing a stronger exchange field for the top site. For both sites, the average value of the peaks (dips) is the same and equal to the magnetic anisotropy  $D$  as graphically indicated in Fig. 5.10(d).

To link the changes in the exchange field to the contrast observed in the constant-height images, we present in Fig. 5.10(e) the ratio between the  $I(V)$  curves acquired above the top and hollow position at  $z = 80$  pm. To explain the bias dependence of the contrast, it is sufficient to remark that when  $-1$  mV, the current in the top position is 3.5 times that of the hollow

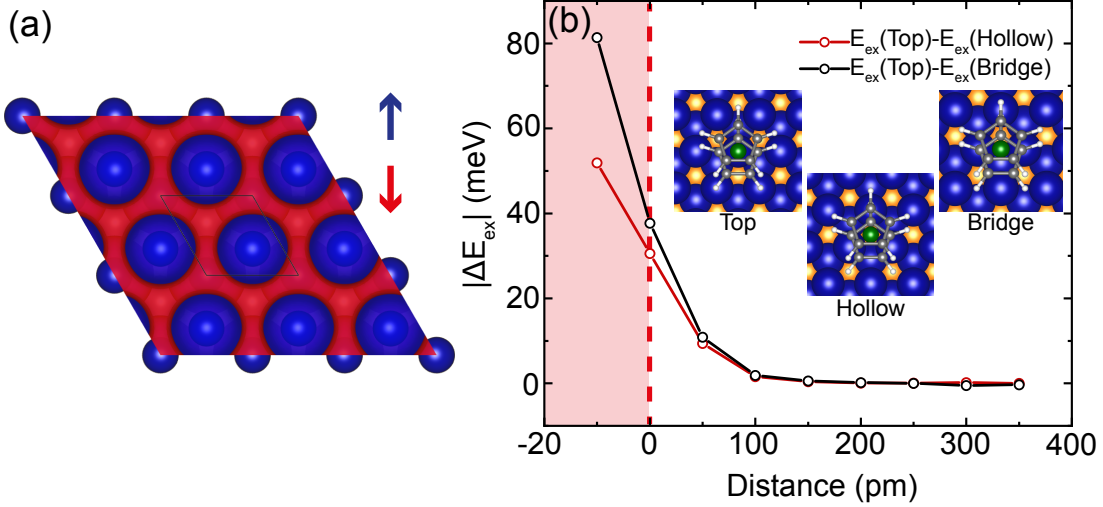


Figure 5.11: **Computed exchange interaction between nickelocene and cobalt.** (a) Isosurface of the spin density for a cobalt bilayer. Spin-down (↓) and spin-up (↑) densities are plotted in red and blue, respectively. Spin-up *d* electrons are mainly located on the Co atoms, while spin-down *sp* electrons are dispersive in nature [44, 46, 183]. The cobalt atoms have a magnetic moment of  $1.76 \mu_B$ , which is mainly carried by the *d* orbitals (*d*:  $1.81 \mu_B$ , *p*:  $-0.04 \mu_B$ , *s*:  $-0.01 \mu_B$ ). The spatial confinement of *sp* electrons within the island [44, 46, 183] is not accounted for. (b) Difference in exchange energy ( $|\Delta E_{ex}|$ ) between the top and the hollow positions (red), and between the top and bridge positions (black). The energy difference was computed as a function of tip distance to the cobalt surface. The filled red area indicates the contact regime where the Nc molecule is covalently bond to the surface. Inset: Junction geometry used in the DFT calculations defining the top, hollow, and bridge site.

position. This ratio, hence the contrast in the image, decreases rapidly reaching 1.2 when the bias is increased to  $-5$  mV. This bias dependence underlines that the contrast is carried by the low-bias structure in the  $dI/dV$  [Fig. 5.10(c)] or in the  $d^2I/dV^2$  [Fig. 5.10(c)] spectra. In particular, when the bias is  $-1$  mV, we have a situation in which the current is dominated by the low-energy dip. When the exchange field varies, the position of this dip changes, approaching or moving away from  $eV = -D$ . This negative or positive shift of the dip then determines the current flowing at  $-1$  mV, yielding the observed contrast. Using Fig. 5.10(d), we associate the maximum of current in Fig. 5.10(a) to the maximum of exchange field, and the minimum of current to the minimum of exchange field. This allows for expressing the corrugation of the image in terms of an exchange field as shown in Fig. 5.10(a).

The contrast observed has magnetic origin. Other experimental evidence can be gathered by remarking that the contrast in the images is lost whenever a splitting is not observed in the spin excitation spectra, i.e. when the tip is sufficiently far away from the surface ( $z > 150$  pm). It is also absent when scanning above non-magnetic Cu(111) under the same tunneling conditions. To confirm the magnetic origin of the contrast, we also computed with DFT the exchange energy  $E_{\text{ex}} = E_P - E_{AP}$  at various tip-surface distances with the Nc-tip above a top, hollow and bridge site of the surface [Fig. 5.11(a)]. Just prior to the contact formation between Nc and the surface, which is the distance interval explored in the experiment, the exchange energy is markedly different between the top and the hollow/bridge sites, because the local character of the  $d$ -electrons starts imprinting a lateral corrugation to the interaction. Figure 5.11(b) shows that the computed exchange energy is stronger for the top site compared to hollow or bridge sites. A different exchange field can then be expected between these sites, in qualitative agreement with our experimental findings of Fig. 5.10(a). We stress that for a quantitative comparison, which is beyond the scope of the present study, the non-collinearity among magnetic moments of Co and Nc should be taken into account.

## 5.2.4 Spin polarization of the islands

As mentioned in § 5.2.2, in the center of the islands we observe a spin asymmetry  $\eta < 5\%$ , in stark contrast to the single Fe adatom. This low value of  $\eta$  suggests that  $\mathcal{T}_{t,\uparrow}\mathcal{T}_{s,\downarrow} \approx \mathcal{T}_{s,\uparrow}\mathcal{T}_{t,\downarrow}$ , i.e. it reflects a compensation of the tip and sample spin-dependent transmissions. Taking as previously  $\mathcal{T}_{t,\uparrow}/\mathcal{T}_{t,\downarrow} = 0.54$  (§ 5.1.4), we find a spin polarization of  $P = -58\%$  for the elastic transmission of the island when  $\eta = 5\%$ , which we attribute to spin-down  $sp$  electrons. Interestingly, Eltschka *et al.* used the Zeeman splitting of a superconducting tip [47], i.e. the Meservey-Tedrow-Fulde effect, to probe the absolute value of the spin polarization of the current above a cobalt island. The spin polarization in the center of the island was seen to reach 60%, in good agreement with our findings —note that we have chosen the  $sp$  electrons of the island to be spin down [Fig. 5.11(a)], hence the opposite sign for our spin polarization.

Despite the low value of the spin asymmetry, it is possible to detect changes in  $\eta$  at the island edges. Figure 5.12(a) presents a close-up image acquired with a Nc-tip positioned above the corner of a cobalt island. The low-bias image shows an atomic-scale contrast similar to that of Fig. 5.10(a). We have acquired a spin excitation spectrum above each top site of the image —two typical spectra are presented in Fig. 5.12(b), one spectrum (labeled A) being acquired

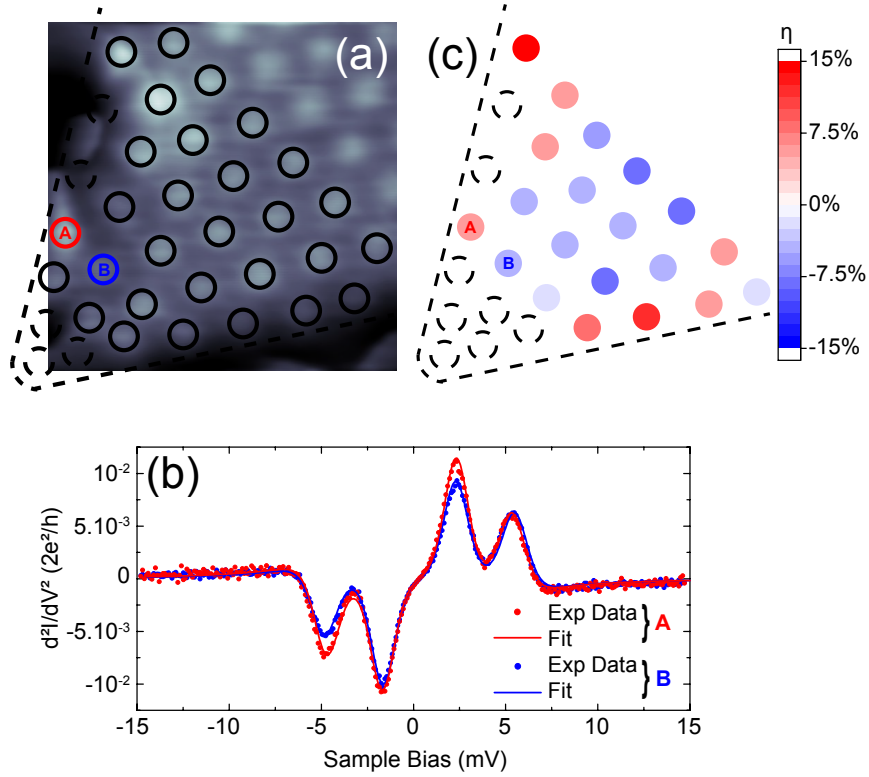


Figure 5.12: **Spin asymmetry at the corner of a cobalt island.** (a) Constant-height image acquired at  $z = 100$  pm of a island corner ( $V = -2$  mV,  $1.5 \times 1.5$  nm<sup>2</sup>). The image shows atomic resolution (top sites are highlighted by black circles in black; the dashed circles represents extrapolated sites). (b)  $d^2I/dV^2$  spectra on the sites labeled A (in red) and B (in blue) in panel (a). (c) Spin asymmetry  $\eta$  evaluated at each top site with  $z = 100$  pm.

at the rim of the island, the other being acquired at a site next to the island rim (labeled B). We then extracted from each spectrum a value of  $\eta$  and plotted the spatial dependence in Fig. 5.12(c). The spin asymmetry presents values between  $\pm 15\%$ , but, remarkably, the change in sign occurs within one atomic spacing. This behavior of  $\eta$  remains unclear.

### 5.3 Conclusion

In this chapter we have demonstrated that the spin excitations produced in a nickelocene molecule attached to the apex of a STM tip can be used to probe at the atomic-scale the magnetic exchange interaction between Nc and surface-supported objects, as well as the spin

asymmetry of these objects. The Nc-tip acts as a spin-sensitive detector for on-surface systems. This technique is limited by the temperature of the STM, in other words to the detection of energies of order 0.5 meV at our working temperature of 2.4 K. This fixes a low limit of 5 T for the detection of effective magnetic. We should note that the experiments we presented are done without an external magnetic field, which, if used, would considerably increase the potential of this technique. For example, by applying an external magnetic field, it would be possible to determine experimentally the sign of the coupling  $J$  between the Nc-tip and the object under investigation [185]. A magnetic contrast would also be gained on antiferromagnetic surfaces. In this sense, this technique offers a nice alternative to magnetic force microscopy experiments [186, 187].



## Conclusion and perspectives

In this work, we studied the magnetic properties of nickelocene molecules deposited on metal electrodes and how they change with the interaction with the direct environment.

We showed that at low coverages the molecule adsorbs individually on the hollow sites of the surface, adopting a vertical configuration where the molecular axis is perpendicular to the surface —the axis runs through the center of the two cyclopentadienyl (Cp) rings. At higher molecular coverages, the T-shape interaction between the Cp rings stabilizes a physisorbed molecular layer where vertical- and horizontal-lying molecules nest together similarly to what was observed for other metallocenes. We showed that the spin and uniaxial magnetic anisotropy of a free nickelocene are preserved upon adsorption on copper. This differentiates nickelocene from usual spin systems that require, instead, a thin insulating layer between them and the metal surface to preserve their spin. The spin excitation spectrum of nickelocene presents also an unusually high 4-to-1 intensity ratio between the inelastic conductance and the elastic conductance. Using the T-matrix theory developed in collaboration with N. Lorente, we showed that this is a characteristic of a spin system close to particle-hole symmetry where the spin is preserved from scattering events by the electrons of the host metal. We confirm this interpretation through a careful analysis of the line shape of the spin excitation spectrum of nickelocene using the dynamical scattering model developed by M. Ternes.

We then showed how the magnetic properties of nickelocene change when it is adsorbed on a metallic STM tip. Remarkably, we found that Nc behaves also as a quantum spin 1 system when attached to the apex of a STM tip. The spectroscopic fingerprint for the molecular tip is similar to that of the molecule on the surface. However, the magnetic behavior of nickelocene on the tip is even closer to that of a free nickelocene as demonstrated by the slightly larger magnetic anisotropy found and by the larger inelastic-versus-elastic conductance ratio (typically 9-to-1) observed. The nickelocene tip has been used to explore new spin-related effects. First, by placing the nickelocene tip above an on-surface nickelocene, we triggered a double spin excitation

with a single tunneling electron. Under these conditions, the spin excitation spectrum presents a record-high 50-to-1 ratio between the inelastic and the elastic conductances. Second, we studied the interaction between the nickelocene tip and a copper surface by controllably engineering a molecular junction. To do so, we moved the nickelocene tip from the tunneling regime to the contact regime by progressively reducing the tip-sample distance. This experiment led to the observation in the contact regime of a Kondo peak in the  $dI/dV$  spectra, which we associated to nickelocene switching its spin from  $S = 1$  to  $S = 1/2$ . A careful analysis of the  $dI/dV$  line shape in the tunnel and contact regimes highlighted an increase of the hybridization of the nickelocene with the surface as the tip displacement is increased. With the support of DFT calculations, the sudden spin switch observed was assigned to a geometrical rearrangement of the junction occurring within a tip displacement of 20 pm.

Last, we showed how to exploit the spin excitations of a nickelocene tip to probe the exchange interaction with a magnetic sample, either a single atom or a magnetic surface. The spin polarization of the inelastic current at the Fermi level, which we name spin asymmetry, can be measured as well. A magnetic contrast on a cobalt surface could be evidenced with atomic-scale resolution, permitting us to visualize the magnetic moments of a cobalt atom within the surface. Work of this kind can be extended to a large variety of magnetic systems relevant to molecular spintronics, either model systems such as single atoms or organometallic molecules. The visualization of complex spin textures should also be possible with an external magnetic field as in pioneering magnetic exchange force microscopy experiments [186, 187]. These systems should also provide a good test ground for evaluating the possible back-action exerted by the nickelocene tip on the sample.

Nickelocene on the apex of a metallic tip provides magnetic sensitivity through its spin  $S = 1$  and its uniaxial magnetic anisotropy. To extend our concept of the quantum spin tip, we have also investigated on another metallocene, cobaltocene, which we believe to be of interest and will be the object of further experiments in the team. Like nickelocene, cobaltocene can be attached to the apex of a metallic tip. Figure 5.13(a) presents a  $dI/dV$  spectrum acquired with a cobaltocene tip positioned above a Cu(100) surface. The spectrum is dominated by a zero-bias anomaly that we assign to a Kondo resonance, which hints to cobaltocene on the tip having a spin  $S = 1/2$ , like the spin of free cobaltocene. This resonance is flanked by inelastic contributions at  $\pm 38$  meV, which we attribute to a Kondo effect mediated by a vibrational excitation, also known as vibrational Kondo effect [188–190]. By the mean of  $dI/dV$  maps realized for a bias close to the vibration threshold energy [Fig. 5.13(b)] and for a bias on



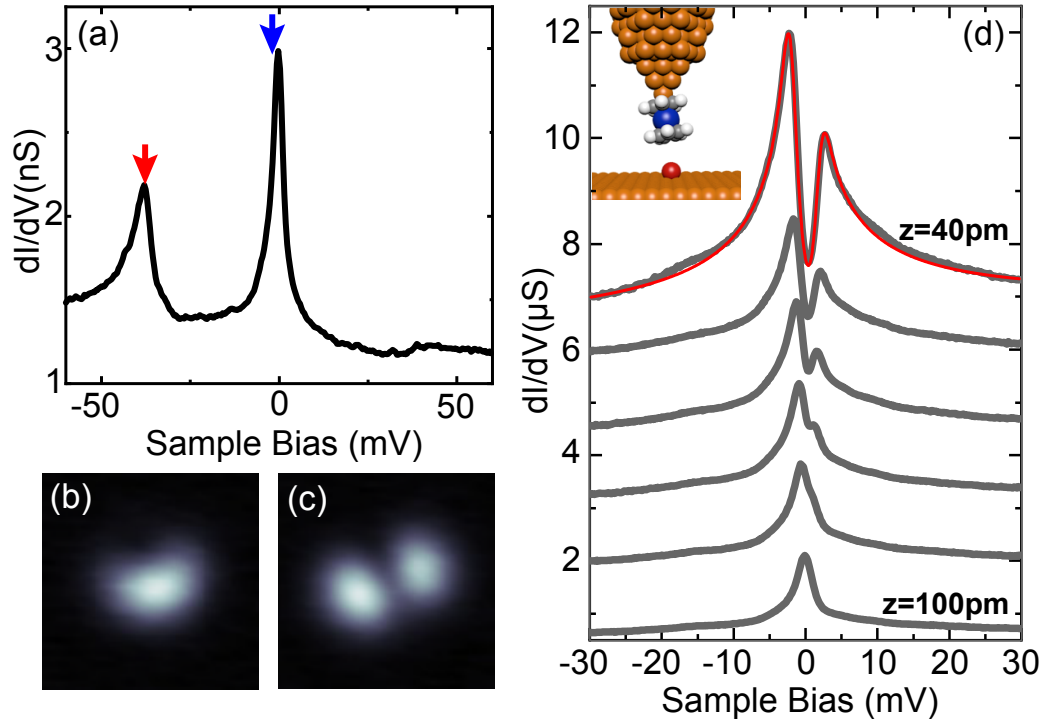


Figure 5.13: **Cobaltocene-terminated tip.** (a)  $dI/dV$  taken with a cobaltocene tip above a Fe adatom on Cu(100) (the tip-adatom distance is large enough for the spectrum to be the same as above Cu(100)). The strong bias asymmetry of the vibrational Kondo is attributed to an asymmetry in the energy position of the molecular orbitals (not shown). Feedback loop opened at  $I = 100$  pA,  $V = -60$  mV. (b) Corresponding constant-height  $dI/dV$  map at  $V = -38$  mV [red arrow in panel (a)], and, (c) at  $V = -2$  mV [blue arrow in panel (a)]. The  $dI/dV$  maps of panel (b) and (c) were acquired at the same tip-sample distance (feedback loop opened at  $I = 100$  pA,  $V = -60$  mV). The Fe adatom is used here to spatially resolve the tip apex as in chapter 4. (d) Evolution of the  $dI/dV$  spectrum of a cobaltocene tip when approached from 100 pm to 40 pm towards a Fe atom on Cu(100). Inset: Sketch showing a cobaltocene tip above a Fe atom.

the Kondo peak [Fig. 5.13(c)], we see that the two STS fingerprints do not share the same location on the molecule. Indeed, the Kondo resonance seems to be localized on the carbons (it would be the p-orbitals of the carbons that are included in the molecular orbital, Dft-based calculations are expected to confirm it). As nickelocene, the cobaltocene tip offers to explore on-surface magnetism. In Fig. 5.13(d), we show, for example, the interaction of a cobaltocene

tip with an iron atom as a function of tip-atom distance. The Kondo resonance splits apart when approaching the Fe atom. We reproduce the line shape with a dynamical scattering model [41] and extract an exchange field of 18 T. Further studies are currently in progress to fully characterize this spin  $1/2$  tip. Interestingly, we note that the spin  $S = 1/2$  nature of the tip may prove interesting for performing STM-ESR experiments (Chapter 1). While nickelocene cannot be used to probe interactions of the order of  $10 \mu\text{eV}$ , *i.e.* dipolar interactions, because of the magnetic anisotropy of  $D = 3.5 \text{ meV}$  separating the ground state from its excited states, this would be instead possible for the doubly degenerated ground state of cobaltocene in the presence of a small external magnetic field or exchange field.

# **Appendices**



## APPENDIX **A**

# Appendix: X-ray adsorption spectroscopy

## A.1 Generalities

In chapter 3, we use X-ray Magnetic Circular Dichroism to analyse the magnetic properties of  $\text{NiCp}_2$  deposited on copper. The experiments were performed at synchrotron SOLEIL, on the DEIMOS beamline. These measurements consist in measuring the absorption of a circularly polarized light (x-rays) by the sample (See Fig. A.1(a)). The incident x-ray photons excite a core electron, here from the 2p Ni shell, to the the unoccupied states, here 3d and 4s orbitals, leaving a whole in the 2p core levels (See figure A.1(b)). Upon de-excitation, secondary electrons are emitted via the Auger process. Some are leaving the sample. This latter being electrically grounded, a current is produced during the absorption process, which is proportional to the absorption coefficient of the sample. This is the so-called total electron yield (TEY). For a fixed helicity ("right" or "left" polarization) of the incoming X-ray beam, the absorption coefficient is different [191, 192] when the sample is magnetic. The difference between the two adsorption spectra gives the so called XMCD signal. Sum rules have been established ([145]), which allow us to extract from this XMCD spectrum both spin and orbital moments of the analysed element. This technique is the only one allowing a direct element-selective measurement of the spin and orbital moments. Note that to obtain a non vanishing XMCD signal, there must be a non-zero projection of the magnetic moment on the photon propagation axis. In our case, a high magnetic field (up to 7 T) allows to control the orientation of the magnetim moment.

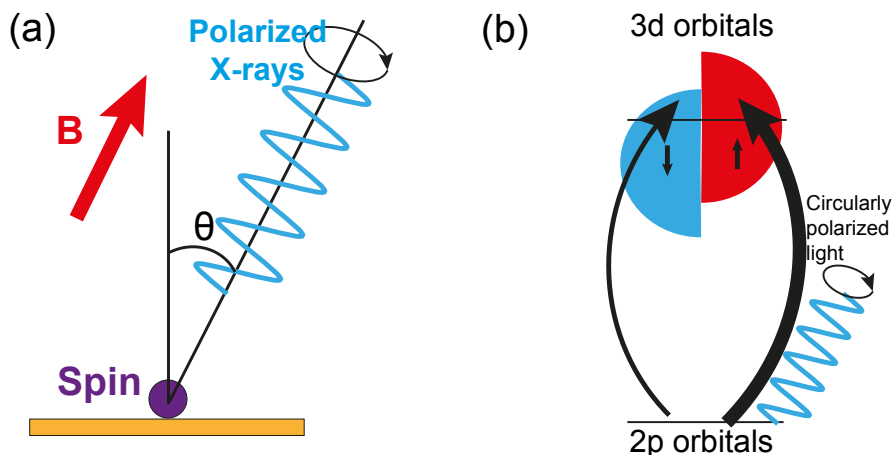


Figure A.1: **X-rays absorption spectroscopy principle**(a) Schematics of a magnetic system under a magnetic field hit by circularly polarized light (b) Sketch of the transitions due to the X-ray absorption, in the case of L-edges the transition occurs for 2p electrons to 3d unoccupied states. Circularly polarized light will excite up and down electrons differently.

Reversing the direction of the field leads to the inversion of the XMCD spectrum sign. An angular analysis also allows to determine the magnetic anisotropy of the sample. In our case, we illuminated NiCp<sub>2</sub> molecules vertically adsorbed on a metallic crystal and defined the main axis of vertical molecules as the z quantification axis. We obtained adsorption spectra with two peaks corresponding to the L<sub>3</sub> and L<sub>2</sub> edges of Ni, respectively located at 864 and 882 eV like the one presented in figure A.2(a). The corresponding XMCD signal is presented in figure A.2(b).

## A.2 Sumrules

We performed the analysis of the XAS and the XMCD using the sum rules at the Ni L<sub>2,3</sub> edges. These rules allow to determine the different components of the magnetic momentum of the studied system, the spin momentum and the orbital momentum. We define the integral of the XAS for a spin averaged beamlight as follows:

$$I_k = \int_{L_k} \left( \frac{1}{2} [\mu_+ + \mu_-] - \mu_{\text{continuum}} \right) dE \quad (\text{A.1})$$

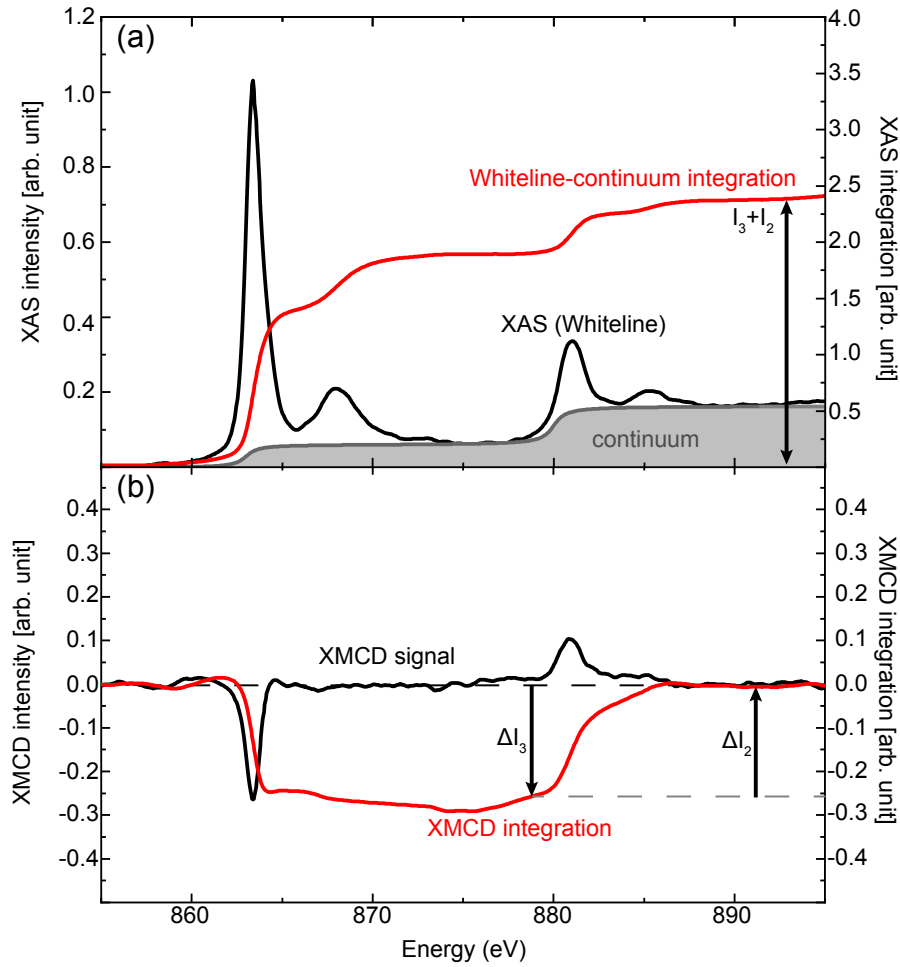


Figure A.2: **XAS, XMCD and sum-rules** (a) Plot of the white-line (sum of the absorption for the two circular polarizations at the  $L_{2,3}$  edges of Ni for Nc molecules adsorbed on Cu(100).  $B = 6.5$  T,  $T = 4.7$  K, angle of incidence  $60^\circ$  of the light. The background function related to the transitions towards the s-states continuum as well as the integral of the continuum subtracted white-line ( $I_3 + I_2$  are represented). (b) Corresponding XMCD signal and its integration ( $\Delta I_3$  the integral over the  $L_3$  edge only and  $\Delta I_2$  the integral over the  $L_2$  edge).

with  $\mu_{\pm}$  the value of the XAS for circular right/left polarization, and  $\mu_{\text{continuum}}$  the component of the spectrum related to the transition from p states to the continuum of s states above the vacuum level. We can express also the integrals of the XMCD signal on the different edges as follows :

$$\Delta I_k = \int_{L_k} ([\mu_+ - \mu_-]) dE \quad (\text{A.2})$$

A graphical representation of these integrals are shown in figure A.2, for XAS measurement performed for a collection of NiCp<sub>2</sub> adsorbed on Cu(100). The thresholds presented are the L<sub>3</sub> and L<sub>2</sub> of Ni. To determine the magnetic momentum of Ni in the molecule we use the so-called sum rules which are presented in a simplified version as follows:

$$\text{Charge sum rule: } \frac{1}{3}[I_3 + I_2] = CN_h \quad (\text{A.3})$$

$$\text{Spin sum rule: } \frac{1}{3}[\Delta I_3 - 2\Delta I_2]_\theta = -\frac{C}{\mu_B} m_{\text{spin},\theta} \quad (\text{A.4})$$

$$\text{Orbital sum rule: } [\Delta I_3 + \Delta I_2]_\theta = -\frac{3C}{2\mu_B} m_{\text{orbital},\theta} \quad (\text{A.5})$$

These sum rules lead to expressions for the spin and orbital momentum projected on the direction of the beam:

$$m_{\text{spin},\theta} = -\frac{N_h \mu_B}{P} \frac{[\Delta I_3 - 2\Delta I_2]_\theta}{[I_3 + I_2]} \quad (\text{A.6})$$

$$m_{\text{orbital},\theta} = -\frac{2N_h \mu_B}{3P} \frac{[\Delta I_3 + \Delta I_2]_\theta}{[I_3 + I_2]} \quad (\text{A.7})$$

P is the degree of polarization of the light which is in our case close to 100%. With these expressions, we find for a beam light at 60° to the normal of the surface and at 4.7 K,  $m_{\text{spin},60^\circ} = 0.67 \mu_B$  and  $m_{\text{orbital},60^\circ} = 0 \mu_B$ .



# Bibliography

- [1] Li, J., Schneider, W.-D., Berndt, R. & Delley, B. Kondo scattering observed at a single magnetic impurity. *Phys. Rev. Lett.* **80**, 2893–2896 (1998).
- [2] Madhavan, V., Chen, W., Jamneala, T., Crommie, M. F. & Wingreen, N. S. Tunneling into a single magnetic atom: Spectroscopic evidence of the Kondo resonance. *Science* **280**, 567–569 (1998).
- [3] Heinrich, A. J., Gupta, J. A., Lutz, C. P. & Eigler, D. M. Single-atom spin-flip spectroscopy. *Science* **306**, 466–469 (2004).
- [4] Loth, S. *et al.* Controlling the state of quantum spins with electric currents. *Nat. Phys.* **6**, 340–344 (2010).
- [5] Baumann, S. *et al.* Electron paramagnetic resonance of individual atoms on a surface. *Science* **350**, 417–420 (2015).
- [6] Natterer, F. D. *et al.* Reading and writing single-atom magnets. *Nature* **543**, 226 (2017).
- [7] Choi, T. *et al.* Atomic-scale sensing of the magnetic dipolar field from single atoms. *Nat. Nanotechnol.* **12**, 420 (2017).
- [8] Willke, P. *et al.* Hyperfine interaction of individual atoms on a surface. *Science* **362**, 336–339 (2018).
- [9] Yang, K. *et al.* Electrically controlled nuclear polarization of individual atoms. *Nat. Nanotechnol.* **13**, 1120–1125 (2018).
- [10] Pietzsch, O., Kubetzka, A., Bode, M. & Wiesendanger, R. Spin-polarized scanning tunneling spectroscopy of nanoscale cobalt islands on Cu(111). *Phys. Rev. Lett.* **92**, 057202 (2004).
- [11] Meier, F., Zhou, L., Wiebe, J. & Wiesendanger, R. Revealing magnetic interactions from single-atom magnetization curves. *Science* **320**, 82–86 (2008).
- [12] Wiesendanger, R., Güntherodt, H.-J., Güntherodt, G., Gambino, R. J. & Ruf, R. Observation of vacuum tunneling of spin-polarized electrons with the scanning tunneling

- microscope. *Phys. Rev. Lett.* **65**, 247–250 (1990).
- [13] Wortmann, D., Heinze, S., Kurz, P., Bihlmayer, G. & Blügel, S. Resolving complex atomic-scale spin structures by spin-polarized scanning tunneling microscopy. *Phys. Rev. Lett.* **86**, 4132–4135 (2001).
- [14] de Haas, W. J. & van den Berg, J. The electrical resistance of gold and silver at low temperatures. *Physica III* **6**, 440 – 449 (1936).
- [15] Anderson, P. W. Localized magnetic states in metals. *Phys. Rev.* **124(1)**, 41 – 53 (1961).
- [16] Kondo, J. Resistance minimum in dilute magnetic alloys. *Progr. Theor. Exp. Phys.* **32**, 37– 49 (1964).
- [17] Schrieffer, J. R. & Wolff, P. A. Relation between the Anderson and Kondo hamiltonians. *Phys. Rev.* **149**, 491–492 (1966).
- [18] Zhang, Y.-h. *et al.* Temperature and magnetic field dependence of a Kondo system in the weak coupling regime. *Nat. Commun.* **4**, 2110 (2013).
- [19] Choi, D.-J., Rastei, M. V., Simon, P. & Limot, L. Conductance-driven change of the Kondo effect in a single cobalt atom. *Phys. Rev. Lett.* **108**, 266803 (2012).
- [20] Choi, D.-J. *et al.* Kondo resonance of a Co atom exchange coupled to a ferromagnetic tip. *Nano Lett.* **16**, 6298–6302 (2016).
- [21] Frota, H. Shape of the Kondo resonance. *Phys. Rev. B* **45**, 1096–1099 (1992).
- [22] Hirjibehedin, C. F., Lutz, C. P. & Heinrich, A. J. Spin coupling in engineered atomic structures. *Science* **312**, 1021–1024 (2006).
- [23] Otte, A. F. *et al.* The role of magnetic anisotropy in the Kondo effect. *Nat. Phys.* **4**, 847–850 (2008).
- [24] Hirjibehedin, C. F. *et al.* Large magnetic anisotropy of a single atomic spin embedded in a surface molecular network. *Science* **317**, 1199–1203 (2007).
- [25] Rau, I. G. *et al.* Reaching the magnetic anisotropy limit of a 3d metal atom. *Science* **344**, 988–992 (2014).
- [26] Binnig, G., Rohrer, H., Gerber, C. & Weibel, E. Surface studies by scanning tunneling microscopy. *Phys. Rev. Lett.* **49**, 57–61 (1982).
- [27] Binnig, G., Rohrer, H., Gerber, C. & Weibel, E.  $7 \times 7$  reconstruction on si(111) resolved in real space. *Phys. Rev. Lett.* **50**, 120–123 (1983).
- [28] Bardeen, J. Tunnelling from a many-particle point of view. *Phys. Rev. Lett.* **6**, 57–59 (1961).
- [29] Tersoff, J. & Hamann, D. R. Theory and application for the scanning tunneling micro-

- scope. *Phys. Rev. Lett.* **50**, 1998–2001 (1983).
- [30] Chen, C. J. Tunneling matrix elements in three-dimensional space: The derivative rule and the sum rule. *Phys. Rev. B* **42**, 8841–8857 (1990).
- [31] Chen, C. J. Effects of  $m \neq 0$  tip states in scanning tunneling microscopy: The explanations of corrugation reversal. *Phys. Rev. Lett.* **69**, 1656–1659 (1992).
- [32] Chen, C. J. *Introduction to the Scanning Tunneling Microscopy* (Oxford University Press, 1993).
- [33] Tersoff, J. & Hamann, D. R. Theory of the scanning tunneling microscope. *Phys. Rev. B* **31**, 805–813 (1985).
- [34] Appelbaum, J. A. & Brinkman, W. F. Theory of many-body effects in tunneling. *Phys. Rev.* **186**, 464–470 (1969).
- [35] Stipe, B. C., Rezaei, M. A. & Ho, W. Inducing and viewing the rotational motion of a single molecule. *Science* **279**, 1907 – 1909 (1998).
- [36] Stipe, B. C., Rezaei, M. A. & Ho, W. Single-molecule vibrational spectroscopy and microscopy. *Science* **280**, 1732 – 1735 (1998).
- [37] Bachellier, N. *et al.* Unveiling nickelocene bonding to a noble metal surface. *Phys. Rev. B* **93**, 195403 (2016).
- [38] Ormaza, M. *et al.* Efficient spin-flip excitation of a nickelocene molecule. *Nano Lett.* **17**, 1877–1882 (2017).
- [39] Strosio, J. A. & Celotta, R. J. Controlling the dynamics of a single atom in lateral atom manipulation. *Science* **306**, 242–247 (2004).
- [40] Ormaza, M. *et al.* Assembly of ferrocene molecules on metal surfaces revisited. *J. Phys. Chem. Lett.* **6**, 395 (2015).
- [41] Ternes, M. Spin excitations and correlations in scanning tunneling spectroscopy. *New J. Phys.* **17**, 063016 (2015).
- [42] Ormaza, M. *et al.* Controlled spin switching in a metallocene molecular junction. *Nat. Commun.* **8**, 1974 (2017).
- [43] Verlhac, B. *et al.* Atomic-scale magnetometry with a single-molecule spin sensor at the apex of a scanning tunneling microscope (2019). URL <http://arxiv.org/abs/1901.04862>.
- [44] Pietzsch, O. *et al.* Spin-resolved electronic structure of nanoscale cobalt islands on Cu(111). *Phys. Rev. Lett.* **96**, 237203 (2006).
- [45] Rastei, M. V. *et al.* Size-dependent surface states of strained cobalt nanoislands on

- Cu(111). *Phys. Rev. Lett.* **99**, 246102 (2007).
- [46] Diekhöner, L. *et al.* Surface states of cobalt nanoislands on Cu(111). *Phys. Rev. Lett.* **90**, 236801 (2003).
- [47] Eltschka, M. *et al.* Probing absolute spin polarization at the nanoscale. *Nano Lett.* **14**, 7171–7174 (2014).
- [48] Loth, S. *et al.* Controlling the state of quantum spins with electric currents. *Nat. Phys.* **6**, 340–344 (2010).
- [49] Heinze, S. *et al.* Real-space imaging of two-dimensional antiferromagnetism on the atomic scale. *Science* **288**, 1805–1808 (2000).
- [50] Yazdani, A., Jones, B. A., Lutz, C. P., Crommie, M. F. & Eigler, D. M. Probing the local effects of magnetic impurities on superconductivity. *Science* **275**, 1767–1770 (1997).
- [51] Li, J., Schneider, W.-D., Berndt, R. & Delley, B. Kondo scattering observed at a single magnetic impurity. *Phys. Rev. Lett.* **80**, 2893–2896 (1998).
- [52] Néel, N. *et al.* Conductance and Kondo effect in a controlled single-atom contact. *Phys. Rev. Lett.* **98**, 016801 (2007).
- [53] Loth, S., Etzkorn, M., Lutz, C. P., Eigler, D. M. & Heinrich, A. J. Measurement of fast electron spin relaxation times with atomic resolution. *Science* **329**, 1628–1630 (2010).
- [54] Thiele, S. *et al.* Electrically driven nuclear spin resonance in single-molecule magnets. *Science* **344**, 1135–1138 (2014).
- [55] Müllegger, S. *et al.* Radio frequency scanning tunneling spectroscopy for single-molecule spin resonance. *Phys. Rev. Lett.* **113**, 133001 (2014).
- [56] Huang, F., Kief, M. T., Mankey, G. J. & Willis, R. F. Magnetism in the few-monolayers limit: A surface magneto-optic kerr-effect study of the magnetic behavior of ultrathin films of co, ni, and co-ni alloys on Cu(100) and Cu(111). *Phys. Rev. B* **49**, 3962–3971 (1994).
- [57] Yayan, Y., Brar, V. W., Senapati, L., Erwin, S. C. & Crommie, M. F. Observing spin polarization of individual magnetic adatoms. *Phys. Rev. Lett.* **99**, 067202 (2007).
- [58] Serrate, D. *et al.* Imaging and manipulating the spin direction of individual atoms. *Nat. Nanotechnol.* **5**, 350 (2010).
- [59] Iacovita, C. *et al.* Visualizing the spin of individual cobalt-phthalocyanine molecules. *Phys. Rev. Lett.* **101**, 116602 (2008).
- [60] Brede, J. *et al.* Spin- and energy-dependent tunneling through a single molecule with intramolecular spatial resolution. *Phys. Rev. Lett.* **105**, 047204 (2010).

- 
- [61] Atodiresei, N. *et al.* Design of the local spin polarization at the organic-ferromagnetic interface. *Phys. Rev. Lett.* **105**, 066601 (2010).
- [62] Khajetoorians, A. A. *et al.* Itinerant nature of atom-magnetization excitation by tunneling electrons. *Phys. Rev. Lett.* **106**, 037205 (2011).
- [63] Gambardella, P. *et al.* Giant magnetic anisotropy of single cobalt atoms and nanoparticles. *Science* **300**, 1130–1133 (2003).
- [64] Abrikosov, A. A. Renormalization group from diamagnetic calculations with Kondo spin represented by pseudofermion. *Physics* **5**, 2 (1965).
- [65] Goldhaber-Gordon, D. *et al.* Kondo effect in a single-electron transistor. *Nature* **391**, 156–159 (1998).
- [66] Cronenwett, S. M., Oosterkamp, T. H. & Kouwenhoven, L. P. A tunable Kondo effect in quantum dots. *Science* **281**, 540–544 (1998).
- [67] Costi, T. A. Kondo effect in a magnetic field and the magnetoresistivity of Kondo alloys. *Phys. Rev. Lett.* **85**, 1504–1507 (2000).
- [68] Wahl, P. *et al.* Exchange interaction between single magnetic adatoms. *Phys. Rev. Lett.* **98**, 056601 (2007).
- [69] Otte, A. F. *et al.* Spin excitations of a Kondo-screened atom coupled to a second magnetic atom. *Phys. Rev. Lett.* **103**, 107203 (2009).
- [70] Tsukahara, N. *et al.* Evolution of Kondo resonance from a single impurity molecule to the two-dimensional lattice. *Phys. Rev. Lett.* **106**, 187201 (2011).
- [71] Bork, J. *et al.* A tunable two-impurity Kondo system in an atomic point contact. *Nat. Phys.* **7**, 901 (2011).
- [72] Spinelli, A. *et al.* Exploring the phase diagram of the two-impurity Kondo problem. *Nat. Commun.* **6**, 10046 EP – (2015).
- [73] Khajetoorians, A. A. *et al.* Tailoring the chiral magnetic interaction between two individual atoms. *Nat. Commun.* **7**, 10620 (2016).
- [74] Oberg, J. C. *et al.* Control of single-spin magnetic anisotropy by exchange coupling. *Nat. Nanotechnol.* **9**, 64–68 (2014).
- [75] Khajetoorians, A. A. *et al.* Tuning emergent magnetism in a Hund's impurity. *Nat. Nanotech.* **10**, 958–964 (2015).
- [76] Dubout, Q. *et al.* Controlling the spin of co atoms on pt(111) by hydrogen adsorption. *Phys. Rev. Lett.* **114**, 106807 (2015).
- [77] Jacobson, P. *et al.* Quantum engineering of spin and anisotropy in magnetic molecular

- junctions. *Nat. Commun.* **6**, 8536 (2015).
- [78] Fu, Y.-S., Xue, Q.-K. & Wiesendanger, R. Spin-resolved splitting of Kondo resonances in the presence of RKKY-type coupling. *Phys. Rev. Lett.* **108**, 087203 (2012).
- [79] von Bergmann, K., Ternes, M., Loth, S., Lutz, C. P. & Heinrich, A. J. Spin polarization of the split Kondo state. *Phys. Rev. Lett.* **114**, 076601 (2015).
- [80] Choi, D.-J., Rastei, M. V., Simon, P. & Limot, L. Conductance-driven change of the Kondo effect in a single cobalt atom. *Phys. Rev. Lett.* **108**, 266803 (2012).
- [81] Choi, D.-J. *et al.* Kondo resonance of a co atom exchange coupled to a ferromagnetic tip. *Nano Lett.* **16**, 6298–6302 (2016).
- [82] Pruser, H. *et al.* Long-range Kondo signature of a single magnetic impurity. *Nat. Phys.* **7**, 203–206 (2011).
- [83] Wahl, P. *et al.* Kondo temperature of magnetic impurities at surfaces. *Phys. Rev. Lett.* **93**, 176603 (2004).
- [84] Binnig, G., Garcia, N. & Rohrer, H. Conductivity sensitivity of inelastic scanning tunneling microscopy. *Phys. Rev. B* **32**, 1336–1338 (1985).
- [85] Persson, B. N. J. & Baratoff, A. Inelastic electron tunneling from a metal tip: The contribution from resonant processes. *Phys. Rev. Lett.* **59**, 339–342 (1987).
- [86] Stipe, B. C., Rezaei, M. A. & Ho, W. Coupling of vibrational excitation to the rotational motion of a single adsorbed molecule. *Phys. Rev. Lett.* **81**, 1263 – 1266 (1998).
- [87] Lorente, N. & Gauyacq, J.-P. Efficient spin transitions in inelastic electron tunneling spectroscopy. *Phys. Rev. Lett.* **103**, 176601 (2009).
- [88] Gauyacq, J.-P., Novaes, F. D. & Lorente, N. Magnetic transitions induced by tunneling electrons in individual adsorbed *m*-phthalocyanine molecules ( $m = \text{Fe}$  and  $\text{co}$ ). *Phys. Rev. B* **81**, 165423 (2010).
- [89] Monturet, S. & Lorente, N. Inelastic effects in electron transport studied with wave packet propagation. *Phys. Rev. B* **78**, 035445 (2008).
- [90] Heinrich, B. W. *et al.* Change of the magnetic coupling of a metal–organic complex with the substrate by a stepwise ligand reaction. *Nano Lett.* **13**, 4840–4843 (2013).
- [91] Paul, W. *et al.* Control of the millisecond spin lifetime of an electrically probed atom. *Nat. Phys.* **13**, 403 EP – (2016).
- [92] Donati, F. *et al.* Magnetic remanence in single atoms. *Science* **352**, 318–321 (2016).
- [93] Balashov, T. *et al.* Magnetic anisotropy and magnetization dynamics of individual atoms and clusters of fe and co on pt(111). *Phys. Rev. Lett.* **102**, 257203 (2009).

- 
- [94] Chilian, B. *et al.* Anomalously large  $g$  factor of single atoms adsorbed on a metal substrate. *Phys. Rev. B* **84**, 212401 (2011).
- [95] Schuh, T. *et al.* Magnetic excitations of rare earth atoms and clusters on metallic surfaces. *Nano Letters* **12**, 4805–4809 (2012). PMID: 22906055.
- [96] Donati, F. *et al.* Magnetism of ho and er atoms on close-packed metal surfaces. *Phys. Rev. Lett.* **113**, 237201 (2014).
- [97] Steinbrecher, M. *et al.* Absence of a spin-signature from a single ho adatom as probed by spin-sensitive tunneling. *Nat. Commun.* **7**, 10454 EP – (2016).
- [98] Tsukahara, N. *et al.* Adsorption-induced switching of magnetic anisotropy in a single Iron(II) phthalocyanine molecule on an oxidized Cu(110) surface. *Phys. Rev. Lett.* **102**, 167203 (2009).
- [99] Persson, M. Theory of inelastic electron tunneling from a localized spin in the impulsive approximation. *Phys. Rev. Lett.* **103**, 050801 (2009).
- [100] Fernández-Rossier, J. Theory of single-spin inelastic tunneling spectroscopy. *Phys. Rev. Lett.* **102**, 256802 (2009).
- [101] Chen, X. *et al.* Probing superexchange interaction in molecular magnets by spin-flip spectroscopy and microscopy. *Phys. Rev. Lett.* **101**, 197208 (2008).
- [102] Khajetoorians, A. A. *et al.* Detecting excitation and magnetization of individual dopants in a semiconductor. *Nature* **467**, 1084–1087 (2010).
- [103] Khajetoorians, A. A. *et al.* Current-driven spin dynamics of artificially constructed quantum magnets. *Science* **339**, 55–59 (2013).
- [104] Novaes, F. D., Lorente, N. & Gauyacq, J.-P. Quenching of magnetic excitations in single adsorbates at surfaces: Mn on cun/cu(100). *Phys. Rev. B* **82**, 155401 (2010).
- [105] Delgado, F., Palacios, J. J. & Fernández-Rossier, J. Spin-transfer torque on a single magnetic adatom. *Phys. Rev. Lett.* **104**, 026601 (2010).
- [106] Hurley, A., Baadji, N. & Sanvito, S. Perturbative approach to the Kondo effect in magnetic atoms on nonmagnetic substrates. *Phys. Rev. B* **84**, 115435 (2011).
- [107] Korytár, R., Lorente, N. & Gauyacq, J.-P. Many-body effects in magnetic inelastic electron tunneling spectroscopy. *Phys. Rev. B* **85**, 125434 (2012).
- [108] Jacob, D. Renormalization of single-ion magnetic anisotropy in the absence of the Kondo effect. *Phys. Rev. B* **97**, 075428 (2018).
- [109] Hamers, R. J. *Scanning Tunneling Microscopy and Spectroscopy. Theory, Techniques and Applications* (VHC, New York, 1993).

- [110] Weisendanger, R. *Scanning Probe Microscopy. Methods and Applications* (Cambridge University Press, Cambridge, UK, 1994).
- [111] Ukraintsev, V. A. Data evaluation technique for electron-tunneling spectroscopy. *Phys. Rev. B* **53**, 11176–11185 (1996).
- [112] Heinrich, B. W., Rastei, M. V., Choi, D.-J., Frederiksen, T. & Limot, L. Engineering negative differential conductance with the Cu(111) surface state. *Phys. Rev. Lett.* **107**, 246801 (2011).
- [113] Natterer, F. D., Patthey, F. m. c. & Brune, H. Distinction of nuclear spin states with the scanning tunneling microscope. *Phys. Rev. Lett.* **111**, 175303 (2013).
- [114] Berndt, R., Gimzewski, J. K. & Johansson, P. Inelastic tunneling excitation of tip-induced plasmon modes on noble-metal surfaces. *Phys. Rev. Lett.* **67**, 3796–3799 (1991).
- [115] Klein, J., Léger, A., Belin, M., Défourneau, D. & Sangster, M. J. L. Inelastic-electron-tunneling spectroscopy of metal-insulator-metal junctions. *Phys. Rev. B* **7**, 2336–2348 (1973).
- [116] Lambe, J. & Jaklevic, R. C. Molecular vibration spectra by inelastic electron tunneling. *Phys. Rev.* **165**, 821–832 (1968).
- [117] Zhang, Y.-h., Wahl, P. & Kern, K. Quantum point contact microscopy. *Nano Lett.* **11**, 3838–3843 (2011).
- [118] Kolasinski, K. W. *Surface Science: Foundations of Catalysis and Nanoscience* (Oxford science publications, 1993).
- [119] Ormaza, M. *et al.* On-surface engineering of a magnetic organometallic nanowire. *Nano Lett.* **16**, 588–593 (2016).
- [120] Zhen-Feng, X., Yaoming, X., Wen-Lin, F. & Henry F., S. Systematic investigation of electronic and molecular structures for the first transition metal series metallocenes  $m(c_5h_5)_2$  ( $m = v, cr, mn, fe, co, \text{ and } ni$ ). *J. Phys. Chem. A* **107**, 2716–2729 (2003).
- [121] Prins, R., van Voorst, J. & Schinkel, C. Zero-field splitting in the triplet ground state of nickelocene. *Chem. Phys. Lett.* **1**, 54 – 55 (1967).
- [122] Baltzer, P., Furrer, A., Hulliger, J. & Stebler, A. Magnetic properties of nickelocene. a reinvestigation using inelastic neutron scattering and magnetic susceptibility. *Inorg. Chem.* **27**, 1543–1548 (1988).
- [123] Zvarykina, A. V., Karimov, Y. S., Leonova, E. V. & Lyubovskii, R. B. *Sov. Phys.-Solid State (Engl. Transl.)* **12**, 385 (1970).
- [124] Li, S., Hamrick, Y. M., Zee, R. J. V. & Jr., W. W. Far-infrared magnetic resonance of



- matrix-isolated nickelocene. *J. Am. Chem. Soc.* **114**, 4433–4434 (1992).
- [125] Vaara, J., Rouf, S. A. & Mare, J. Magnetic couplings in the chemical shift of paramagnetic nmr. *J. Chem. Theory Comput.* **11**, 4840–4849 (2015).
- [126] Li, Y. *et al.* Trends in charge transfer and spin alignment of metallocene on graphene. *Phys. Rev. B* **83**, 195443 (2011).
- [127] Marocchi, S. *et al.* Graphene-mediated exchange coupling between a molecular spin and magnetic substrates. *Phys. Rev. B* **88**, 144407 (2013).
- [128] Welipitiya, D. *et al.* The adsorption of nickelocene part 1: molecular bonding on Ag(100). *Surf. Sci.* **393**, 34–46 (1997).
- [129] Welipitiya, D. *et al.* The adsorption of nickelocene: Part 2: decomposition and selective area deposition. *Surf. Sci.* **418**, 466–478 (1998).
- [130] Pugmire, D. L., Woodbridge, C. M., Root, S. & Langell, M. A. Nickelocene adsorption on single-crystal surfaces. *J. Vac. Sci. Technol. A* **17**, 1581–1586 (1999).
- [131] Borca, C. N., Welipitiya, D., Dowben, P. A., & Boag, N. M. Bonding configurations for nickelocene on Ag(100) and steric effects in thermal desorption. *J. Phys. Chem. B* **104**, 1047–1049 (2000).
- [132] Pugmire, D., Woodbridge, C., Boag, N. & Langell, M. Adsorption and decomposition of nickelocene on ag(1 0 0): a high-resolution electron energy loss spectroscopy and temperature programmed desorption study. *Surf. Sci.* **472**, 155 – 171 (2001).
- [133] Vieyra-Eusebio, M. T. & Rojas, A. Vapor pressures and sublimation enthalpies of nickelocene and cobaltocene measured by thermogravimetry. *J. Chem. Eng. Data* **56**, 5008–5018 (2011).
- [134] Klimes, J., Bowler, D. R. & Michaelides, A. Chemical accuracy for the van der waals density functional. *J. Phys.: Condens. Matter* **22**, 022201 (2010).
- [135] Bader, R. F. W. *Atoms in molecules: A quantum theory* (Oxford University Press: Oxford, 1990).
- [136] Bader, R. F. W., Popelier, A., P. L. & Kleith, T. A. Theoretical definition of a functional group and the molecular orbital paradigm. *Angew. Chem., Int. Ed.* **33**, 620–631 (1994).
- [137] Li, L.-J., Khlobystov, A. N., Wiltshire, J. G., Briggs, G. A. D. & Nicholas, R. J. Diameter-selective encapsulation of metallocenes in single-walled carbon nanotubes. *Nat. Mater.* **4**, 481–485 (2005).
- [138] García-Suárez, V. M., Ferrer, J. & Lambert, C. J. Tuning the electrical conductivity of nanotube-encapsulated metallocene wires. *Phys. Rev. Lett.* **96**, 106804 (2006).

- [139] Zhou, L. *et al.* One-dimensional iron-cyclopentadienyl sandwich molecular wire with half metallic, negative differential resistance and high-spin filter efficiency properties. *J. Am. Chem. Soc.* **130**, 4023–4027 (2008).
- [140] Wang, L. *et al.* Novel one-dimensional organometallic half metals: Vanadium-cyclopentadienyl, vanadium-cyclopentadienyl-benzene, and vanadium-anthracene wires. *Nano Lett.* **8**, 3640–3644 (2008).
- [141] Liu, R., Ke, S.-H., Baranger, H. U. & Yang, W. Organometallic spintronics: A dicobaltocene switch. *Nano Lett.* **5**, 1959–1962 (2005).
- [142] Yi, Z. *et al.* Tuning the magneto-transport properties of nickel-cyclopentadienyl multi-decker clusters by molecule-electrode coupling manipulation. *ACS Nano* **4**, 2274–2282 (2010).
- [143] Abufager, P., Robles, R. & Lorente, N. Fecocp<sub>3</sub> molecular magnets as spin filters. *J. Phys. Chem. C* **119**, 12119–12129 (2015).
- [144] Ohresser, P., Ghiringhelli, G., Tjernberg, O., Brookes, N. B. & Finazzi, M. Magnetism of nanostructures studied by x-ray magnetic circular dichroism: Fe on cu(111). *Phys. Rev. B* **62**, 5803–5809 (2000).
- [145] Thole, B. T., Carra, P., Sette, F. & van der Laan, G. X-ray circular dichroism as a probe of orbital magnetization. *Phys. Rev. Lett.* **68**, 1943–1946 (1992).
- [146] Carra, P., Thole, B. T., Altarelli, M. & Wang, X. X-ray circular dichroism and local magnetic fields. *Phys. Rev. Lett.* **70**, 694–697 (1993).
- [147] Gauyacq, J.-P., Lorente, N. & Novaes, F. D. Excitation of local magnetic moments by tunneling electrons. *Progress in Surface Science* **87**, 63 – 107 (2012).
- [148] Rubio-Verdú, C. *et al.* Orbital-selective spin excitation of a magnetic porphyrin. *Commun. Phys.* **1**, 15 (2018).
- [149] Anderson, P. W. Localized magnetic states in metals. *Phys. Rev.* **124**, 41–53 (1961).
- [150] Miyamachi, T. *et al.* Stabilizing the magnetic moment of single holmium atoms by symmetry. *Nature* **503**, 242–246 (2013).
- [151] Limot, L., Pehlke, E., Kröger, J. & Berndt, R. Surface-state localization at adatoms. *Phys. Rev. Lett.* **94**, 036805 (2005).
- [152] Schull, G., Frederiksen, T., Brandbyge, M. & Berndt, R. Passing current through touching molecules. *Phys. Rev. Lett.* **103**, 206803 (2009).
- [153] Heinrich, B. W. *et al.* Dispersion and localization of electronic states at a ferrocene/Cu(111) interface. *Phys. Rev. Lett.* **107**, 216801 (2011).

- 
- [154] Heinrich, B. W., Braun, L., Pascual, J. I. & Franke, K. J. Tuning the magnetic anisotropy of single molecules. *Nano Lett.* **15**, 4024–4028 (2015).
- [155] Wende, H. *et al.* Substrate-induced magnetic ordering and switching of iron porphyrin molecules. *Nat. Mater.* **6**, 516–520 (2007).
- [156] Bernien, M. *et al.* Tailoring the nature of magnetic coupling of fe-porphyrin molecules to ferromagnetic substrates. *Phys. Rev. Lett.* **102**, 047202 (2009).
- [157] Rizzini, A. L. *et al.* Coupling of single, double, and triple-decker metal-phthalocyanine complexes to ferromagnetic and antiferromagnetic substrates. *Surf. Sci.* **630**, 361 – 374 (2014).
- [158] Frisenda, R. *et al.* Stretching-induced conductance increase in a spin-crossover molecule. *Nano Lett.* **16**, 4733–4737 (2016). PMID: 27088578.
- [159] Bartolomé, J. *et al.* Reversible fe magnetic moment switching in catalytic oxygen reduction reaction of fe-phthalocyanine adsorbed on ag(110). *J. Phys. Chem. C* **119**, 12488–12495 (2015).
- [160] Wäckerlin, C. *et al.* Ammonia coordination introducing a magnetic moment in an on-surface low-spin porphyrin. *Angew. Chem. Int. Ed.* **52**, 4568–4571 (2013).
- [161] Miguel, J., Hermanns, C. F., Bernien, M., Krüger, A. & Kuch, W. Reversible manipulation of the magnetic coupling of single molecular spins in fe-porphyrins to a ferromagnetic substrate. *J. Phys. Chem. Lett.* **2**, 1455–1459 (2011).
- [162] Wäckerlin, C. *et al.* Controlling spins in adsorbed molecules by a chemical switch. *Nat. Commun.* **1** (2010).
- [163] Mugarza, A. *et al.* Spin coupling and relaxation inside moleculemetal contacts. *Nat. Commun.* **2**, 490 (2011).
- [164] Zhang, Y. & Deng, M. Electrical control of spin states of ferrocene on cu(111). *J. Phys. Chem. C* **119**, 21681–21687 (2015).
- [165] Harzmann, G. D., Frisenda, R., van der Zant, H. S. J. & Mayor, M. Single-molecule spin switch based on voltage-triggered distortion of the coordination sphere. *Angew. Chem. Int. Ed.* **54**, 13425–13430 (2015).
- [166] Meded, V. *et al.* Electrical control over the fe(ii) spin crossover in a single molecule: Theory and experiment. *Phys. Rev. B* **83**, 245415 (2011).
- [167] Rösner, B. *et al.* Reversible photoswitching of a spin-crossover molecular complex in the solid state at room temperature. *Angew. Chem. Int. Ed.* **54**, 12976–12980 (2015).
- [168] Warner, B. *et al.* Temperature- and light-induced spin crossover observed by x-ray spec-

- troscopy on isolated Fe(II) complexes on gold. *J. Phys. Chem. Lett.* **4**, 1546–1552 (2013).
- [169] Khajetoorians, A. A. *et al.* Tuning emergent magnetism in a hund's impurity. *Nat. Nanotechnol.* **10**, 958–964 (2015).
- [170] Dubout, Q. *et al.* Controlling the spin of co atoms on Pt(111) by hydrogen adsorption. *Phys. Rev. Lett.* **114**, 106807 (2015).
- [171] Karan, S. *et al.* Shifting the voltage drop in electron transport through a single molecule. *Phys. Rev. Lett.* **115**, 016802 (2015).
- [172] Schull, G., Dappe, Y. J., González, C., Bulou, H. & Berndt, R. Charge injection through single and double carbon bonds. *Nano Lett.* **11**, 3142–3146 (2011).
- [173] Hewson, A. *The Kondo Problem to Heavy Fermions* (Cambridge University Press, Cambridge, England, 1997).
- [174] Žitko, Peters, R. & Pruschke, T. Splitting of the Kondo resonance in anisotropic magnetic impurities on surfaces. *New J. Phys.* **11**, 053003 (2009).
- [175] Žitko, R., Peters, R. & Pruschke, T. Properties of anisotropic magnetic impurities on surfaces. *Phys. Rev. B* **78**, 224404 (2008).
- [176] Misiorny, M., Weymann, I. & Barnaś, J. Underscreened Kondo effect in  $s = 1$  magnetic quantum dots: Exchange, anisotropy, and temperature effects. *Phys. Rev. B* **86**, 245415 (2012).
- [177] Choi, D.-J., Abufager, P., Limot, L. & Lorente, N. From tunneling to contact in a magnetic atom: The non-equilibrium Kondo effect. *J. Chem. Phys.* **146**, 092309 (2017).
- [178] Goldhaber-Gordon, D. *et al.* From the Kondo regime to the mixed-valence regime in a single-electron transistor. *Phys. Rev. Lett.* **81**, 5225–5228 (1998).
- [179] van der Wiel, W. G. *et al.* The Kondo effect in the unitary limit. *Science* **289**, 2105–2108 (2000).
- [180] Tao, K. *et al.* Switching a single spin on metal surfaces by a STM tip: Ab initio studies. *Phys. Rev. Lett.* **103**, 057202 (2009).
- [181] Sanvito, S. Molecular spintronics. *Chem. Soc. Rev.* **40**, 3336–3355 (2011).
- [182] Pasupathy, A. N. *et al.* The Kondo effect in the presence of ferromagnetism. *Science* **306**, 86–89 (2004).
- [183] Oka, H. *et al.* Spin-dependent quantum interference within a single magnetic nanostructure. *Science* **327**, 843–846 (2010).
- [184] Heinrich, B. W. *et al.* Spin structure of an atomic protrusion: Probing single atoms on cobalt nanoislands. *Phys. Rev. B* **79**, 113401 (2009).

- 
- [185] Muenks, M., Jacobson, P., Ternes, M. & Kern, K. Correlation-driven transport asymmetries through coupled spins in a tunnel junction. *Nat. Commun.* **8**, 14119 (2017).
  - [186] Kaiser, U., Schwarz, A. & Wiesendanger, R. Magnetic exchange force microscopy with atomic resolution. *Nature* **446**, 522 (2007).
  - [187] Grenz, J., Köhler, A., Schwarz, A. & Wiesendanger, R. Probing the nano-skyrmion lattice on Fe/Ir(111) with magnetic exchange force microscopy. *Phys. Rev. Lett.* **119**, 047205 (2017).
  - [188] Paaske, J. & Flensberg, K. Vibrational sidebands and the Kondo effect in molecular transistors. *Phys. Rev. Lett.* **94**, 176801 (2005).
  - [189] Parks, J. J. *et al.* Tuning the Kondo effect with a mechanically controllable break junction. *Phys. Rev. Lett.* **99**, 026601 (2007).
  - [190] Fernández-Torrente, I., Franke, K. J. & Pascual, J. I. Vibrational Kondo effect in pure organic charge-transfer assemblies. *Phys. Rev. Lett.* **101**, 217203 (2008).
  - [191] Erskine, J. L. & Stern, E. A. Calculation of the  $M_{23}$  magneto-optical absorption spectrum of ferromagnetic nickel. *Phys. Rev. B* **12**, 5016–5024 (1975).
  - [192] Schütz, G. *et al.* Absorption of circularly polarized x rays in iron. *Phys. Rev. Lett.* **58**, 737–740 (1987).



# List of Figures

1	Détection du magnétisme de surface sous STM. . . . .	IV
2	STM polarisé en spin. . . . .	V
3	Principe de l'effet Kondo . . . . .	VII
4	Couplage d'échange avec le bain électronique. . . . .	VIII
5	Spectroscopie d'excitation de spin . . . . .	IX
6	Principe du microscope à effet tunnel. . . . .	X
7	Boucle d'asservissement du mode courant constant d'un STM. . . . .	XI
8	(a) Image STM d'un Nc isolé et de deux adatomes de Fe ( $40 \times 40 \text{ \AA}^2$ , 20 mV, 50 pA). Encadré image en régime contact de la surface Cu(100) ( $16.5 \times 16.5 \text{ \AA}^2$ , 10 mV, 8 nA) (b) Image STM d'un réseau par de molécules montrant les différents paramètres de maille. ( $70 \times 70 \text{ \AA}^2$ , 20 mV, 20 pA) Encadré : Image STM du même réseau montrant des molécules verticales (cercle) et des molécules horizontales (sabliers). ( $28 \times 28 \text{ \AA}^2$ , 1 mV, 10 pA). . . . .	XIII
9	(a) Diagramme en énergie des états de moment de spin du nickelocène. (b) STS faisant apparaître $dI/dV$ et $d^2I/dV^2$ réalisée sur un Nc. ( $I = 50 \text{ pA}$ ; $V = -15 \text{ mV}$ ).XIV	XIV
10	(a) Image STM d'un adatomes de Fe sur Cu(100) réalisé avec la pointe de Nc ( $2 \times 2 \text{ nm}^2$ , $-15 \text{ mV}$ , 30 pA). Encadré : simulation par DFT de la pointe moléculaire avec la simulation de l'apex de la pointe. (b) Spectre en $dI/dV$ de la pointe moléculaire au dessus de la surface ed Cu(100) ( $I = 1 \text{ nA}$ , $V = -20 \text{ mV}$ ). (c) Spectre en $d^2I/dV^2$ correspondant. . . . .	XVI

11	(a) Image STM réalisé avec la pointe moléculaire en contact avec la surface Cu(100) ( $2 \times 1.4 \text{ nm}^2$ , 30 mV, 300 nA) (b) $G/G_0(z)$ réalisé en top (croix rouge (a)) d'un atome avec le régime tunnel (en bleu) et le régime contact (en rouge) démarqués par un saut de conductance positionné en zéro définissant le point de contact. (c) Spectre en $dI/dV$ en régime tunnel. (d) Spectre en $dI/dV$ en régime de contact (rouge). . . . .	XVII
12	(a) Représentation de la jonction avec la pointe STM fonctionnalisée par un Nc et un adatome de Fe adsorbé sur la surface. (b) $d^2I/dV^2$ réalisé avec la pointe moléculaire au dessus d'un adatome de Fe pour une distance $z$ entre Nc et Fe de 133 pm et 80 pm. . . . .	XIX
13	(a) Spectre en $d^2I/dV^2$ réalisé à 80 pm présentant la définition de du champ d'échange $B$ et de l'asymétrie $\eta$ . (b) Champ d'échange $B$ modélisant le couplage en fonction de $z$ . (c) Asymétrie $\eta$ extraite des spectres en fonction du champ d'échange. . . . .	XX
14	(a) Image STM d'un îlot de Co avec des Nc sur Cu(111) ( $25 \times 25 \text{ nm}^2$ , -20 mv, 20 pA) (b) Champ d'échange $B$ en fonction de $z$ pour la pointe de Nc au dessus d'un îlot de Co. Encadré : diagramme en énergie pour les états de moment de spin de Nc. . . . .	XXI
15	(a) Image STM à hauteur constante montrant la résolution atomique de l'îlot. ( $z = 80 \text{ pm}$ , $V = -1 \text{ mV}$ , $1 \times 1 \text{ nm}^2$ ) (b) Même image mais réalisée à $V = -5 \text{ mV}$ (c) $d^2I/dV^2$ réalisé avec la pointe moléculaire au dessus du site "top" (bleu) et au dessus du site "hollow" (rouge) de l'îlot de Co ( $z = 80 \text{ pm}$ ) (d) Rapport entre le courant mesuré en position "top" et le courant mesuré en position "hollow" pour $z = 80 \text{ pm}$ . . . . .	XXII
1.1	Spin-detection with STM. . . . .	2
1.2	Spin-polarized STM of cobalt islands. . . . .	4
1.3	Single-atom magnetization curve. . . . .	5
1.4	Anderson model. . . . .	6
1.5	Elastic spin-flip scattering. . . . .	7
1.6	Kondo ground state. . . . .	8
1.7	Detecting the Kondo resonance with STM. . . . .	10
1.8	Kondo effect from tunnel to contact. . . . .	11



---

1.9	Spin excitation spectrum of a Mn atom on $\text{Al}_2\text{O}_3$ .	13
1.10	Spin excitation spectrum revealing magnetic anisotropy.	16
1.11	Spin excitation spectrum of coupled spins.	18
1.12	Spin excitation spectrum revealing spin pumping.	19
1.13	Spin excitation spectrum revealing Kondo scattering.	21
2.1	Electron tunneling across a one-dimensional barrier.	25
2.2	Tersoff and Hamann tip representation	27
2.3	Tunneling barrier for positive and negative sample bias	29
2.4	IETS fingerprint.	31
2.5	Smearing functions in STS	34
2.6	Smearing functions in IETS	35
2.7	Sketch of the feedback loop of the STM	37
2.8	The STM used in this thesis.	38
3.1	Structure and configuration of metallocenes.	42
3.2	Deposition setup.	43
3.3	Adsorption geometries of nickelocene.	44
3.4	Single-molecule adsorption.	45
3.5	Apparent height of single molecules and molecular layers.	47
3.6	Paired layer.	48
3.7	Computed paired layer.	50
3.8	Compact layer.	51
3.9	Magnetic configuration of free nickelocene.	53
3.10	DFT-computed spin-polarized PDOS of single nickelocene on Cu(100).	54
3.11	XMCD measurements of nickelocene on Cu(100).	55
3.12	Spin excitation spectroscopy of nickelocene on Cu(100).	58
3.13	Inelastic conductance versus apparent height of nickelocene on Cu(100).	59
3.14	NEGF-DFT calculations.	61
3.15	Simulated spin excitation spectrum of nickelocene on Cu(100).	63
4.1	Attaching nickelocene to the tip apex.	68
4.2	Imaging with a nickelocene tip.	70
4.3	Spectroscopic fingerprint of a nickelocene tip.	72

4.4	Double spin excitation. . . . .	74
4.5	Tunnel versus contact regime. . . . .	77
4.6	Telegraphic spectra. . . . .	78
4.7	Simulated spin excitation spectra versus tip-sample distance. . . . .	79
4.8	Spin-flip scattering by an impurity. . . . .	80
4.9	Spin-1/2 Kondo effect. . . . .	81
4.10	DFT-computed single-nickelocene junction. . . . .	83
4.11	Electronic structure in tunnel and contact regimes. . . . .	85
5.1	Tip-adatom distance. . . . .	88
5.2	Spin excitation spectra above the Fe adatom. . . . .	90
5.3	Magnetic coupling . . . . .	92
5.4	Exchange field. . . . .	94
5.5	Spin asymmetry. . . . .	96
5.6	Computed electronic structure for the Fe-Nc junction. . . . .	98
5.7	Electronic structure of a cobalt island. . . . .	100
5.8	Nickelocene adsorption on cobalt. . . . .	101
5.9	Spin excitation spectra above a cobalt surface. . . . .	102
5.10	Atomically resolving the exchange field. . . . .	103
5.11	Computed exchange interaction between nickelocene and cobalt. . . . .	104
5.12	Spin asymmetry at the corner of a cobalt island. . . . .	106
5.13	Cobaltocene-terminated tip . . . . .	111
A.1	X-rays absorption spectroscopy principle . . . . .	116
A.2	XAS, XMCD and sum-rules . . . . .	117

# Curriculum Vitae

## Education

### **2015-2018: PhD in Nanoscience and Quantum Physics**

*Atomic-scale spin-sensing with a single molecule at the apex of a scanning tunneling microscope*

IPCMS (UMR 7540), University of Strasbourg, CNRS (Strasbourg, France)

Funding: French Ministry of Research

Thesis supervisor: Laurent Limot

### **2013-2015: MSc Research in Physics**

University of Toulouse (Toulouse, France)

### **2012-2013: BSc Physics**

University of Toulouse (Toulouse, France)

### **2010-2012: Preparatory classes Math-Physics**

Lycée Gay Lussac (Limoges, France)

Eligibility for National Competitive Examination: Télécom-INT

## Internships

### **2015: MSc internship, 5 months**

IPCMS (UMR 7540), University of Strasbourg, CNRS (Strasbourg, France)

Subject: Transport through an organometallic nanowire. Worked on a low-temperature STM

Supervisor: Laurent Limot

**2014: MSc internship, 2 months**

CEMES (UPR 8011) (Toulouse, France)

Subject: Study of a Ru-complex by STM and STS. Worked on a low-temperature STM and in a clean room

Supervisor: Roland Coratger

**2013: Created a photovoltaic cell from bulk silicon, 4 days**

“l'Atelier Interuniversitaire de Micro-Nano Electronique” (Toulouse, France)

**2013: Internship for the initiation to experimental research, 1 month**

Worked on a low-temperature STM and in a clean room

Supervisor: Roland Coratger

## Teaching experience

**Solid-state physics:** 42 hours for engineering students at Télécom Strasbourg

**Physics of semiconductors:** 21 hours for engineering students at Télécom Strasbourg

## Miscellaneous

Attended the **Synchrotron Radiation and Magnetism School** in Mittelwhir (2018), France

Participated to the **Doctoriales d'Alsace 2017**, Munster, France

Workshop for Ph.D. students with the purpose to simulate the elaboration of a start-up company. The workshop is carried out with the help of professionals and is concluded by a presentation in front of a committee of local CEO's. During the workshop I presented a poster on my thesis.

## Lab involvement

Member of the electoral committee for the IPCMS Lab Council

Member for the Ph.D. students of the IPCMS Lab Council

# Publications and presentations

## Publications

1. B. Verlhac, N. Bachellier, L. Garnier, M. Ormaza, P. Abufager, R. Robles, M.-L. Bocquet, M. Ternes, N. Lorente, L. Limot  
*Atomic-scale magnetometry with a single-molecule spin sensor at the apex of a scanning tunneling microscope*  
arXiv:1901.04862 (2019).
2. N. Bachellier, B. Verlhac, L. Garnier, J. Zaldívar, C. Rubio-Verdú, P. Abufager, M. Ormaza, D.-J. Choi, M.-L. Bocquet, J.I. Pascual, N. Lorente, L. Limot  
*Vibron-assisted spin excitation in a magnetically anisotropic nickelocene complex*  
arXiv:1906.00660 (2019).
3. M. Ormaza, P. Abufager, B. Verlhac, N. Bachellier, M.-L. Bocquet, N. Lorente, L. Limot  
*Controlled spin switching in a metallocene molecular junction*  
Nat. Commun. **8**, 1974 (2017)
4. M. Ormaza, N. Bachellier, M.N. Faraggi, B. Verlhac, P. Abufager, P. Ohresser, L. Joly, M. Romeo, F. Scheurer, M.-L. Bocquet, N. Lorente, L. Limot  
*Efficient spin-flip excitation of a nickelocene molecule*  
Nano Lett. **17**, 1877 (2017)
5. N. Bachellier, M. Ormaza, M. Faraggi, B. Verlhac, M. Vérot, T. Le Bahers, M.-L. Bocquet, L. Limot  
*Unveiling nickelocene bonding to a noble metal surface*  
Phys. Rev. B **93**, 195403 (2016)

## Presentations

1. Oral presentation: B. Verlhac, M. Ormaza, N. Bachellier, P. Abufager, F. Scheurer, M.-L. Bocquet, N. Lorente, L. Limot  
*Manipulation de spin d'une molécule par courant tunnel*  
**Forum des Sondes Locales**, Besançon, France, March 2016.
2. Oral presentation: B. Verlhac, M. Ormaza, N. Bachellier, P. Abufager, F. Scheurer, M.-L. Bocquet, N. Lorente, L. Limot  
*Manipulation de spin d'une molécule par courant tunnel*  
**Journées de la Matière Condensée**, Bordeaux, France, August 2016.
3. Poster: B. Verlhac, M. Ormaza, N. Bachellier, P. Abufager, M.-L. Bocquet, N. Lorente, L. Limot  
*On-surface engineering of a magnetic organometallic nanowire*  
**Labex NIE meeting, IPCMS scientific day**, Strasbourg, France, November 2016.
4. Oral presentation: B. Verlhac, M. Ormaza, N. Bachellier, L. Garnier, L. Limot, N. Lorente, M.-L. Bocquet  
*Molecular spin coupling at the tip of a STM*  
**European Conference On Surface Science 33**, Szeged, Hungary, September 2017.
5. Oral presentation: B. Verlhac, M. Ormaza, N. Bachellier, L. Garnier, L. Limot, N. Lorente, M.-L. Bocquet  
*Molecular spin coupling at the tip of a STM*  
**Colloque Louis Néel**, Paris, France, September 2017.
6. Oral presentation: B. Verlhac, M. Ormaza, N. Bachellier, L. Garnier, L. Limot, N. Lorente, M.-L. Bocquet  
*Molecular spin coupling at the tip of a STM*  
**One Day Workshop: Magnetic Nano-Objects, Université de la Grande Région**, Nancy, France, October 2017.
7. Poster: B. Verlhac, M. Ormaza, N. Bachellier, P. Abufager, M.-L. Bocquet, N. Lorente, L. Limot

*Controlled spin switch in a nickelocene molecular junction*

**Journée Surfaces et Interfaces**, Strasbourg, France, January 2018.

8. Oral presentation: B. Verlhac, N. Bachellier, M. Ormaza, P. Abufager, M.-L. Bocquet, N. Lorente, L. Limot

*Tip-assisted spin switching for a metallocene molecule in STM*

**Deutsche Physikalische Gesellschaft Spring Meeting 2018**, Berlin, Germany, March 2018.

9. Oral presentation: B. Verlhac, N. Bachellier, M. Ormaza, M.-L. Bocquet, N. Lorente, M. Ternes, L. Limot

*Superexchange detection through a nickelocene molecule in STM*

**Deutsche Physikalische Gesellschaft Spring Meeting 2018**, Berlin, Germany, March 2018.







# Atomic-scale spin-sensing with a single molecule at the apex of a scanning tunneling microscope

## Résumé

L'étude présentée dans ce manuscrit s'inscrit dans le domaine du magnétisme de surface, qui a connu de grands développements ces dernières années grâce au microscope à effet tunnel (STM). Elle a pour but de montrer qu'une molécule simple, le nickelocène  $[\text{Ni}(\text{C}_5\text{H}_5)_2]$ , peut être attachée au sommet d'une pointe STM afin de produire une pointe-sonde magnétique, qui, dans le cadre de l'imagerie magnétique, présente des avantages indéniables comparés à des pointes conventionnelles. À la différence d'autres systèmes moléculaires étudiés avec le STM, nous montrons que les propriétés magnétiques du nickelocène en phase gazeuse sont préservées en présence d'un métal, même lorsque la molécule est attachée au sommet d'une pointe STM. Nous présentons trois résultats marquants avec cette pointe-sonde moléculaire: 1) Nous montrons que l'on peut contrôler le spin du nickelocène, activant à souhait un effet Kondo ; 2) Nous produisons à l'aide du courant tunnel des excitations entre les états de spin du nickelocène, que nous pouvons aisément identifier au travers de la conductance moléculaire. Ces états sont sensibles à toute perturbation magnétique extérieure au nickelocène; 3) Au travers de ces excitations, nous sondons alors le magnétisme de surface. Nous montrons qu'en couplant magnétiquement la pointe-sonde moléculaire avec des atomes, soit isolés soit dans une surface ferromagnétique, nous pouvons mesurer leur polarisation de spin, ainsi que le couplage d'échange nickelocène-atome. Ce dernier permet d'obtenir un contraste magnétique en imagerie STM à l'échelle atomique.

**Mots clés** : STM, STS, spectroscope par excitation de spin, métallocène, nanomagnétisme, spintronique moléculaire, effet Kondo.

## Résumé en anglais

The study presented in this manuscript is part of the field of surface magnetism, which has undergone major developments in recent years thanks to the scanning tunneling microscope (STM). It aims to show that a single molecule, nickelocene  $[\text{Ni}(\text{C}_5\text{H}_5)_2]$ , can be attached to the tip of a STM to produce a magnetic probe-tip, which, in the context of magnetic imaging, has undeniable advantages compared to conventional tips. Unlike other molecular systems studied with STM, we show that the magnetic properties of nickelocene in the gas phase are preserved in the presence of a metal, even when the molecule is attached to the tip of a STM. We present three remarkable results with this molecular probe-tip: 1) We show that we can control the spin of nickelocene, activating at will a Kondo effect; 2) We monitor the spin states of nickelocene by producing electrically-driven excitations, which we can easily identify through the molecular conductance. These states are sensitive to the magnetic environment surrounding nickelocene; 3) We use these states to probe surface magnetism. We show that by magnetically coupling the molecular probe tip with single atoms, either isolated or in a ferromagnetic surface, we can measure their spin polarization, as well as the nickelocene-atom exchange coupling. By monitoring this coupling it is possible to obtain a magnetic contrast in the STM images with atomic-scale resolution.

**Keywords** : STM, STS, spin excitation spectroscopy, metallocene, nanomagnetism, molecular spintronics, Kondo effect.